SRS

SPECTRA RESEARCH SYSTEMS

SOUTHEASTERN OPERATIONS
555 SPARKMAN ☐ SUITE 1406 ☐ HUNTSVILLE, ALABAMA 35805 ☐ (205) 830-0375

SRS SPECTRA RESEARCH SYSTEMS
SOUTHEASTERN OPERATIONS
☐ 555 SPARKMAN ☐ SUITE 1406 ☐ HUNTSVILLE, ALABAMA 35805 ☐ (205) 830-0375

SRS/SE-TR84-022
CN60

BEARING TESTER DATA COMPILATION, ANALYSIS, AND REPORTING AND BEARING MATH MODELING

FINAL REPORT

VOLUME I

MAY 1984

PREPARED BY:
SPECTRA RESEARCH SYSTEMS
SOUTHEASTERN OPERATIONS
555 SPARKMAN DRIVE, SUITE 1406
HUNTSVILLE, AL 35805

UNDER CONTRACT NAS8-34686

FOR THE

GEORGE C. MARSHALL SPACE FLIGHT CENTER
NATIONAL AERONAUTICS AND SPACE ADMINISTRATION

FOREWORD

This report was prepared by Spectra Research Systems under Contract No. NAS8-34686 entitled "Bearing Tester Data Compilation, Analysis, and Reporting and Bearing Math Modeling" for the George C. Marshall Space Flight Center of the National Aeronautics and Space Administration. The work was administered under the technical direction of the Materials and Processes Laboratory, Engineering Physics Division of the George C. Marshall Space Flight Center with Mr. Fred J. Dolan acting as project manager.

This report describes the work performed by Spectra Research Systems Southeastern Operations during the July 1982 - April 1984 period. Mr. Rodney Bradford was the Spectra Research Systems Project Manager. The project technical staff was directed by Mr. Joseph C. Cody who was the Project Engineer. A listing of the key project staff members is shown below:

Dr. D. David Marshall
Mr. Edward E. Montgomery
Ms. Linda S. New
Mr. M. Anthony Stone
Mr. Bruce K. Tiller.

TABLE OF CONTENTS

VOLUME I

SECTION PAGE

TABLE OF CONTENTS

SECTION PAGE

TABLE OF CONTENTS

SECTION PAGE

VOLUME II

LIST OF FIGURES

LIST OF FIGURES (CONTINUED)

LIST OF FIGURES (CONTINUED)

LIST OF FIGURES (CONTINUED)

LIST OF FIGURES (CONTINUED)

1.0 INTRODUCTION

This report describes the work accomplished during the contract period July 1982 - April 1984 in support of the MSFC Bearing and Materials Tester (BMT) Program. The objective of this activity is to support the development and operation of the BMT including data reduction and evaluation. Since the Shuttle Main Engine (SSME) turbopump bearings operate in an environment considerably more severe than conventional bearing systems, traditional analysis methods and bearing life models are not directly applicable.

The MSFC BMT Program is therefore directed toward a better understanding of the various parameters that effect/or determine the SSME turbopump bearing operational characteristics and service life and to develop and verify design tools applicable to these systems. Support of this program involves a broad spectrum of engineering analysis activities including static analysis of the BMT Shaft Bearing System, high-speed bearing system analysis, contact stress evaluation, bearing failure mode evaluation and thermal modeling of the bearing and cryogenic flow system. The tasks described in this report do not represent the total analysis effort for the design and development of the BMT. The enclosed work was done to support the development of the BMT in specialized areas as problems occurred and to support the stated objectives. BMT test data are reduced, evaluated, and correlated with analyses where applicable. Since test data applicable to the turbopump bearing system are limited and the system and operating conditions are of such complexity that theoretical modeling requires unprecedented extrapolations, additional data from the BMT are required to fully substantiate turbopump bearing analysis results and bearing life predictions.

2.0 SUMMARY

Thermal and mechanical models of high-speed angular contact ball bearings operating in LOX and LN_2 have been developed and verified with limited test data during the contract period. The work thus far demonstrates that a combined analytical-test approach is required to understand and evaluate these severe and complex bearing operating conditions.

Significant progress has been made in understanding and adapting the SHABERTH bearing analysis computer program for evaluation of cryogenic bearing systems. This program was developed for the analysis of jet engine shaft/bearing systems operating above room temperature with normal hydrocarbon lubricants. Through continued analysis effort, it has been possible to adapt this tool to the evaluation of shaft bearing systems operating in cryogenics.

Effects such as fluid drag, radial temperature gradients, outer race misalignments and clearance changes have been simulated and evaluated. In addition, the speed and preload effects on bearing radial stiffness has been evaluated. The SHABERTH program has also been used to provide contact stresses from which contact geometry has been calculated to support other analyses such as the determination of cryogenic fluid film thickness in the contacts and evaluation of surface and subsurface stresses necessary for bearing failure evaluation. This program has been a vital tool for the thermal analysis of the bearing in that it provides the heat generation rates at the rolling element/race contacts for input into a thermal model of the bearing/shaft assembly.

Although the SHABERTH computer code (See Reference 41) has a thermal subroutine, it is not capable of accommodating varying thermal properties and two phase flow. A bearing thermal model with this capability has been developed using the SINDA thermal analyzer. The bearing/shaft assembly and cryogenic coolant flow are thermally simulated by a nodal network and the model provides a detailed description of the bearing and assembly component temperatures and gradients. The model accounts for the various heat transfer regimes encountered in a two phase flow system and allows the assessment of parameters such as load, speed, flow rate, fluid subcooling, etc. on bearing component temperatures. Bearing contact surfaces are modeled in detail, to assess the maximum surface temperatures, and complete descriptions of component temperature gradients are provided. This can be important in assessing the characteristics such as fluid film thickness, film lubricant requirements, and effects on contact friction. Test data from the BMT has been used when possible to calibrate and verify the thermal model. Additional test data at varied tester operating conditions will be required for further model verification.

Iteration between the SHABERTH bearing model and the SINDA thermal model is necessary for complete analysis of the bearing/shaft assembly. This is necessary due to the strong coupling between bearing component temperatures and internal operating clearances. As the inner race temperature exceeds that of the outer race, thermal growth reduces or eliminates the operating clearances. This in turn increases the contact stresses and forces which, increase the frictional heat generated. This is a cycle that will cause premature bearing failure if it proceeds unchecked. This condition has been simulated by utilizing the SHABERTH bearing program and the SINDA bearing thermal model. By this analysis method, preliminary bounds have been established for stable operation in LN_2. These limits have been established in terms of fluid flow, fluid inlet temperature, and axial load for a shaft speed of 30,000 RPM.

It is very important to conduct this analysis procedure to determine preliminary bounds for stable operation in LOX. Additional analyses of this nature have been done for a range of shaft speeds to determine the effects of shaft speed on bearing operating characteristics and temperatures.

The importance of understanding and developing reliable analysis tools for estimating the mechanical/thermal interactions of the bearing system and these effects on bearing performance and life cannot be over emphasized. There are many deficiencies in the analytical methods available and applicable test data is nonexistent. Therefore, these gaps must be filled with additional BMT test and operational data before reliable predictions concerning Shuttle Main Engine turbopump bearing performance and life can be made.

There is a strong mechanical/thermal interaction in the turbopump shaft/ bearing system. This is especially critical in cryogenically cooled systems because of the drastically changing cooling ability as the fluid changes from liquid to vapor. As an example, an increase in load can cause transition from forced convection liquid cooling to forced convection vapor cooling with a significantly large increase in component temperatures. Such increases can rapidly eliminate internal clearances, increase contact stresses and frictional heat causing further heating until failure occurs. This unstable condition can further be aggravated by extremely high temperatures in the contact areas which can cause breakdown of the dry film lubricant, significantly increasing the frictional heat generation.

In addition to rapid bearing failure, less severe cases can cause failures different from the subsurface fatigue failures experienced by conventional oil lubricated bearings. As will be discussed later, increased surface friction moves the maximum shear stresses to the surfaces and therefore, the failure occurs in the surface rather than below the surface. Furthermore, the high temperatures predicted will significantly degrade the material properties in the surface and this, combined with loss of lubricant, allows surface wear to become a potential failure mode. Due to the steep thermal gradients at the bearing contact surfaces, there is a strong possibility that thermally induced stresses are significant contributors to bearing failure. These conditions and failure modes are vastly different from those experienced by conventionally operated and lubricated rolling bearings. Therefore, the data base for conventional bearing life predictions has severely limited validity when extrapolated to high-speed bearings operating in cryogenics.

Estimating coolant flow requirements for cryogenically cooled bearing systems, typical of the SSME turbopumps, requires consideration of mechanical/thermal coupling of the system. Analysis has shown that system heat generation is not a simple function of applied load. As previously discussed, the establishment of a temperature gradient across the bearing will increase the frictional heat generated. For example, the coolant outlet temperature is essentially linear with flow for a constant heat input which, for a bearing of uniform temperature, would indicate a constant load. However, for a condition (this could be a low-flow case) that allows an adverse temperature gradient to establish itself across the bearing, the heat generated will be considerably greater for the same axial load causing a higher coolant outlet temperature. Therefore, rather than a linear coolant outlet temperature increase with decreasing flow, the outlet coolant temperature increase can become exponential with decreasing coolant flow. The required coolant flow should be specified to maintain the essentially linear relationship between flow and outlet coolant temperature for given load and bearing speed conditions.

Contact stress analyses show that the maximum shear stress occurs in the surface of the contact for friction factors greater than 0.19. For marginally lubricated bearings operating in cryogenics, it is very likely that the contact friction factor is greater than 0.19. This is especially true when the bearing contact temperatures are significantly above the cryogenic saturation temperature. This condition precludes any liquid film support between the contact. In addition, many dry film lubricants fail at temperatures approaching 500-700°F. Consequently, surface failure modes are strong candidates for bearings operating in these environments.

Further research is needed to characterize the performance of dry film lubricants operating in cryogenics and the effects of contact surface temperature on the performance of these lubricants. The contact lubrication and traction, for bearing systems similar to those studied in this report, probably vary considerably with operation time and contact temperature. A key part of the bearing thermal analysis is the determination of the friction heat generated in the bearing contacts. This requires knowledge of local friction forces and slip velocities and the interdependency of these variables for the specific lubrication system being analyzed. For example, the friction coefficient is generally a function of slip velocity and may be enhanced by metal oxide formation when operating in liquid oxygen. Additional test data characterizing these effects are required before reliable contact heat generation estimates can be made.

Additional work is also needed to characterize the heat transfer mechanisms for high-speed bearings operating in high-flow, subcooled, cryogenic systems. No data has been located in the literature search that is directly applicable to these conditions.

3.0 BEARING TESTER DATA EVALUATION AND TEST SUPPORT

3.1 LOX Test Incident Analysis

In support of the Bearing and Material Tester (BMT) incident investigation, a scenario has been developed which describes the potential hazards associated with operating the tester bearings in the temperature regimes that produce two phase conditions in the coolant flow. The synergism of heating rate and flow pressure losses is much more pronounced in the two phase flow regime than in the single phase regime. A simplified flow network for the BMT is shown in Figure 3.1.1. Since each pair of bearings is cooled by flow circuits in parallel, the flow resistances of each circuit must be equal for equal flow and pressure loss. Furthermore, any flow losses upstream of the bearings must be the same in each circuit.

As indicated in the figure, this is not the case for the seal leakage. This is probably not a serious factor since the absolute value of the real leakage is small. However, if the bearing component temperatures exceed the saturation temperature of the LOX coolant flow, vapor generation can significantly increase the resistance to flow through the hot bearing. This in turn can cause a reduction in flow, reduced cooling, and further increases in bearing temperature.

The effect of increased vapor generation on flow pressure loss is shown in Figure 3.1.2. This is the correlation for steam/water mixtures developed by Martinelli and Nelson. Although the correlation is for steam/water flow, it is general in the sense that the same effect is experienced with other two phase mixtures. As shown in the figure, there is a significant increase in pressure loss over the single phase value as the percentage of vapor is increased. In a parallel flow network similar to the BMT coolant circuit, this will reduce the flow to the bearing running the hottest and producing the most vapor.

Another problem with operating in the two phase regime is the possibility of exceeding the critical heat flux for nucleate boiling. This can cause a rapid increase in component surface temperature. An example of this characteristic is shown in Figure 3.1.3. Shown in this figure is the measured outer race temperature for the failed bearing superimposed on the pool boiling curve for oxygen. The bearing temperature shown is for the outer race which is the lowest expected temperature for any of the bearing components (inner race, balls, etc.). The other bearing components will be running at a temperature in excess of the measured outer race temperature.

Referring to Figure 3.1.3, it is evident that a small increase in load (heat flux) will cause the operating conditions to immediately shift to point E with a corresponding large increase in component temperature. The shift from C to D is not reversible. A reduction in load will cause the operating point to follow the path E to D and then move to the solid part of the curve horizontally across from point D. It is recognized that the boiling curve shown is for pool boiling and does not completely describe the high velocity flow through the bearings. In general, the velocity effect will be to increase the critical heat flux point. However, as stated previously, the measured temperature is the lowest expected for any bearing component. These two opposing factors will tend to cancel and the possibility of the operating point shifting as previously described is highly probable.

Supporting data indicating possible effects of vapor generation in the load side coolant path are shown in Figures 3.1.4 and 3.1.5. This data represents the LOX

SIMPLIFIED PRESSURE/FLOW NETWORK

FIGURE 3.1.1

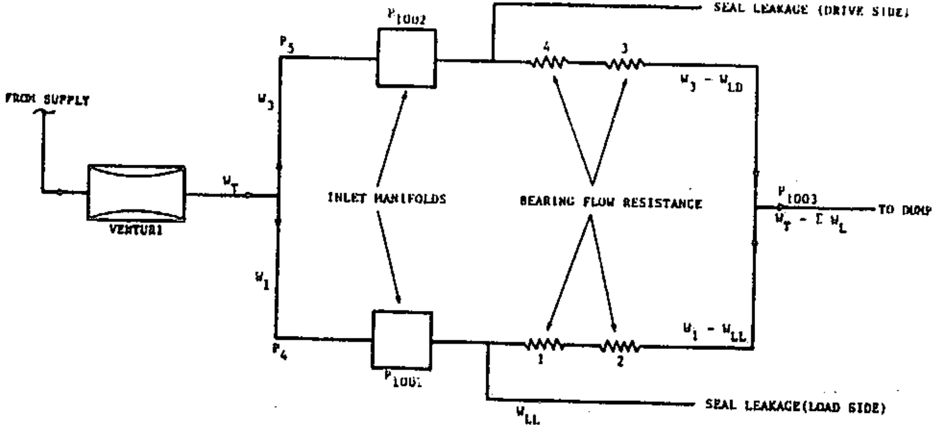

- RATIO OF LOAD END TO DRIVE END SEAL LEAK PRESSURE = 14/8.25
- RATIO OF LOAD END TO DRIVE END LEAK RATE $\sim \sqrt{14/8.25} = 1.30$
- INDICATES ABOUT 30% MORE LEAKAGE ON LOAD END, WITH CORRESPONDING LESS FLOW TO BEARINGS 1 & 2

INFLUENCE OF VAPOR GENERATION ON PRESSURE LOSS

FIGURE 3.1.2

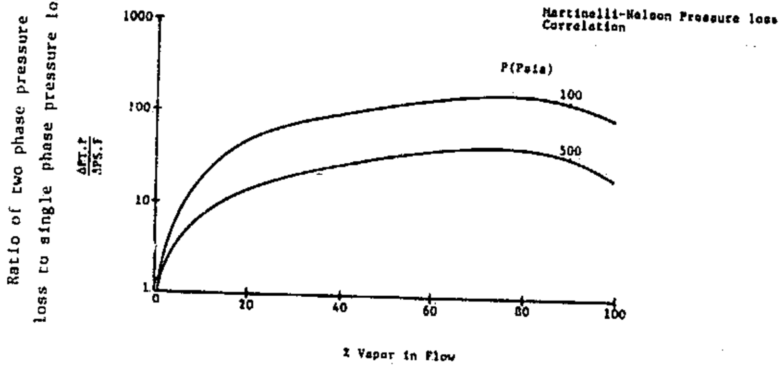

BOILING CURVE FOR OXYGEN
(Pressure=377 Psia)

FIGURE 3.1.3

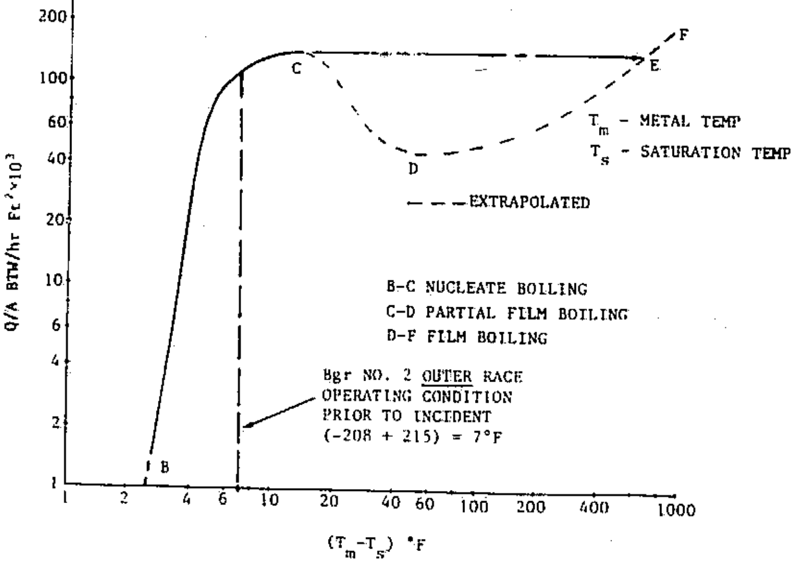

- The region of multivalue temperature difference should be avoided because of possible sudden increase in surface temperature
- Example: If point C is reached and the heat flux is increased, a first order instability occurs and the stable point rapidly shifts to point E.

ORIGINAL PAGE IS
OF POOR QUALITY

FIGURE 3.1.4 LOX INLET CAVITY PRESSURE (LOAD SIDE)

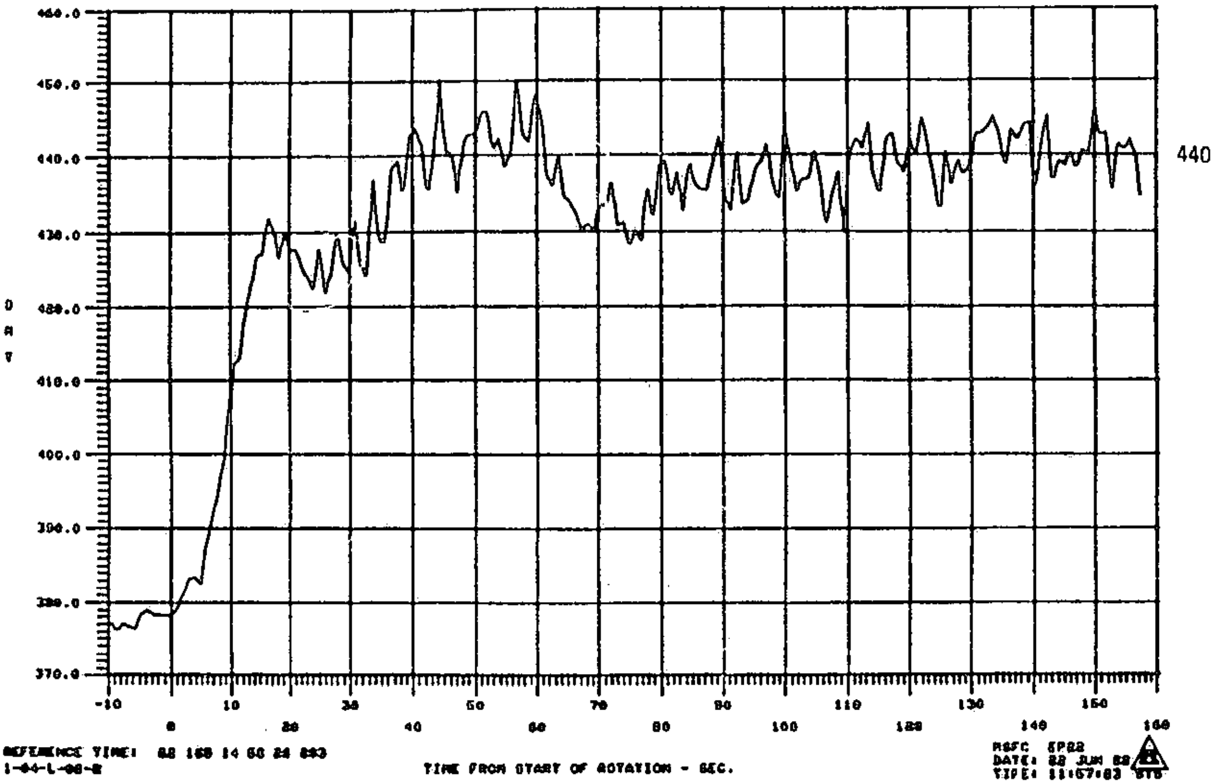

FIGURE 3.1.5 LOX INLET CAVITY PRESSURE (DRIVE SIDE)

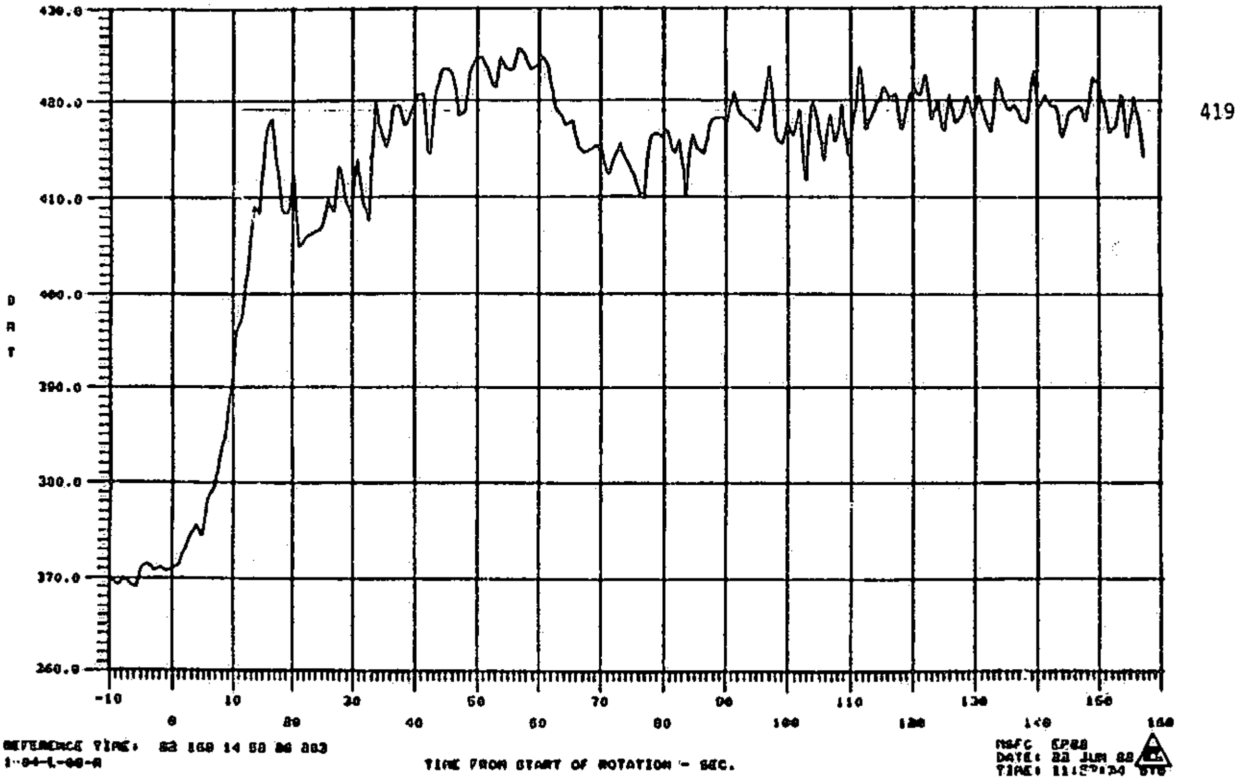

inlet manifold pressure for the flow circuits indicated. The mean steady pressure for the load side (P_{1001}) is about 440 psi, and the equivalent value for the drive side is about 419 psi. There is, however, a bias difference of about 7 psi at the no rotational point (time=0). Considering the bias, there is about a 14 psi difference between the two pressures with the load side being the greater. This could be caused by vapor generation in the load side circuit (bearings 1 and 2).

Based on the above discussion, the following conclusions can be stated:

(a) First order instabilities can occur when operating in a two phase regime near the peak flux region. This can cause a rapid increase in component temperature with a small increase in heat load. It appears, as a first order approximation, that bearing 2 was operating near this condition prior to the incident.

(b) The parallel flow arrangement in the BMT requires stable flow resistances in both paths for equal coolant flow. Large variations in flow resistance can occur due to unequal heat generation in the bearings if the flow is two phase.

(c) The combination of coolant flow reduction, increased vapor generation, and loss of cooling efficiency can cause a "run away" situation causing rapid increase in component temperature and subsequent failure.

(d) Based on the above, the BMT bearing components should not be operated above the coolant saturation temperature unless absolutely necessary. If operating above the saturation temperature is required, the operating condition should be evaluated with respect to the peak flux condition to assure adequate cooling margin and sufficient coolant flow to each flow circuit.

3.2 Recommended Coolant Temperature Limits for 57 mm Bearing Operating in LN_2

Since the liquid density of LN_2 is approximately 43% less than LOX at the nominal operating temperatures and pressures for the BMT, the viscous work done on the LN_2 is estimated to be approximately 43% less than the work done on the LOX, provided the tester configuration was identical for the LN_2 and LOX tests. The overall energy balances (Figure 4.3.6) for the LN_2 and LOX tests show that the energy input to the coolant is about 11% higher for the LN_2 tests. This apparent contradiction may be due to any of the following:

a) Changes made to the BMT following the LN_2 tests. Changes were made to the slinger and could account for part of the apparent high heat input during the LN_2 tests.

b) The LOX may provide a better lubrication medium than the LN_2. Since LN_2 is inert, any oxide films would not be reformed once worn away. Such films could improve the friction coefficient.

c) Inaccurate measurement of coolant temperature and flow.

The conservative approach is to assume that the tester changes will reduce the viscous work by the density ratio (.70) and therefore the heat generated in the bearing should be limited such that a maximum value of contact stresses (∿425 K psi) will not be exceeded. The value selected corresponds to a 100°C temperature difference across the bearing, as shown in Figure 3.2.1. This is a relatively high value for sustained operation (For sustained running, the Hertz stress should be limited to ~350 K psi) but should be adequate for establishing cutoff limits.

Reducing the previously estimated viscous energy for LOX (Figure 4.3.6) to account for the lower LN_2 density, gives a value for LN_2 viscous work of 106.3 kW. The frictional heat generated by the bearings at 100°C ΔT is 15.2 kW. This gives a total heat input into the LN_2 of 121.5 kW. Based on the above values, the data provided in Figure 3.2.2 can be generated. At flow rates less than 10 lbs/sec, the limiting criteria is to maintain the coolant outlet temperature about 30° below the saturation temperature. Since the outlet temperature for the second LN_2 tests (see Figure 3.2.3) rose about 30°F, restricting average inlet flow to 160°R would give an outlet temperature of 190°R which is approximately 30° below the saturation temperature of LN_2 at 400 psia. This provides a safety factor of 2 with regard to the outlet flow conditions.

The above values provide limits based on an overall energy balance. It is also necessary to monitor and limit the energy generated by each bearing pair. To establish the limiting ΔT across the bearing, the bearing viscous work and friction heat were estimated assuming a 100°C radial temperature difference across the bearing (limits Hertz stress to ~450 K psi). The combined viscous and friction heat for one bearing pair was estimated to be 32 kW. Based on this value, the data provided in Figure 3.2.4 were generated. The curves in Figures 3.2.2 and 3.2.4 are cut horizontally (dashed lines) at specific values of ΔT available across the tester. The available ΔT is approximately 60°R ($T_{SAT} - T_{IN}$). Thirty degrees of this value was used as a safety factor. At a flow rate of 10lbs/sec (total), about 12 degrees ΔT occurs across the bearing. This would allow about 18° for viscous work on the fluid excluding that done by the bearing. This is the minimum flow that will meet the imposed temperature restrictions. However, since a new tester configuration is being tested for the first time, flow rates less than those previously used, 12.6 lbs/sec, are not recommended. Based on a flow of 12.6 lbs/sec, an inlet temperature of 160°R, and a limiting ΔT of 18°R across the tester, the cutoff outlet temperature should be 178°R or -282°F, and the ΔT across the bearing should not exceed 9°R.

To gain a clearer understanding of the magnitudes of the viscous and bearing frictional heat generation and to minimize the risk to the BMT, it is recommended that a low speed (~10,000 RPM) test be performed with no applied load prior to runs at design speed. Data from this test could be used to verify heat generation estimates for updating temperature cutoff values. In view of the uncertainties in the analysis, the cutoff values provided should be considered preliminary for design speed and load tests. These analyses should be verified and/or updated based on additional data from the recommended low speed test. These cutoff values should be adequate for the low speed tests. In addition, it is recommended that the outer race temperatures be limited to 200°R. This is about 20°R below the saturation temperature at 400 psia.

3.3 Comparison of Bearing Tester Data with Thermal Model Results

A comparative analysis was performed between the test data for an LN_2 run and temperature data from the thermal model for various operating conditions. The outer edge of the outer race is divided into several nodes as shown in Figures 3.3.1 thru 3.3.4. Model temperatures are shown superimposed on the outer race thermocouple measurement. The operating conditions for the thermal analysis are noted on each figure.

FIGURE 3.2.1

CONTACT ANGLE AND STRESSES VS. BEARING TEMP DIFFERENCE

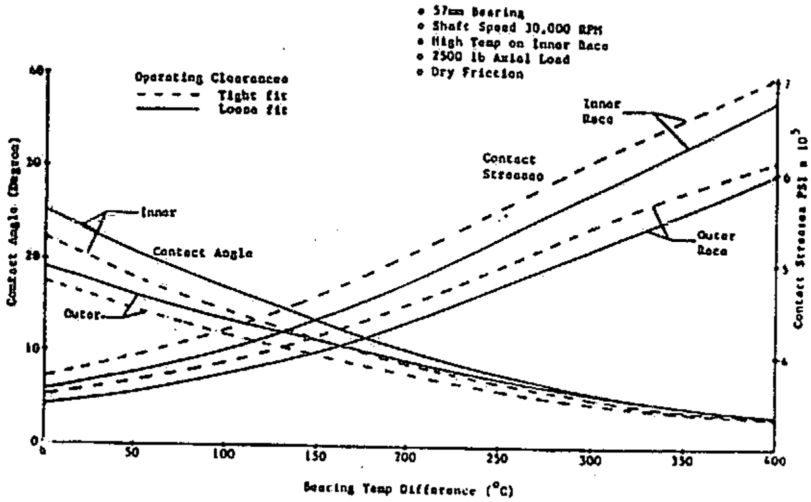

FIGURE 3.2.2

LIMITING TEMPERATURE ACROSS BEARING AND MATERIALS TESTER

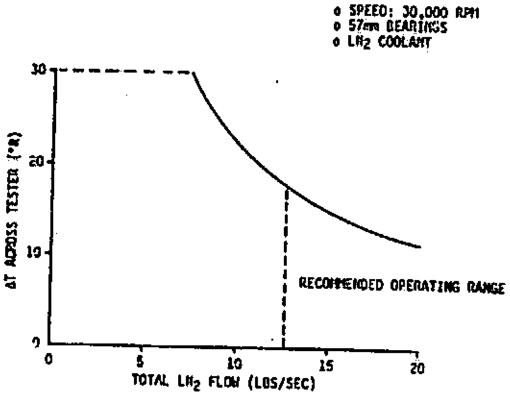

FIGURE 3.2.3

RUN NO. 2 INLET AND OUTLET TEMPERATURE vs. TIME

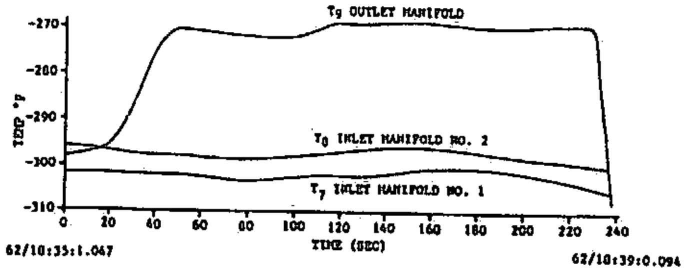

FIGURE 3.2.4

LIMITING TEMPERATURE DIFFERENCE ACROSS SINGLE BEARING PAIR

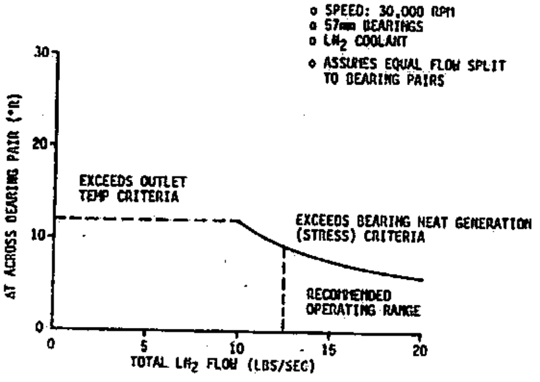

FIGURE 3.3.1. COMPARISON OF EXPERIMENTAL TEST DATA WITH THERMAL MODEL RESULTS

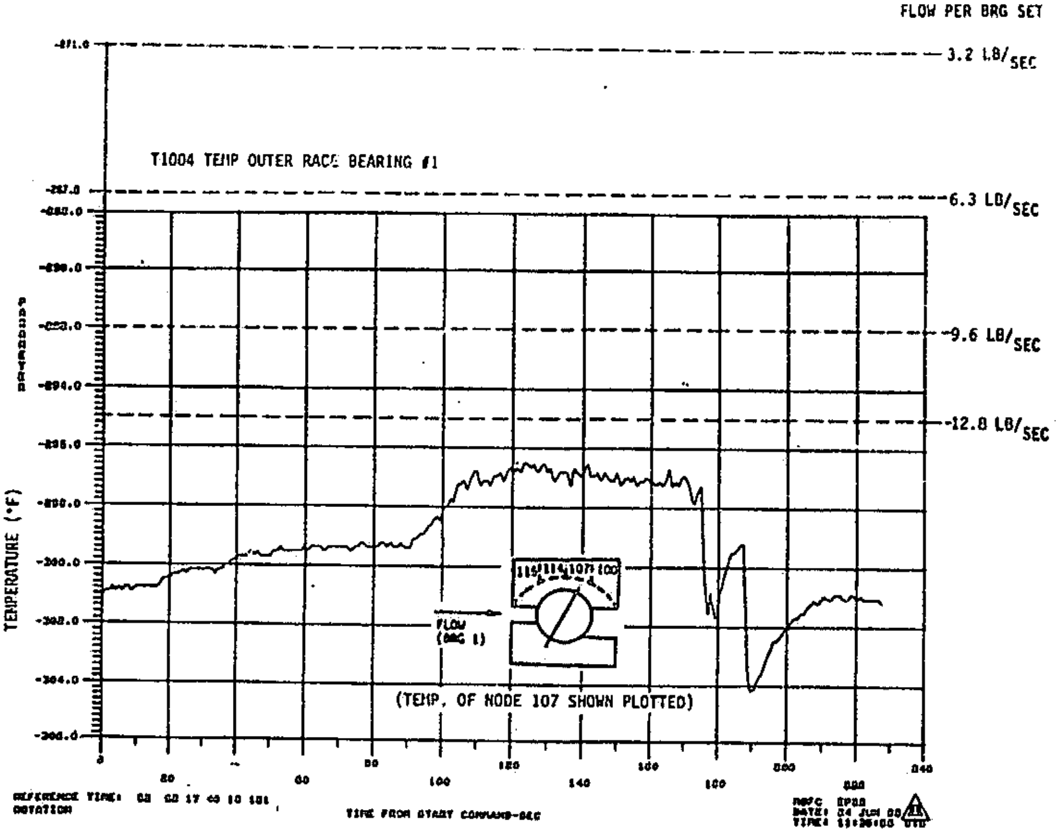

FIGURE 3.3.2 COMPARISON OF EXPERIMENTAL TEST DATA WITH THERMAL MODEL RESULTS

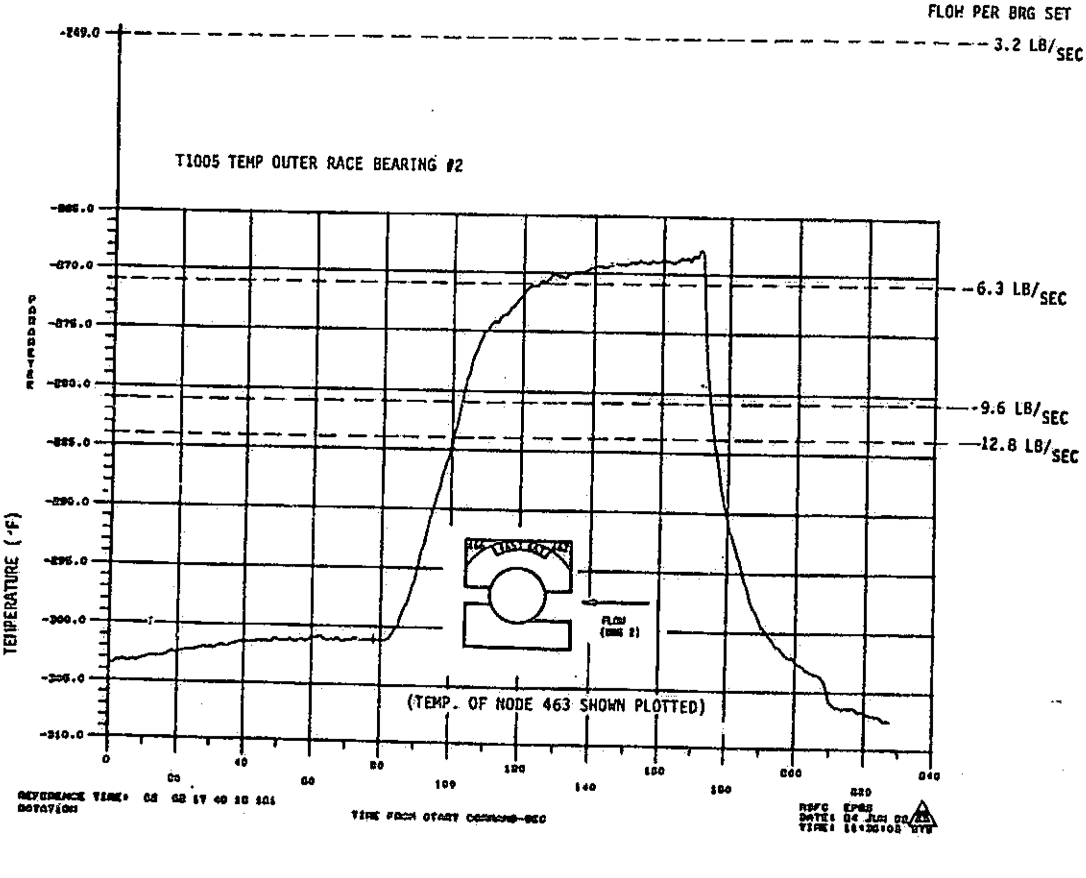

ORIGINAL PAGE IS
OF POOR QUALITY

FIGURE 3.3.3 COMPARISON OF EXPERIMENTAL TEST DATA WITH THERMAL MODEL RESULTS

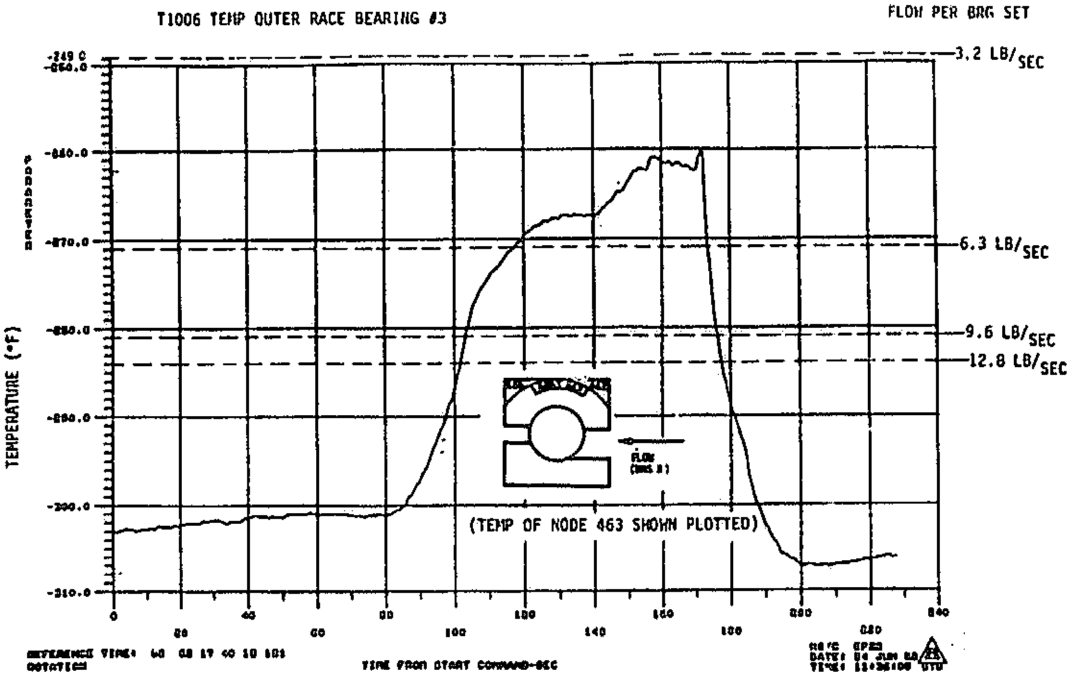
T1006 TEMP OUTER RACE BEARING #3

FLOW PER BRG SET

(TEMP OF NODE 463 SHOWN PLOTTED)

FIGURE 3.3.4 COMPARISON OF EXPERIMENTAL TEST DATA WITH THERMAL MODEL RESULTS

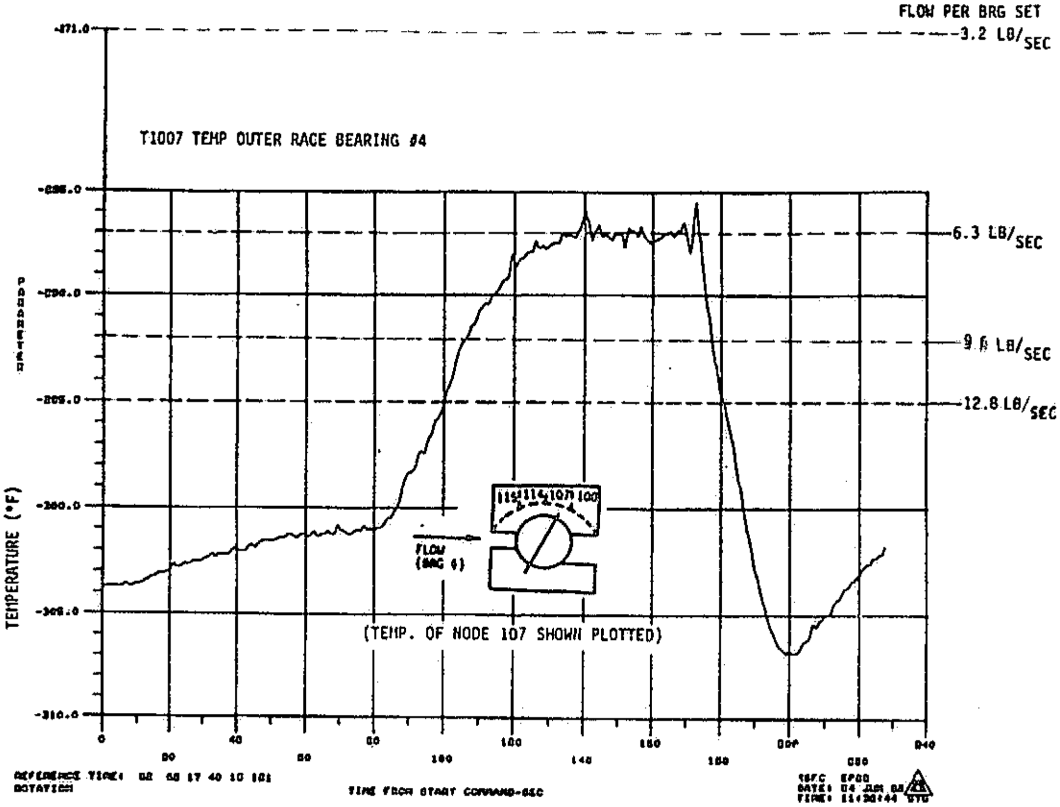
FLOW PER BRG SET

T1007 TEMP OUTER RACE BEARING #4

(TEMP. OF NODE 107 SHOWN PLOTTED)

Figure 3.3.1 shows the data from thermocouple number T1004 located on the back side of the outer race of bearing number 1. The dashed lines indicate the predicted thermal model temperatures for the nodes illustrated in the sketch. As noted in Figure 3.3.1, this analysis was conducted for an LN_2 coolant flow rate of 6.3 lb/sec per bearing set, an inlet coolant temperature of -305°F and an axial reaction of 500 pounds.

These analyses considered an axial load on the carrier of 2,500 lbs caused by the pressure differential across the carrier. This loads bearings 2 and 3 to 2,500 lbs, and unloads bearings 1 and 4 to 500 lbs (nominal preload for all bearings is 1,000 lbs).

A comparison of these data does not indicate a significant flow unbalance between bearing pairs. There does appear to be measurement problems with T1004; the outer race temperature of Bearing 1. This temperature rises only about 4° during the test, while the comparable temperature of bearing 4 rises 17°F. Further comparison of bearing 1 outer race temperature rise (T1004) with comparable measurements taken during rotational test 03-30-84, which reached a speed of about 15,000 RPM indicates that the measurement is suspect. The outer race temperature rise for bearing 1 during the 03-30-84 test rose 3.3°F which is almost as much as the data shown in 3.3.1. Since the speed during this run was approximately 30,000 RPM the outer race temperature rise should be significantly higher. Assuming T1004 is a bad measurement, the thermal model results compare reasonably well with the measured data for a coolant flow of 6.3 lbs/sec per bearing pair. These results are shown in Figures 3.3.2 through 3.3.4. Additional tester data is obviously necessary to arrive at firm conclusions concerning bearing loads coolant flow effects.

3.4 Analysis of Bearing Temperatures and Operating Characteristics

3.4.1 Sensitivity of Node Temperatures as a Function of Flow Rate and Degree of Subcooling

The LN_2 data base developed as a part of the bearing thermal model was set up with heat generation conditions to simulate a 500 pound axial reaction on bearing 1 and a 2500 and 6000 pound axial reaction on bearing 2 for a 57 mm bearing set. During the course of this investigation four different flow rates thru the bearing set; 3.2, 6.3, 9.6 and 12.8 lbs/sec were considered. For each different mass flow rate and loading condition, the thermal model was exercised for two different values of subcooled temperature; -285°F and -305°F. The frictional heat generated was determined based on a friction coefficient of 0.2 and a ΔT across the bearing as predicted by the SHABERTH bearing analysis program.

The sensitivity of several node temperatures was examined to determine the effect of changing mass flow rate, degree of subcooling and loading conditions. In figure 3.4.1 a plot of the temperature of the hottest track node on the inner race versus the mass flow rate of the coolant for several loading conditions is shown for different degrees of subcooling.

As can be seen in Figure 3.4.1 for bearing 1, the effect of coolant flow, and subcooling on race temperature is about the same for the range of variables investigated. The higher load cases, 2500 and 6000 pounds on bearing 2, shows a stronger influence on coolant flow on track temperatures; especially for the case of coolant inlet temperatures of -305°F. The bearing 2 data in Figure 3.4.1 show that for the lower flows, the race temperature becomes less sensitive to subcooling. It also shows that for marginal subcooling, increasing coolant flow is not as effective in

FIGURE 3.4.1. FLOW RATE VS. INNER RACE TRACK TEMPERATURE

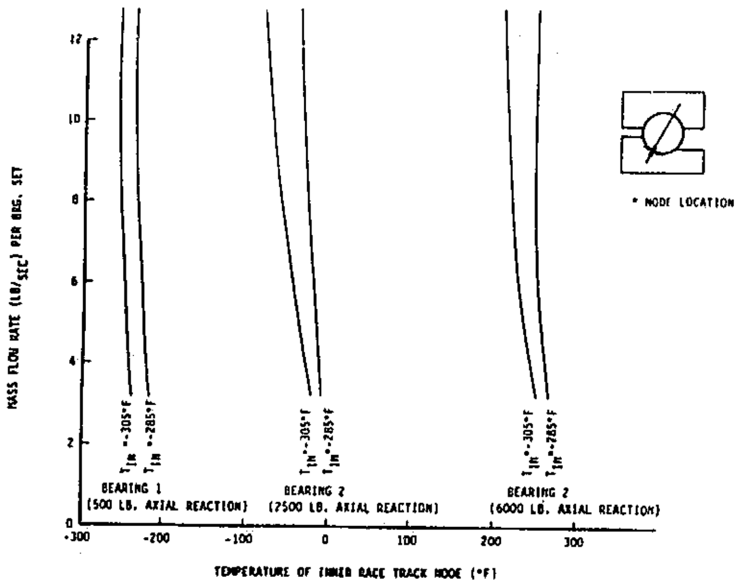

FIGURE 3.4.2. BEARING OUTLET COOLANT TEMPERATURE AND HEAT INPUT -VS- COOLANT FLOW RATE

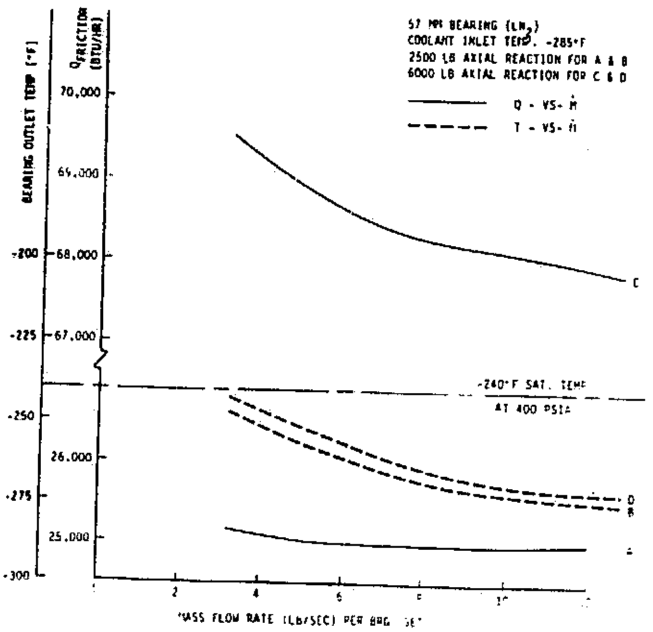

FIGURE 3.4.3. BEARING OUTLET COOLANT TEMPERATURE AND HEAT INPUT -VS- COOLANT FLOW RATE

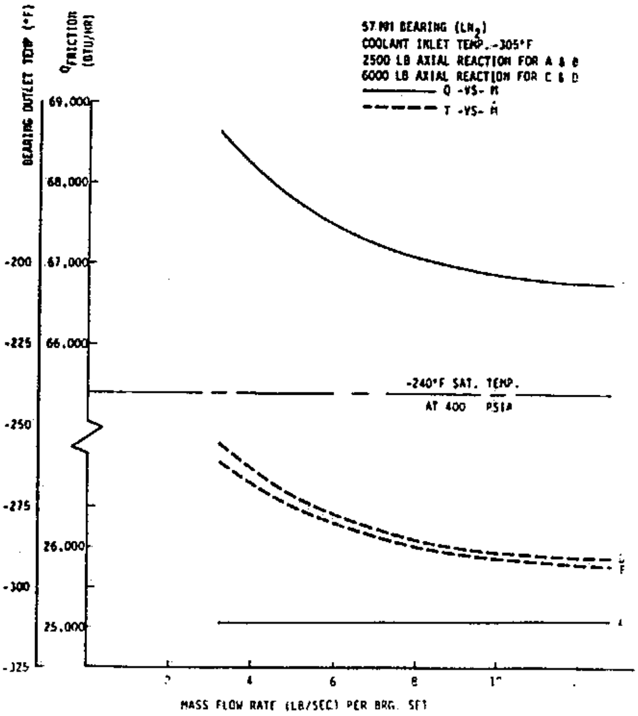

controlling race temperature. Consequently, both flow and subcooling need to be adequate for proper bearing cooling.

The dependence of bearing cooling on coolant flow is complicated due to the dependence of bearing internal clearances on component temperature. As internal clearances are reduced due to thermal growth of the inner race, with respect to the outer race, the normal forces and stresses at the contact surfaces are increased resulting in further increases in frictional heat generation and increased temperatures. Therefore, the bearing is not necessarily a constant heat generator for fixed load, speed, and varying coolant flow. Local subcooled boiling is accounted for by using two-phase boiling heat transfer correlations. This represents the physical system provided the outlet coolant temperature does not equal or exceed the coolant saturation temperature. As shown in Figure 3.4.2, for a pressure of 400 psia, the saturation temperature of LN_2 is -240°F. For a inlet coolant temperature of -285°F and an axial reaction of 2500 and 6000 pounds, the bearing outlet coolant temperature approaches the LN_2 saturation temperature at low flows. Outlet pressure slightly less than 400 psia could easily result in a condition of bulk vapor generation at the bearing outlet, increased flow resistance, and subsequent bearing failure due to inadequate cooling.

Figures 3.4.2 and 3.4.3 illustrate the dependence of frictional heat load, bearing outlet temperature, and coolant flow for the fixed conditions of axial load and coolant inlet temperatures. The 6000 lb axially loaded case shows an increase in frictional heat load as the coolant flow rate is reduced. As the coolant flow is decreased, there are two factors causing an increase in bearing outlet coolant temperature: increased heat load and flow reduction. If thermal equilibrium cannot be attained at a higher temperature compatible with bearing survival then failure occurs. The 2500 lb load case did not experience a heat load increase over the flow range investigated for either -285°F or -305°F inlet coolant temperature (Figures 3.4.4 and 3.4.5 respectively).

Test data from the planned BMT tests are critical to guide and verify the analysis effort. This program is providing considerable insight into the thermomechanical interactions of the bearings which will, when verified, provide extremely valuable information for improving the design and life of flight hardware.

3.4.2 Bearing Operating Characteristics as a Function of Speed and Axial Load

Observed wear tracks of bearing races and rolling elements can be used as a tool for estimating the loads experienced by the bearing components by matching the measured contact angles and wear tracks with predicted values. Shown in Figures 3.4.4 through 3.4.7 are contact angles and wear track half widths (semi-major axis of contact ellipse) as a function of shaft speed and axial loads. Future work in this area should include the correlation of test observations from the BMT with the enclosed data generated from the SHABERTH bearing code.

3.4.3 Bearing Coolant Flow Effects on Bearing Heat Generation, Component Temperatures, Operating Clearances, Hertz Stresses, and Contact Angles

The 57mm angular contact ball bearing (LOX turbopump turbine end bearing) was analyzed to investigate the effects of varying the coolant flow rate (LN_2) on bearing temperatures and operating characteristics such as clearances, contact angles and contact stresses. These effects were investigated for an LN_2 coolant inlet temperature range of -285°F to -305°F.

FIGURE 3.4.4 CONTACT ANGLES & CONTACT ELLIPSE SEMI MAJOR AXIS VS AXIAL REACTION

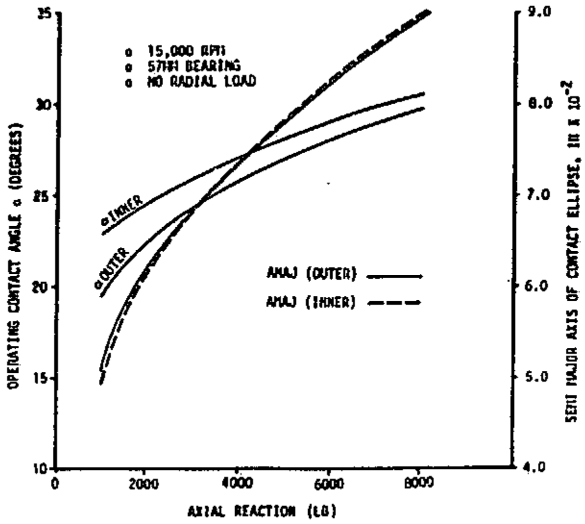

FIGURE 3.4.5
CONTACT ANGLES & CONTACT ELLIPSE SEMI MAJOR AXIS VS AXIAL REACTION

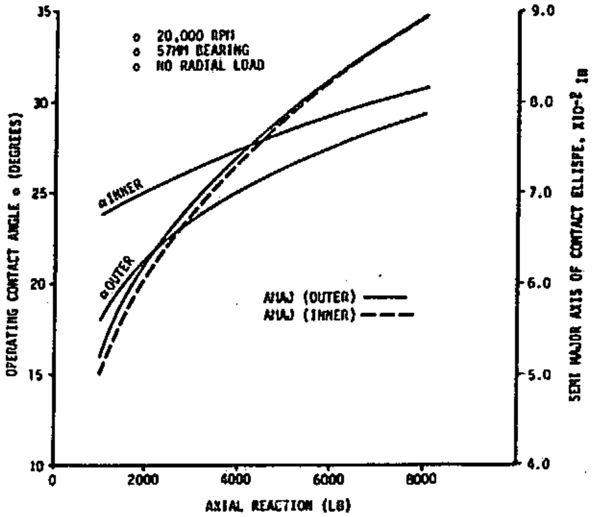

FIGURE 3.4.6 CONTACT ANGLES & CONTACT ELLIPSE SEMI MAJOR AXIS VS AXIAL REACTION

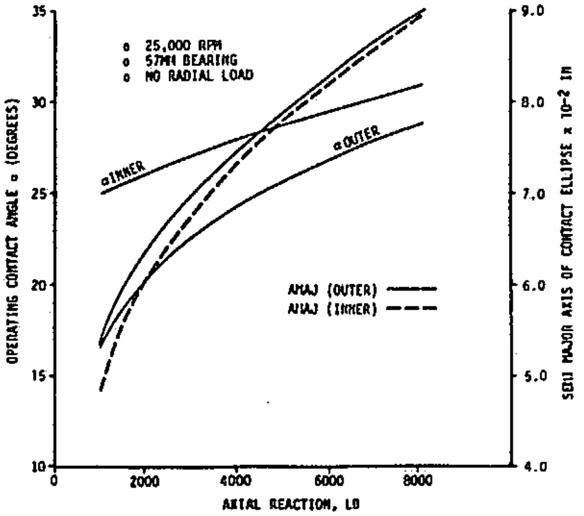

FIGURE 3.4.7 CONTACT ANGLE AND CONTACT ELLIPSE SEMI MAJOR AXIS VS AXIAL REACTION

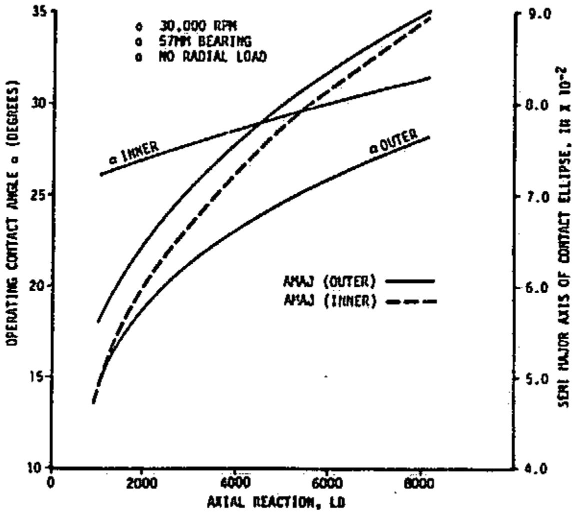

The bearing thermal model provides a detailed representation of the bearing component temperatures and gradients. Due to high frictional heat generated in the contact area of the bearing and the low (cryogenic) temperatures of the coolant, extremely high thermal gradients are present in the contact areas. Figure 3.4.8 provides the total heat generated by a bearing pair and the coolant outlet temperature as a function of the coolant flow rate for the conditions indicated. This analysis was performed for an axial reaction on bearing #2 of 2500 lbs. The heat generated, as shown in Figure 3.4.8, includes the viscous energy dissipated to the fluid and the friction heat generated in the bearing contacts. As indicated, there is very little change in slope of the heat generation curve as the coolant flow decreases. This implies that the net heat, due to the loading conditions indicated, is not large enough to significantly reduce clearances and contact angles as the coolant flow decreases. Therefore, thermal runaway should not be a problem for these operating parameters.

Also, as indicated in Figure 3.4.8, the coolant outlet temperature is approaching the coolant saturation temperature. If the coolant leaving the bearing pair becomes saturated, net vapor generation occurs and vapor effects on coolant pressure losses can become important considerations.

Frictional heat rate profiles over the contact surfaces are shown in Figures 3.4.9 and 3.4.10 for the inner and outer races, respectively. The detail of the bearing thermal models used for the analysis allows this estimation of the distribution of frictional heat within the elliptical contacts and the resulting temperature distributions over the contact ellipse area. The frictional heat rates obtained from the SHABERTH bearing model for the contacts is distributed to the corresponding surface nodes in the thermal model to obtain temperature profiles for the bearing components. Figure 3.4.11 shows the maximum temperatures estimated in the bearing contacts for the conditions shown. As expected, the estimated maximum contact temperatures are higher than the coolant saturation temperature, therefore, the bearing contacts are operating in gas rather than liquid. Consequently, the LN_2 acts as a medium for removing the heat generated and little or no lubrication is provided.

The average bearing component temperatures (rolling element, inner race, and outer race) are shown in Figure 3.4.12. This information is necessary input to the SHABERTH bearing model and is obtained from a code incorporated into the SINDA thermal analyzer program which averages individual node temperatures taking into account the volume of each node. At this time, the bearing thermal model is composed of over 600 nodal points. Figure 3.4.12, which shows the average component temperatures, indicates that the ball has the highest average temperature with the inner and outer race following. Considerable vapor will be generated locally due to the component temperatures that exceed the LN_2 saturation temperature. Vapor that is generated locally will be condensed and leave the tester as liquid since the bulk outlet temperature of the coolant remains below the saturation temperature as indicated in Figure 3.4.8.

The loss of internal or operating clearance as a function of coolant flow is shown in Figure 3.4.13 along with the increase in contact stresses as the flow is reduced. As shown, the reduction in clearance becomes more pronounced at flow rates below about 8 lb/sec per bearing pair. Figure 3.4.14 illustrates the trend in contact angles as the coolant flow is decreased. As indicated, the change in contact angle as a function of the coolant flow rate is very small for an axial reaction of 2500 pounds.

ORIGINAL PAGE IS
OF POOR QUALITY

FIGURE 3.4.8

TOTAL HEAT GENERATED (BRG./PAIR) AND COOLANT OUTLET TEMP VS COOLANT FLOW RATE

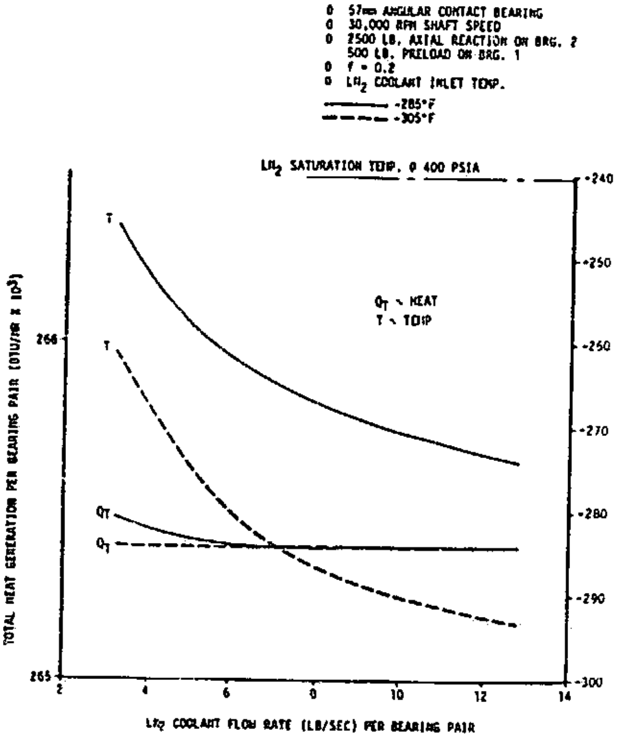

FIGURE 3.4.10

OUTER RACE HEAT GENERATED AT CONTACT ELLIPSE

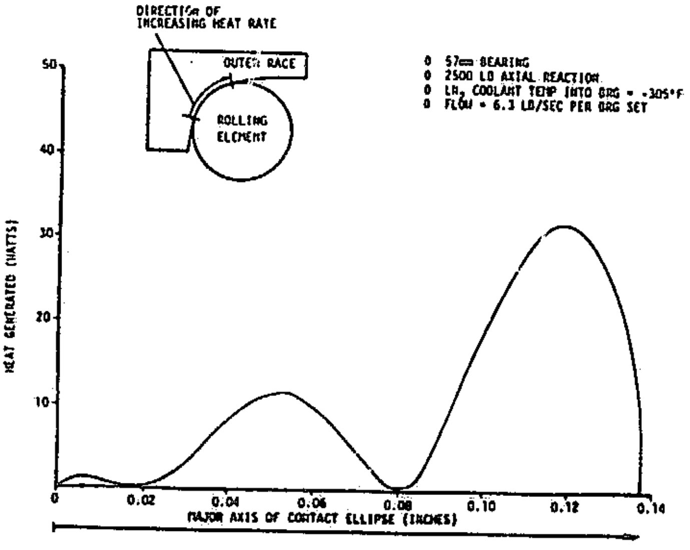

FIGURE 3.4.9

INNER RACE HEAT GENERATED AT CONTACT ELLIPSE

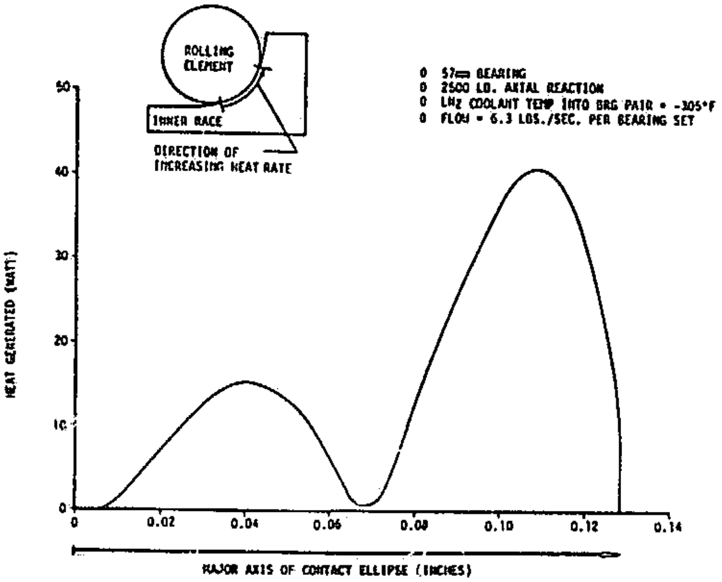

FIGURE 3.4.11

BEARING CONTACT TEMPERATURES VS COOLANT FLOW

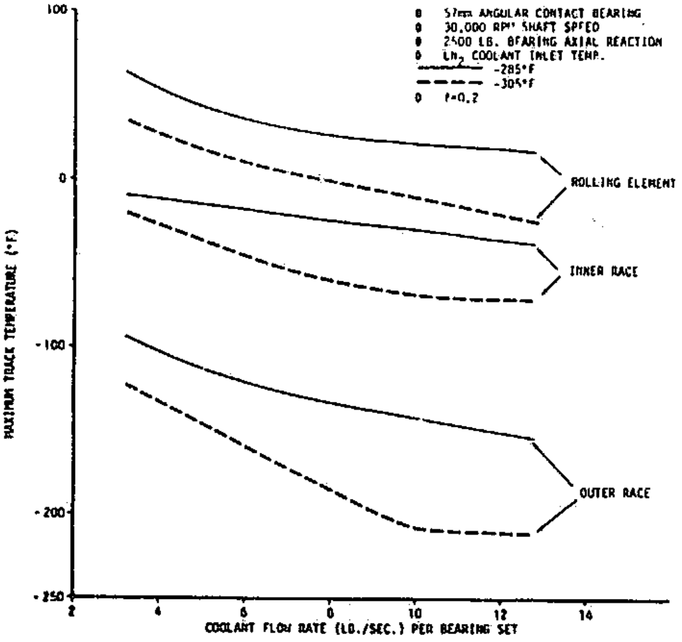

ORIGINAL PAGE IS
OF POOR QUALITY

FIGURE 3.4.12

AVERAGE BEARING COMPONENT TEMPERATURE VS COOLANT FLOW

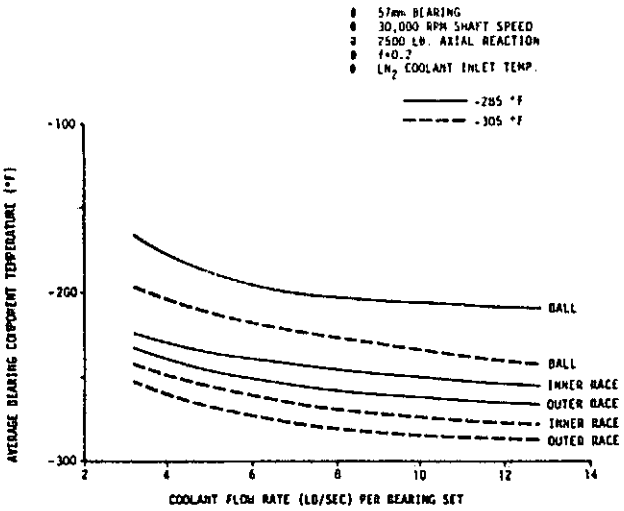

FIGURE 3.4.14

CONTACT ANGLE VS COOLANT FLOW

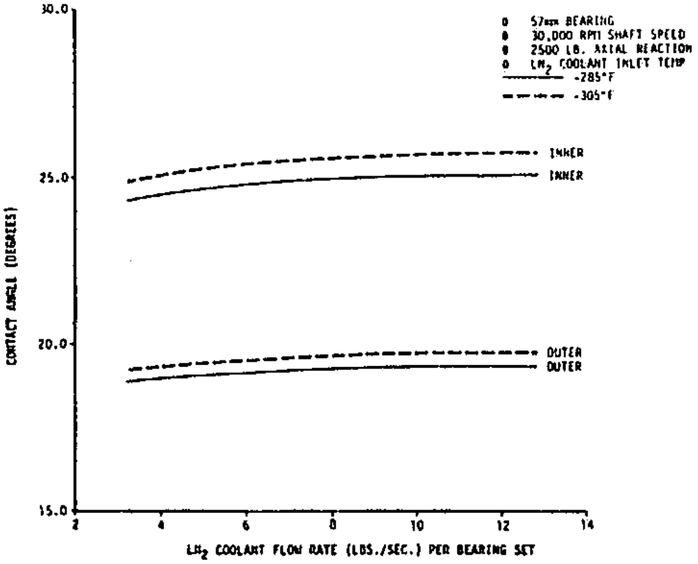

FIGURE 3.4.13

HERTZ STRESS & OPERATING CLEARANCE VS COOLANT FLOW

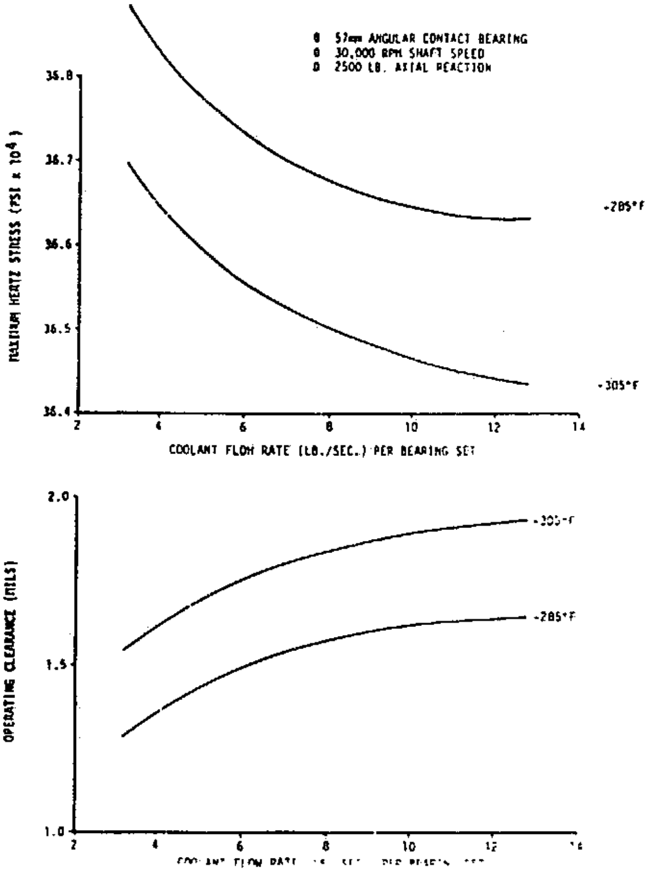

FIGURE 3.4.15

TOTAL HEAT GENERATED (Bgr/Pair) AND COOLANT OUTLET VS COOLANT FLOW RATE

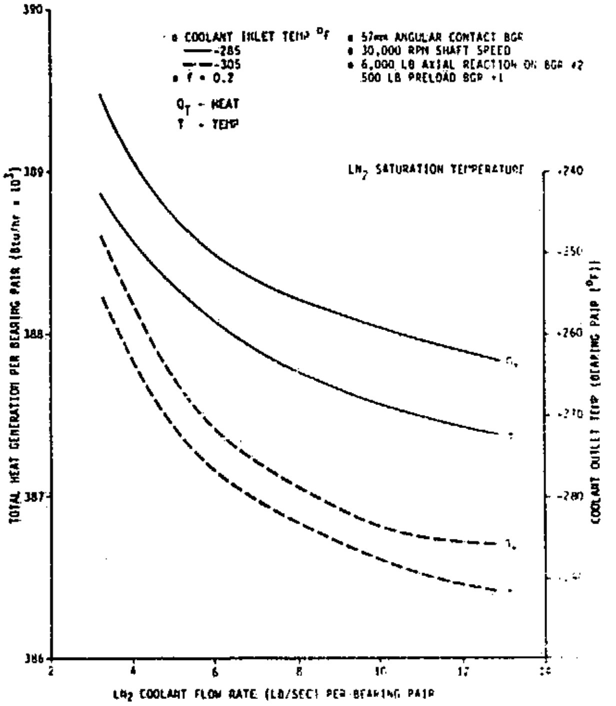

A similar analysis was conducted for an axial reaction of 6000 pounds on bearing #2. the results of this analysis are found on Figures 3.4.15 through 3.4.19. Figure 3.4.15 provides the total heat generated by a bearing pair and the coolant outlet temperature as a function of coolant flow for the conditions noted. The heat generated includes the viscous energy dissipated to the fluid and the friction heat generated in the bearing contacts. Test data from the BMT have been used as an aid in estimating the viscous energy dissipated in the LN_2 coolant. Additional data are necessary to improve the confidence in these estimates, especially for LOX cooled bearings. As shown, there is a change in slope of the heat generation curve as the coolant flow decreases below about 8 lbs/sec per bearing pair. This is the result of the "amplification" of loads due to reduction in clearances and contact angles as the coolant flow is decreased. It is also significant to note that the coolant outlet temperature is approaching the coolant saturation temperature. In the event the coolant outlet becomes saturated, net vapor generation occurs and vapor effects on bearing coolant pressure losses can become significant.

As was previously done, frictional heat rate distributions from the SHABERTH bearing model were input into the SINDA thermal model to provide temperature distributions. Frictional heat rate profiles over the contact surfaces are shown in Figure 3.4.16 and 3.4.17 for the inner and outer races. These heat rates are distributed to the proper elements in the thermal model to obtain temperature profiles for the bearing components. Shown in Figure 3.4.18 are the maximum temperatures estimated in the bearing contacts for the conditions noted. As indicated, the estimated contact temperatures are relatively high compared to the cryogenic coolant temperature. Since the saturation temperature of LN_2 is -240°F at 400 psia, the bearing contacts are operating in gas rather than liquid, and liquid film separation of the contacts does not exist as in conventionally lubricated bearings. Consequently, the LN_2 is expected to provide very little if any contribution to bearing lubrication and serves only as a medium for removing the heat generated, as previously discussed. This emphasizes the importance of the dry film transfer lubrication technique employed in this bearing. Loss of lubricant can cause increased friction in the contacts increasing not only wear but heat generation which, due to increased temperature, can cause loss of operating clearances and ultimately bearing failure.

As discussed, the SINDA bearing thermal model is a finite element representation of the bearing components and provides a two dimensional representation of the temperature profile in the bearing. The SHABERTH model, however, requires the average temperature of each rolling element component (inner race, ball and outer race) to be supplied as input. To meet this need, a temperature averaging capability for each element of the bearing has been developed in the thermal model. These average component temperatures are shown in Figure 3.4.19. The ball has the highest average temperature with the inner and outer race following. The ball and inner race average temperatures exceed the LN_2 saturation temperature for the conditions noted and, consequently, considerable vapor will be generated locally. Since the bulk outlet temperature of the coolant remains below the saturation temperature, this vapor will be condensed and leave the tester as liquid. It is also important to note that the inner race and ball temperature exceed the outer race temperature. This causes a loss in bearing operating clearances due to the thermal growth of the ball and inner race relative to the outer race.

The loss of internal or operating clearance as a function of coolant flow is shown in Figure 3.4.20 along with the increase in contact stresses as the coolant flow is reduced. As indicated, the reduction in clearance becomes more pronounced at

ORIGINAL PAGE IS
OF POOR QUALITY

FIGURE 3.4.16

INNER RACE HEAT GENERATED AT CONTACT ELLIPSE

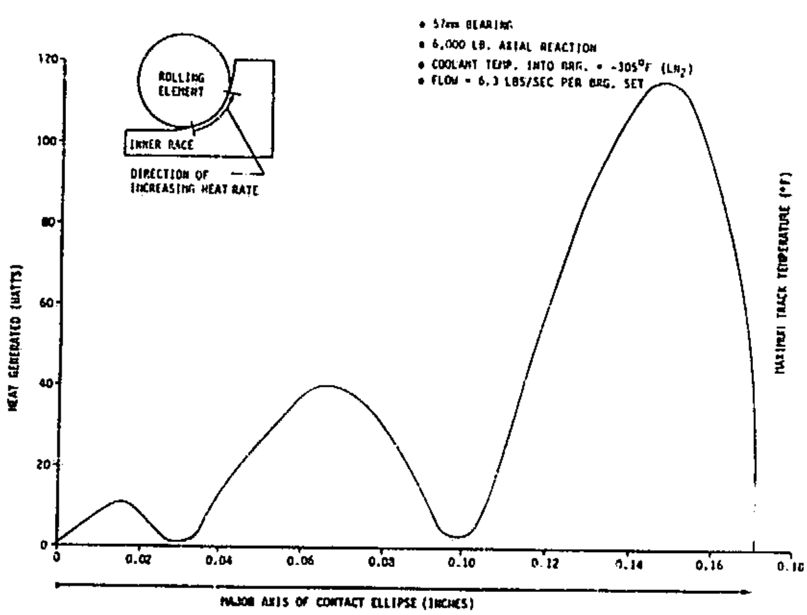

FIGURE 3.4.17

OUTER RACE HEAT GENERATED AT CONTACT ELLIPSE

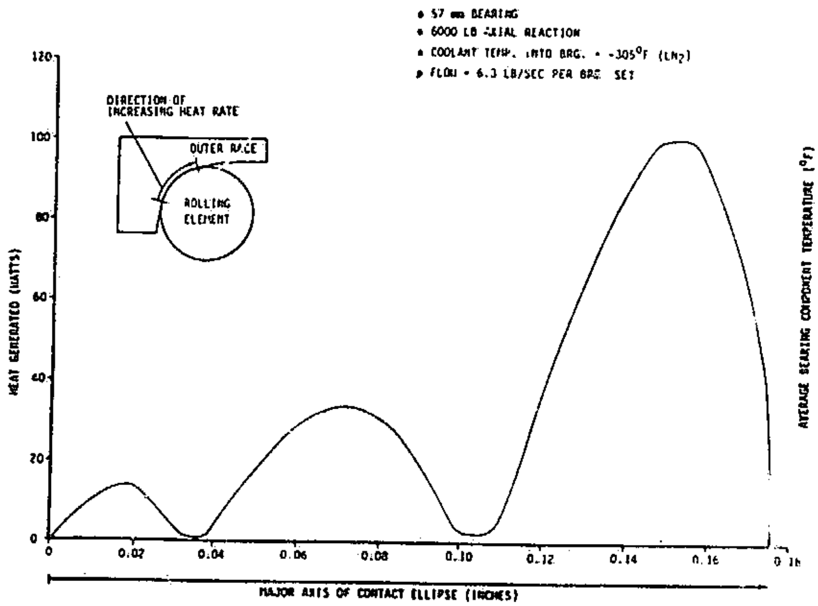

FIGURE 3.4.18

BEARING CONTACT TEMPERATURES VS COOLANT FLOW

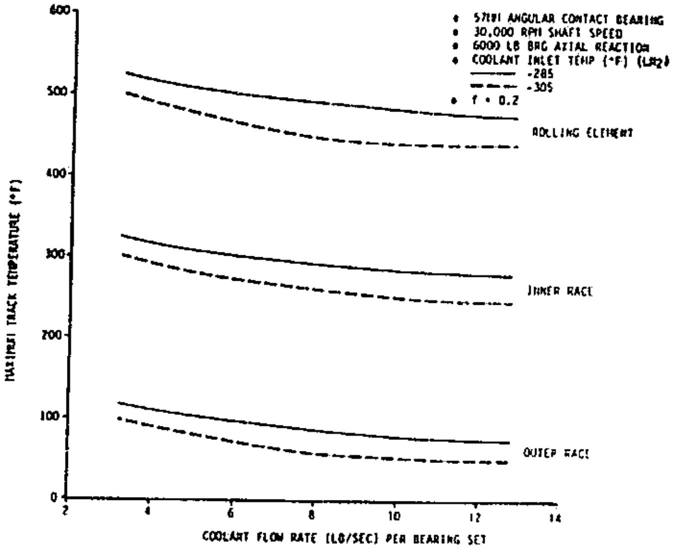

FIGURE 3.4.19

AVERAGE BEARING COMPONENT TEMPERATURE VS COOLANT FLOW

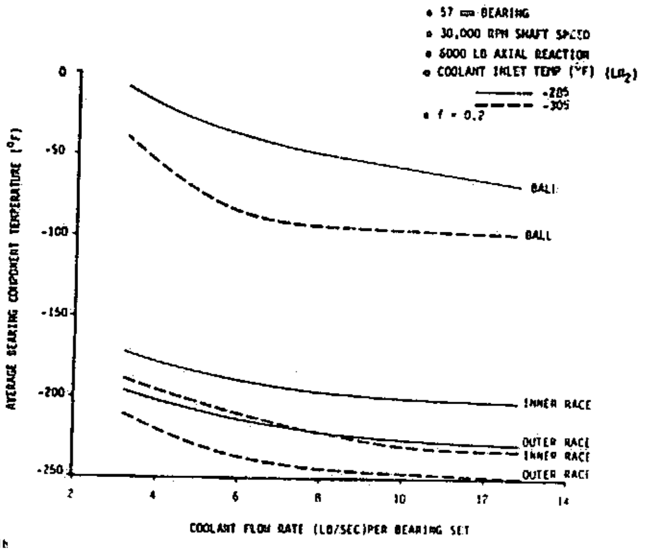

ORIGINAL PAGE IS
OF POOR QUALITY

FIGURE 3.4.20 HERTZ STRESS & OPERATING CLEARANCE VS COOLANT FLOW

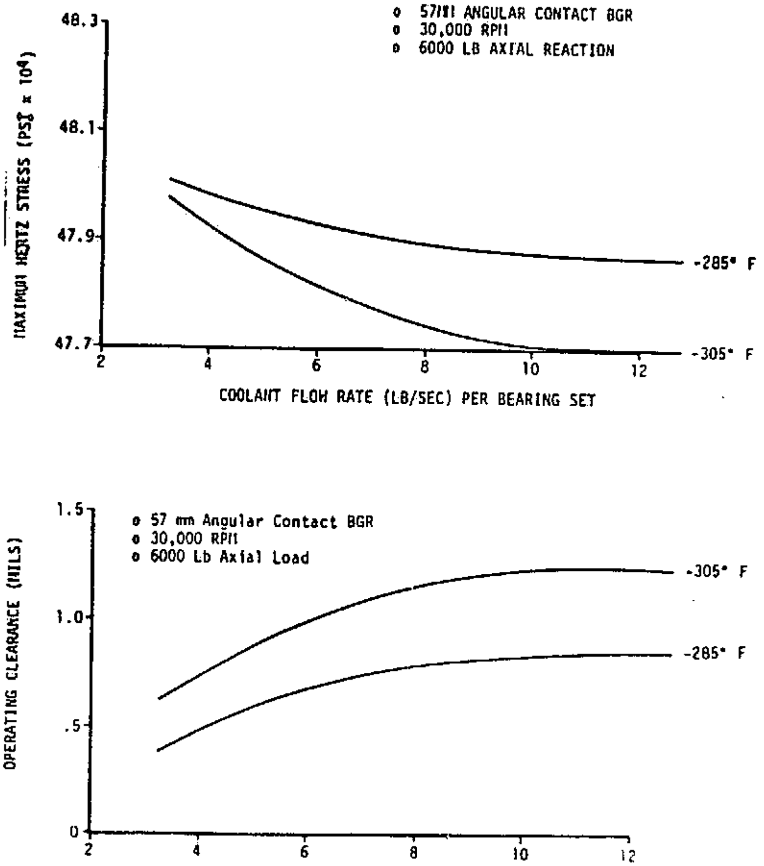

FIGURE 3.4.21 CONTACT ANGLE VS COOLANT FLOW

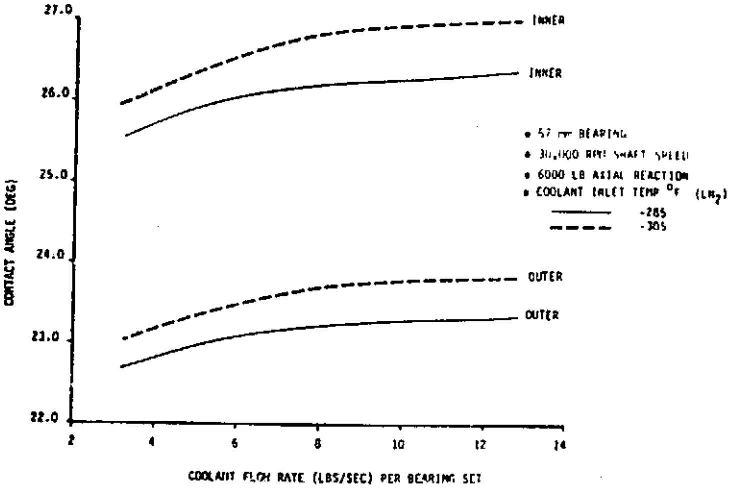

FIGURE 3.4.22 BEARING VISCOUS HEAT TRENDS* VS SPEED

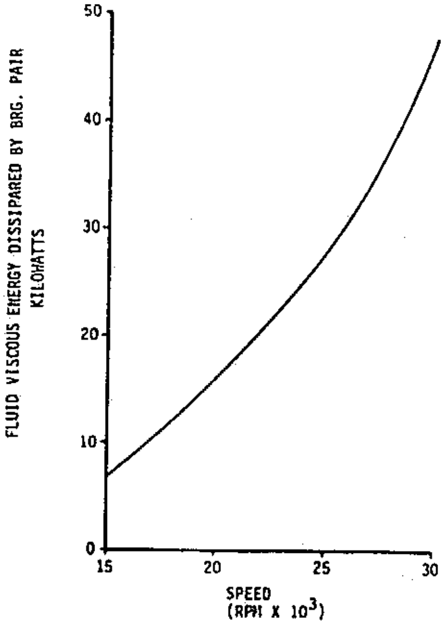

- o 57 MM BGR PAIR
- o LOX TURBO PUMP TURBINE END BGRS.

*ADDITIONAL TEST DATA FROM BGR & MATERIALS TESTER NEEDED TO VERIFY CONDITIONS IN LOX.

flow rates below about 8 lbs/sec per bearing pair. Figure 3.4.21 shows the reduction in contact angles as the coolant flow is decreased. This is the principal contribution to the increase in contact stresses. These analyses indicate that bearing failure can occur if conditions are present that allow thermal growth to reduce the operating clearances such that additional heat is generated, thus further reducing the clearances.

3.4.4 Bearing Viscous and Frictional Heat Generated as a Function of Speed and Radial Load

Parametric analyses were done to determine the relationship between the heat generated, in a bearing pair, and shaft speed and radial load. The SSME LOX pump turbine end bearing pair was modeled on the SHABERTH computer code. Heat is generated during bearing operation by two mechanisms; viscous energy dissipation into the coolant, and friction generated in the bearing contacts. The SHABERTH code is not used to estimate the viscous energy. Although SHABERTH provides a capability to estimate the viscous energy dissipated due to ball drag, this is not a complete description of the energy dissipated to the fluid. For example, fluid frictional energy is dissipated, due to the relative velocity of the fluid and shaft, as the coolant flows from the first to the second bearing. In addition, the rolling elements not only orbit the shaft but spin relative to their own axis. This spin motion produces a surface velocity relative to the fluid velocity contributing to the dissipation of viscous energy.

Figure 3.4.22 is a representation of the viscous energy dissipated as a function of shaft speed for a pair of bearings. Shown in Figure 3.4.23 is the friction heat generated in the bearing contacts as a function of radial reaction and shaft speed. Figures 3.4.24 and 3.4.25 show the frictional heat generated at the inner and outer races as a function of shaft speed and radial load. Figure 3.4.26 is a cross plot of the data shown in Figure 3.4.23. It is evident that the heat generated is nonlinear with shaft speed. Since the LOX turbopump coolant flow increase, with shaft speed, is essentially linear, an increase from rated power level (RPL) reduces bearing cooling margin as power level increases.

Similar parametric analyses were performed to determine the relationship between the friction heat generated in a bearing pair and shaft speed and axial load. Figure 3.4.27 is a representation of the friction heat generated in the bearing contacts as a function of axial reaction and shaft speed. Figures 3.4.28 and 3.4.29 illustrate the friction at the inner and outer races as a function of the shaft speed and axial load for the conditions noted. Figure 3.4.30 is a cross plot of the data shown in Figure 3.4.27. It is apparent that the heat generated is nonlinear with shaft speed. The friction heat generation data presented assumes no thermal gradients across the bearing and, therefore, should be considered as trends only. A combined thermal/mechanical analysis will be required to accurately estimate the friction heat generated especially at the higher loading conditions.

3.4.5 Investigation of Bearing Temperature Gradients on Operational Characteristics

A single 57 mm ball bearing was modeled on the SHABERTH computer program. Several temperature gradients were imposed and their effects on contact angle, normal forces, contact stresses, operating clearances, and heat generation were determined. The results, shown in Figures 3.4.31 through 3.4.34 are for a bearing with .0036 inch radial play at a contact angle of 20°.

ORIGINAL PAGE IS
OF POOR QUALITY

FIGURE 3.4.23

TOTAL BEARING PAIR FRICTIONAL HEAT GENERATED VS SHAFT SPEED

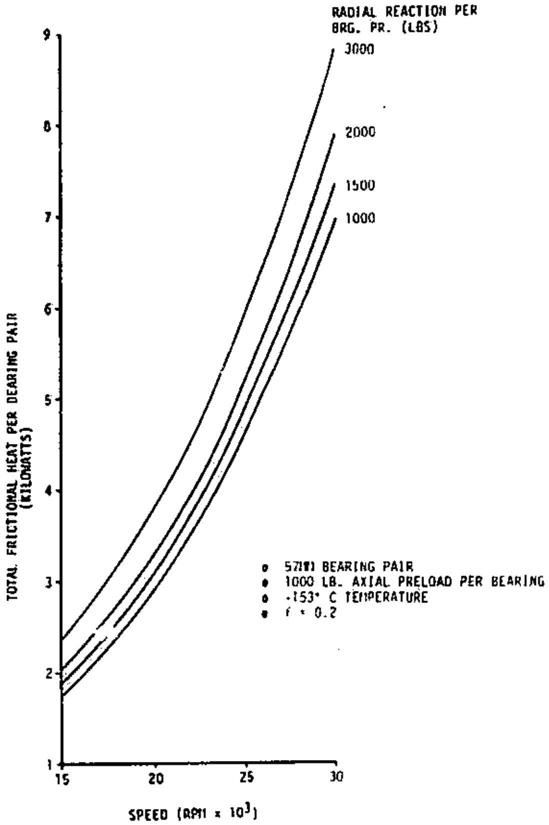

FIGURE 3.4.24

INNER RACE FRICTIONAL HEAT VS SHAFT SPEED

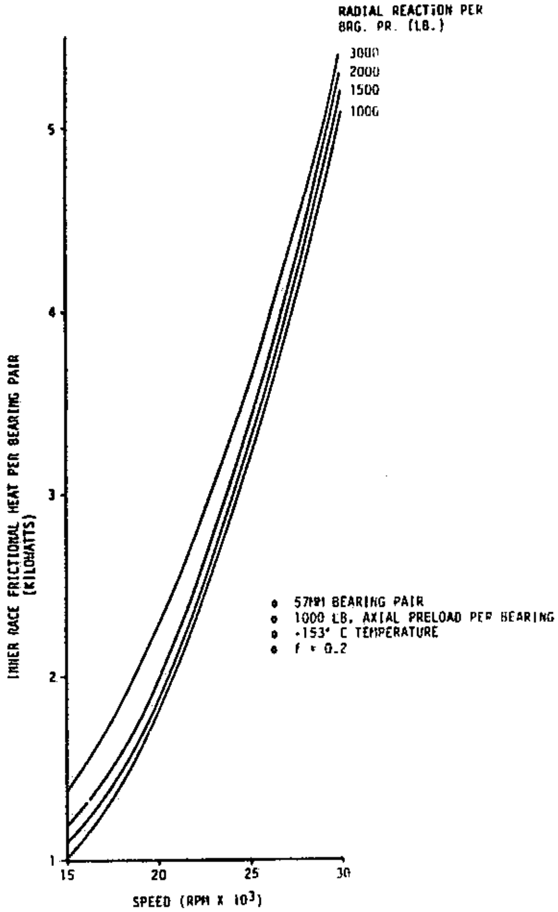

FIGURE 3.4.25

OUTER RACE FRICTIONAL HEAT VS SHAFT SPEED

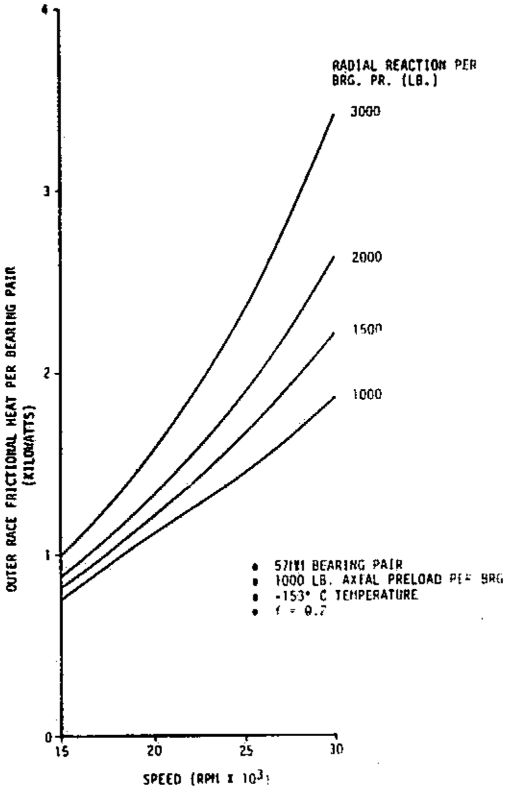

FIGURE 3.4.26

TOTAL BEARING PAIR FRICTIONAL HEAT GENERATED VS RADIAL LOAD

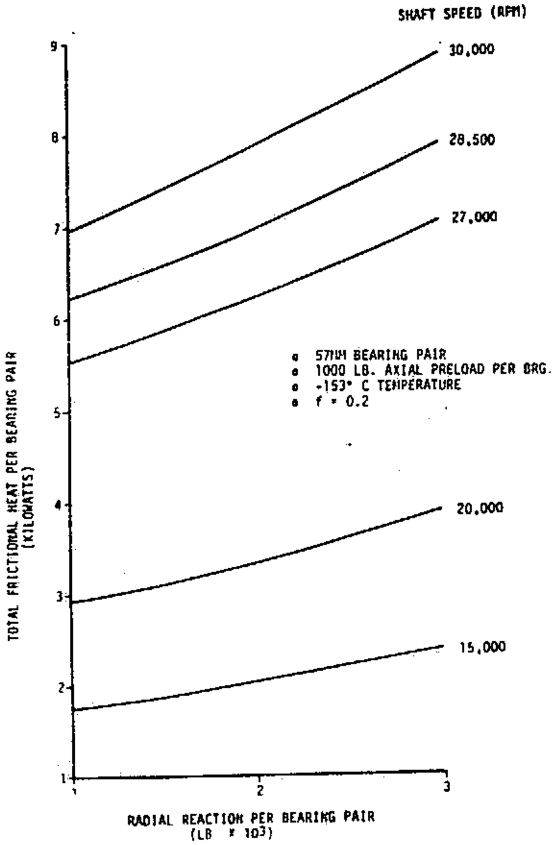

ORIGINAL PAGE IS
OF POOR QUALITY

FIGURE 3.4.27

TOTAL FRICTIONAL HEAT GENERATED PER BRG. PAIR - VS - SHAFT SPEED

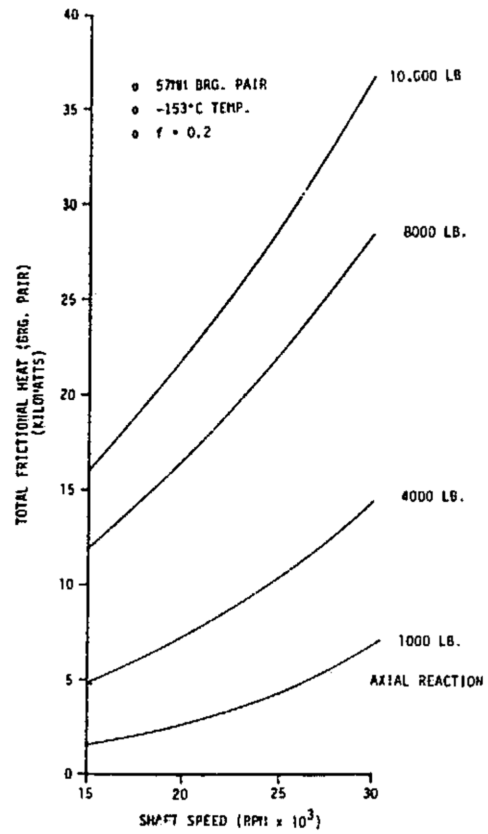

FIGURE 3.4.28

INNER RACE HEAT GENERATED PER BRG. PAIR - VS - SHAFT SPEED

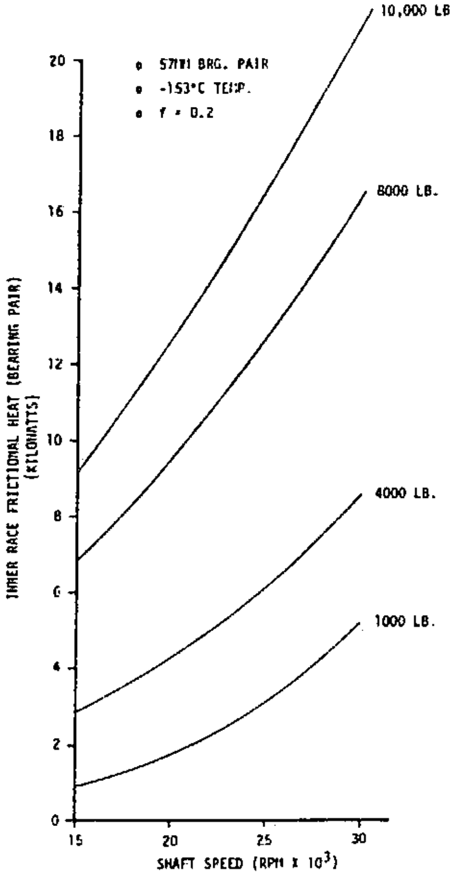

FIGURE 3.4.29

OUTER RACE FRICTIONAL HEAT GENERATED PER BRG. PAIR - VS - SHAFT SPEED

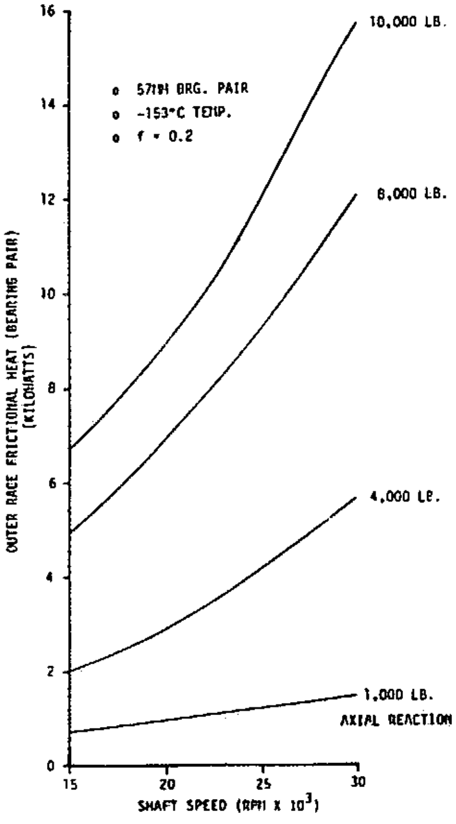

FIGURE 3.4.30

TOTAL FRICTIONAL HEAT GENERATED (PER BRG. PR) - VS - AXIAL REACTION

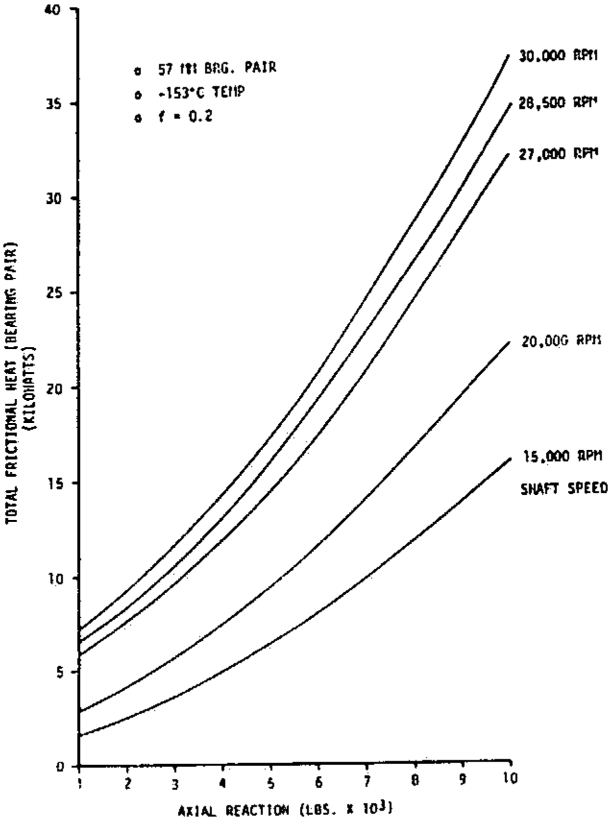

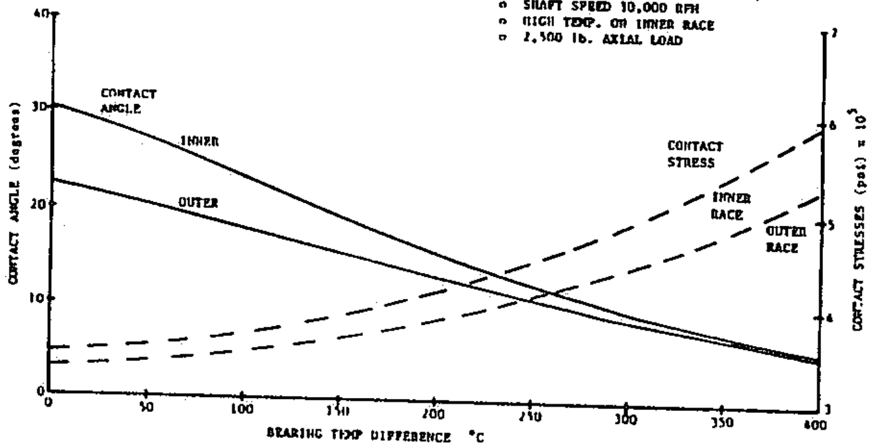

FIGURE 3.4.31 CONTACT ANGLE AND STRESSES vs. BEARING TEMPERATURE DIFFERENCE

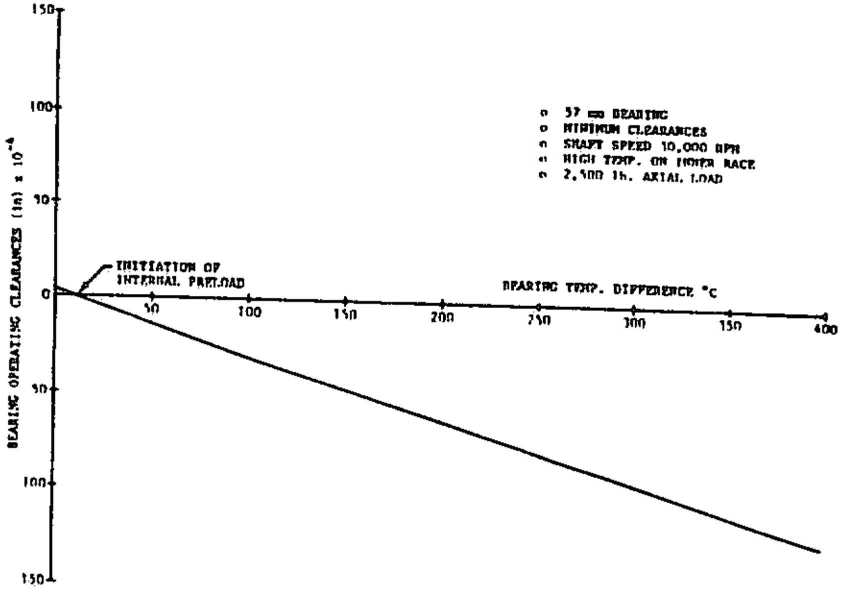

FIGURE 3.4.32 BEARING OPERATING CLEARANCES vs. TEMPERATURE DIFFERENCE

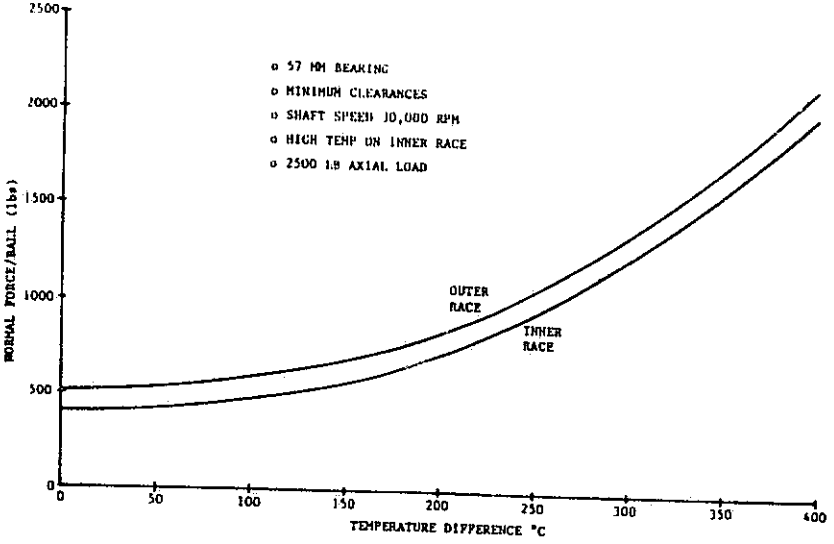

FIGURE 3.4.33 NORMAL FORCES vs. BEARING TEMPERATURE DIFFERENCE

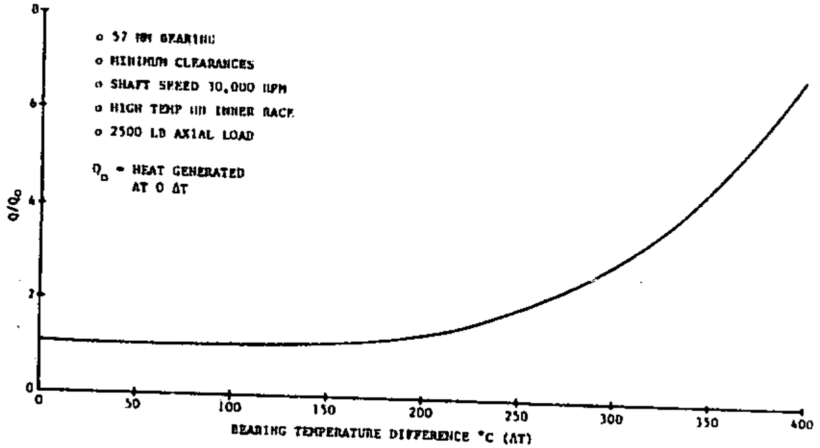

FIGURE 3.4.34 INCREASE IN HEAT GENERATED vs. BEARING TEMP. DIFFERENCE

FIGURE 3.4.35 CONTACT ANGLE AND STRESSES VS BEARING TEMP. DIFFERENCE

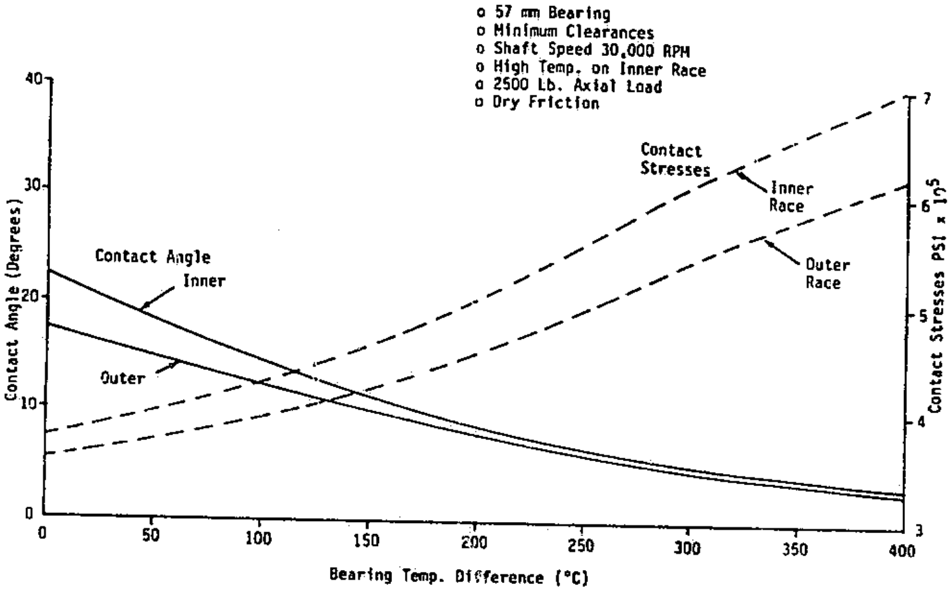

FIGURE 3.4.36 BEARING OPERATING CLEARANCE VS TEMPERATURE DIFFERENCE

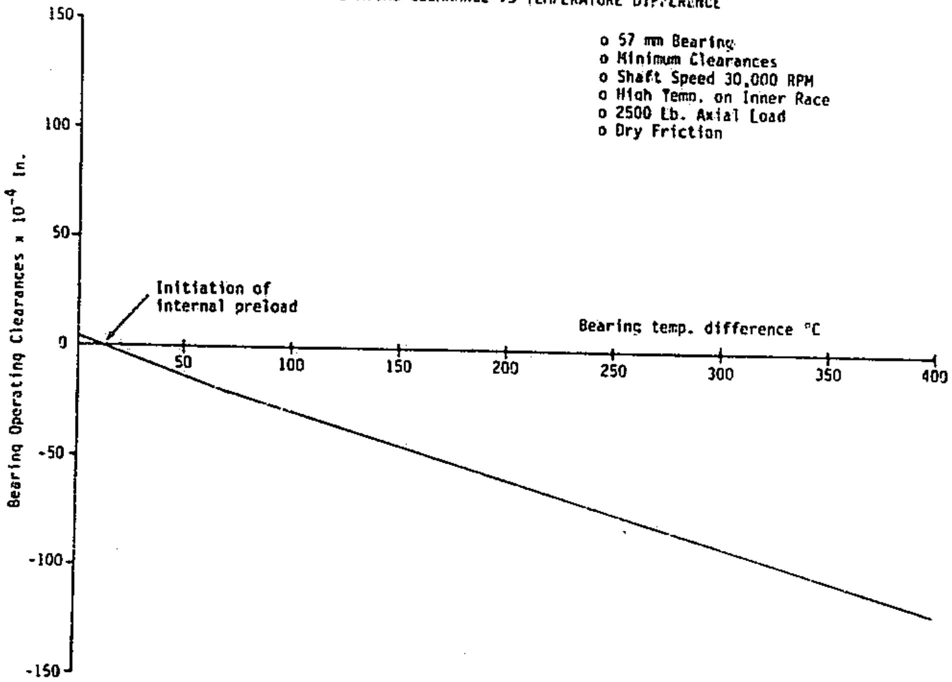

FIGURE 3.4.37 NORMAL FORCES VS. BEARING TEMP DIFFERENCE

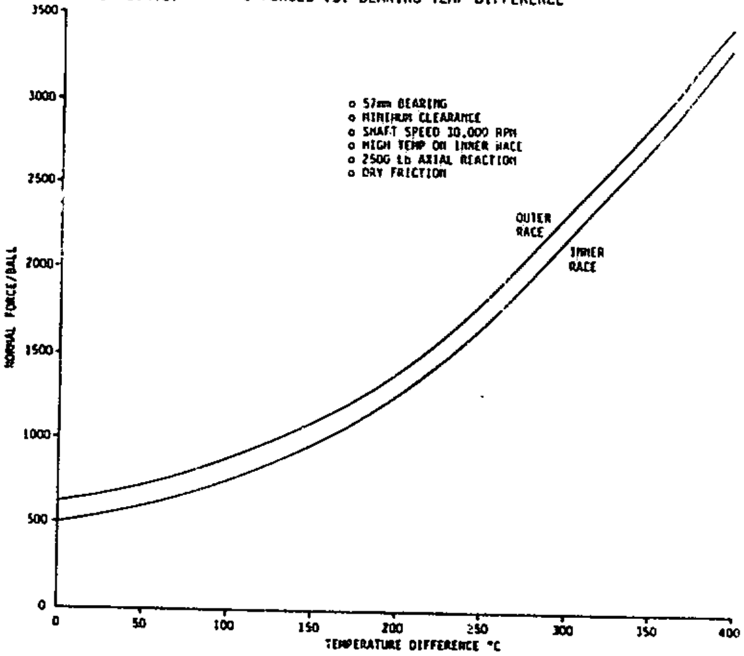

FIGURE 3.4.38 INCREASE IN HEAT GENERATED VS BEARING TEMP. DIFFERENCE

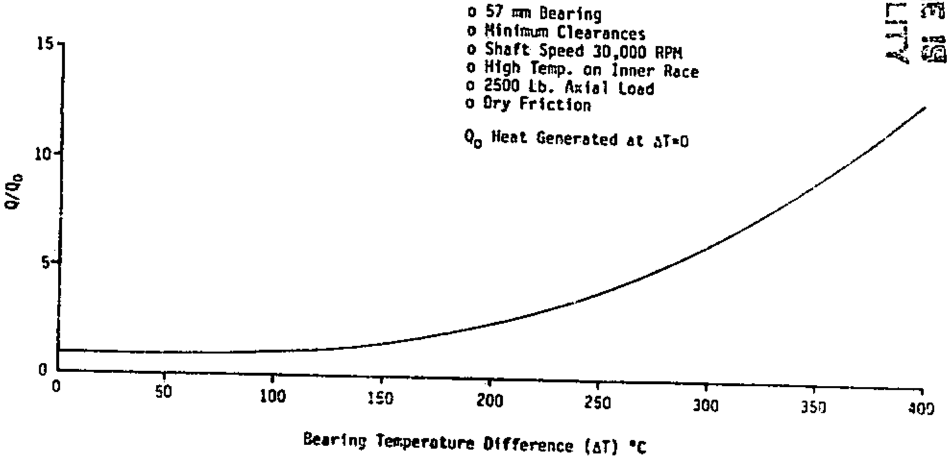

Figure 3.4.31 shows the variation of inner and outer race contact angles and stresses as a function of bearing temperature difference. The positive temperature gradient is from the shaft to the bearing housing. The shaft and inner race are assumed to be at the high temperature and the ball temperature is assumed to be the average of the inner and outer race. As shown, the operating contact angles exhibit a significant decrease at the higher temperature differences with a corresponding increase in contact stresses. Figure 3.4.32 shows the effect of the temperature differences on the bearing operating clearances. As the clearances go from positive to negative, an internal preload is introduced which in effect increases the bearing preload. As shown, this occurs for a rather small temperature difference. It should be pointed out, however, that these analyses were made using the worst case stack up of tolerances to minimize the bearing clearances.

Shown in Figure 3.4.33 are the normal forces per ball for the inner and outer races as they are influenced by the bearing temperature differences. The forces appear to be approximately linear up to a temperature difference of 150^{o}C and become a power function or exponential function as the ΔT increases. Shown in Figure 3.4.34 is this effect on the increase in heat generated at the contact surfaces. After about 200^{o}C ΔT, there is a sharp rise in heat generated as the ΔT across the bearing is increased. The increase in heat generated will increase the bearing ΔT and, in turn, the ΔT effects will increase the heat generated. This can result in an unstable condition causing premature bearing failure.

This analysis was repeated for a bearing having zero radial play at a contact angle of 20°, which is representative of the test bearing. These results are shown in Figures 3.4.35 through 3.4.38. In comparing Figure 3.4.35 with Figure 3.4.31, it is evident that eliminating the radial play reduces the contact angle and increases the contact stresses, as should be expected. Comparison of the operating clearances (Figure 3.4.36) indicates a slight reduction in clearance for the case of no radial play. This results in an increase in frictional heat generated at the contact surfaces as can be seen by comparing Figure 3.4.38 with Figure 3.4.34.

Elimination of the radial play slightly increased the sensitivity of operating conditions to bearing temperature differences. The previously discussed charts are labeled "minimum clearances". However, there may be other combinations of clearances that produce slightly tighter operating clearances. The lower range of operating temperature for these analyses was -180^{o}C or 168^{o}R, which is representative of the LH_2 test environment. The higher temperature of the LOX (193^{o}R) will have a slight effect on the clearance values.

3.5 Pretest Predictions of Thermal Conditions for the BMT

Estimates have been made for coolant and bearing temperatures expected during the first rotational test of the BMT (Build #1). The speed-flow profile for the first test is shown in Figure 3.5.1. The various conditions analyzed are shown in Figure 3.5.2. A total of 114 SHABERTH and SINDA computer runs were necessary to evaluate the conditions shown.

The rate of energy dissipation due to viscous mixing was estimated for each value of shaft speed. Bearing friction heat was estimated for each load and shaft speed. This information is shown in Figure 3.5.3. These data were used in the bearing thermal model to estimate the thermal conditions of the coolant and bearing temperatures at the measurement locations in the BMT.

FIGURE 3.5.1 SPEED/FLOW PROFILE FOR BSMT LN_2(002) BUILD #1 ROTATIONAL TEST #1 BASELINE TEST #1

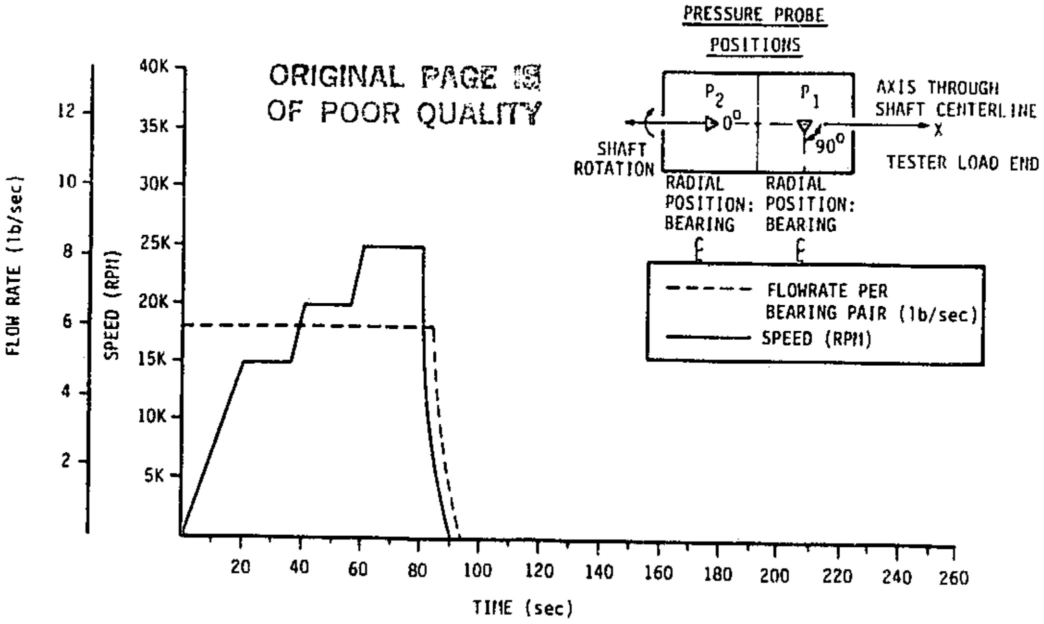

FIGURE 3.5.2 CONDITIONS EVALUATED FOR FIRST ROTATIONAL TEST OF THE BMT (LN_2)

AXIAL REACTION (lbs)	2500 4000	2500 4000
SPEED (RPM)		
15,000	-300	-280
20,000	-300	-280
25,000	-300	-280
	COOLANT INLET TEMP °F	

COOLANT FLOW FOR ALL CASES (6 lb/sec BGR Pair)

FIGURE 3.5.3 HEAT GENERATED AT LOAD END OF THE BMT AS A FUNCTION OF SHAFT SPEED AND AXIAL LOAD (LN_2 COOLANT)

COMPONENT	SHAFT SPEED (RPM)					
	15,000		20,000		25,000	
LOAD(lbs)	2500	4000	2500	4000	2500	4000
STINGER	3.11	3.11	7.1	7.1	11.2	11.2
SPACER	1.18	1.18	2.7	2.7	4.45	4.45
SHAFT	4.0	4.0	9.15	9.15	15.1	15.1
BGR #1						
VISCOUS	5.77	5.77	14.01	14.01	23.07	23.07
FRICTION (500*)	.402	.402	.721	.721	1.12	1.12
BGR #2						
VISCOUS	1.175	1.175	2.66	2.66	4.38	4.38
FRICTION	2.42	4.48	3.64	6.44	5.29	8.86
TOTAL	18.1	20.1	40	42.8	64.6	68.2

* Axial load (Lbs) assumed to be constant on BGR #1

Temperatures for a coolant inlet temperature of -300°F and axial reaction of 2,500 lbs are shown in Figure 3.5.4. A shaft speed of 25,000 RPM obviously produces the highest temperatures. The bearing outlet coolant temperature for this condition is -282°F. If a 30°F margin is added, the allowable saturated outlet temperature is -252°F and the corresponding saturation pressure is 290 psia. Therefore, the pressure at the bearing exit should be greater than 290 psia to meet the stated outlet temperature criteria. This will allow a pressure loss of 110 psi from tester inlet to bearing outlet assuming an inlet pressure of 400 psia. This condition is shown in Figure 3.5.5. As indicated, conditions at the lower speeds are less severe and the allowable pressure loss though the tester increases as speed decreases. Similar data for an axial reaction of 4,000 lbs are shown in Figure 3.5.6. As indicated in Figure 3.5.5, the 4,000 lbs load and 25,000 RPM case allows a pressure (inlet-to-bearing exit) of about 100 psi.

Two load conditions were evaluated for an inlet coolant temperature of -280°F. Results of the 2,500 lb case are shown in Figure 3.5.7 and Figure 3.5.8 provides similar results for a 4,000 lb axial reaction. As shown at 25,000 RPM, the coolant temperature at the bearing outlet is -262°F. Adding 30° of subcooling gives an allowable outlet of -232°F. Since the critical temperature of LN_2 is -232.8 at 493 psia, the above allowable outlet temperature exceeds the critical temperature. This requires the inlet and outlet coolant pressure conditions to be super critical. Since this is undesirable, an inlet temperature of at least -300°F should be provided. The inlet pressure requirement is a function of pressure loss from tester inlet to bearing exit. A preliminary estimate of the pressure loss from inlet to the bearing exit is on the order of 100 psi. Since pressure loss estimates for the BMT coolant contain unknown error margins, the bearing inlet pressure should be as high as practical and the pressure losses during the low speed runs should be evaluated to determine the possibility of exceeding the exit temperature criteria at the higher speed.

The outer race and ball track temperatures for bearing No. 2 are shown in Figure 3.5.9 for loading and coolant inlet conditions indicated. This information was generated from the SHABERTH bearing code and the SINDA thermal model. As indicated, these temperatures are not expected to be severe for the load and speed conditions of the test. Shown in Figure 3.5.10 are the estimated average temperatures for the ball, inner race and outer race.

FIGURE 3.5.4 ESTIMATED COOLANT TEMPERATURE VS SHAFT SPEED

OPERATING CONDITIONS
COOLANT INLET - 300°F
COOLANT FLOW 6 Lbs/sec BGR PAIR
AXIAL REACTION 2500 lbs

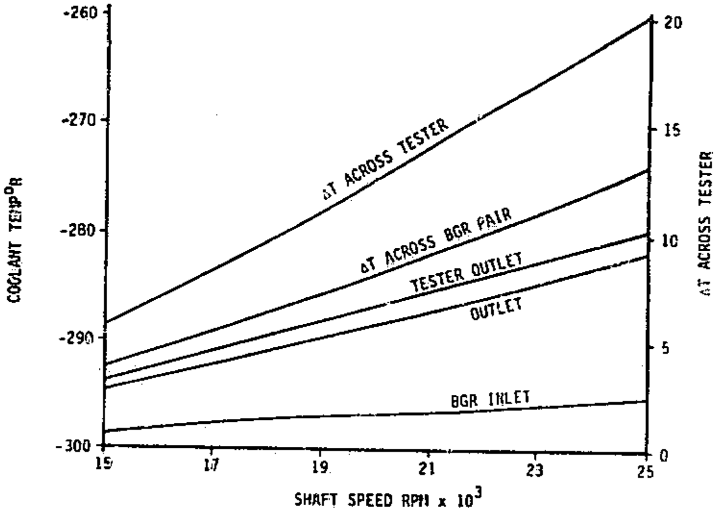

FIGURE 3.5.5 BEARING OUTLET TEMPERATURE & PRESSURE LIMITATIONS

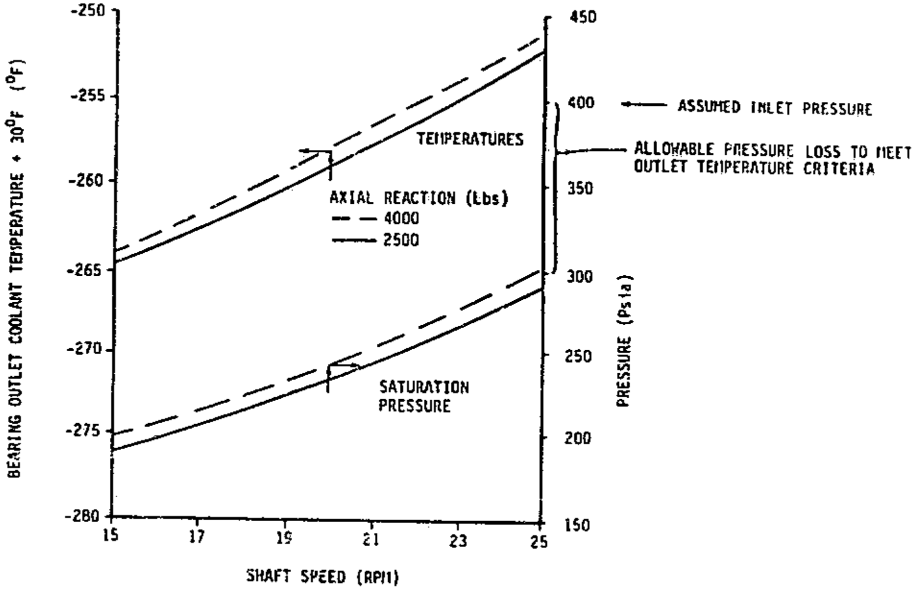

FIGURE 3.5.6 ESTIMATED COOLANT TEMPERATURE VS SHAFT SPEED

OPERATING CONDITIONS
COOLANT INLET - 300°F
COOLANT FLOW 6 lbs/sec BGR PAIR
AXIAL REACTION 4000 Lbs

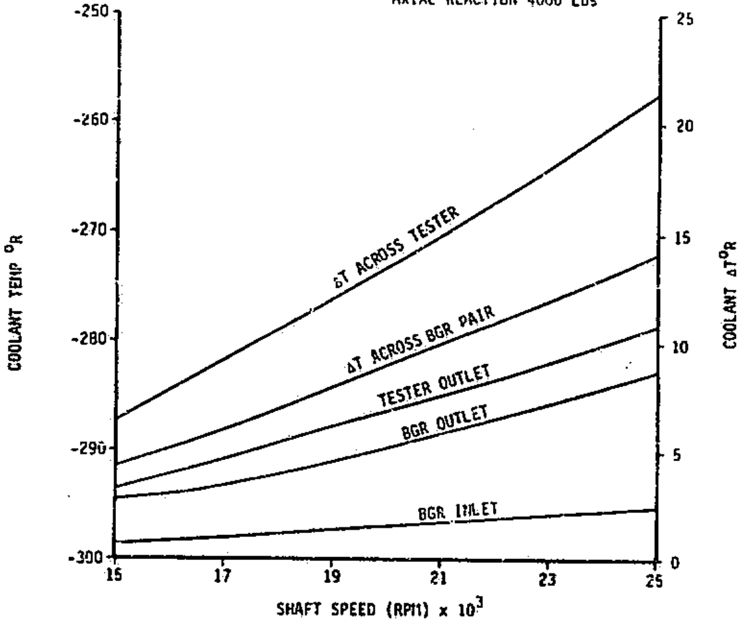

FIGURE 3.5.7 ESTIMATED COOLANT TEMPERATURES VS SHAFT SPEED

OPERATING CONDITIONS
COOLANT INLET -280°F
COOLANT FLOW 6 Lb/sec BGR PAIR
AXIAL REACTION 2500 Lbs

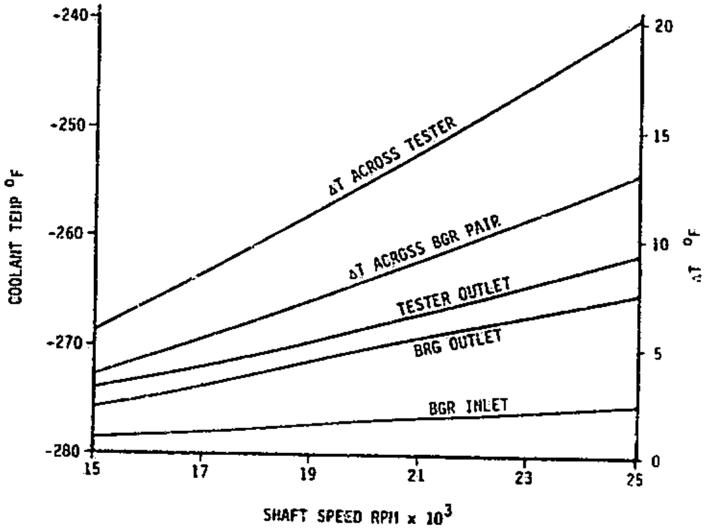

FIGURE 3.5.8 ESTIMATED COOLANT TEMP VS SHAFT SPEED

OPERATING CONDITIONS
COOLANT INLET - 280°F
COOLANT FLOW 6 Lbs/sec BGR PAIR
AXIAL REACTION 4000 Lbs.

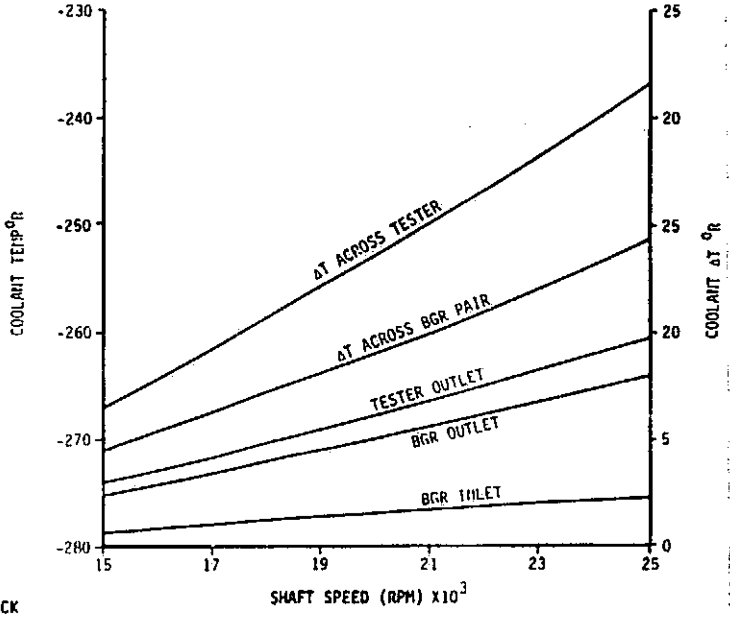

FIGURE 3.5.9 BALL TRACK AND BACK SURFACE OUTER RACE TEMPERATURES VS SHAFT SPEED

OPERATING CONDITIONS
COOLANT INLET TEMP - 300°F
COOLANT-FLOW 6 Lb/BGR PAIR
AXIAL REACTION (Lbs)
--- 4000
— 2500

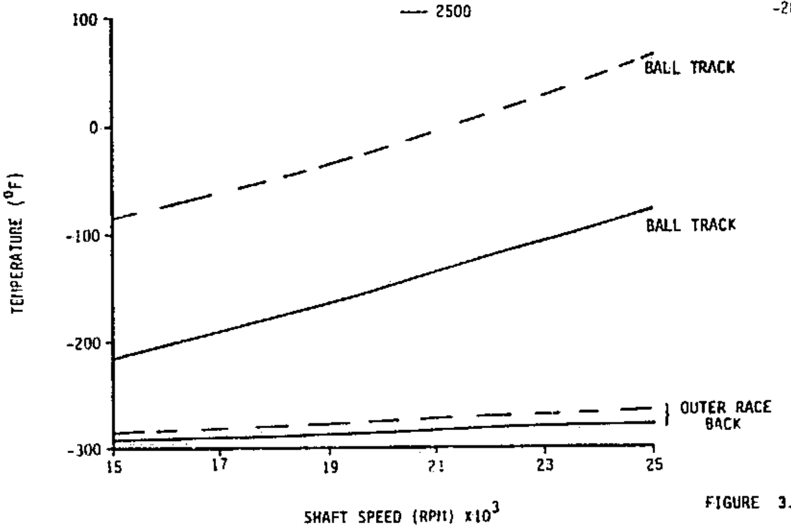

FIGURE 3.5.10 AVERAGE BEARING COMPONENT TEMPERATURE VS SHAFT SPEED

OPERATING CONDITIONS
COOLANT INLET -300°F
COOLANT FLOW 6 Lbs/sec BGR PAIR
AXIAL REACTION (Lbs)
--- 4000
— 2500

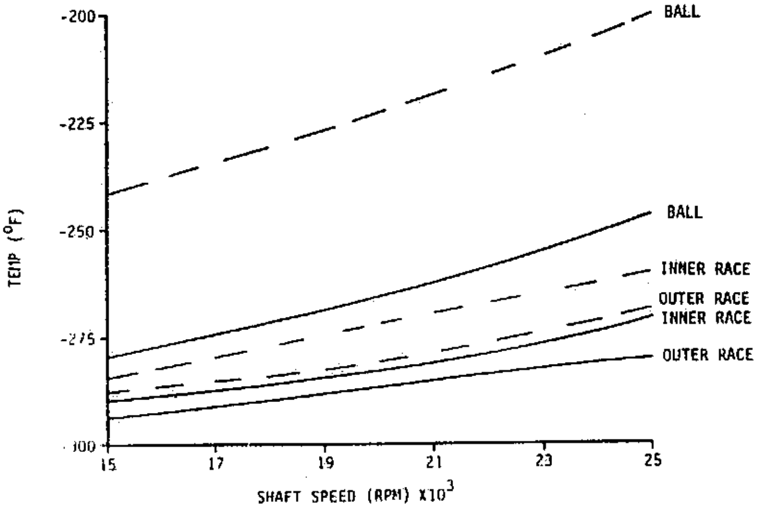

4.0 BEARING THERMAL MODEL DEVELOPMENT

The development, refinement, modification and preliminary verification of a thermal model using geometrical configurations of the 57 mm LOX Bearing and Materials Tester has been accomplished during the contract period of July 1982 to April 1984. The primary analytical tools used in this development were: 1) SINDA - a numerical differencing computer code used primarily for thermal systems, 2) SHABERTH - a state-of-the-art bearing analysis program.

4.1 Bearing and Materials Tester Data Base

A data base composed of a finite element representation of a pair of 57 mm back-to-back duplex mounted ball bearings as well as the shaft, carrier, housing, and coolant has been established using the dimensions of the Bearing and Materials Tester (See Figure 4.1.1). In lieu of modeling the entire bearing, a pie-shaped slice as shown in 4.1.2, encompassing 1 of the 13 rolling elements in the bearing, was used as a boundary for the thermal model.

Figure 4.1.3 illustrates the detail involved in the node analysis of the races and rolling element. This level of detail is necessary, especially in the track area, due to the large thermal gradients, present as shown in Figure 4.1.4 for the rolling element. This data indicates a rather large temperature gradient of 2300°F/-inch in the rolling element.

A data base has been established for both LOX and LN_2 coolant flow through the Bearing and Materials Tester (See Appendix A). This data base includes all node and conductor data along with temperature varying thermal property data and film coefficient data. The data base has been designed to facilitate modification due to changing operating parameters such as flow rates, axial load, and degree of subcooling or inlet coolant temperature. The bearing thermal model is composed of 630 diffusion nodes, 9 arithmetic nodes and 3 boundary nodes for a total of 642 nodes, as well as 1387 linear conductors.

SINDA, a software system which possesses the capabilities that make it well suited for solving lumped parameter representations of physical problems governed by diffusion-type equations, is used in conjunction with the data base. The system is designed as a general thermal analyzer accepting resistor-capacitor network representations of thermal systems.

4.2 Bearing Thermal Model Temperatures

The bearing thermal model, when executed, achieves a system heat balance for steady state conditions and when the model meets convergence criteria concerning the allowable temperature change between iterations, the final node temperatures are printed as shown in a representative case in Appendix B. Representative bearing component temperature distributions are shown in Figures 4.2.1 through 4.2.8 for conditions of loading, and coolant flow rate and temperature as noted. As shown, the gradients in the track area are significant for the higher loading conditions. Track surface temperatures, for the larger loads, are of concern due to the possibility of high temperature breakdown of the solid film lubricant. Since the track temperatures are critical to lubricant performance and in order to develop a better understanding of the effects of a distributed heat load in the contact area of the bearing, modifications were implemented into SHABERTH in order to determine a node-by-node heat

FIGURE 4.1.1 SCHEMATIC OF BEARING SET

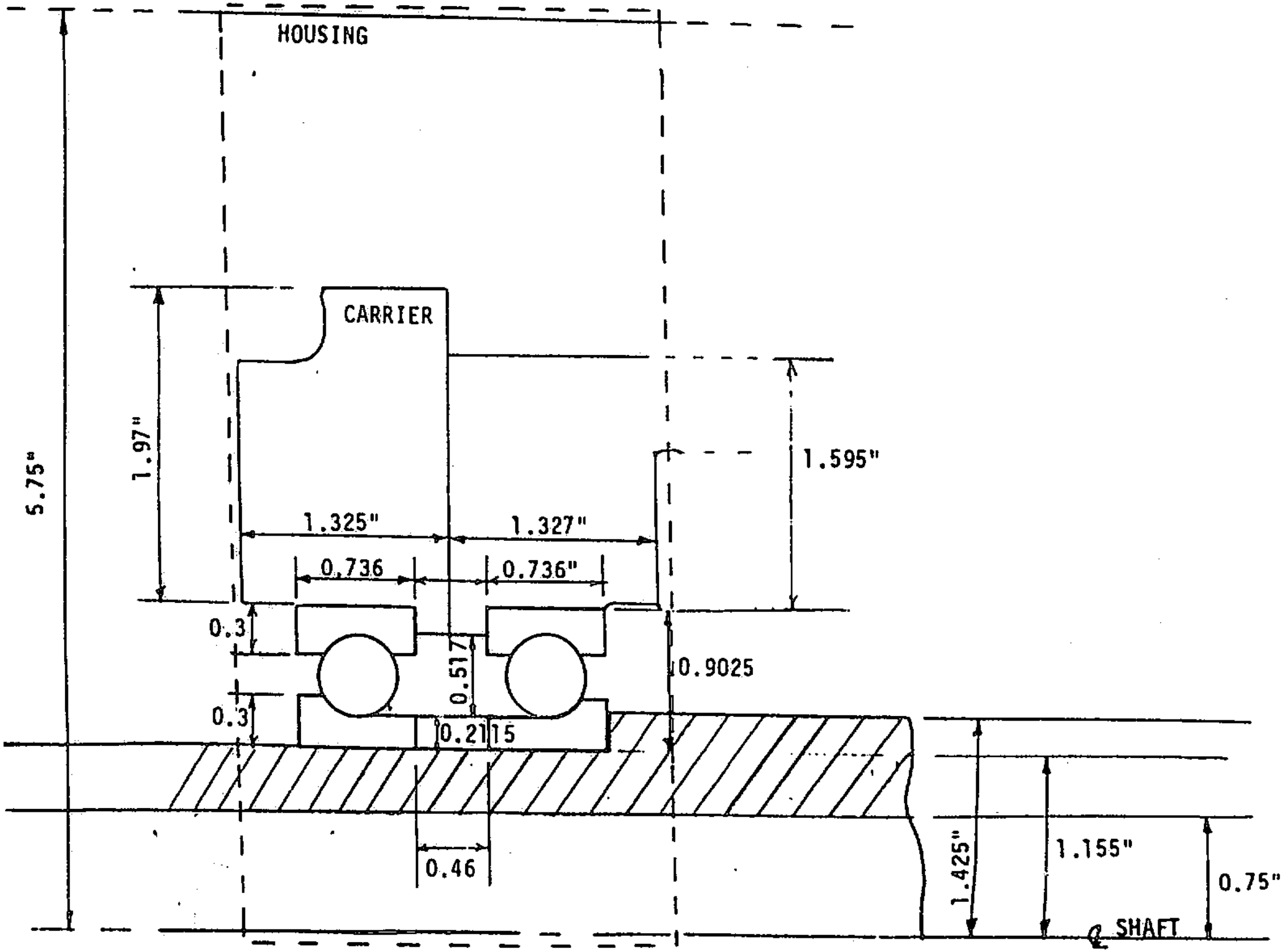

ORIGINAL PAGE IS
OF POOR QUALITY

FIGURE 4.1.2 CROSS-SECTIONAL VIEW OF SHAFT, BEARING, CARRIER AND HOUSING

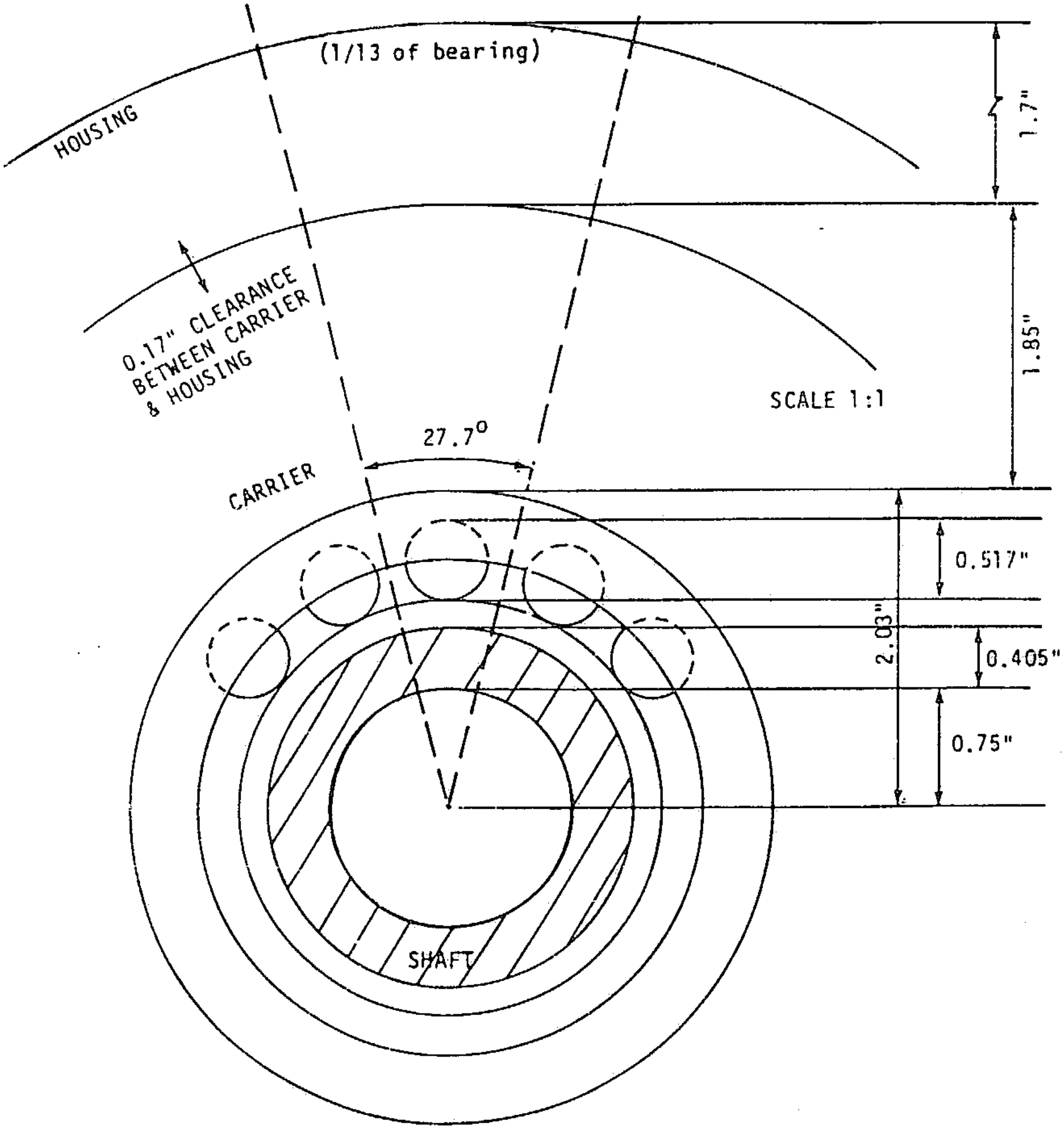

FIGURE 4.1.3 DETAILED NODAL REPRESENTATION OF 57mm BEARING

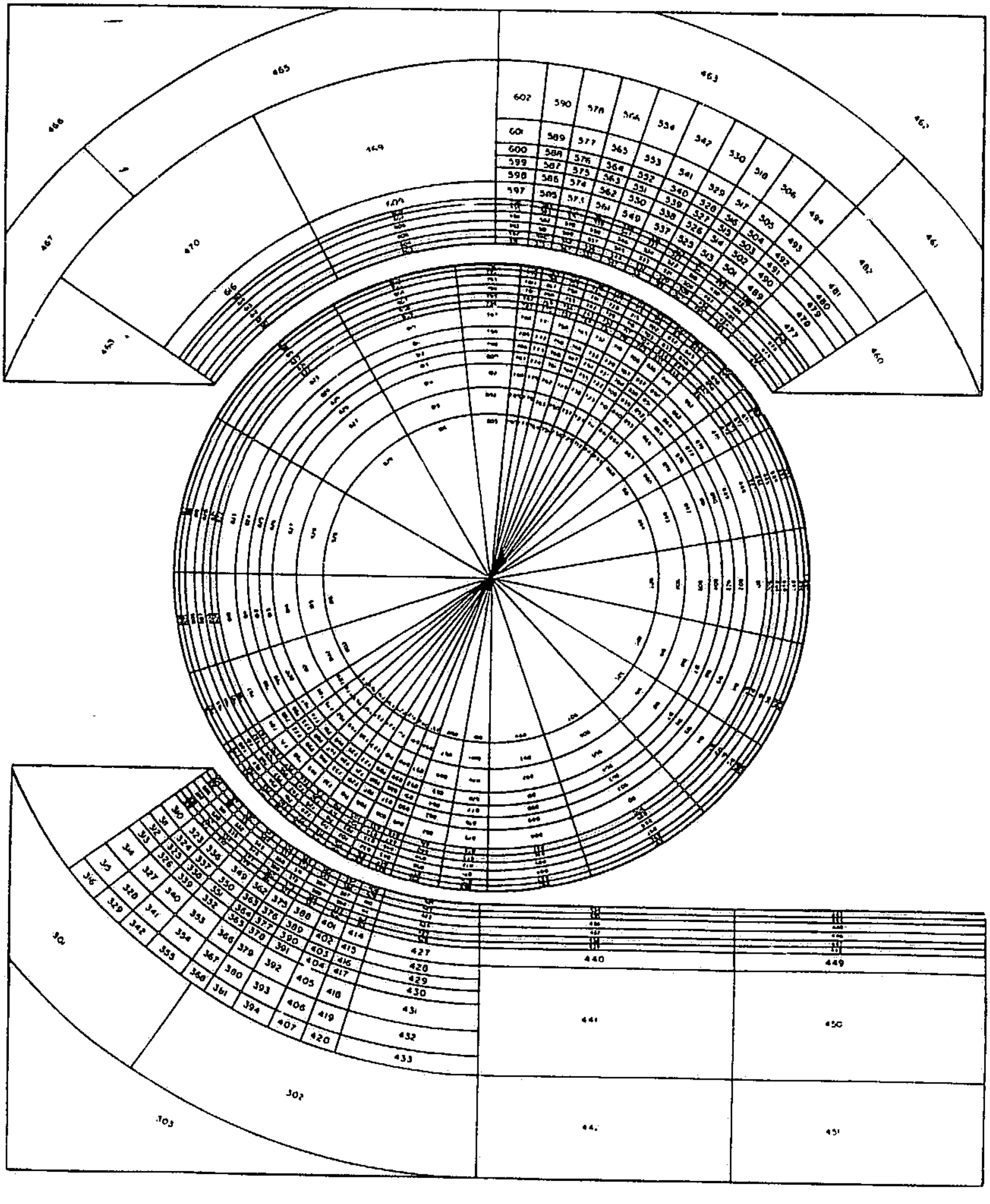

ORIGINAL PAGE IS
OF POOR QUALITY

FIGURE 4.1.4. TEMPERATURE -VS- DEPTH BELOW SURFACE OF ROLLING ELEMENT

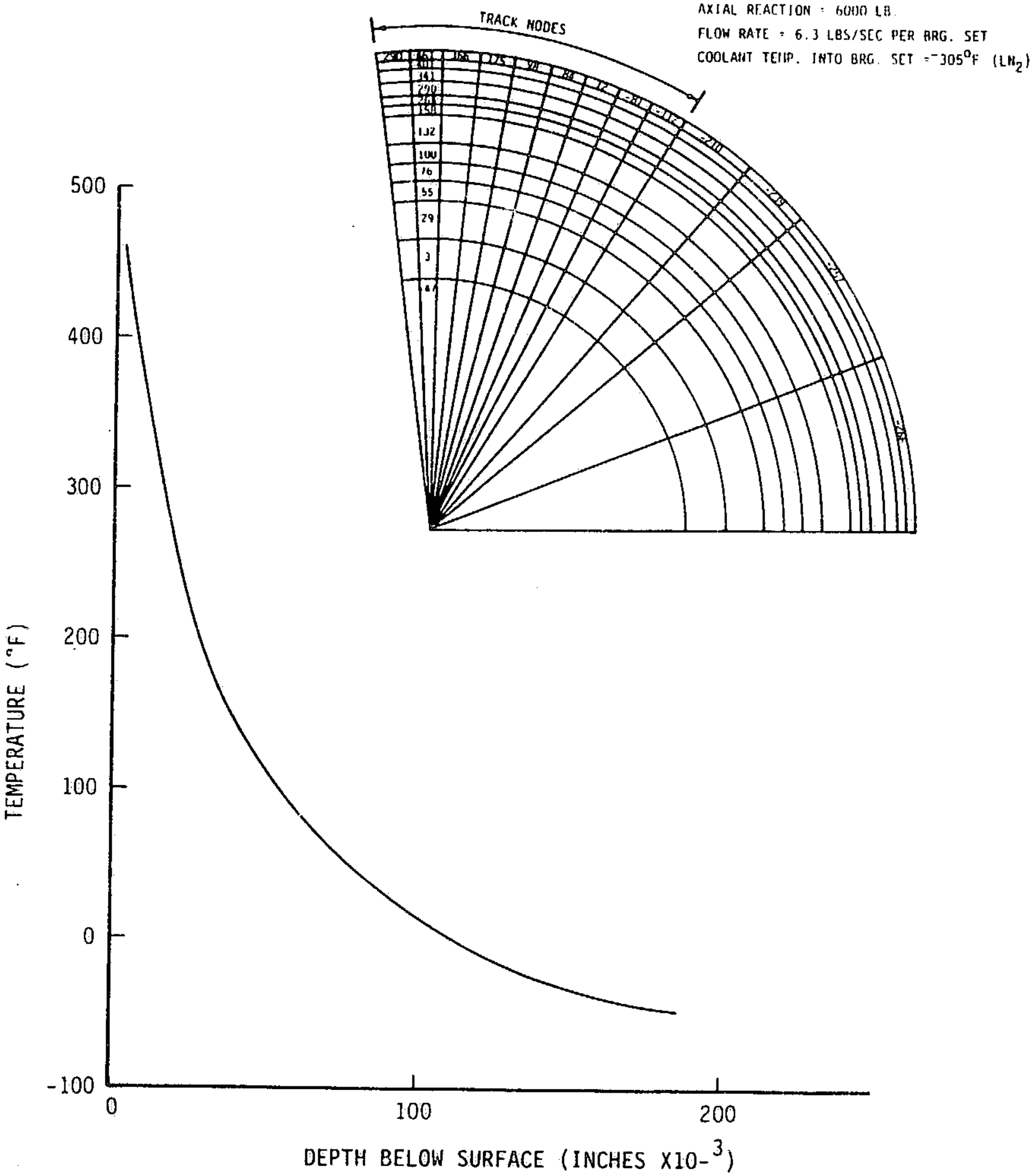

AXIAL REACTION = 6000 LB.
FLOW RATE = 6.3 LBS/SEC PER BRG. SET
COOLANT TEMP. INTO BRG. SET = $^-305^{\circ}$F (LN_2)

FIGURE 4.2.1
ROLLING ELEMENT TEMPERATURE DISTRIBUTION FOR LOX PUMP TURBINE END BEARING

(TEMPERATURES IN DEGREES FARENHEIT)
AXIAL REATION = 2500 LB.
FLOW RATE = 6.3 LBS/SEC PER BRG. SET
COOLANT TEMP. INTO BRG. SET -305°F(LN_2)

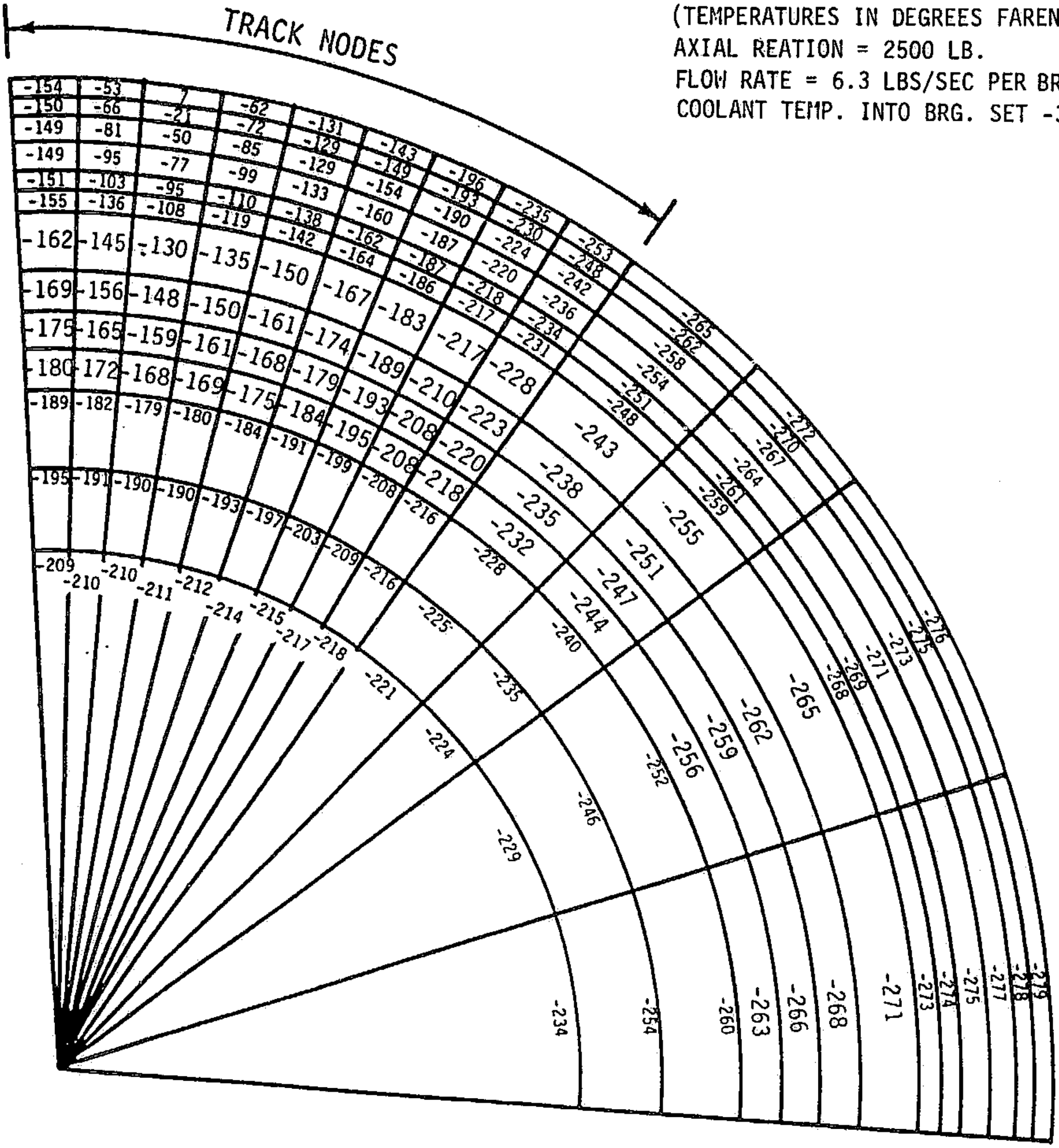

FIGURE 4.2.2 INNER AND OUTER RACE TEMPERATURE DISTRIBUTIONS

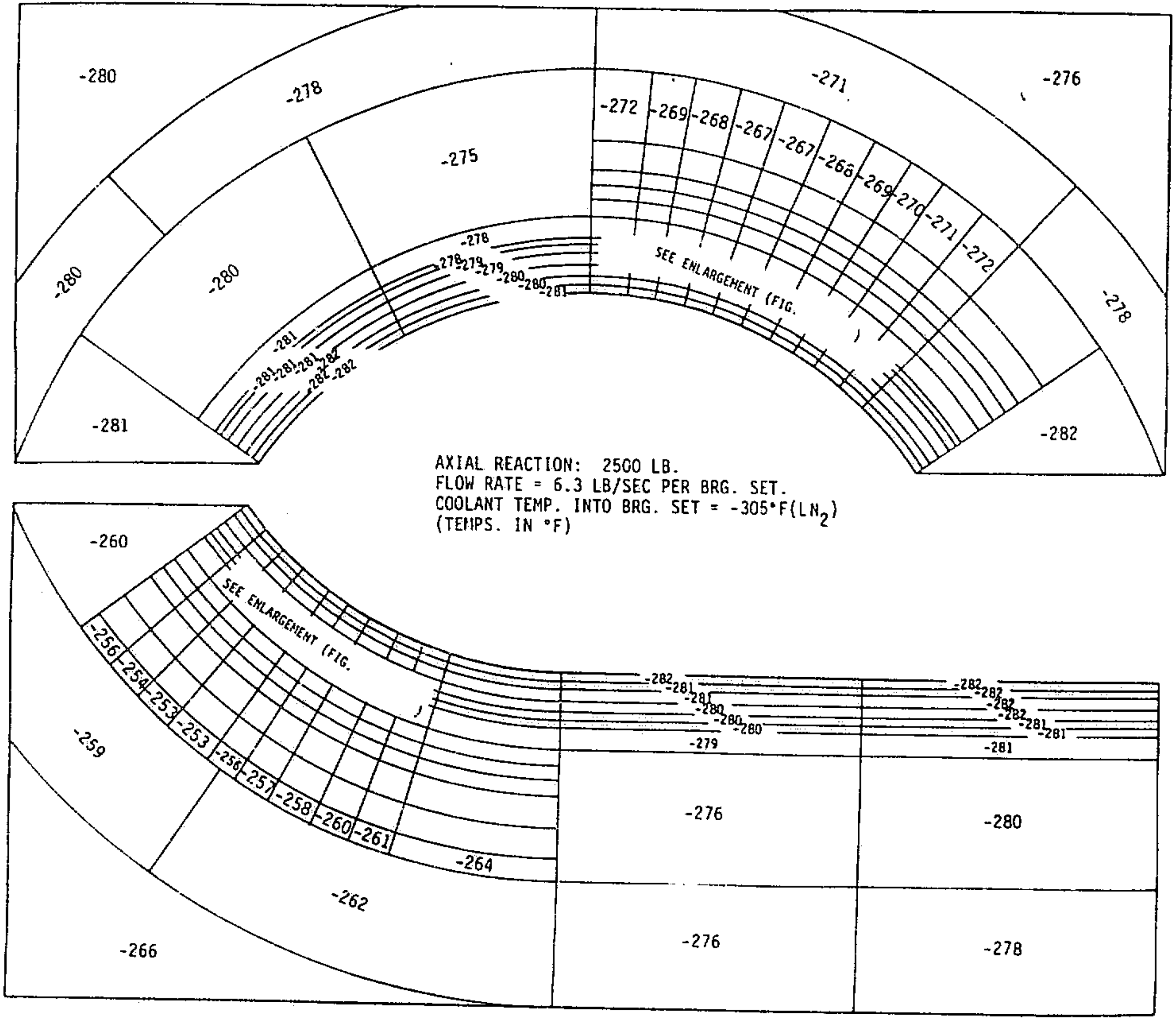

AXIAL REACTION: 2500 LB.
FLOW RATE = 6.3 LB/SEC PER BRG. SET.
COOLANT TEMP. INTO BRG. SET = -305°F(LN_2)
(TEMPS. IN °F)

FIGURE 4.2.3 OUTER RACE TEMPERATURE DISTRIBUTION FOR LOX PUMP TURBINE END BEARING

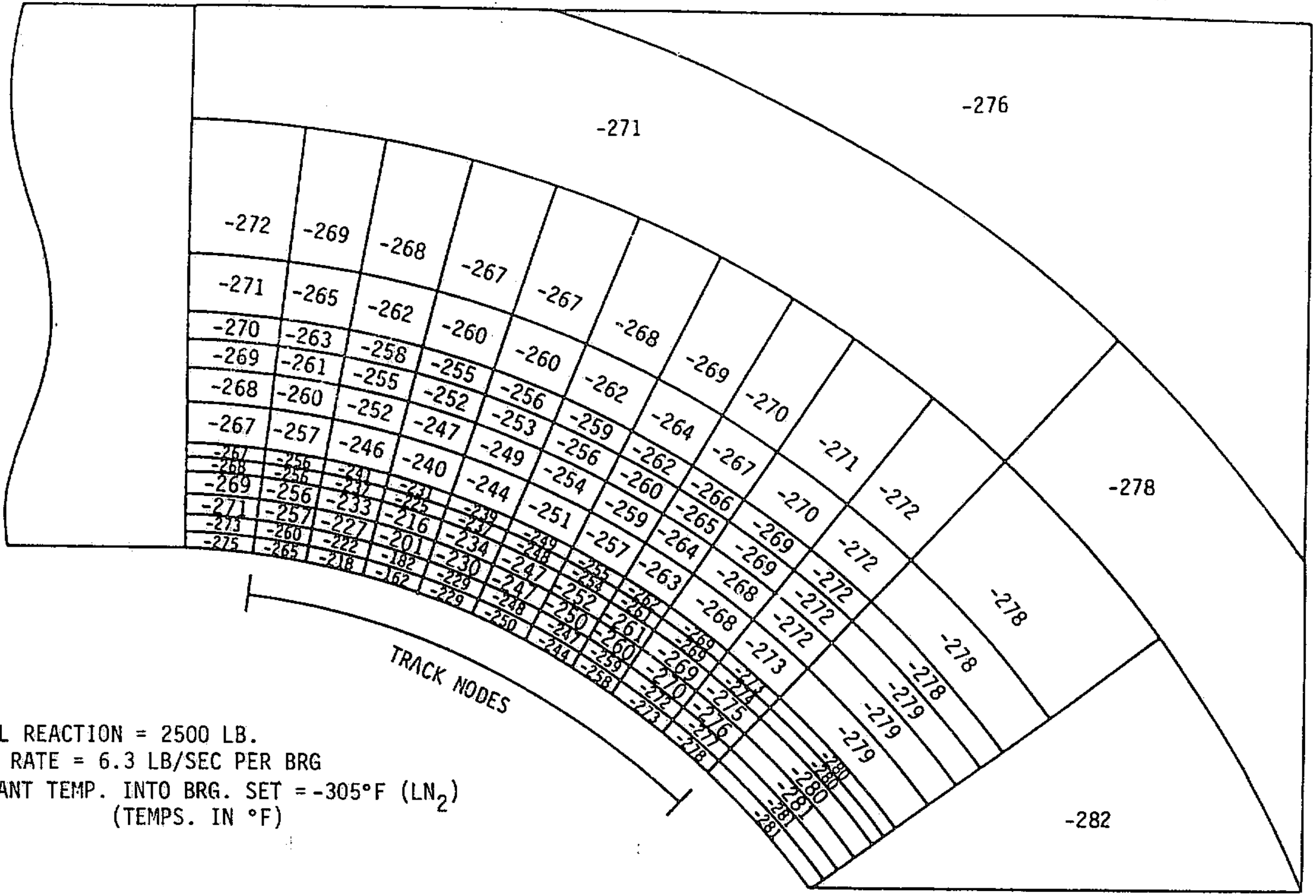

AXIAL REACTION = 2500 LB.
FLOW RATE = 6.3 LB/SEC PER BRG
COOLANT TEMP. INTO BRG. SET = -305°F (LN_2)
(TEMPS. IN °F)

FIGURE 4.2.4 INNER RACE TEMPERATURE DISTRIBUTION FOR LOX PUMP TURBINE END BEARING

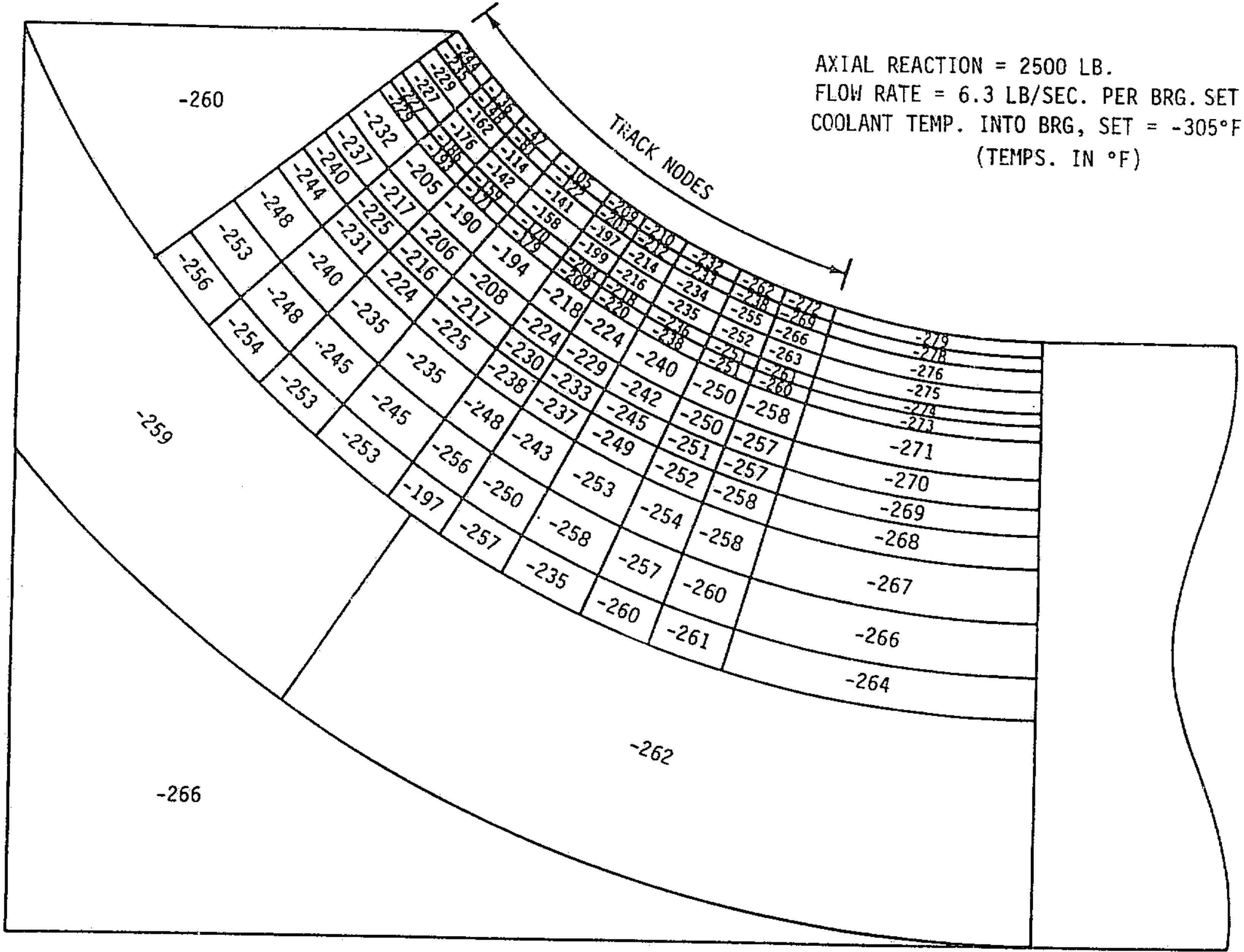

AXIAL REACTION = 2500 LB.
FLOW RATE = 6.3 LB/SEC. PER BRG. SET
COOLANT TEMP. INTO BRG, SET = -305°F (LN_2)
(TEMPS. IN °F)

FIGURE 4.2.5

ROLLING ELEMENT TEMPERATURE DISTRIBUTION FOR LOX PUMP TURBING END BEARING

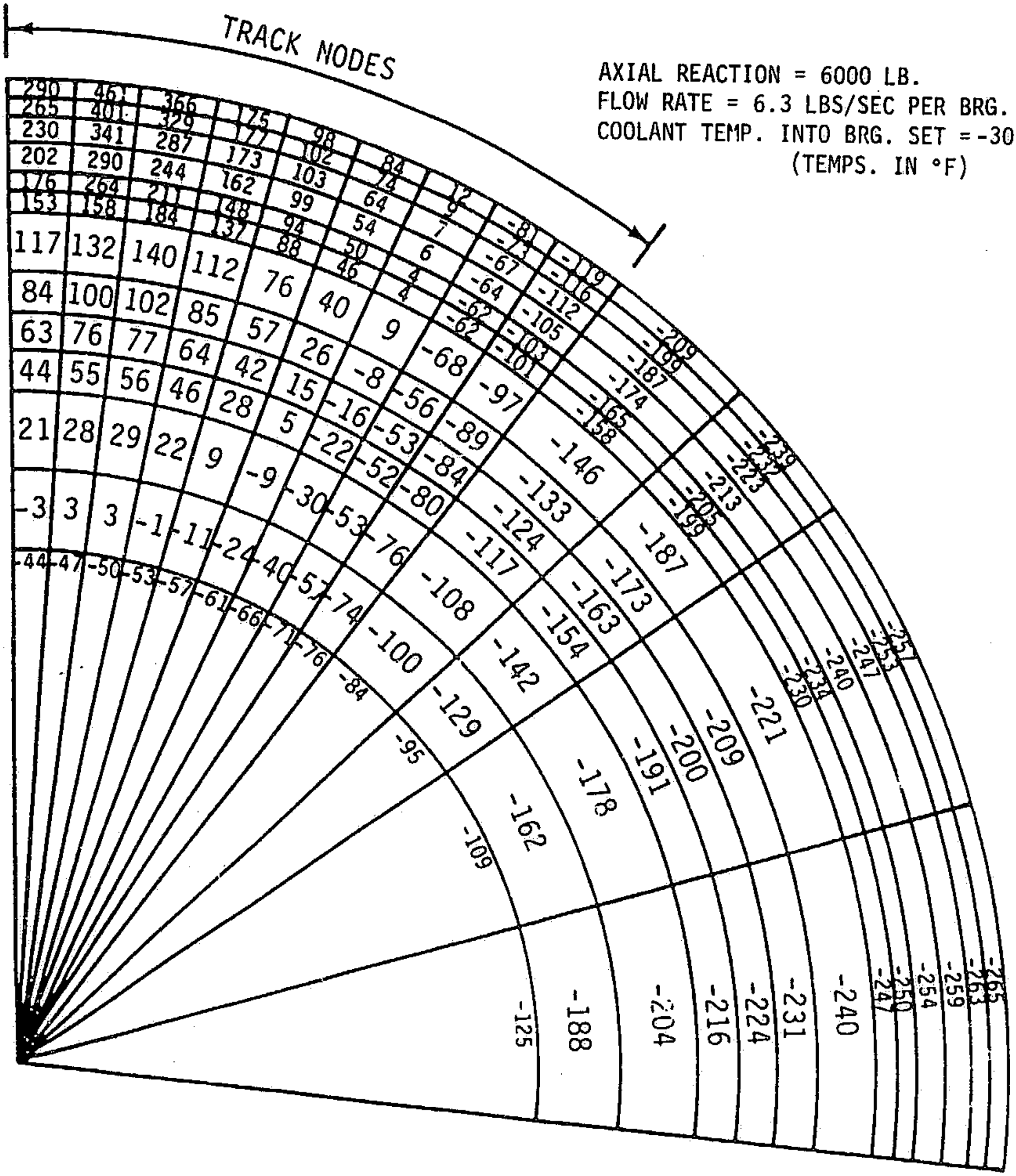

AXIAL REACTION = 6000 LB.
FLOW RATE = 6.3 LBS/SEC PER BRG. SET
COOLANT TEMP. INTO BRG. SET = -305°F (LN_2)
(TEMPS. IN °F)

FIGURE 4.2.6 INNER AND OUTER RACE TEMPERATURE DISTRIBUTION

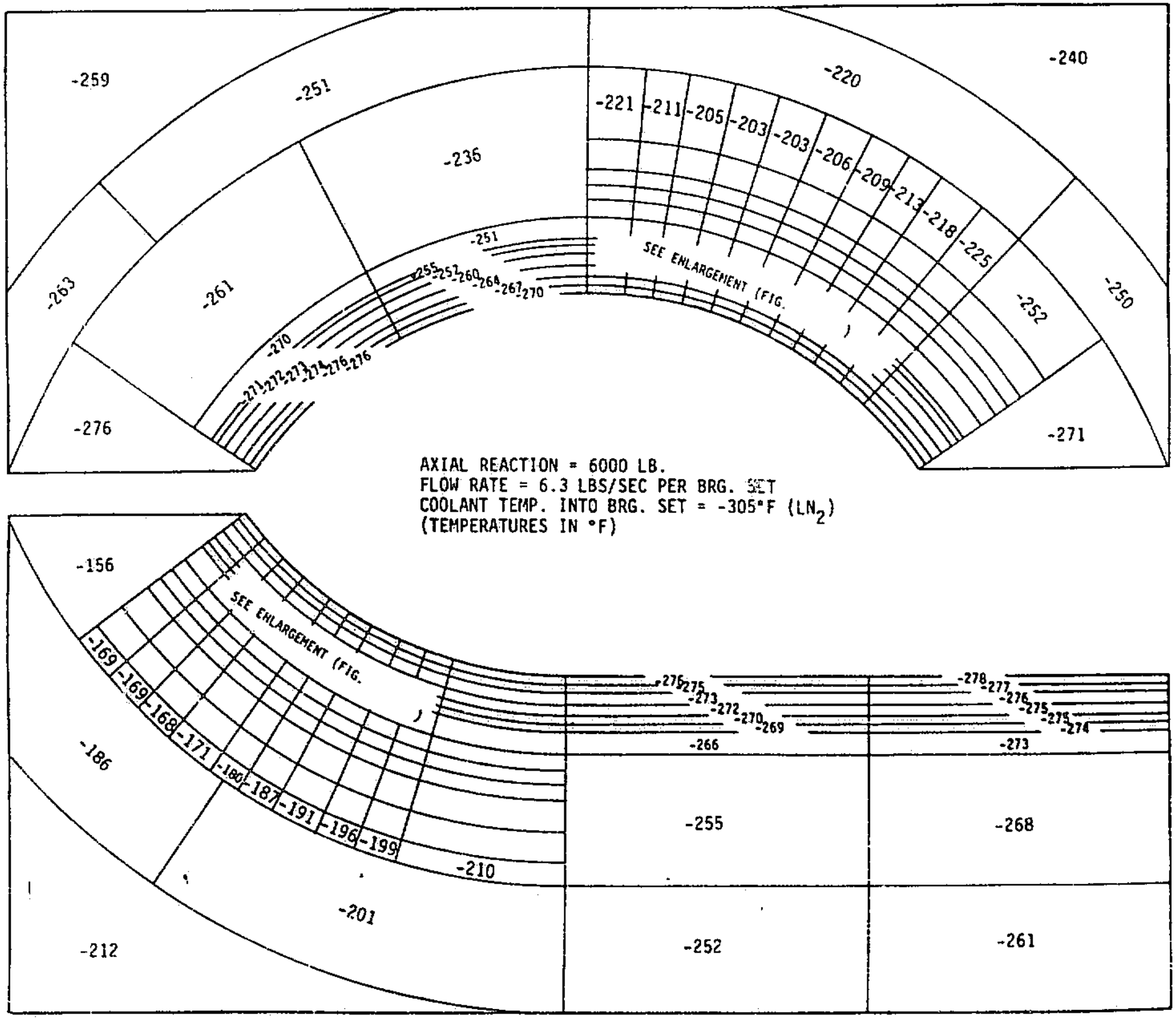

AXIAL REACTION = 6000 LB.
FLOW RATE = 6.3 LBS/SEC PER BRG. SET
COOLANT TEMP. INTO BRG. SET = -305°F (LN_2)
(TEMPERATURES IN °F)

FIGURE 4.2.7 OUTER RACE TEMPERATURE DISTRIBUTION FOR LOX PUMP TURBINE END BEARING

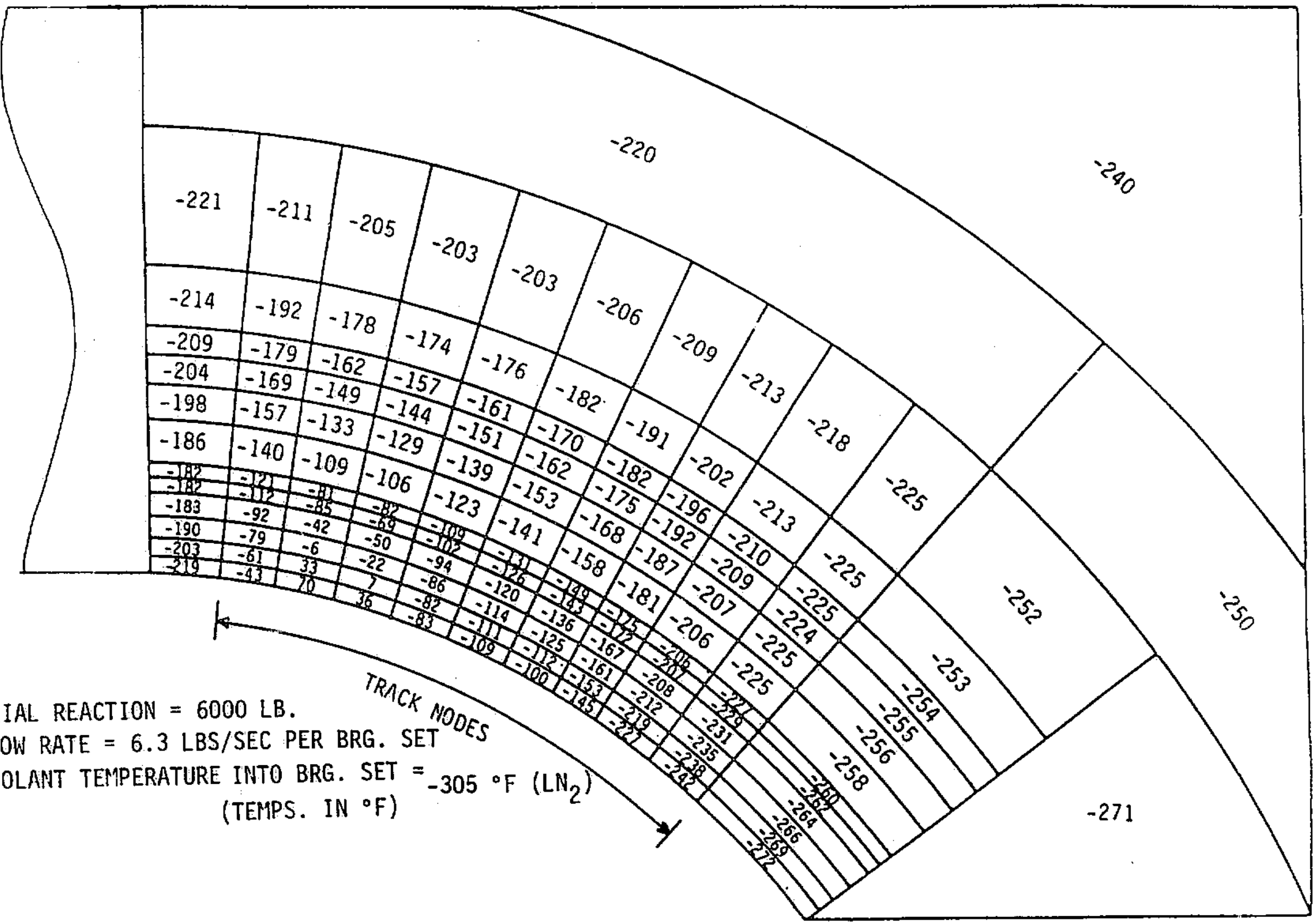

AXIAL REACTION = 6000 LB.
FLOW RATE = 6.3 LBS/SEC PER BRG. SET
COOLANT TEMPERATURE INTO BRG. SET = -305 °F (LN_2)
(TEMPS. IN °F)

ORIGINAL PAGE IS
OF POOR QUALITY

FIGURE 4.2.8 INNER RACE TEMPERATURE DISTRIBUTION FOR LOX PUMP TURBINE END BEARING

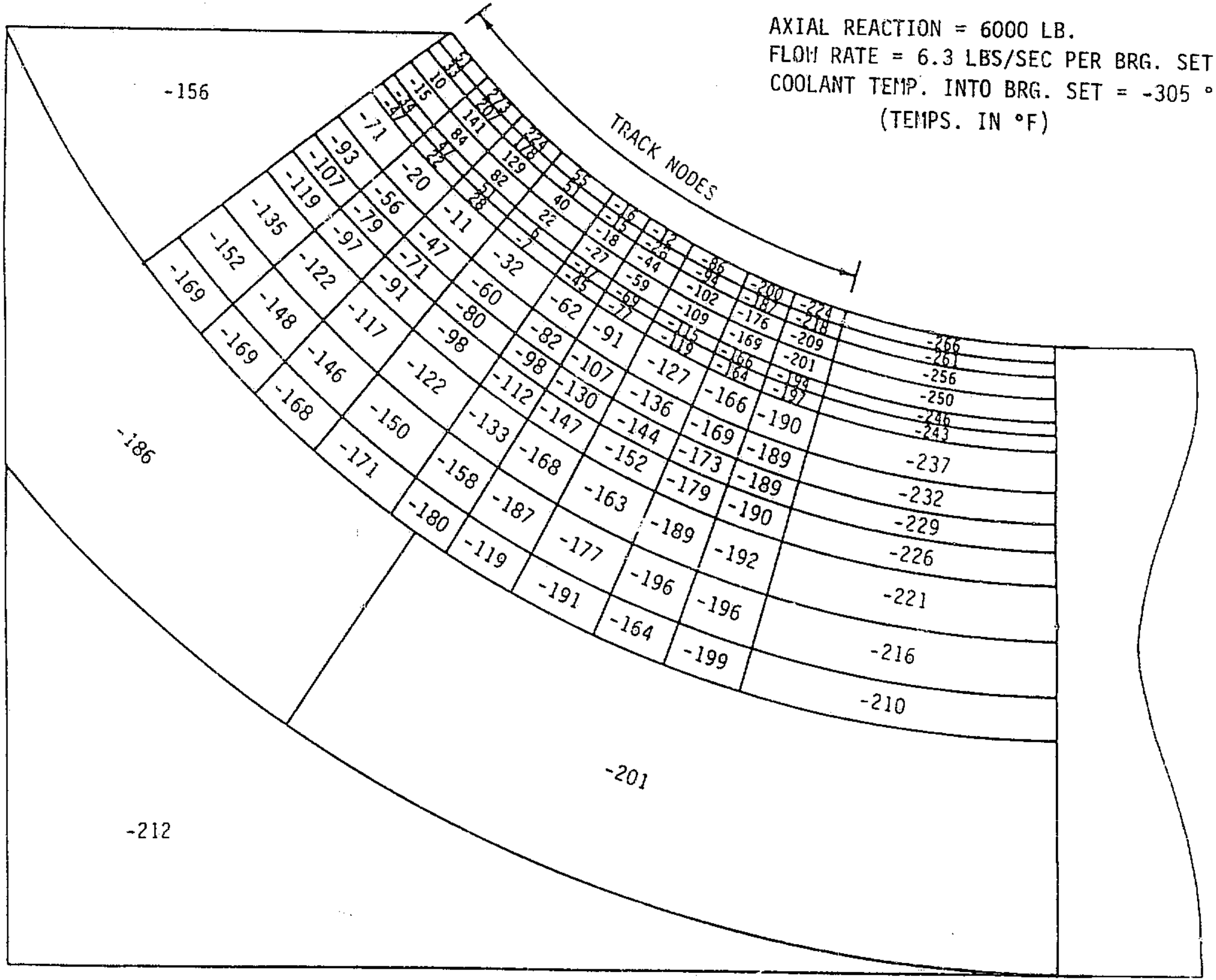

AXIAL REACTION = 6000 LB.
FLOW RATE = 6.3 LBS/SEC PER BRG. SET
COOLANT TEMP. INTO BRG. SET = -305 °F (LN_2)
(TEMPS. IN °F)

generation value as a function of loading for input into the bearing thermal model. The modifications to SHABERTH are further discussed in Section 4.5.

Experimental rotational data from the BMT (Bearing and Materials Tester) is essential in order to verify the accuracy of the bearing model which has been developed.

4.3 Thermodynamics of the Bearing System

4.3.1 Energy and Flow Balance Estimates

Energy and flow balance analyses were conducted to investigate the differences in energy flow into and out of the tester during the LN_2 tests and LOX tests. In addition, inlet and outlet pressure measurements were evaluated in an attempt to compare tester flows during the LN_2 and LOX tests. Four test conditions were evaluated: (1) LOX flow, (2) LOX rotational, (3) LN_2 flow, and (4) LN_2 rotational. The flow tests were evaluated to judge the validity of pressure and temperature readings and to estimate the heat gain of the tester flow from the atmosphere. Figures 5.3.1, 5.3.2, 5.3.3, and 5.3.4 provide a summary of the four test conditions. These figures show the test values and schematically locate the instrumentation of interest. Test identification information is shown in the upper right corner of each figure.

The flow test data (tester not rotating) are shown in Figures 5.3.1 and 5.3.2. As indicated in the lower left corner of Figure 5.3.1, temperature measurements T_{1001} through T_{1003} are resistance bulb (RB) thermometers and the other temperature measurements are thermocouples. There appears to be a problem with the RB's during the LOX test since they show a decrease in temperature across the tester in the flow direction (see Figure 5.3.1). They also read about 6°F lower than the thermocouples in comparable locations. The RB's are in fair agreement with the thermocouples during the LN_2 flow tests (Figure 5.3.2). Since the RB's appeared to be in error during the LOX tests, the thermocouple measurements at the entrance and exit manifolds were used to estimate the heat flow.

Pressure measurement P_6 is inconsistent with the upstream and downstream pressure measurements for both LOX test conditions. T_{1002} is not provided for the LOX tests and T_4 is a bad measurement. As stated above, the LOX flow test data were evaluated to determine the ambient heat flow into the tester. As shown in Figure 5.3.1, there is very little temperature gain as the flow moves from the inlet to the exit manifold. Using the stated LOX flow rate of 9.1 lbs/sec. and the inlet and outlet temperature difference, an ambient heat input of about .5 Btu/sec was calculated from the LOX flow test data.

The BMT thermal system was defined as follows:

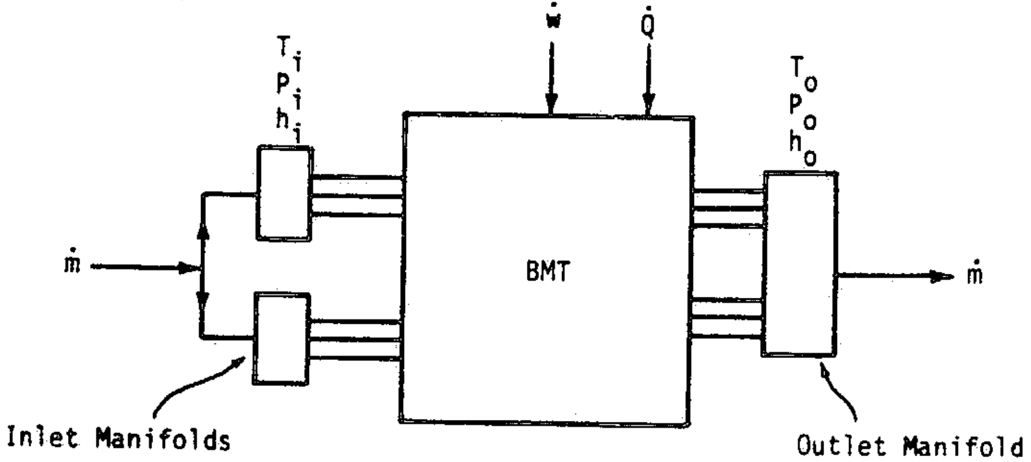

ORIGINAL PAGE IS
OF POOR QUALITY

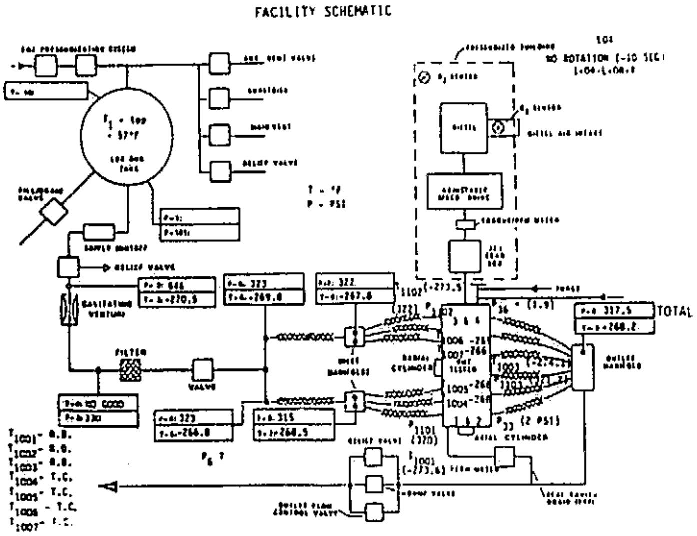

FIGURE 4.3.1 LOX TEST CONDITIONS (T = -10 sec.)

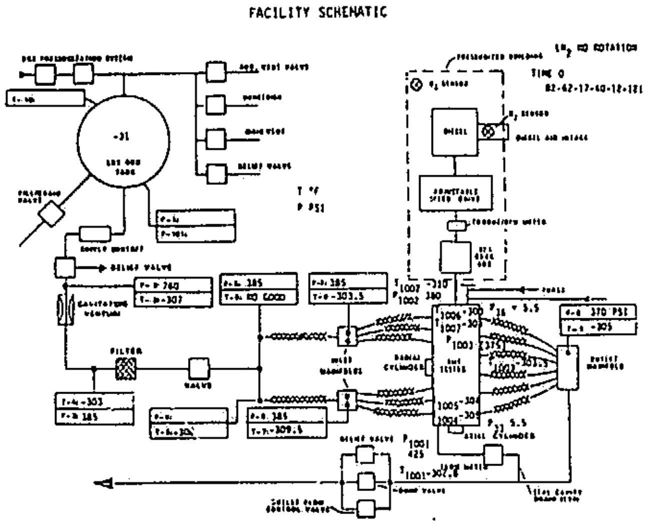

FIGURE 4.3.2 LN$_2$ TEST CONDITIONS (T = 0)

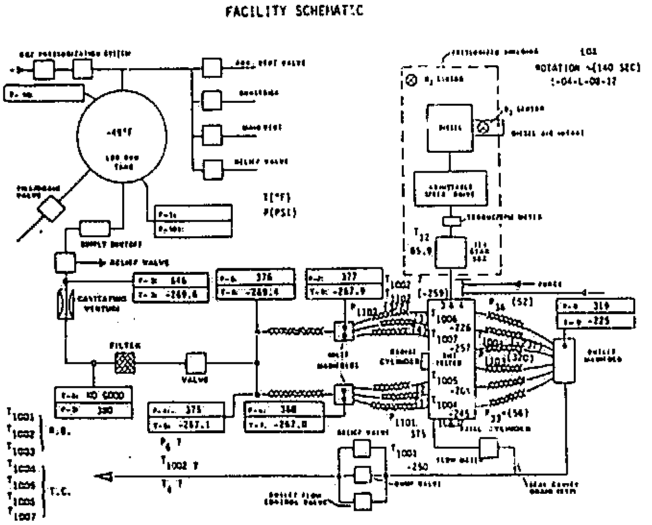

FIGURE 4.3.3 LOX TEST CONDITIONS (T = 140 sec.)

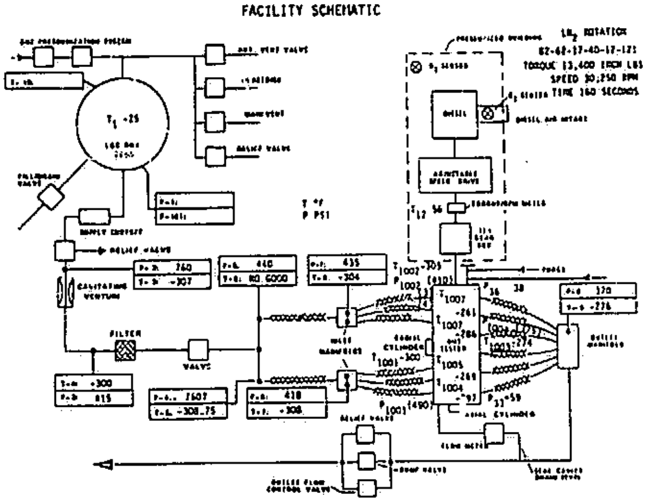

FIGURE 4.3.4 LN$_2$ TEST CONDITIONS (T = 160 sec.)

where:	$\dot{m}$	mass flow rate
	T	temperature
	P	pressure
	$\dot{Q}$	heat rate
	$\dot{W}$	power
	h	fluid enthalpy
subscripts:	i	inlet conditions
	o	outlet conditions

An energy balance on the system defined above is as follows:

$$\dot{W} + \dot{Q} = \dot{m}(h_o - h_i) + \frac{dE}{dt}$$

where: $\frac{dE}{dt}$ is the time rate of change of internal energy assumed to be zero, thus implying steady state conditions.

The power term (W) is determined from the torque and speed measurements and, as stated previously, the ambient heat flow term was evaluated from the flow test data and assumed to be the same for the rotating tests. Shown on Figure 4.3.5 are the terms of the above heat balance for the four test conditions. As shown in the figure, there is an excess of energy not accounted for in the steady state energy balance. The LOX test gives about 21 kw and the LN_2 test about 9.4 kw excess energy input into the system. This is a maximum error of 12% and 5% for the LOX and LN_2 heat balances.

Although this is fairly good agreement, there are several possible explanations for the energy imbalance. The calculation of power input to the tester is questionable because the torque is measured at the gear box input. This requires the gear box torque to be determined at no load conditions and subtracted from the test value. Since the loaded gear box torque is very likely greater, and the gear box torque can be affected by gear box temperature, etc., this method of determining the BMT torque has several uncertainties. A torque measurement at the gear box outlet is needed to eliminate these questions.

Other sources of potential error are the temperature and flow measurements, and the storage of energy in the tester hardware. Since the tester housing temperature does increase during the rotation tests, some energy is being stored. An accurate estimate of the amount is difficult due to the complicated geometry of the tester. Assuming for the moment that the energy storage term is small and the power input is correct, it is interesting to note that the energy input to the coolant flow ($m\Delta h$) is about 11% greater during the LN_2 runs as compared to the LOX tests. Because of the higher LOX density it would be expected that the viscous work done on the LOX would be considerably greater than done on the LN_2. This could suggest higher bearing friction in the LN_2.

Based on the preceding evaluation, the following conclusions can be stated:

1) An overall system energy balance is a valuable tool for evaluating the validity of the temperature, pressure, torque, speed, and flow data.

2) To improve the capability of this technique several changes should be made in the tester instrumentation as suggested below:

FIGURE 4.3.5 ENERGY BALANCE SUMMARY

		POWER INPUT $\dot{W}$ (WATTS)	AMBIENT HEAT INPUT Q (WATTS)	ENERGY REMOVED BY FLOW ($\dot{m}\Delta h$) (WATTS)	ENERGY UNBALANCE FOR STEADY CONDITIONS (WATTS) $\dot{W} + Q - \dot{m}\Delta h$
LOX	NON-ROTATING (FLOW)	0	527	0	0
	ROTATING	202.8×10^3	527*	182.1×10^3	21.2×10^3
LN_2	NON-ROTATING (FLOW)	0	527*	0	0
	ROTATING	210.9×10^3	527*	202×10^3	9.4×10^3

* ASSUMED TO BE THE SAME DURING ALL TESTS.

FIGURE 4.3.6

POWER GENERATION VS. TEMPERATURE DIFFERENCE ACROSS BEARING
POWER IN (KW)

ΔT °C ACROSS BEARINGS 2 & 3

		0	100	200	300
COMPONENT*					
Slinger (Smooth Sides)		31.9	31.9	31.9	31.9
Spacers		10	10	10	10
Shaft		42.9	42.9	42.9	42.9
	Sub Total	84.8	84.8	84.8	84.8
BEARINGS					
Viscous					
1 & 4		**65.9	65.9	65.9	65.9
2 & 3		***2.0	7.0	2.0	2.0
	Sub Total	67.9	67.9	67.9	67.9
FRICTION					
1 & 4		2.2	2.2	2.2	2.2
2 & 3		10.8	13.0	27.5	68.7
	Sub Total	13.0	15.2	29.7	70.9
	Total	165.7	167.9	182.4	223.6

*Although the Component Power & Viscous Power will be reduced as the fluid temperature increases, this effect was assumed to be within the uncertainties introduced by the assumption made in the power calculations.

**Assumes no fluid rotation prior to entering the bearing.

***Assumes fluid enters bearings 2 & 3 with rotational velocity equal to cage speed.

FIGURE 4.3.7 ENERGY VS. BEARING ΔT

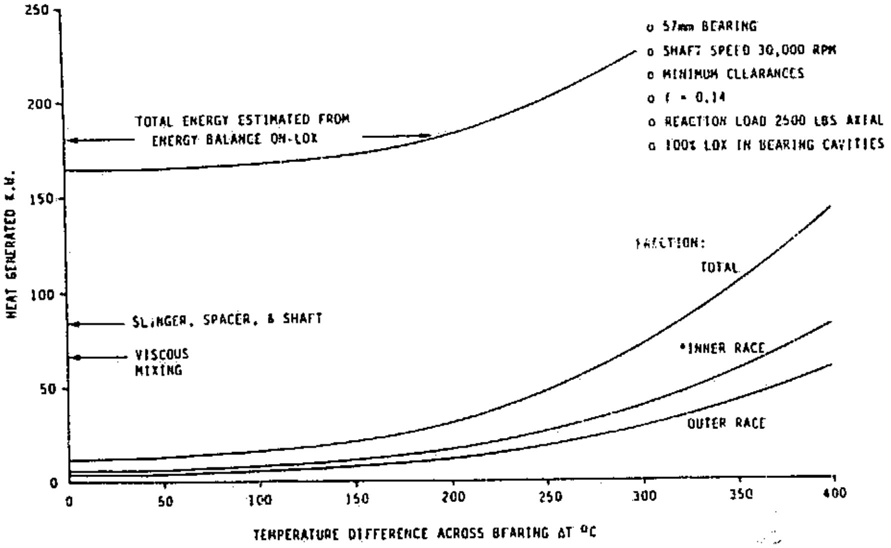

* INNER & OUTER RACES OF BGRS. 2 & 3.
BGRS 1 & 4 WERE UNLOADED; A CONSTANT RATE OF
2.2 K.W. WAS ESTIMATED FOR THE RACE FRICTION HEAT.

a) Provide a torque measurement at the drive end of the BMT.

b) Add additional temperature and pressure measurements at the entrance and exit manifolds of the tester to assure more than one measurement at these critical locations. The temperature measurements should be that of the fluid and not the metal.

3) It is highly desirable to determine the flow rate to each pair of bearings as well as the total flow through the tester. Since flow is such a critical parameter, redundant measurements need to be considered.

4.3.2 Correlation of Tester Internal Power Dissipation with Bearing Temperature Differences

To determine the sources and magnitudes of heat generated in the BMT, each component was evaluated and an estimate of the amount of energy dissipated was made. The total amount dissipated was then compared to the total energy transferred to the LOX coolant flowing through the bearings. As will be shown, the total energy estimated from the component analysis is less than the energy transferred to the LOX coolant. The LOX coolant and component energy can be balanced, however, by assuming a temperature gradient across the bearing. The temperature gradient causes increased internal loading and heat generation.

The power estimates for each component in the BMT are shown in Figure 4.3.6. This information was calculated using semiempirical relationships provided in Reference 2 and viscous ball drag obtained from the bearing computer program. Several assumptions were necessary to complete the power estimates. The most significant are as follows:

1) The fluid has no rotational speed prior to entering bearings 1 and 4.

2) Front faces (face to shaft shoulder) of bearings 2 and 3 are rotating in stagnant fluid.

3) Fluid is rotating at cage speed between bearings 1 and 2 and between bearings 3 and 4.

4) The power dissipated by the shaft section between bearings 2 and 3 was determined by averaging the power estimates based on inlet fluid properties and exit fluid properties.

5) The power estimated for disks and cylinders can be superimposed to obtain the combined slinger-shaft power.

As shown in Figure 4.3.6, only the bearing frictional power for the loaded bearings (2 and 3) was varied as a function of bearing temperature differences. Energy values for other components downstream of bearings 2 and 3 would vary as additional heat is added to the coolant. This effect was considered secondary in view of the other uncertainties in the analysis. The other side of the energy balance is the energy absorbed by the bearing coolant flow. This was estimated, and the summary results are provided in Figure 4.3.5. As shown, 182.1 kW of energy was estimated to be absorbed by the bearing coolant flow. Since this is in excess of the 165.7 kW estimated to be generated, it is suggested that a temperature gradient across the bearings could explain the discrepancy. Figure 4.3.7 illustrates, in graphical form, the information provided in Figure 4.3.6. Also shown in Figure 4.3.7 is the temperature gradient across the bearings (2 and 3) necessary to achieve an overall energy balance.

In summary, the results of the analysis strongly indicate that the inner races of bearings 2 and 3 are considerably higher in temperature than the outer races. This condition can become unstable causing excessive internal loads and temperatures resulting in rapid deterioration and failure of the bearing. In addition, careful consideration must be taken to ensure the unloaded bearings (1 and 4) do not become unloaded to the extent that significant slip or skidding can occur between the balls and inner races.

4.3.3 Estimation of Heat Loads for the BMT Thermal Model

Heat is generated in the BMT from mechanical friction and viscous work done on the coolant. To realistically estimate bearing component temperature, this energy must be evaluated and applied correctly in the BMT thermal model. An estimate of the total energy generated can be obtained from an overall energy balance on previous test data. This was done in Section 4.3.2and is shown in Figure 4.3.5. Once the total energy is determined, the problem remaining is to correctly evaluate the distribution of viscous and frictional energy. The bearing contact surface temperatures are obviously much more sensitive to frictional energy changes than changes in viscous energy.

The distribution of energy for the BMT thermal model, with LN_2 coolant, was evaluated as follows:

1) Estimate total energy generated from a heat balance on the coolant (see Figure 4.3.5 of Section 4.3.2).
2) Calculate the viscous energy generated by each component in the tester (see Figure 4.3.6 of Section 4.3.2).
3) Using measured torque values, estimate appropriate friction coefficients, and calculate friction energy distribution (i.e. inner race, outer race).
4) Adjust viscous energy distribution such that the total input matches the overall heat balance determined from test data.

Steps 1 and 2 had already been done and the results provided in Section 4.3.2.

Battelle (Reference 34) measured the bearing torque as a function of axial load and surface conditions. Figure 4.3.8 is a reproduction of their data. Also shown, for comparison, is the bearing torque predicted by SHABERTH I. The predicted torque curve was generated using a friction coefficient of 0.2. The predicted curve is reasonably close to the PTFE burnished condition. The referenced value of friction coefficient for this surface condition is .08. The reason for this difference is not evident, however, since power and heat rate are equivalent, a coefficient of friction of 0.2 in the SHABERTH program provides a value reasonably close to the measurement. A further verification of the analysis is shown in Figure 4.3.9. This is data taken from the same reference, compared with results from the SHABERTH I bearing analysis computer code. Although the calculated and measured axial deflections diverge with increased load, the contact angles agree fairly well. Consequently a friction coefficient of 0.2 was used in SHABERTH to obtain frictional heat generation values for the thermal model.

To complete the frictional heat evaluation the bearing load as well as the friction coefficient must be known. There is uncertainty in the axial load seen by the bearings due to the unknown pressure loss across the carriers. According to the measured ΔP the axial load on the bearing should be about 2500 pounds. Although this value is suspect because of fluid vortices, it is probably the most representative at this time.

ORIGINAL PAGE IS
OF POOR QUALITY

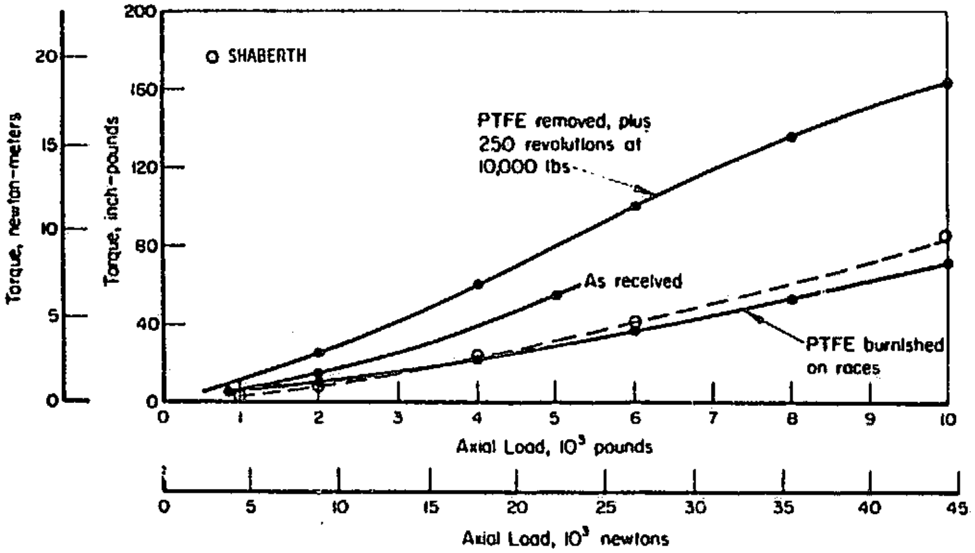

FIGURE 4.3.8 BEARING TORQUE AS A FUNCTION OF AXIAL LOAD

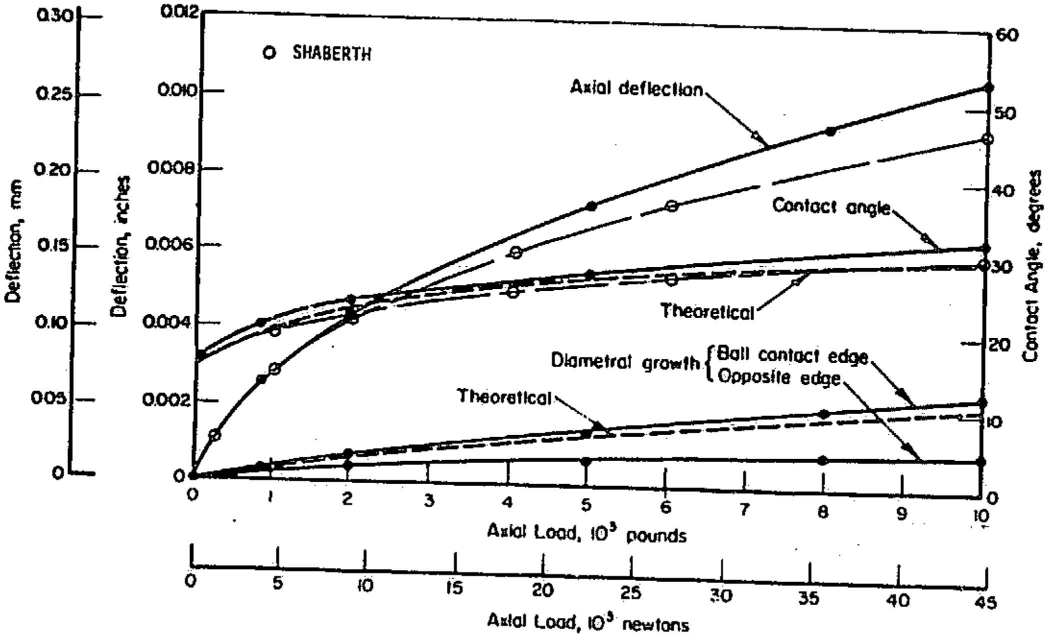

FIGURE 4.3.9 BEARING DEFLECTIONS AND CONTACT ANGLE AS A FUNCTION OF AXIAL LOAD

Therefore this axial load in combination with a friction value of 0.2 was used to estimate the frictional heat generated. The amount of friction energy was subtracted from the total measured energy, and the remainder was assumed to be viscous. The viscous energy was distributed in the proper proportions as indicated by the viscous work analysis done in Section 4.3.2. It was assumed that no lubrication was provided by the LN_2 coolant. This assumption will be reevaluated for the analyses of the LOX coolant.

Another important parameter, with a high degree of uncertainty, is the two phase heat transfer coefficient. There is no experimental data on this parameter that corresponds to the operating conditions of the bearing. Therefore, extrapolations have been made to estimate these parameters for the thermal model. The uncertainty in these extrapolations are unknown.

The above points out two critical areas of cryogenic bearing analysis requiring experimental work: 1) Evaluation of the friction coefficient for high speed bearings using film transfer lubrication in cryogenics, and 2) Evaluation of two phase heat transfer coefficients for high speed bearings in cryogenics.

4.3.4 Iterative Determination of Distributed Frictional Heat Generation in Bearing Contacts

The bearing thermal model has the capability of allowing the frictional heat generated in the rolling element/race contact to be distributed along the major axis of the contact ellipse. The SHABERTH bearing analysis code provides the frictional heat generated in the bearing contacts. The calculation technique used by the code solves for the friction force and slip velocity at finite increments in the contact ellipse. The sum of the product of these parameters is the friction heat generated in the contact. By modification of the SHABERTH code, the heat generation rate distribution along the major axis of the contact ellipse can be obtained. Examples of these distributions are shown in Figures 4.3.10 and 4.3.11 for the inner and outer races respectively. It is of interest to observe that the maximum normal force does not coincide with the location of maximum heat generation. The most heavily stressed area of the contact is therefore not at the highest contact temperature. This is a fortunate condition for those cases where material properties become marginal due to high temperatures.

An iteration procedure has been developed to determine the temperature gradient across the BMT bearing utilizing the "SHABERTH" bearing program and the Bearing Thermal Model with "SINDA" used for analyzing the thermal system represented in electrical analog or lumped parameters form. A specific axial reaction is selected for analysis and put into the "SHABERTH" data base which is set up with configuration data for a 57 mm bearing. A first estimate temperature gradient across the bearing is assumed and added to the data base along with appropriate temperature varying thermal property data for the shaft, inner race, rolling element, outer race and housing. A friction coefficient of 0.2 was used. The "SHABERTH" model is then exercised with this data base and the resultant information contains the frictional heat generated at the track areas of the races and rolling element for a specific axial reaction. This heat, generated from mechanical friction, is input into the Bearing Thermal Model data base along with heat generated from viscous work done on the coolant.

The thermal model is then exercised for a specific data base with the resulting output being steady state temperatures for each node. The average temperature for

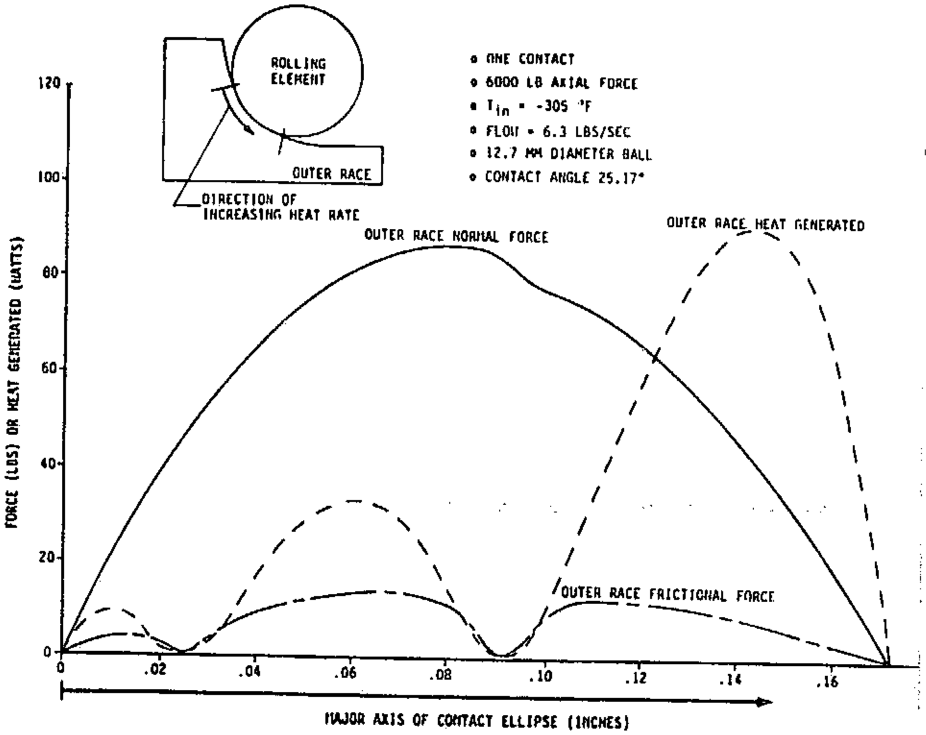

FIGURE 4.3.10 NORMAL FORCE AND HEAT GENERATED IN OUTER RACE CONTACT ELLIPSE

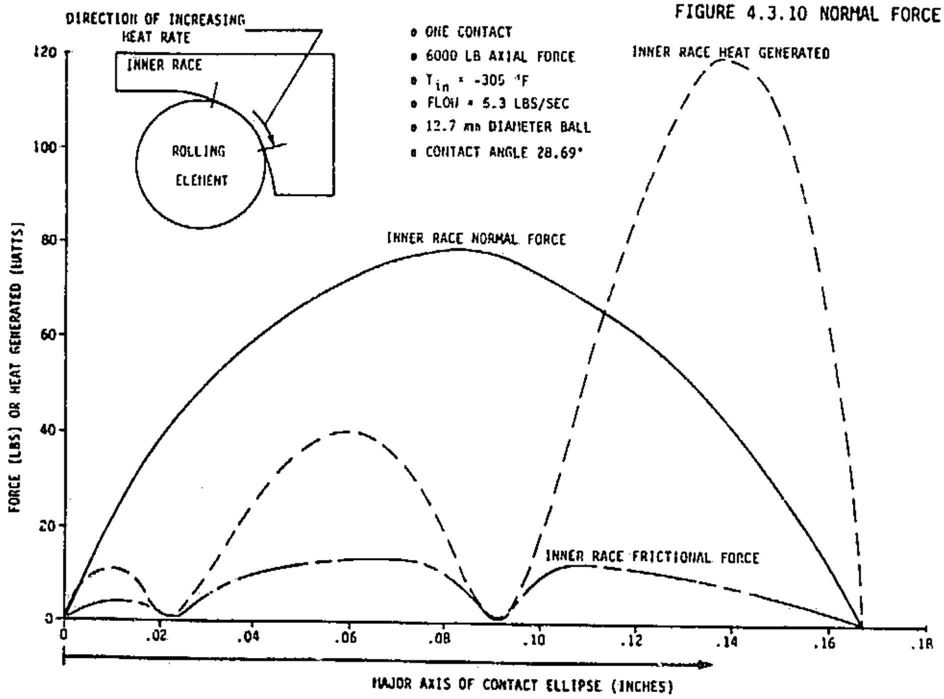

FIGURE 4.3.11 NORMAL FORCE AND HEAT GENERATED IN INNER RACE CONTACT ELLIPSE

PRELIMINARY TEMPERATURE ITERATION RESULTS FOR 2500 POUND AXIAL REACTION MASS FLOW RATE = 3.2 LB/SEC PER BEARING SET INLET COOLANT TEMPERATURE = -176°C (-285°F)

(HEAT GENERATION DATA IS FOR 1/13 OF A BEARING OF ONE ROLLING ELEMENT)

*DATA OBTAINED FROM PRELIMINARY SHABRETH RUN USING ΔT ACROSS THE BEARING OF 200°C AND A FRICTION COEFFICIENT OF 0.14

BEARING COMPONENT	*PRELIMINARY FRICTIONAL HEAT GENERATION DATA (Btu/hr)	AVERAGE TEMPERATURES FROM BEARING THERMAL MODEL (°C)	FIRST ITERATION FRICTIONAL HEAT GENERATION DATA (Btu/hr)	AVERAGE TEMPERATURES FROM BEARING THERMAL MODEL (°C)	SECOND ITERATION FRICTIONAL HEAT GENERATION DATA (Btu/hr)
INNER RACE	1001	-128	537	-137	558
ROLLING ELEMENT	1905	-44	954	-122	953
OUTER RACE	804	-137	416	-162	395

FIGURE 4.3.12

each bearing component (i.e., shaft, inner race, rolling element, outer race, and housing is then calculated as shown

$$T_A = \frac{1}{V_T} \sum_{i=1}^{i=N} T_i V_i$$

T_i = Temp. of Node
V_i = Volume of Node
N = Total Number of Nodes
V_T = Total Volume of N Nodes

The Bearing Thermal Model has been coded to calculate the average temperatures of the bearing components and to determine the thermal property data needed from derived curve fit equations.

The average temperature values for the bearing components are then placed back into the "SHABERTH" data base and replace the original assumed values. Appropriate temperature varying thermal property data is also replaced in the data base. The "SHABERTH" program is then executed again to determine new distributed frictional heat generation data. This data is compared with the previously obtained values to determine whether another iteration is required. It is important to obtain not only the correct ΔT across the bearing, but also the correct bearing component temperatures. The ΔT across the bearing changes the bearing internal clearance. Reduced clearance results in a larger load on the bearing which in turn increases the frictional heat generated. The individual component temperatures are used to determine such thermal property data as the coefficient of thermal expansion and the modulus of elasticity, the values of which, also affect the bearing internal clearances.

The iteration procedure outlined above was performed for an axial reaction of 2500 pounds. The operating parameters; inlet coolant temperature of $-176^{\circ}C$ and mass flow rate of 3.2 LB/SEC per bearing set, were selected for a "worst case" situation. The results of this iteration are shown in Figure 4.3.12. The preliminary frictional heat generation data was obtained from a "SHABERTH" run with an initial assumed ΔT across the bearing of $200^{\circ}C$. This temperature gradient was then resubmitted into the "SHABERTH" bearing data base along with a friction coefficient of 0.2. The first iteration frictional heat generation data is significantly smaller than the preliminary data. Therefore, the Bearing Thermal Model does not support the original assumption of a $200^{\circ}C$ ΔT across the bearing. A second iteration shows the heat generation data holding relatively constant which supports a preliminary ΔT across the bearing of $25^{\circ}C$ and average temperatures of $-137^{\circ}C$, $-122^{\circ}C$ and $-162^{\circ}C$ for the inner race, rolling element, and outer race respectively. This indicates a stable set of thermal conditions, i.e., the heat generated and bearing temperatures do not increase without limit.

4.4 Heat Transfer Coefficients for Bearing Thermal Model

4.4.1 Two-Phase Heat Transfer in Cryogenic Systems

In any attempt to predict failure using the bearing thermal model, the effects of surface boiling on the coolant performance must be considered. Preliminary SINDA runs showed, as expected, several 'hot spots' near the ball-race contact areas where frictional heat generation is high. Local boiling can occur here (even though the bulk of the fluid is subcooled) causing an abrupt reduction in the surface heat transfer coefficient and potential increases over the maximum heat flux temperature difference. Therefore, a boiling curve (heat transfer coefficient versus surface temperature) must be established.

Test data or published correlations for heat transfer coefficients for subcooled, high pressure, high flow, boiling cryogenic systems have not been found in the literature (See Reference 16-18, 20-33, and 38-40). There appears to be no test data that matches the thermal and flow conditions in the bearing tester. Therefore, available information must be extrapolated to the bearing tester conditions and later verified by data from the tester.

The following describes the rationale for extrapolating existing data/correlation to represent the thermal and flow conditions in the bearing tester. Although similar techniques will be used for liquid oxygen, the results of the following development are for LN_2.

The forced convection subcooled boiling process can be separated into four phases:

1) Forced convection to single liquid phase.
2) A combination of forced convection and nucleate boiling until a maximum heat flux is reached. This maximum heat flux is commonly referred to as the "burnout" heat flux.
3) Partial film boiling.
4) Stable film boiling.

The forced convection phase occurs without vapor generation and this phase of the heat transfer process is fairly well represented with published correlations and test data.

Nucleate boiling is characterized by a very high heat transfer rate for small temperature differences. There are two subregimes in nucleate boiling: local boiling and bulk boiling. Local boiling is nucleate boiling in a subcooled liquid which is characteristic of the conditions in the bearing tester. Bulk boiling is nucleate boiling in a saturated liquid which will not occur in the tester unless the outlet fluid temperature reaches the saturated value. As will be discussed later, the effects of local nucleate boiling are significantly influenced by flow velocity and subcooling. When the population of bubbles becomes too high the bubbles leaving the surface restrict the flow of liquid to the surface and insulate it thus causing a rapid rise in surface temperature. This is defined as the "burnout" heat flux. It is important to define this point because in general the heat transfer mechanism changes from nucleate boiling to stable film boiling with a significant increase in surface temperature. Stable operation in the partial film boiling regime generally does not occur. Generally when the peak flux or "burnout" point has been passed the system moves to the stable film boiling regime.

In order to account for these various heat transfer mechanisms in the bearing thermal model, criteria was established for the changing modes of heat transfer as functions of the surface temperature of the specific nodal network. For example, as the inner race or ball surface node temperature increase from the subcooled liquid temperature to temperatures considerably in excess of the fluid saturation temperature, all the above modes of heat transfer will have been encountered. Consequently, the node surface temperature range for each mode of heat transfer must be established and the appropriate heat transfer correlation determined.

FORCED CONVECTION HEAT TRANSFER

As long as the surface temperature is below the local fluid saturation temperature, forced convection is the heat transfer mechanism. The appropriate heat transfer correlation for these conditions is the Dittus - Boelter equation for the inner and outer race surfaces and other surfaces in the flow stream with the exception of the ball. The heat transfer correlation for the ball was taken from Reference 40 which correlates a wide range of heat transfer data for spheres.

The Dittus - Boelter equation is as follows:*

1) $$\frac{h_c D_e}{k} = .023\, N_{re}^{.8}\, N_{pr}^{.4}$$

And Katsnellson's equation for spheres (Ref 40) is:

2) $$\frac{h_c D}{k} = 2 + 0.03\, N_{pr}^{0.33}\, N_{re}^{0.54} + 0.35 N_{pr}^{0.356} N_{re}^{0.58}$$

FORCED CONVECTION NUCLEATE BOILING

In this heat transfer regime, both forced convection and subcooled boiling occur simultaneously and no generalized correlations, for subcooled cryogenics, have been found. The first step in developing an approach for extropolation of available information to these conditions is to select a pool boiling correlation that matches test data for high pressure LN_2. There are several pool boiling correlations available to select from. Examples are: Rohsenow, Forster - Zuber, Borishanskiy - Minchenko, Kutateladze and others. Reference 38 compares these correlations with nucleate boiling test data for several cryogens including LN_2. Figure 4.4.1 shows a sample of those comparisons. As shown, there is a considerable pressure effect on the boiling heat flux at a given value of ΔT. Also shown is the superior correlation with test data of the Russian equation compared to Rohsenhow's expression. Based on these results, the Borishanskiy - Minchenko correlation was selected as the best representation of pool boiling LN_2 data. This equation can be expressed as follows:

3) $$T_w - T_s = f(P)\, q_b^{0.3}$$

The next step in defining the heat transfer regimes is to determine the node surface temperature at the peak heat flux or "burnout" point. An expression, developed by Kutateladze, was selected based on the comparison with pool boiling burnout flux for LN_2 provided in Reference 38. This expression is as follows:

4) $$\dot{q}_{bm} = 0.16\, f(P)$$

Since the bearing tester operates in subcooled liquid, the effects of subcooling on heat flux should be accounted for. Reference 39 provides the following expression for correcting saturated pool boiling heat flux for subcooling.

5) $$\frac{q_{sb}}{q_b} = 1 + \emptyset\, [T_s - T_L]$$

The above boiling data correlations are for static boiling systems, wherein the flow velocity is small or non existent. The procedure for extrapolating these correlations to a high flow subcooled boiling cryogenic system is as follows.

* Refer to nomenclature on page 59 for definition of terms.

1) Estimate the surface temperature at which nucleate boiling initiates in the flow system.
2) Estimate the surface temperature at the burnout or maximum heat flux conditions.

After the above conditions are established it will be assumed that:

1) Forced convection is the dominant mode of heat transfer prior to the surface temperature reaching the incipient nucleate boiling temperature.
2) When the surface temperature is between the incipient boiling and the temperature corresponding to peak boiling, a combination of forced convection and nucleate boiling occurs.
3) When the surface temperature exceeds the temperature corresponding to the peak flux condition, stable film boiling occurs and this condition can be represented by the forced convection relationships using vapor properties.

ESTIMATION OF SURFACE TEMPERATURE FOR BOILING INITIATION

It is assumed that nucleate boiling will begin when the boiling heat flux as represented by equation 3 equals the heat that can be removed by forced convection. For example:

$$6) \qquad \dot{q}_c = h_c(t_w - T_L)$$

Then from equation 3:

$$7) \qquad T_w - T_s = f(P) \;\; [h_c(T_w - T_L)]^{0.3}$$

In the above equation Tw is the surface temperature required to initiate nucleate boiling.

ESTIMATION OF SURFACE TEMPERATURE AT MAXIMUM HEATING CONDITIONS

The pool boiling "burnout" heat flux is estimated from equation 4 and corrected for the appropriate subcooling by equation 5. For the high flow system both boiling and forced convection occur throughout the nucleate boiling regime. Therefore, at burnout the total heat flux is assumed to be a combination of these mechanisms. The following expression can be written assuming that the nucleate boiling relationship still holds.

$$8) \qquad T_w - T_s = f(P) \;\; [h_c(T_w - T_L) + q_{sb}]^{0.3}$$

Tw in this case is the wall temperature at "burnout" and when this temperature is exceeded stable film boiling is assumed to occur.

The above technique has been programmed for computer evaluation of the thermal conductors required in the SINDA bearing thermal model. In general, it was found that forced convection heat transfer dominated in the high velocity regions. Heat transfer from the high-speed components, inner races, balls, etc, is affected very little by nucleate boiling. The major effect is at the point where the surface is estimated to be vapor blanketed (i.e., the point of "burnout").

NOMENCLATURE FOR SECTION 4.4.1

C_p	Specific Heat
D	Diameter
g	Acceleration of Gravity
g_c	Conversion Factor
h	Heat Transfer Coefficient
H	Enthalpy
k	Thermal Conductivity
P	Pressure
q	Heat Flux
T	Temperature
σ	Surface Tension
ρ	Density
α	Thermal Diffusivity
N_{re}	Reynolds Number
N_{pr}	Prandel Number

f(P) $$\frac{\sqrt{\frac{\sigma}{\rho_L - \rho_g}}}{8.7 \times 10^{-4}\ k \left[\frac{1}{\alpha\ \rho_g\ H_{Lg}} \sqrt{\frac{\sigma}{\rho_L - \rho_g}}\right]^{.7} \left[\frac{P}{\sigma} \sqrt{\frac{\sigma}{\rho_L - \rho_g}}\right]^{.7}}$$

F(P) $$H_{LG}\ \rho_g \left[\frac{g g_c \sigma (\rho_L - \rho_g)}{\rho_g{}^2}\right]^{1/4}$$

Ø $$\frac{0.1}{\rho_g H_{Lg}} \left(\frac{\rho_g}{\rho_L}\right)^{1/4} CPL\ \rho_L$$

	Subscripts
b	Boiling
bm	Maximum Boiling
C	Convection
e	Equivalent
g	Vapor
L	Liquid
Lg	Saturated Liquid/Gas
sb	Subcooled Boiling
s	Saturated
w	Wall

The magnitude of the "burnout" heat flux can also be significantly affected by surface conditions such as roughness, coatings, etc. The maximum heat flux condition can be reached prematurely if flow instabilities or oscillation occurs. These rapid changes in flow can lower the local pressure increasing the local superheat near the wall and cause rapidly increased boiling. These added uncertainties along with the lack of experimental data relative to the thermodynamic conditions in the bearing tester emphasizes the importance of experimental data from the tester. By comparing measured and calculated temperature data the validity of the thermal model can be assessed.

SENSITIVITY OF BEARING COMPONENT TEMPERATURES TO TRANSITION TO FILM BOILING

Temperature measurements can serve as a guide in evaluating the transition point from forced convection nucleate boiling (burnout flux) to film boiling. An example of the importance in evaluating this parameter is shown in Figure 4.4.2. The average bearing component temperatures are shown as a function of the maximum wall superheat $(Tw-Ts)_{MAX}$ for forced convection nucleate boiling. As the maximum superheat is increased, considerably more surface area of the bearing components remains in the nucleate boiling regime. Therefore, these areas do not become vapor blanketed and the surface-to-fluid heat transfer remains relatively high resulting in lower temperatures. As $(Tw-Ts)_{MAX}$ is increased to the point that all surfaces remain in the nucleate boiling regime, the component temperatures become independent of the transition from nucleate to film boiling. In other words, for a given heat load, the transition point can be increased such that the surface temperature does not reach the transition point and film boiling does not occur. In Figure 4.4.2 this is represented by the higher ΔT_{MAX} values where the bearing component temperatures become independent of ΔT_{MAX}.

The analysis described herein predicts that the peak flux will be reached at surface temperatures between 2.6 and 3.3°R, above saturation, depending on the magnitude of the forced convection heat transfer coefficient. Also shown is a temperature measurement for the number 2 bearing outer race. This measurement is in reasonable agreement with the calculated outer race temperature at the estimated ΔT_{MAX} point.

4.4.2 Fluid Heat Transfer Regimes and Film Coefficients for LOX and LN_2

Techniques developed in Section 4.4.1 were used to evaluate the surface temperature for the incipient nucleate boiling range for LOX. The heat transfer regimes as a function of wall superheat (T_w-T_s) are shown in Figure 4.4.3. As shown, nucleate boiling for the forced convection LOX flow begins for a wall superheat of 12.8°R and the "burnout" heat flux occurs at a wall superheat of 13.8°R. This indicates that typical bearing surfaces will become vapor blanketed when the surface temperature exceeds the LOX saturation temperature by about 13°R. This compares with a value of about 3°R for LN_2 coolant as shown in Figure 4.4.4.

4.4.3 Transition to Film Boiling Temperature for LN_2

An analysis was performed using the Bearing Thermal Model to evaluate the transition temperature at which LN_2 film boiling starts in the BMT bearing component. When the transition superheat (3°F) predicted by an earlier calculation was used, the steady state outer race temperatures compared favorably with the limited BMT thermocouple data. Therefore, this value (ΔT = 3°F) will continue to be used until more test data becomes available. The bearing analysis assumed an axial load of 2,500

ORIGINAL PAGE IS
OF POOR QUALITY

FIGURE 4.4.1 COMPARISON OF NUCLEATE BOILING CORRELATIONS

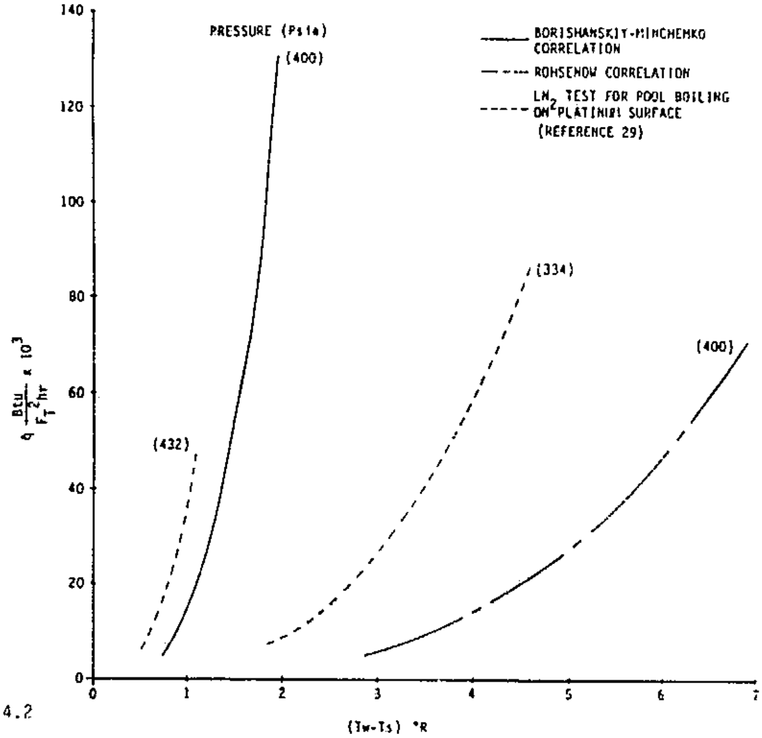

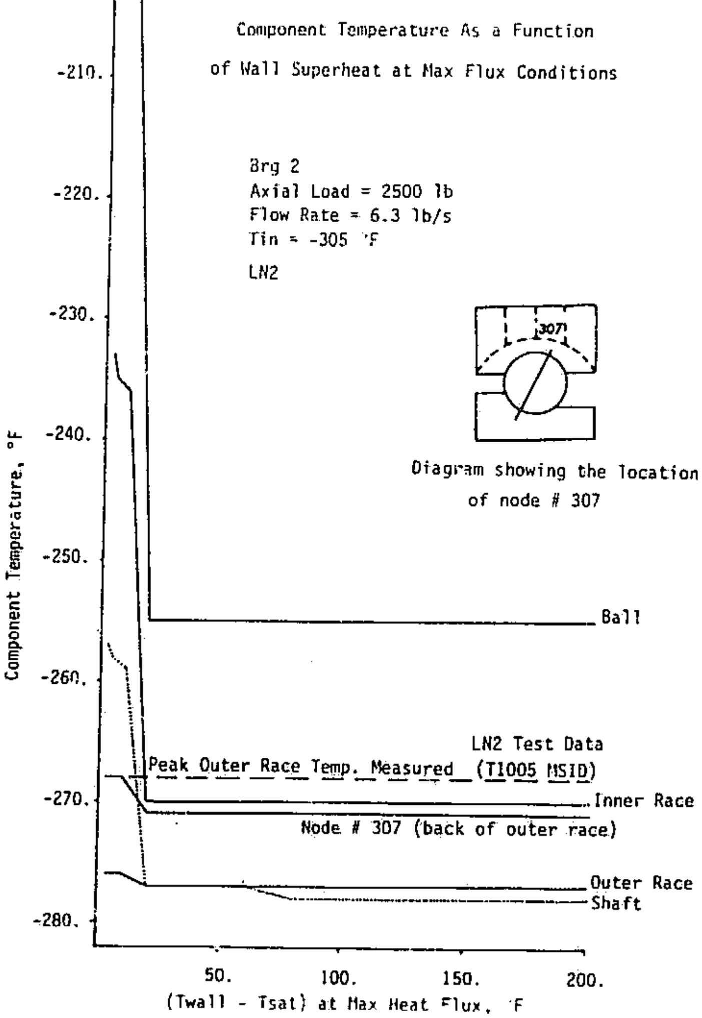

FIGURE 4.4.2

Component Temperature As a Function

of Wall Superheat at Max Flux Conditions

Brg 2
Axial Load = 2500 lb
Flow Rate = 6.3 lb/s
Tin = -305 °F
LN2

Diagram showing the location
of node # 307

ORIGINAL PAGE IS OF POOR QUALITY

FIGURE 4.4.3 HEAT TRANSFER REGIMES FOR LOX

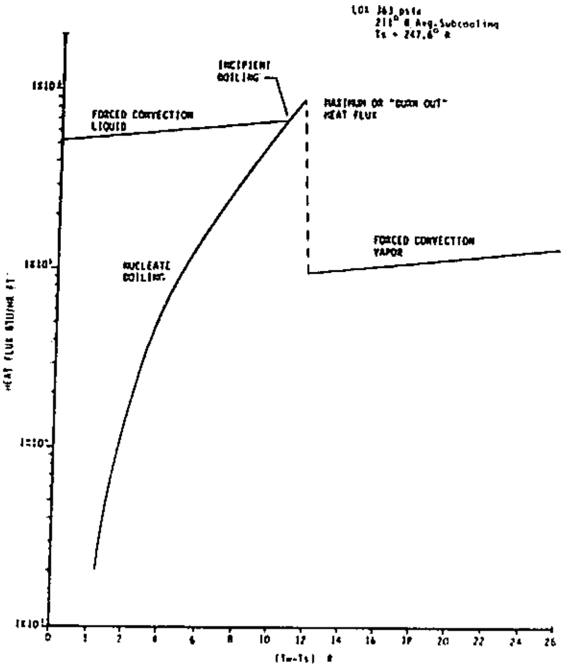

FIGURE 4.4.4 HEAT TRANSFER REGIMES FOR LN₂

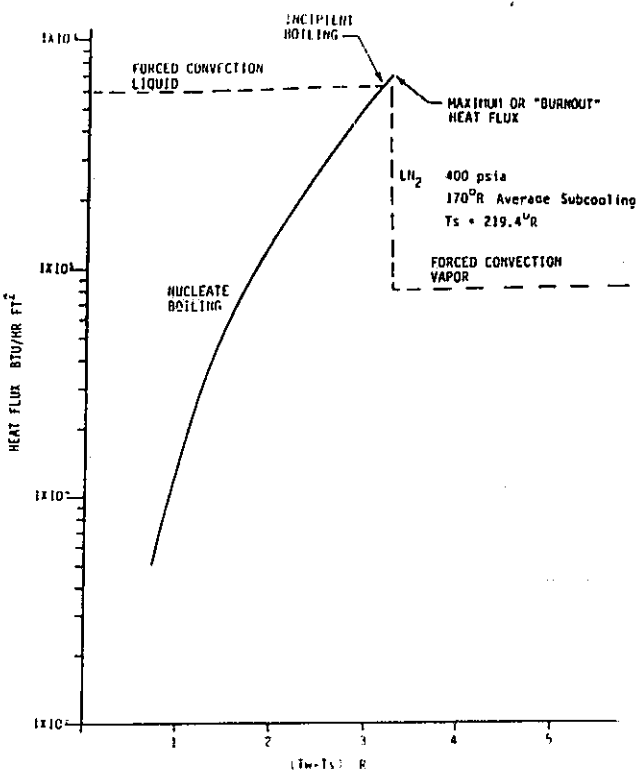

FIGURE 4.4.5 Component Temperature As A Function of Wall Superheat at Max Heat Flux Conditions (LOX Turbopump Turbine End Bearing - 57 mm)

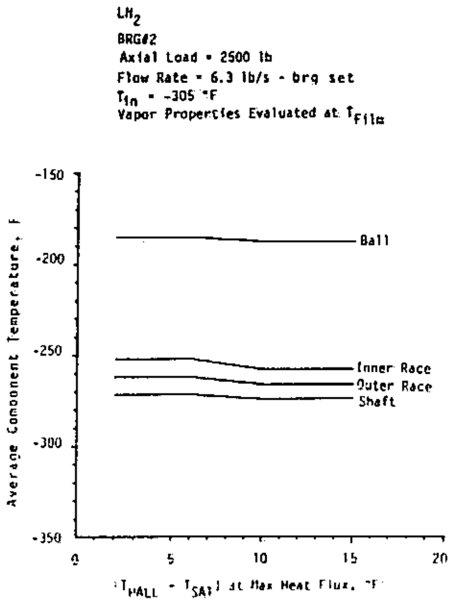

FIGURE 4.4.6 Outer Race Node Temperature As A Function of Wall Superheat at Max Flux Conditions (LOX Turbopump Turbine End Bearing - 57 mm)

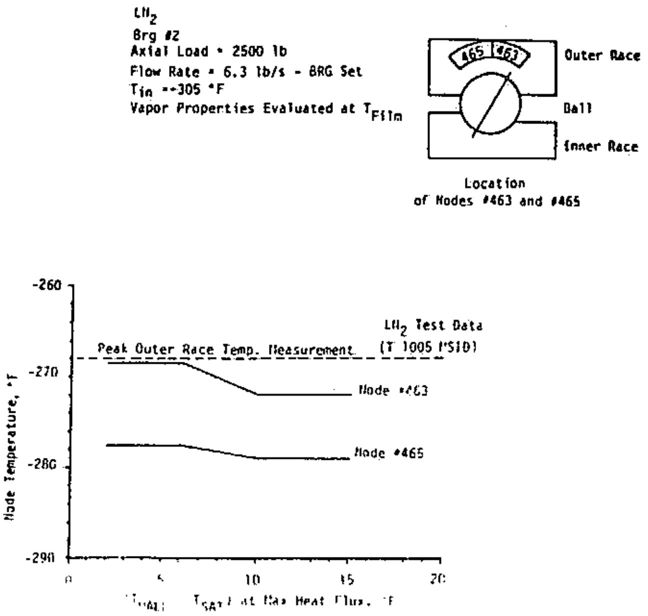

lbs, an LN_2 flow rate of 6.3 lbs/sec brg set, with an inlet temperature of -305°F. The steady state average component temperatures (bearing #2) at the transition superheats were:

Ball	-185°F
Outer Race	-252°F
Inner Race	-262°F
Shaft	-272°F.

Although the favorable agreement of analysis and test data is encouraging, considerable additional test data at varied operating conditions are required for bearing model verifications.

The Bearing Thermal Model was exercised for various transition temperatures using LOX as the coolant. The transition temperature for the bearing - coolant combination is that temperature at which the maximum surface boiling heat flux occurs. This temperature is also called the "burnout" temperature because a higher heat flux causes the surface to dry out causing it to become blanketed with a vapor film and the surface temperature to drastically increase. This transition temperature can be expressed as transition superheat - the difference between the surface temperature and the fluid's saturation temperature at the maximum boiling heat flux..

Analyses results are shown in Figures 4.4.5 through 4.4.7. Figure 4.4.5 shows the average, steady state component temperatures as a function of the transition superheat. The average temperatures as a function of the transition superheat. The average temperatures are not very sensitive to transition superheat changes in the range investigated (ΔT = 2, 15°F). Figure 4.4.4 shows the temperatures of the two outer race nodes whose location most closely corresponds to the placement of the thermocouples in the BMT. Also shown, for comparison, is an outer race temperature measured on the BMT under similar conditions. A previous calculation (Section 4.4.1), predicted a transition superheat of about 3°F for LN_2. This value gives a very close match between node #463 and the measured temperature of -268°F. Therefore, we will continue to use this value (ΔT = 3°F) for the transition superheat in future studies until more test data is available and a more comprehensive correlation can be established. Figure 4.4.5 shows the maximum track node temperatures for the races and the ball. At the transition superheat of 3°, all the track nodes have surface temperatures well above the LN_2 saturation temperature of -241°F. Consequently, the loaded contact surfaces are vapor blanketed and receive little, if any, lubrication from the LN_2. At the transition superheat of 3°F, the track nodes had the following temperatures:

Ball Track	+130°F
Inner Race Track	+52°F
Outer Rack Track	-132°F

The bearing pair analyzed has an applied axial load of 2,500 lbs, an LN_2 flow rate of 6.3 lb/sec brg set, and an inlet temperature of -305°F.

4.4.4 Transition to Film Boiling Temperature for LOX

The transition temperature for the bearing - LOX combination is that temperature at which the maximum forced convection nucleate boiling heat flux occurs and subsequently causes stable film boiling to take place on the bearing surfaces. This can also be expressed as a temperature difference between the surface and the saturation temperature of the fluid (superheat) at the maximum heat flux.

FIGURE 4.4 Track Node Temperature As A Function of Wall Superheat at Max Flux Conditions
(LOX Turbopump Turbine End Bearing - 57 mm)

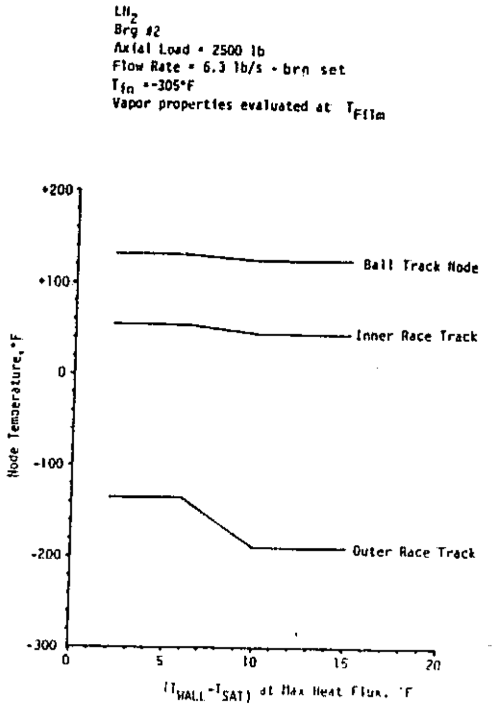

FIGURE 4.4.8 COMPONENT TEMPERATURE AS A FUNCTION OF WALL SUPERHEAT AT MAX FLUX CONDITIONS

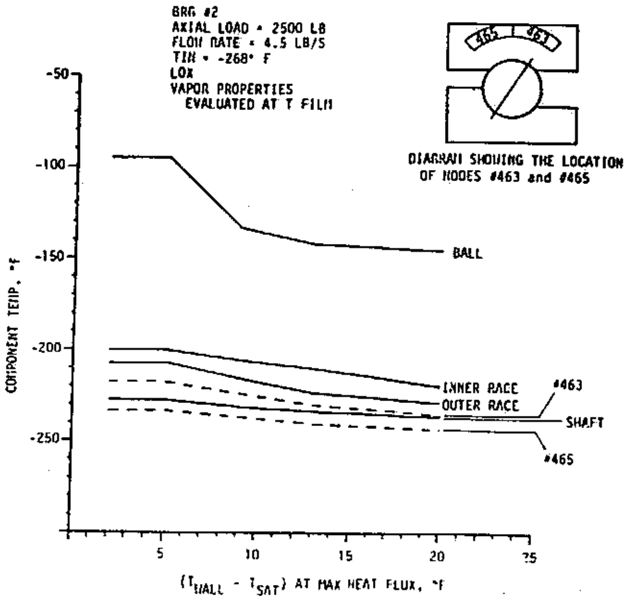

FIGURE 4.4.9 COMPONENT TEMPERATURE AS A FUNCTION OF WALL SUPERHEAT AT MAX FLUX CONDITIONS

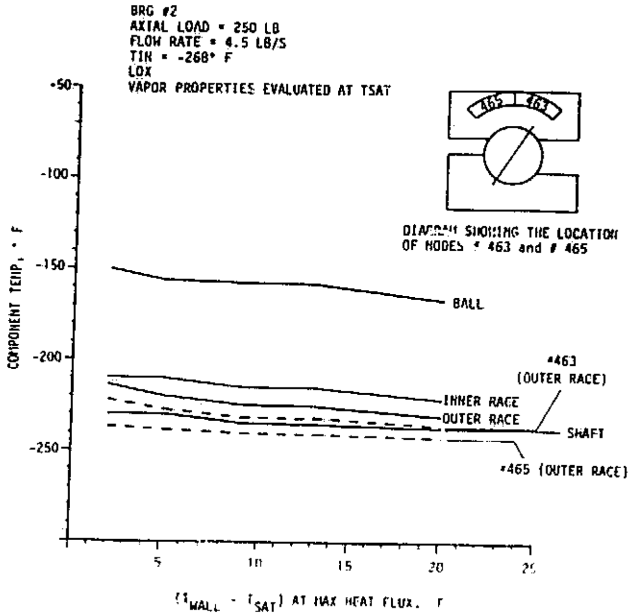

FIGURE 4.4.10 TRACK NODE TEMPERATURES AS A FUNCTION OF WALL SUPERHEAT AT MAX FLUX CONDITIONS

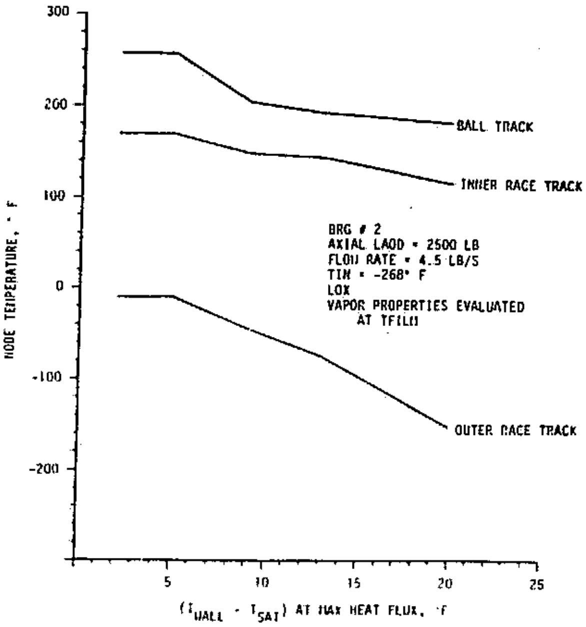

A second parameter, the temperature at which the vapor properties were evaluated in the fluid heat transfer coefficient calculations, was investigated. During vapor generation on a surface, the temperature gradient between the surface and the subcooled liquid is unknown, and the vapor properties must be evaluated at some reference temperature. Two possibilities were examined: (1) A film temperature equal to the average of the surface temperature and the fluid's saturation temperature, and (2) The saturation temperature.

The analysis was performed using the Bearing Thermal Model to evaluate the temperature at which the transition to film boiling occurs for LOX in the BMT. Vapor properties needed for the conductance calculations were evaluated at both film temperature and saturation temperature. The resulting outer race temperatures were compared to the BMT thermocouple data for the LOX test to provide a comparison of predicted and measured temperatures. A superheat of 5°F with the vapor properties evaluated at the film temperature was chosen for the transition temperature. This produced an outer race temperature for Bearing #2 of -217°F and the following average component temperatures:

Ball	- 96°F
Outer Race	-207°F
Inner Race	-200°F
Shaft	-227°F.

This bearing pair had an applied axial load of 2500 lb, a LOX flow rate of 4.5 lb/sec and a LOX inlet temperature of -268°F.

The results of this effort provide detailed thermal and mechanical data to support the design and performance evaluation of high-speed angular contact ball bearings operating in cryogenic oxygen. Similar models can be developed for bearings operating in other cryogenic fluids.

The Bearing Thermal Model was exercised for various transition temperatures using LOX as the coolant. The results are shown in Figures 4.4.8 through 4.4.12. For Figures 4.4.8 and 4.4.10, the vapor properties used in the conductance equations were evaluated at the film temperature. For Figures 4.4.9 and 4.4.11, the vapor properties were evaluated at saturated conditions. These curves show, in general, that the longer forced convection nucleate boiling is allowed to occur before the "burnout" temperature is reached (when vapor begins to blanket the surface), the lower the surface temperature becomes at steady state conditions. A comparison of Figures 4.4.8 and 4.4.9 shows that the use of a film temperature to evaluate the vapor properties increases the component temperatures significantly at lower "burnout" temperatures but not at the higher values. Also plotted on Figures 4.4.8 and 4.4.9 are the outer race node temperatures for Bearing #2. These values are compared with the LOX BMT outer race measurements in Figure 4.4.12. The closest match with Bearing #2 is curve A; the outer race temperature is -217°F. This corresponds to a superheat of 5°F at the burnout point with the vapor properties evaluated at the film temperature. Even though an earlier calculation (Section 4.4.2) predicted that the maximum heat flux would occur at a surface superheat of 13°F, the 5°F value will be used in future thermal model analyses because it more closely matches the limited data available. When additional LOX tester data becomes available, this parameter will be reevaluated.

Figures 4.4.10 and 4.4.11 show the track node temperatures of Bearing #2 as a function of the wall superheat at the max flux condition. The use of the film

FIGURE 4.4.11 TRACK NODE TEMPERATURE AS A FUNCTION OF WALL SUPERHEAT AT MAX FLUX CONDITIONS

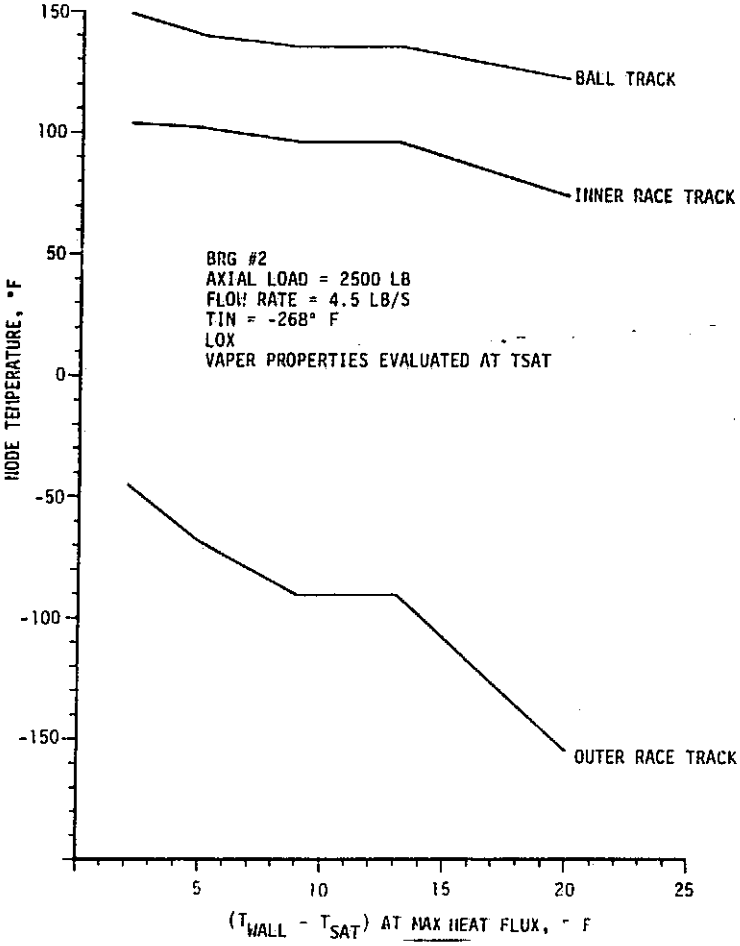

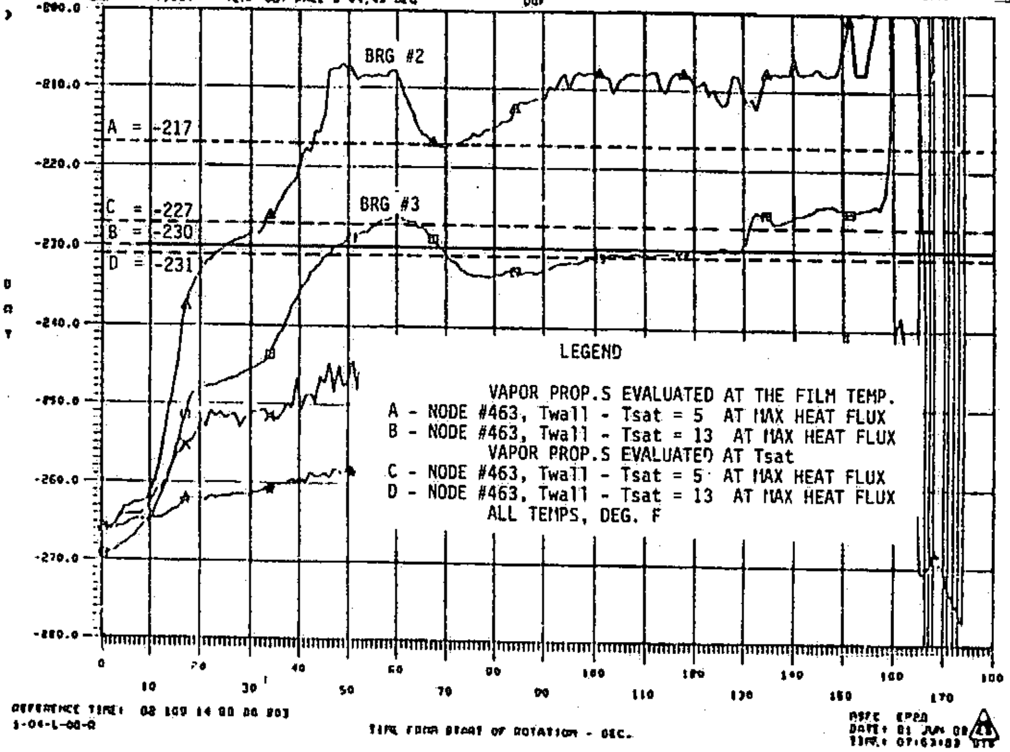

FIGURE 4.4.12 THERMAL MODEL PREDICTED TEMPERATURES COMPARED WITH LOX TEST DATA

properties produces a strong difference in these curves. Using the chosen superheat of 5°F at burnout, the track nodes have the following steady state temperatures:

Ball Track	+257° F
Inner Race Track	+170° F
Outer Race Track	-10° F.

While these temperatures are the highest in the contact areas, all the track node temperatures are well above the saturation temperature of the LOX. Consequently the loaded contact surfaces are vapor blanketed and receive very little if any film lubrication from the LOX. This bearing pair had a 2500 lb applied axial load, a LOX flow rate of 4.5 lb/sec, and an inlet coolant temperature of -268° F.

4.5 Software Modifications and Development

Two large computer programs, SHABERTH and SINDA were used for many of the analyses conducted during the contract period. SINDA, a numerical analysis program designed specifically for solving resistor-capacitor network representations of thermal systems by forward-backward differencing methods, was used to build the SRS Bearing Thermal Model data base. Appendix A contains a representative data base and illustrates the variety and magnitude of data considered in the thermal model. Appendix B illustrates the basic steady-state output temperature data. In addition to the basic node data and conductor data common to most thermal analyses, the SRS Bearing Thermal Model data base contains temperature varying thermal property data, capacitance values for each node to allow transient analyses, time varying heat source capabilities, as well as data manipulation capabilities. SHABERTH, a large program that predicts general bearing performance characteristics, was used to model the Bearing and Materials Tester using geometrical dimensions from the original LOX tester. A representative input data file and output data file for this program is shown in Appendix C. The SHABERTH program considers such factors of bearing operation as clearances, pitch diameter, rail-land width and diameter, cage weight, number of rolling elements, number of bearings, steel data, ball diameter, curvatures, CLA roughness, RMS asperity slope, friction coefficients, fit data, axial and radial loading, material properties, temperature gradients across bearing, shaft geometry and is considered a state-of-the-art bearing analysis program. SHABERTH output contains such information as axial and radial shaft deflections, reaction forces, moments, frictional heat generation, friction torque, bearing operating clearances, cage speed data, rolling element angular speeds, speed vector angles, normal forces, Hertz stresses, and contact angles.

Many modifications were made to these programs to adapt them to the specific problems of the BMT. Also, several other smaller routines were developed to enhance the capabilities of both SHABERTH and SINDA. When SHABERTH was first acquired, it would not run under the current version of Fortran available on the MSFC Univac computer. The code was finally updated to Fortran V and is now fully updated to ASCII Fortran (also known as Fortran 77). Besides the code changes necessary to update the SHABERTH code, two subroutines, FRINT and FMIX, were modified to store the characteristics of the ball-race contact ellipse. SHABERTH models these ellipses by slices. The width of each slice, the frictional heat generated at each slice and the major and minor axis dimension of both the inner and outer race contact ellipse are stored for use in the SRS Bearing Thermal Model.

SINDA is capable of computing both steady-state and transient heat source temperature profiles and allows for the addition of user-written subroutines to be added and compiled along with the standard library of subroutines available. A routine has been added to compute the mechanical and thermal properties of the bearing set at the predicted temperatures. The subroutine, called VARIABLES 2, reads a file that contains the volumes of each node in the SRS Bearing Thermal Model. It then computes the average temperature of each component of the bearing (inner race, outer race, and rolling element) based on these volumes. The modulus of elasticity and coefficient of thermal expansion for each bearing component is then calculated. VARIABLES 2 is included in the SINDA input file listed in Appendix A.

The SRS Bearing Thermal Model was designed to be adaptable to changing various operating parameters such as coolant flow rate, coolant inlet temperature, and axial load for either LOX or LN_2 coolant. However, these changes require re-calculation of over 1,000 conductance values for each run. To calculate each by hand would be a laborious and time consuming process. The following special routines were developed to facilitate this process and are listed in Appendix D: COND/SRS, HEAT/SRS, SRS-DATA, and UPDATE/SRS. These subroutines have been combined with SHABERTH to form a new program called SHABERTH/SRS that updates a Bearing Thermal Model file quickly and efficiently when new operating conditions are being considered. The routines and their functions are described below.

COND/SRS - This subroutine calculates the surface-to-fluid conductances for the SRS Bearing Thermal Model. The heat transfer coefficient is also calculated using methods outlined in Section 4.4. For each node, a table of conductances vs. temperature is produced that accounts for the changing conductances through the different heat transfer phases (forced convection, boiling, and film boiling). The output of COND/SRS is a list of these tables arranged in SINDA input format. SINDA can then interpolate through these tables to get the conductance for the surface nodes as a function of temperature. COND/PROG also adds commends to the SINDA file that identify the run and describe the operating conditions.

HEAT/SRS - This subroutine distributes the frictional heat generated at the bearing contact surfaces, that is calculated by SHABERTH, to the proper nodes on the ball and races in the SRS Thermal Model data base. As mentioned above, the FRINT and FMIX subroutines of SHABERTH isolate the frictional heat generated into slices of the contact ellipse. HEAT/SRS also calculates the metal-to-metal conductances between the ball and the races since the contact surface area is dependent upon the load applied.

UPDATE/SRS - This subroutine takes the output of COND/SRS and HEAT/SRS and updates a SRS Bearing Thermal Model input file with the re-calculated conductances and frictional heat generation.

SRSDATA - This is a FORTRAN BLOCK DATA subroutine that contains all the constants needed by the COND/SRS and HEAT/SRS, including various LOX and LN_2 properties (density, specific heat, thermal conductivity, Prandtl number, viscosity), the thermal conductivities for the four metals used in the BMT (Inconel, Armalon, 440-c Stainless Steel, Waspaloy), and several node properties of the Bearing Thermal Model (surface area, depth, location relative to shaft center, hydraulic diameter of the passage at the node's surface, and a relative velocity indicator). This data is held in COMMON blocks that the other subroutines can access.

5.0 BEARING ANALYSES

This section provides detailed descriptions of specific tasks accomplished and the results obtained from the bearing modeling efforts. These analyses were performed in support of the Bearing and Materials Tester Program, as required, and do not represent the total analysis effort for the design and development of the BMT.

5.1 Bearing Life Prediction Analysis

5.1.1 Modification of Bearing Life Formulas for Rolling Bearings Operating in Cryogenic Environment

Accepted techniques (4,6,12) have been developed to predict life for well lubricated bearings. These techniques lack experimental verification for high-speed rolling bearings operating in cryogenics, it is therefore advantageous to investigate the potential for modifying current bearing life formulas for rolling bearings operating in a cryogenic environment. Typical cryogenics (LH_2, LN_2 LOX) have good heat removal characteristics; however, they lack the viscous properties necessary to provide a fluid film of sufficient strength to prevent metal-to-metal contact between the rolling elements and the race. The degree these films support the interface loads has not been experimentally determined.

Another uncertainty is the role cryogen film lubrication plays when solid lubricants are used to provide a lubricating surface film. The interaction between the solid film and fluid film are not known. This can be further complicated when the contact surface temperature exceeds the saturation temperature of the coolant to the extent that the surfaces become vapor blanketed and the surface film is that of a gas. Some experiments (15) indicate that LOX is potentially a better lubricant than non-reactive cryogens such as LH_2 and LN_2. This results from the formation of surface films (oxides) that provide a measure of protection for the metal surfaces in contact. Here again, the rate of oxide formation can be a function of surface temperature and the degree of protection can be a function of the sliding velocity or rate of film removal. Considerably more work is needed to establish the film lubrication properties of various bearing materials and solid lubricants operating in cryogenics.

The classical failure mode of a rolling contact between hard steel surfaces is contact fatigue. The life formula as developed by Lundberg (4) is based on the assumption that the failure is initiated by a decisive stress amplitude located at some distance below the surface. The relationship between loads, stresses, and stress location is developed from the bearing dynamics and Hertz theory of contact stresses. Bearing life dispersion has been obtained by applying the Weibull distribution function to bearing life data. Experience has shown that this technique adequately predicts bearing life for well lubricated bearings. Since better lubricants and materials have become available, the original life formula has been modified by factors to account for the improved life derived from these improvements (6,12). These factors, however, do not account for the conditions encountered in cryogenic operation. As an example, the development of stresses from the Hertz theory does not account for tangential forces. Since the contact friction forces with cryogenic fluids is expected to be significantly larger than the forces encountered in oil lubricated bearings, the maximum shear force will probably be at, or near, the surface rather than below the surface. Furthermore, the solid film lubricant will enhance the asperity friction. Consequently the apparent contact friction force should fall somewhere between dry asperity friction and hydrodynamic film friction. This presents a problem in determining the life adjustment factor for lubrication that will account for the degradation of lubrication capability of the cryogenic.

The SHABERTH I bearing analysis computer program has been used as an aid in predicting bearing life. This program uses the life formula developed in reference 4 with life adjustment factors to account for improved materials and lubrication film thickness. The life adjustment factors will be adjusted to represent cryogenic operations as data becomes available from the bearing tester program.

SHABERTH I uses the following technique for estimating bearing life:

Eq 1

$$L_{10m} = \left(\frac{Q_{cm}}{Q_{em}}\right)^3$$

L_{10m} is the raceway fatigue life in millions of revolutions, as determined by Lundberg and Palmgren (4), and Q_{cm} is the dynamic capacity which is the load for which the bearing raceway will have 90% assurance of surviving one million revolutions. Q_{em} is the raceway equivalent load. Q_{cm} and Q_{em} are calculated by the SHABERTH computer program.

Since experience has shown, for ball bearings, that the races usually fail before the balls due to the changing axis of rotation as the balls orbit the shaft, the bearing fatigue life is based on the life of the races. The L_{10} life for a raceway is given by:

$L_{10n} = a_2\, a_3\, a_3^*\, L_{10m}$ where

a_2 is a life improvement factor to account for improved materials,

a_3 is a life improvement factor to account for full film lubrication, and

a_3^* is a factor less than one when full film lubrication is not obtained.

a_3^* is a reduction factor accounting for the effect of surface asperity interaction and was deduced from a best fit to a large body of rolling contact life test data (12). This function was extracted from the SHABERTH I program and is shown in Figure 5.1.1. Also shown is the lubricant life factor used by SHABERTH II, which will be discussed later. As shown, the SHABERTH I lubrication factor is always ≤ 1 and is therefore never a life improvement factor. If the film thickness to surface roughness ration (h/σ) is greater than about 3.5, a life improvement factor >1 can be input (a_2).

A limiting value of about 0.52 is shown for h/σ approaching zero, or zero film thickness. Since this condition is believed to be approached in LN_2, LOX, and LH_2, this is the value that would be applied with these fluids. The determination of this life factor did not, however, consider the benefits of the solid lubricant film transfer system used to lubricate the tester bearings. The effectiveness of this lubrication on bearing life can be evaluated from the bearing and materials tester data. SHABERTH II has, in effect, combined the life reduction and improvement due to lubrication into one function. This function is developed in Reference 6. The

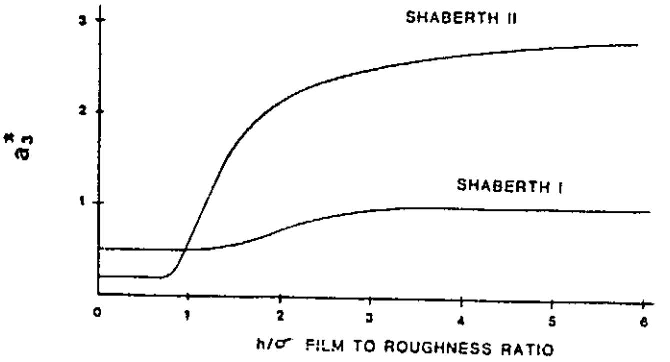

FIGURE 5.1.1 LUBRICATION LIFE ADJUSTMENT FACTORS

FIGURE 5.1.4 EXAMPLE OF DATA UTILIZATION TO CORRELATE BEARING LIFE AND OPERATING TEMPERATURE

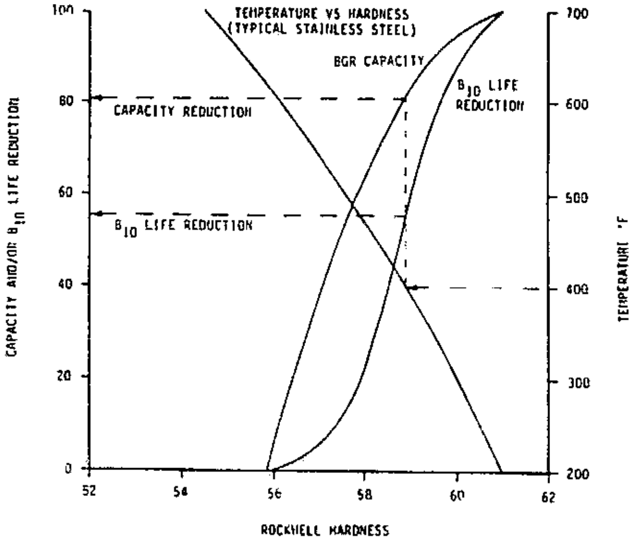

FIGURE 5.1.5 BALL SPIN/ROLL RATIO vs. BEARING °T

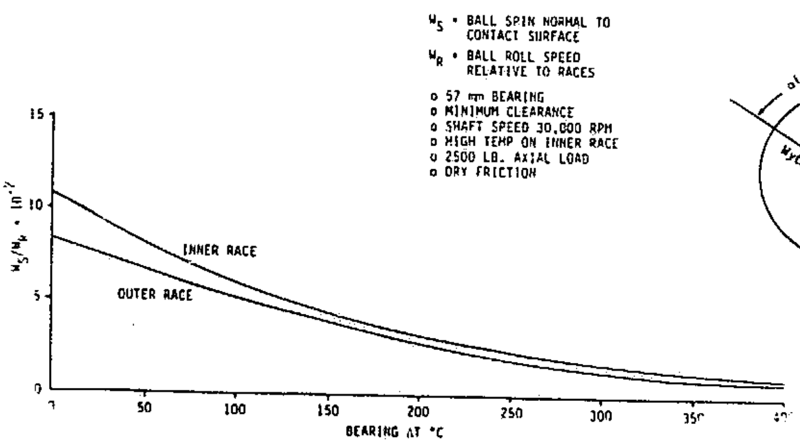

FIGURE 5.1.6 BALL SPIN VECTOR DIAGRAM

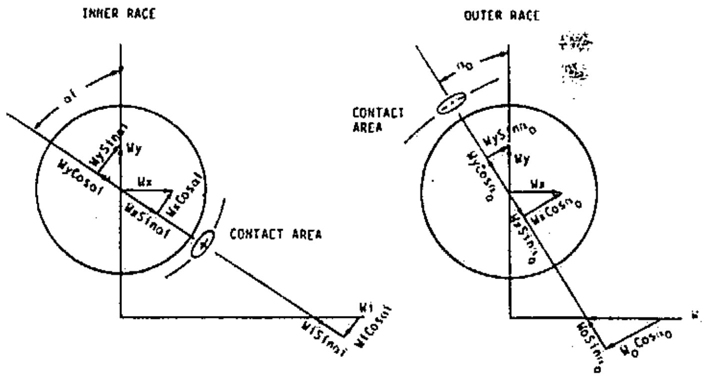

INNER RACE BALL SPIN NORMAL TO CONTACT AREA

$$W_{si} = (W_s + W_o)\sin\alpha_i + W_x\sin\alpha_i - W_y\cos\alpha_i$$

OUTER RACE BALL SPIN NORMAL TO CONTACT AREA

$$W_{so} = -W_o\sin\alpha_o + W_x\sin\alpha_o - W_y\cos\alpha_o$$

W_s = Shaft Speed
W_o = Cage Speed
W_i = Relative Speed

important point is that for h/σ approaching zero, the life reduction factor is 0.21, which is less than half the factor used in SHABERTH I. This, again, illustrates the need for experimental data for cryogenic operation in these low film regions.

As stated earlier, the L_{10m} is the raceway fatigue life for 90% survivability. Since the bearing has two races the L_{10} life for the bearing is

Eq 2
$$L_{10b} = \left[L_{101}^{-e} + L_{102}^{-e} \right]^{-1/e}$$

where 1, 2 denote inner and outer races.

Since one bearing set consists of two bearings, the L_{10} life of the bearing set is:

Eq 3
$$L_{10bs} = \left[L_{10b1}^{-e} + L_{10b2}^{-e} \right]^{-1/e}$$

And the life of the total bearing system is:

Eq 4
$$L_{10bst} = \left[L_{10bs1}^{-e} + L_{10bs2}^{-e} \right]^{-1/e}$$

Equation 4 is the 90% survivability life for all the bearings on the tester shaft. Since a 10% failure rate is not acceptable for Shuttle components, Equation 4 must be modified to predict probabilities of success greater than 99%. Techniques to correlate failure rates in these low regimes are addressed in References 1 and 5. These techniques suffer from the same deficiencies as discussed earlier when applied to bearings operating in low viscosity fluids such as LN_2, LOX and LH_2. However, they do provide a technique for evaluating the data derived from the Bearing and Materials Tester.

The previous discussion has addressed fatigue type failures which is the dominant failure mode for well designed and lubricated bearings. Obviously, there are other type failures such as excessive wear, overheat cracking, overload cracking, destruction by material softening due to unstable overheating, etc. These type failures must be overcome before life data relating to bearing fatigue can be obtained.

The effort to date has provided a bibliography of reference material pertaining to bearing fatigue life (References 3 through 15). Life data relating to bearings operating in cryogenics is scarce and relating existing semi-empirical life formulas to these conditions require additional test data. The Weibull distribution does not represent the data in the region of reliabilities >90%. Techniques have been found that represent current data in these regimes and should, with modification, represent the data obtained from the cryogenic tests.

5.1.2 Cumulative Load Assessment for BMT Bearing Life

A basic problem in fatigue analysis is the prediction of life for an element when time-dependent loading is applied. By progressively loading an element, damage accumulates within the material. Miner and Palmgren have postulated that failure resulting from multistage loading can be defined as:

(1) $$\sum \frac{n_i}{N_i} = 1 \quad \text{Miner's Rule}$$

Miner's Rule assesses the "damage" produced by a stress σ_i for n_i cycles as n_i/N_i and assumes the individual damages are additive and independent of sequence. [36]

If Miner's Rule is assumed to correctly predict the cumulative damage for the BMT, the following equation can be stated:

(2) $$t_1/T_1 + t_2/T_2 + t_3/T_3 + \ldots + t_n/T_n = 1$$

where t_n = time at load F_n
T_n = Total time to failure at given stress level (S-N curve)

Since $T_n = L_n$, where L_n = life to failure predicted by a Weibul distribution, Equation (2) can be rewritten as

(3) $$\frac{t_1}{L_1} + \frac{t_2}{L_2} + \frac{t_3}{L_3} + \ldots + \frac{t_n}{L_n} = 1$$

or (4) $$\sum_{i=1}^{i=n} \frac{t_i}{L_i} = 1$$

Harris [1] defines a relationship based on the dynamic loading capacity as

(5) $$L_i = \left(\frac{C}{F_i}\right)^P$$

where C = dynamic loading capacity
P = 3 for rolling bearings.

Defining a ratio such that

(6) $$\frac{L_1}{L_2} = \left(\frac{F_2}{F_1}\right)^P$$

allows the life to be related to the applied axial reaction load and to failure at a given stress (force) level.

Defining Equation 6 in general terms gives

(7) $$\frac{L_n}{L_{n+1}} = \left(\frac{F_{n+1}}{F_n}\right)^P$$

Substituting Equation (7) into (3) and assuming 3-stage loading gives

(8) $$\frac{t_1}{L_2\left(\frac{F_2}{F_1}\right)^P} + \frac{t_2}{L_2} + \frac{t_3}{L_3} = 1$$

A similar equation can be written for L_2 such that

(9) $$\frac{t_1}{L_3\left(\frac{F_3}{F_2}\right)^P\left(\frac{F_2}{F_1}\right)^D} + \frac{t_2}{L_3\left(\frac{F_3}{F_2}\right)^P} + \frac{t_3}{L_3} = 1$$

or

$$(10) \quad L_3 = \frac{t_1}{\left(\frac{F_3}{F_1}\right)^P} + \frac{t_2}{\left(F_3/F_2\right)^P} + t_3$$

Equation (10) may be expanded to a general form:

$$(11) \quad L_n = \frac{t_1}{\left(F_n/F_1\right)^P} + \frac{t_2}{\left(F_n/F_2\right)^P} + \frac{t_3}{\left(F_n/F_3\right)^P} + \ldots + \frac{t_{n-1}}{\left(F_n/F_{n-1}\right)^P} + t_n$$

or

$$(12) \quad L_n = t_n + \sum_{i=1}^{i=n-1} \frac{t_i}{\left(F_n/F_i\right)^P}$$

Recall that a summation can be represented by the integration of a function so that

$$L_n = t_n + \int_0^t \left(\frac{F_i}{F_n}\right)^P dt$$

Therefore,

$$\left(\frac{1}{F_n}\right)^P = \int_0^t \left(F_i\right)^P dt$$

the integral term represents the area under a $(Fi)^P$ vs. Time curve. If a plot of $(Fi)^P$ vs time is given (See Figure 5.1.2), the life at a particular load can be graphically determined by calculating the area under the curve using the prescribed boundary conditions.

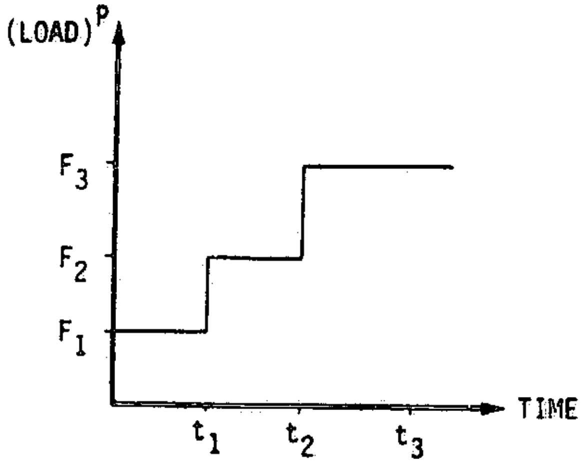

FIGURE 5.1.2 LOAD VS TIME

5.1.3 Application of the Double Linear Damage Rule to Bearing Life Predictions

Although Miner's Rule has been used to analyze cumulative damage, it does not account for the effects of load sequencing. Miner's Rule assumes that when the summation of cycle ratios (n/N) equals one, failure occurs. However, the cycle ratios can sum to be less than or greater than one when high-low or low-high load sequencing, respectively, is followed.

In the BMT, bearings will experience various load sequences and it is necessary to account for these associated effects to correctly predict bearing life. The application of the Double Linear Damage Rule (DBDR) to bearing life predictions is being evaluated. Most of the work by Halford at the Lewis Research Center has been with 0.25 inch diameter specimens. Discussions have been held with Dr. Halford concerning the feasibility of applying the DLDR to bearings, and indications are that it can be applied.

5.1.4 Assessment of 57 mm Turbine Bearing Life as a Functions of Radial and Axial Load

An analysis was conducted to evaluate the 99% (B_1) survival life of the 57mm LOX pump turbine end bearing as a function of axial and radial load. The analysis consisted of using the B_{10} (90% survival life) predicted by the Shaberth I bearing code and modifying the results, as described in previous sections, to estimate the B_1 life. The lubrication life reduction factor used for the Shaberth II bearing code was used to account for the reduction in life due to marginal lubrication in the cryogenic coolant. It is recognized that the bearing life formulas used in the computer codes are for conventionally lubricated bearings and extrapolation to the cryogenic environments experienced by the turbopump bearing produce unknown errors. However, because of the unavailability of life data for bearings operating in cryogenics, these are the best estimates possible and should at least provide a measure of the sensitivity of bearing life to the load factors.

In general, a Weibull distribution adequately correlates the life dispersion of conventionally operated rolling bearings experiencing fatigue type failures in the range of 10% to 50% failures. Designers of aerospace hardware are interested in reliabilities of 99% or greater. Consequently, the deviation of the available test data from the Weibull distribution is of particular interest in the region of high survival probabilities. The following is a synopsis of the method used to estimate the B_1 life information shown in Figure 5.1.3.

Assuming a Weibull distribution, the bearing life can be related to a given probability of survival as follows:

$$1)\qquad B = B_{10}\left[\frac{L_n\ 1/S}{L_n\ 1/.9}\right]^{1/e}$$

B	bearing life
B_{10}	bearing life for 90% survival
S	Probability of survival
e	dispersion parameter (10/9 for ball bearings)

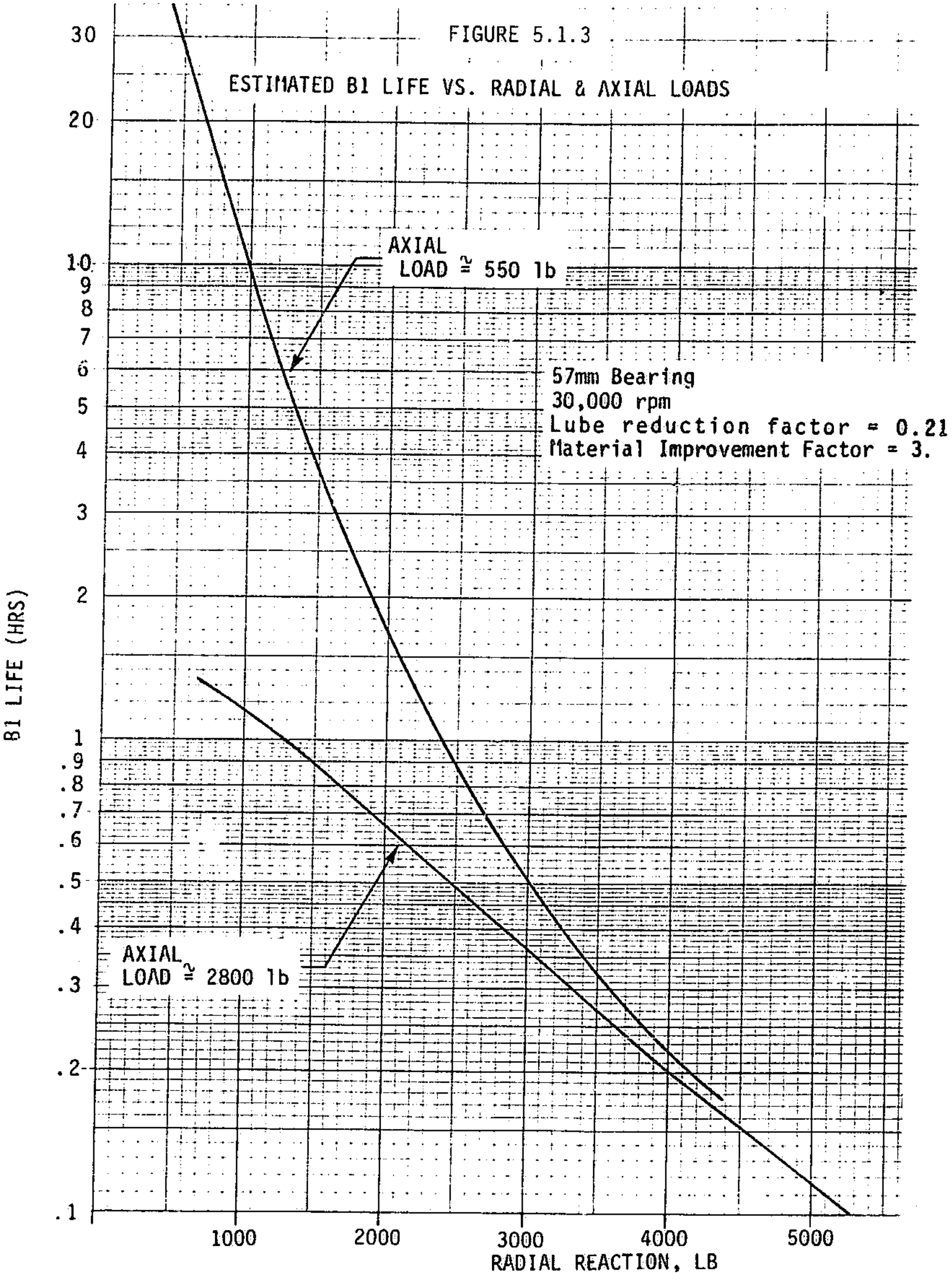

FIGURE 5.1.3

ESTIMATED B1 LIFE VS. RADIAL & AXIAL LOADS

Equation 1 does not adequately represent the test experience for high probability of survival (S>90%). As an example, for 100% survival Equation 1 predicts zero life. A technique has been developed in Reference 44 to correct for the deviation between the Weibull distribution and test experience. The following expression was developed in the reference.

$$2)\quad B = B_{10}\left[\frac{L_n\ 1/S + Ye}{L_n\ 1/.9}\right]^{1/e}$$

Ye is the standardized excess life as defined below:

Probability of Survival %	Standardized Theoretical Life	Standardized Excess Life
$S \geq 99.9$	$Y \leq .001$	$Y + Ye = .004$
$99.9 \geq S \geq 95$	$.001 < Y < .05$	$Ln(Y + Ye) =$ $0.69\ Ln\ (.328Y)$
$95 \geq S \geq 40$	$.05 < Y < .9$	$Ye = 0.013$

$$3)\quad Ye = \left(\frac{L}{L_{50}}\right)^{e} L_n 2$$

Equation 3 can be expressed in terms of survival probability as follows:

$$4)\quad Y = \left(\frac{L_n\ 1/S}{L_n\ 1/.5}\right) L_n 2 = L_n\ 1/S$$

Therefore, for 99% survival

$$5)\quad Y = L_n \frac{1}{.99} = .01$$

The standardized excess life can be determined from the appropriate expression in Table 1.

$$6)\quad Ye = [.328Y]^{.69} - Y = [(.328)\ (.01)]^{.69} - .01 = .0093$$

The relation between B_1 and B_{10} life can be determined from equation 2.

$$7)\quad B_1 = B_{10}\left[\frac{L_n\ 1/.99 + .0093}{L_n\ 1/.9}\right]^{.9} = 0.22B_{10}$$

Without the excess life term (Ye), the B_1 life estimate would be (.12 B_{10}). Therefore for this specific case, the B_1 life is approximately twice that predicted by the Weibull distribution. The other factor considered in this analysis is the reduction in life due to marginal lubrication. Lubrication reduction factors used in the Shaberth II bearing code are as low as 0.21. Applying this value to Equation 7 gives:

8) $B_1 = .046\ B_{10}$

The bearing life data shown in Figure 5.1.3 were generated by adjusting the B_{10} life predicted by Shaberth I, as indicated by Equation 8. As shown, the bearing life at the higher radial loads is relatively short. Due to the uncertainties in the extrapolation of life data from conventional to cryogenic environments, the results shown should be used with caution, especially in the regions of high radial loading (> 2000 lbs). Other factors such as contact temperature and dry lubrication performance at elevated temperature have not been considered. These factors will be more critical at the higher loads due to increased heat generated in the contacts.

The following is a suggested technique for relating bearing life to contact temperature. This method relies on the assumption that the dominant temperature effect is the loss of hardness in the contacts. This assumption may be adequate up to the temperature level at which the solid lubricant begins to deteriorate.

Several investigations (References 45 and 46) have attempted to relate bearing fatigue life to surface hardness. As pointed out in Reference 45, hardness appears to be a dominant factor determining life, all other factors being equal. Therefore, if data were available to relate bearing fatigue life to hardness, and hardness to temperature, the effect of bearing temperature could be factored into the life equation. This proposed procedure is shown graphically in Figure 5.1.4. This is an example only and does not reflect the performance of 440C material. As discussed later, the necessary data to construct such a chart for 440C has not been found in the literature.

The reduction in bearing capacity and B_{10} life can be obtained from bearing fatigue testing at specific hardness values. The relationship between temperature and hardness is needed to factor temperature into the life equation. As an example (See Figure 5.1.4), if a bearing contact is operating at 400°F, the dynamic capacity would be reduced by a factor of 0.81 and the life would be reduced by a factor of 0.56. This assumes the bearing life is related to the cube of the load. Review of the literature indicates a deficiency in the data necessary to construct curves for 440C such as those shown in Figure 5.1.4. Fatigue data relating the life of 440C to hardness, and hardness to temperature, would be of considerable interest. The availability of this information would allow the temperature estimates from the bearing thermal model to be used to gain further understanding of the thermal effects on bearing life.

5.1.5 Investigation of Ball Spin-to-Roll Ratio

An important factor in bearing life is the amount of slip occurring between the ball and races. The Lundberg - Palmgren method (Reference 1, page 411) for evaluating rolling bearing fatigue life is based on the assumption that bearings are lubricated and operated "properly". Proper operation means proper alignment, adequate loading to preclude skidding, free of contaminants such as dirt, etc. When the bearing is operated properly, sliding occurs in the contact area due to deformation of the surfaces. Since the Lundberg-Palmgren fatigue model is based on empirical data, this type of sliding is assumed to be accounted for in the fatigue life equations. Sliding which occurs because of skidding is not accounted for. According to Reference 1, the following expression can be used to reduce the dynamic capacity of the point contact due to ball spin.

$$\dot{Q}_c = \left[1 - \frac{b}{a}\frac{W_s}{W_{roll}}\right]^{\Phi} Q_c$$

Presumably Φ must be determined experimentally, and

b = Semi minor axis of contact ellipse
a = Semi major axis of contact ellipse
W_s = Ball spin normal to contact surface
W_{roll} = Ball roll relative to contact surface.

As a start in investigating this effect, the ball spin to roll ratio for the 57 mm bearing was calculated as a function of ΔT across the bearing. Since the SHABERTH computer program does not provide this calculation directly, additional computations were performed. The necessary ball rotational information generated by SHABERTH is as follows:

W_x = x component of ball speed
W_y = y component of ball speed
W_z = z component of ball speed
W_r = Resultant ball speed

Using this information, the ball spin (W_s) and roll (W_r) can be determined by constructing a vector diagram as shown in Figure 5.1.5. From Figure 5.1.5, the following expressions can be obtained:

Ball Spin:

$$W_{si} = (W_s - W_o)\ \mathrm{Sin}\ \alpha_i + W_x\ \mathrm{Sin}\ \alpha_i - W_y\ \mathrm{Cos}\ \alpha_i$$

$$W_{so} = W_{so} = -W_o\ \mathrm{Sin}\ \alpha_o + W_x\ \mathrm{Sin}\ \alpha_o - W_y\ \mathrm{Cos}\ \alpha_o$$

Ball Roll:

$$W_{ri} = (W_s - W_o)\ \mathrm{Cos}\ \alpha_i + W_x\ \mathrm{Cos}\ \alpha_i + W_y\ \mathrm{Sin}\ \alpha_i$$

$$W_{ro} = W_o\ \mathrm{Cos}\ \alpha_o - W_x\ \mathrm{Cos}\ \alpha_o - W_y\ \mathrm{Sin}\ \alpha_o$$

Where: W_{si}, W_{so} = Ball spin normal to inner and outer races respectively.
W_s = Shaft speed
W_o = Ball orbital speed
α_i, α_o = Inner and outer contact angles
W_{ri}, W_{ro} = Ball roll speed relative to inner and outer races

The spin-to-roll ratios can therefore be expressed as follows:

Inner Race:

$$\frac{W_{si}}{W_{ri}} = \frac{(W_s - W_o)\sin\alpha_i + W_x \sin\alpha_i - W_y \cos\alpha_i}{(W_s - W_o)\cos\alpha_i + W_x \cos\alpha_i + W_y \sin\alpha_i}$$

Outer Race:

$$\frac{W_{so}}{W_{ro}} = \frac{-W_o \sin\alpha_o + W_x \sin\alpha_o - W_y \cos\alpha_o}{W_o \cos\alpha_o - W_x \cos\alpha_o - W_y \sin\alpha_o}$$

The inner and outer race ball spin-to-roll ratios are shown in Figure 5.1.6 as a function of bearing temperature difference. As shown, the ball spin is reduced as the temperature difference is increased. This is the result of increased normal loads and friction forces and the reduced differences in inner and outer contact angles. It is evident that for a given set of conditions; load, speed, friction coefficients, etc., there is an optimum bearing configuration, contact angle, inner and outer race curvature, etc., that will minimize the combined effects of ball spin and heat generation and maximize bearing life. These analyses have been conducted using a clearance stack producing a minimum contact angle.

5.2 Shaft Deflection and Bearing Reaction Analyses

5.2.1 LOX Tester Shaft Deflection as a Function of Bearing Eccentricities and Radial Loads

The results of the deflection analysis to support the redesign of the LOX tester are shown in Figure 5.2.1. These data were generated from a SHABERTH model of the LOX tester shaft bearing system shown in Figure 5.2.2. The deflection curve shown is the sum of deflections due to bearing eccentricities, outer race to carrier clearances, and bearing and shaft deflections due to radial loading. As shown, the "no load" (deflection at zero radial load) is dependent on the assumed component operating temperature. Over the temperature range investigated, this is a small effect. All bearings except No. 4 was assumed to be axially perloaded to 1,000 lbs. Bearing No. 4 preload was 500 lbs. Five hundred pounds is the minimum preload expected with an axial load large enough to bottom the preload spring of bearing No. 3. Since the bearing radial stiffness decreases with axial preload, this is a worst case conditions for shaft radial deflection.

The individual bearing reactions as a function of radial load are shown in Figure 5.2.3. As shown, the applied load is not distributed equally to the bearings. The principal reasons for this are that the bearings are not located equidistant from the point of load application and the axial preload is not the same for all bearings. These differences will change as the shaft is axially loaded and deflects in the axial direction. For these reasons, bearing radial reactions should be measured at each bearing to provide known loading conditions for correlation of loading effects on bearing life.

5.2.2 Bearing Reactions and Deflections for the LOX Bearing Tester

This analysis was done for the latest preliminary design of the LOX Bearing and Materials Tester. The model used is shown in Figure 5.2.4. The results of the deflection analysis are shown in Figure 5.2.5. The deflection curve shown is the sum

ORIGINAL PAGE IS
OF POOR QUALITY

FIGURE 5.2.1 MAXIMUM SHAFT DEFLECTION VS. APPLIED RADIAL LOAD

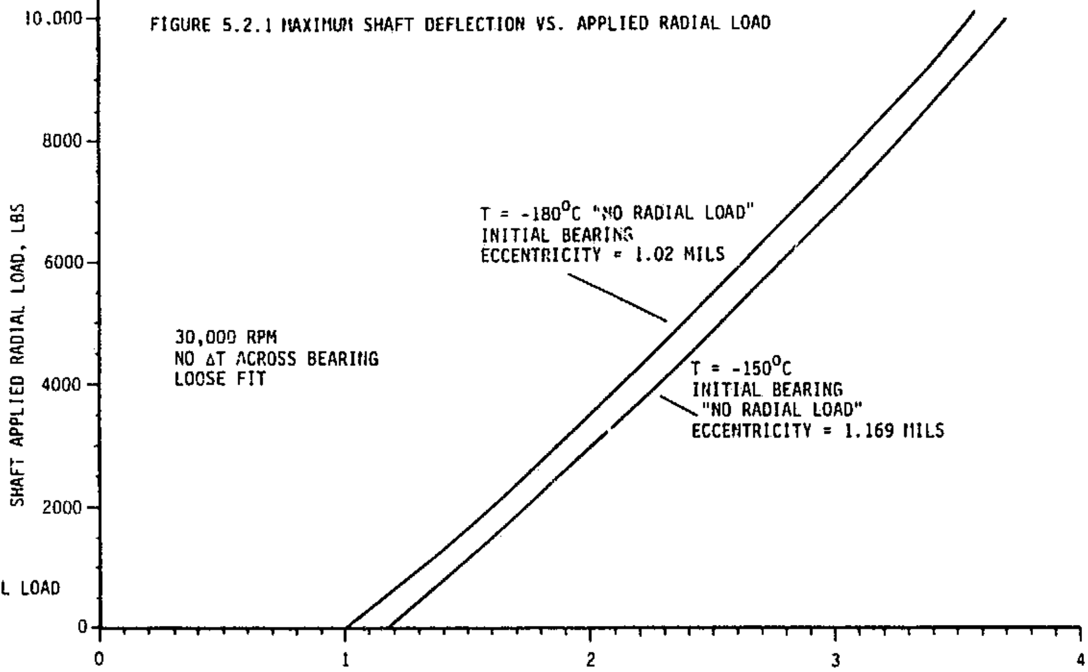

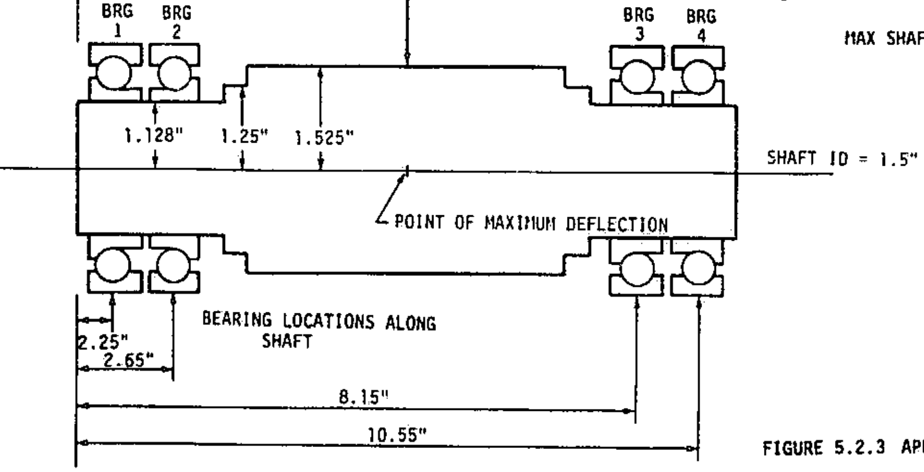

FIGURE 5.2.2 LOX TESTER SIMULATION MODEL

FIGURE 5.2.3 APPLIED LOAD VS RADIAL REACTION
(LOX TESTER)

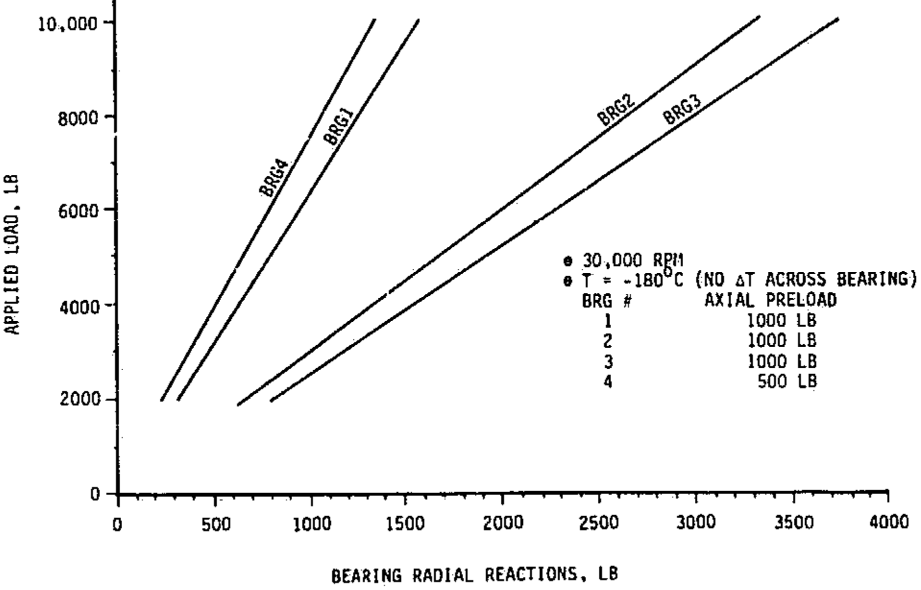

ORIGINAL PAGE IS
OF POOR QUALITY

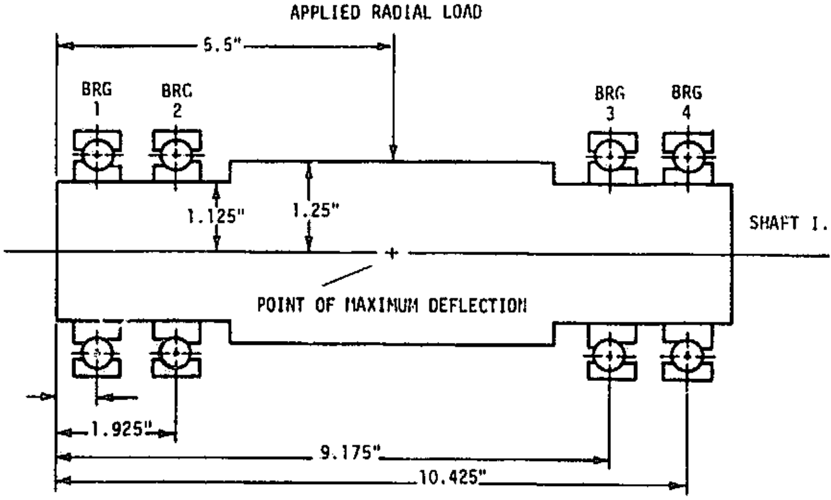

FIGURE 5.2.4 LOX TESTER SIMULATION MODEL
DIMENSIONS SCALED FROM DRAWING #30A85200-1

FIGURE 5.2.5
MAXIMUM SHAFT DEFLECTION VS APPLIED RADIAL LOAD

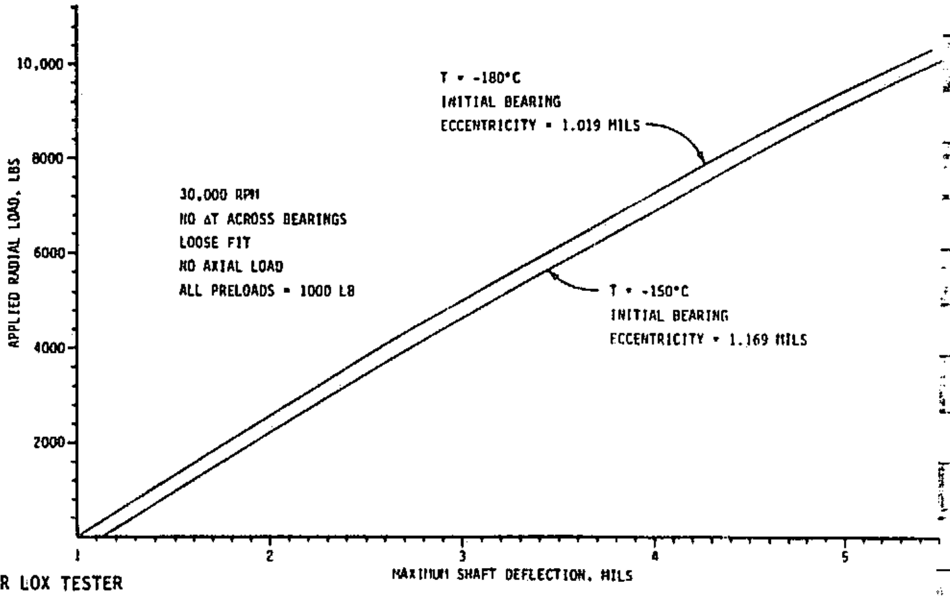

FIGURE 5.2.6 SHAFT DEFLECTIONS FOR LOX TESTER

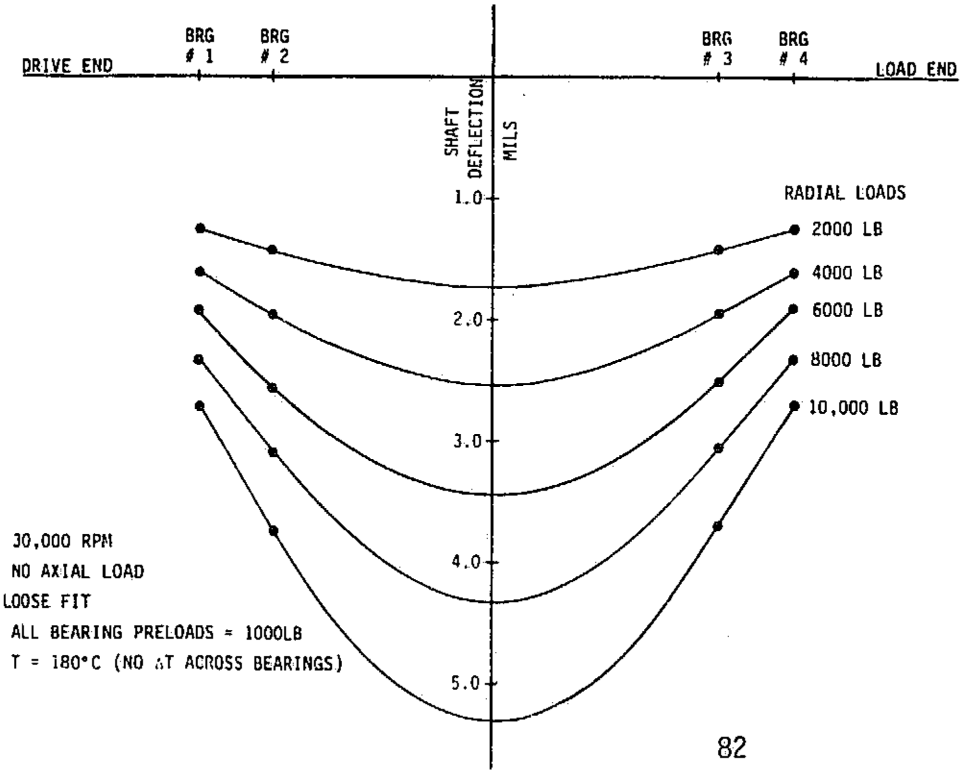

of deflection due to bearing eccentricities, outer race and carrier clearances, and bearing and shaft deflections due to radial loading only. All bearings were assumed to be axially preloaded to 1,000 lbs. As shown, the maximum shaft deflection for the 4,000 lbs radial load was found to be approximately 2.5 mils. Figure 5.2.6 shows the deflections for each bearing on the shaft as a function of radial load.

Figure 5.2.7 shows the individual bearing radial reactions as a function of applied radial load with no axial loading. An axial load will change the distribution of these radial reactions and further analysis would be required to estimate the radial reactions under combined radial and axial loading.

5.2.3 Bearing Axial Reactions Resulting from Carrier Axial Loads

The design of the Bearing and Materials Tester requires that bearing axial loads be applied by loading the bearing carrier rather than the shaft. The bearing carrier can be loaded by activating the axial load cells. Another source of loads on the carrier is the fluid pressure difference across the carrier. The fluid pressure over the carrier faces is difficult to estimate because of the uncertainty in the fluid rotation effects on local static pressure; therefore, the resulting pressure load is uncertain. Figure 5.2.8 provides the relationship of bearing carrier loads to bearing reactions. Since it is difficult, as explained in Section 5.10, to separate the load cell and fluid ΔP loads, the carrier loads in Figure 5.2.8 should be considered the sum of these loads. As shown, the preload spring constant uncertainty affects the initial preload about 20% and has a smaller effect as the carrier load is increased. Also of interest is the reduction in preload of bearings 1 and 4. Although the preload for these bearings is reduced to about 400 pounds, it has been shown in a previous analysis (see Section 5.8) that this load is sufficient to prevent ball skid due to fluid drag.

5.3 Bearing Stiffness Analyses

5.3.1 Stiffness Characteristics of the Turbine End LOX Pump Bearing

An analysis was conducted to estimate the radial stiffness of the LOX pump turbine end bearing as a function of axial preload and shaft speed. The bearing radial stiffness is defined as the ratio of radial load change to radial deflection change ($dF/d\delta$).

Approximately 21 computer runs were made using the SHABERTH bearing analysis program. These runs were made to determine the relationship of load versus deflection as affected by axial load and shaft speed. The bearing stiffness was then determined as the slope ($dF/d\delta$) of the force versus deflection curves. The radial load was varied from 100 to 400 lbs. At higher loads these curves can become nonlinear, i.e., the deflection can decrease as the radial load increases. As shown in Figure 5.3.1, the relationship is linear for axial loads greater than 1136 lbs. For the axial load case of 607 lbs, the curve is linear to about 200 lbs radial load. Since the computer solution failed to converge at higher radial loads, it is not recommended to extrapolate the stiffness versus axial reaction curve shown in Figure 5.3.2 to axial loads below about 600 lbs and radial loads greater than 200 lbs when the axial reaction is less than approximately 1000 lbs.

As expected, the radial stiffness of the bearing increased with increasing axial reaction or preload as shown in Figure 5.3.2. As previously discussed, the curve shown in Figure 5.3.2 represents the linear portion of the radial reaction versus

FIGURE 5.2.7 APPLIED LOAD VS RADIAL REACTION
(LOX TESTER)

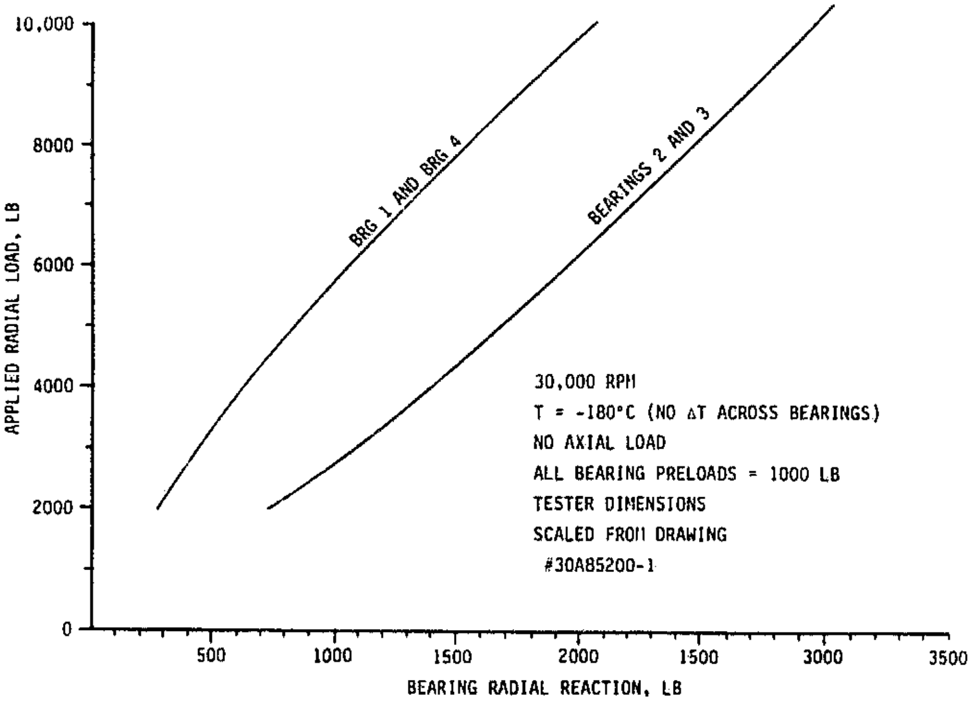

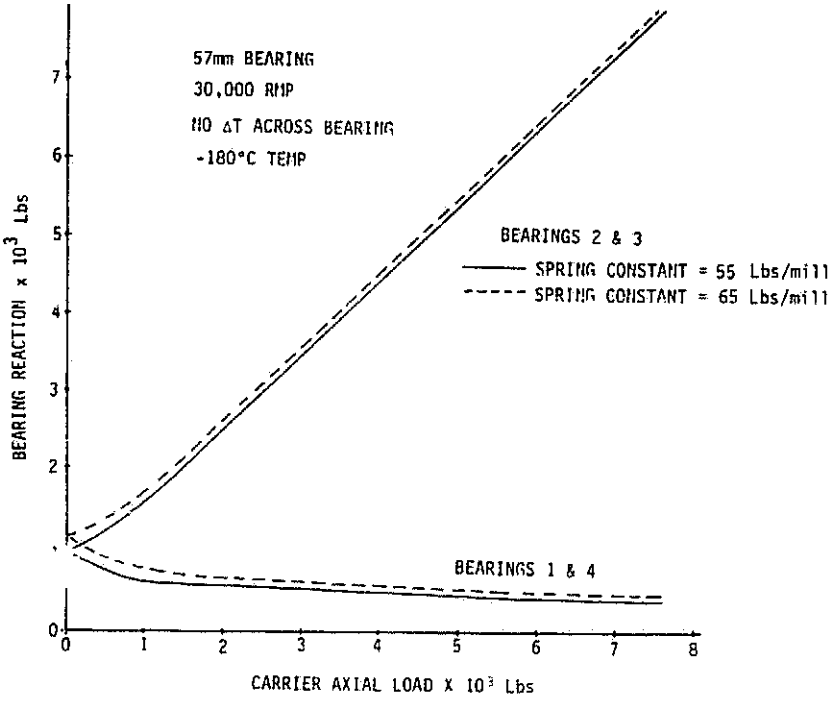

FIGURE 5.2.8 BEARING REACTION Vs CARRIER AXIAL LOAD

FIGURE 5.3.1 RADIAL LOAD VERSUS RADIAL DEFLECTION

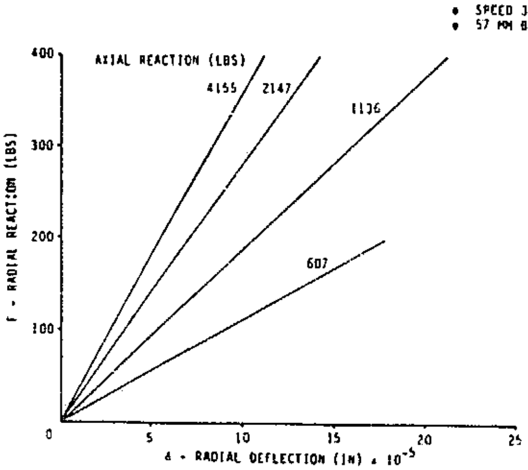

FIGURE 5.3.2 RADIAL STIFFNESS VERSUS AXIAL REACTION

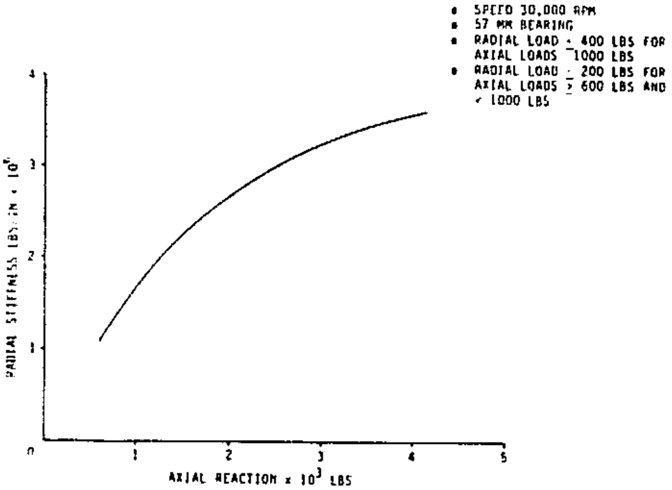

FIGURE 5.3.3 RADIAL LOAD VERSUS RADIAL DEFLECTION

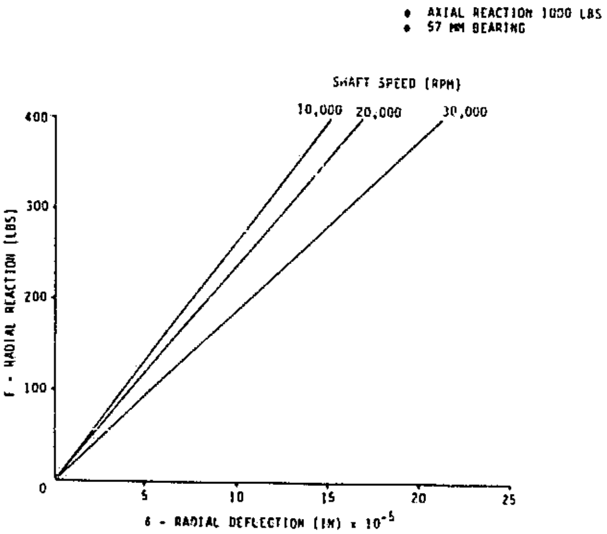

FIGURE 5.3.4 BEARING RADIAL STIFFNESS VERSUS SHAFT SPEED

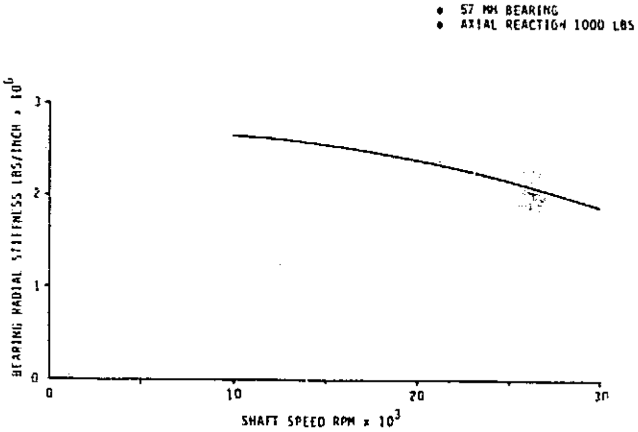

deflection bearing characteristics shown in Figure 5.3.1. A similar analysis was done to determine the effects of shaft speed on bearing stiffness. Figure 5.3.3 provides the bearing radial deflection as affected by radial reaction and shaft speed. Shown in Figure 5.3.4 is the bearing radial stiffness as a function of shaft speed. As shown, the bearing becomes less stiff in the radial direction as the shaft speed increases. This is primarily due to the increase in centrifugal force effects on the outer ring.

5.3.2 Bearing Radial Stiffness as a Function of Ball Wear

The SHABERTH I computer code was used to evaluate bearing radial stiffness as a function of ball wear. Although the highest level solution would not converge, a lower level solution that still considered friction was obtained. Judging by the few third level computer runs that did converge, the calculated radial stiffness of the bearing did not differ significantly between solution levels.

Four radial loads (100, 200, 300, and 500 lbs) were applied to bearings at five different stages of ball wear. The results of these runs are shown in Figure 5.3.5. This analysis suggests that even a decrease in ball diameter of 0.0008 inches is enough to reduce the radial stiffness by half.

5.3.3 Investigation of the Radial Stiffness of the BMT 57 mm Bearings

An analysis has been conducted to evaluate the effects on bearing operating characteristics (stresses, radial stiffness) caused by impressed radial loads. The purpose of this investigation is to identify these characteristics for input to test planning to determine the radial dynamic response of the bearing shaft system. The radial load range investigated was 500 to 6000 lbs. with axial loads of approximately 500 to 2800 lbs. Assuming an impressed axial load of approximately 2500 lbs due to the pressure differential across the bearing carriers, the two inboard bearings will be axially loaded to that value and the two outboard bearings will be unloaded. Preload is 1000 lbs to approximately 500 to 800 lbs. Since axial loads tend to stiffen an angular contact ball bearing in the radial direction, it was expected that the unloaded bearing would be the most distressed at high radial loads.

Shown in Figure 5.3.6 are the bearing deflections versus radial reactions. As expected, the bearing with the larger axial load exhibits the larger stiffness. There is also a stiffness change as the load increases. This is due to the increased radial deflections unloading balls, i.e., the total load is supported by fewer rolling elements. It is interesting to note that the unloaded bearing has three apparent stiffness values. The first change in slope (stiffness) occurs for the same reason as described above. The second change in stiffness is believed to be caused by the remaining load carrying balls being forced down on the inner race shoulder. Since at this location the inner contact angle is approaching zero, the only radial deflection possible is caused by compressing the balls (i.e., all ball movement is prevented). Shown in Figure 5.3.7 is the inner contact angle as a function of radial loads for the unloaded bearing. The bearing is reacting the radial load at an azimuth angle of zero. Notice that at this position, the inner contact angle drastically decreases as the load increases. As this happens, the ball is forced down to the shoulder of the inner race. Also observe, at an azimuth angle of 166°, the inner contact angle goes to zero for radial loads above about 1000 lbs. This indicates that the balls at this location have left the inner race and, due to centrifugal force, are following the outer race. At the higher radial loads only three balls are supporting the load. At the higher axial loads, this does not occur, and all balls are in contact with the inner race.

ORIGINAL PAGE IS
OF POOR QUALITY

FIGURE 5.3.5 CHANGE IN RADIAL STIFFNESS AS A FUNCTION OF BALL WEAR

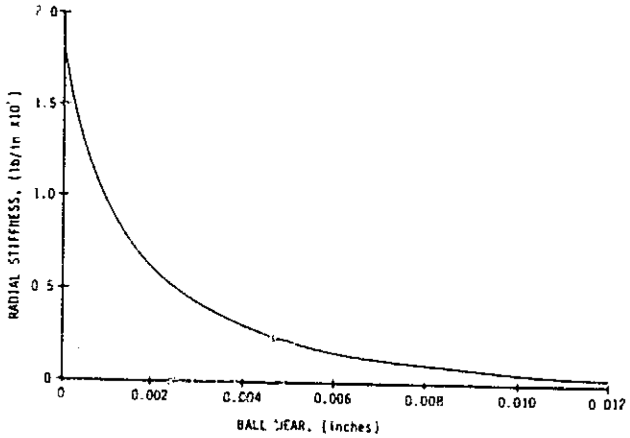

FIGURE 5.3.6

BEARING RADIAL REACTION VS DEFLECTION

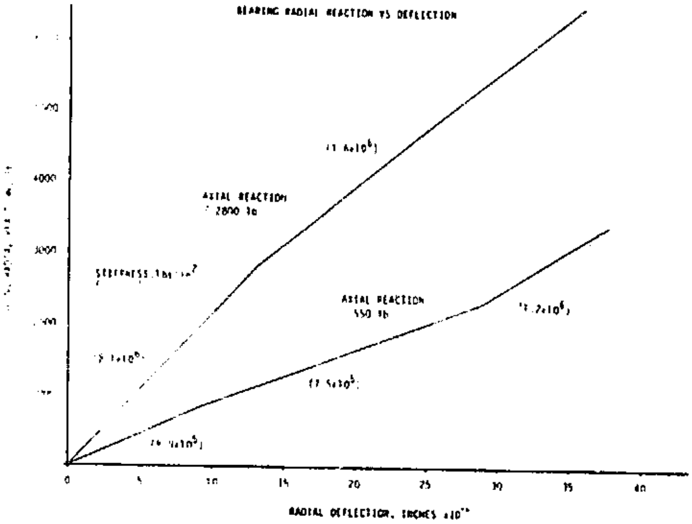

FIGURE 5.3.7

INNER RACE CONTACT ANGLE VS. RADIAL LOAD
AXIAL LOAD = 500 lbs/brg

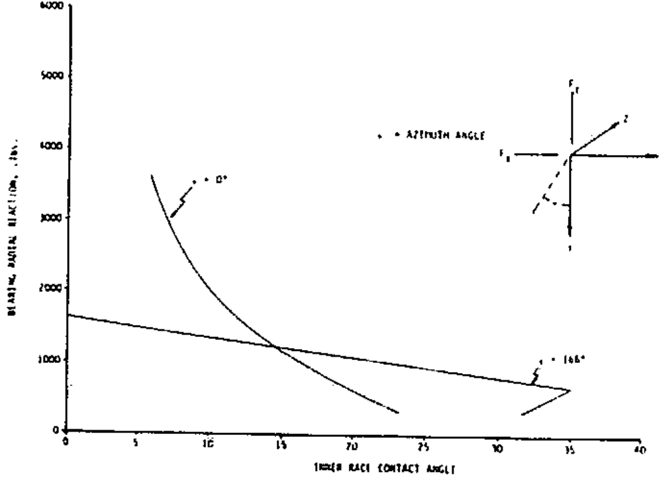

FIGURE 5.3.8

MAXIMUM CONTACT STRESSES - VS-
AXIAL AND RADIAL REACTION

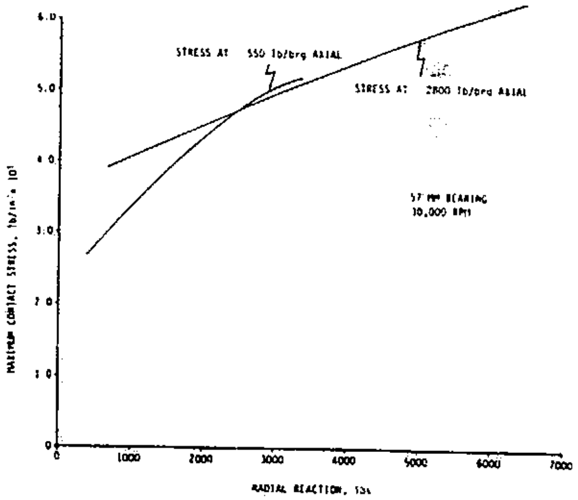

C - 2

The influences of radial and axial loads on contact stresses are shown in Figure 5.3.8. The highest contact stress is produced in the unloaded bearing, and as shown, exceeds 500 ksi. This could cause permanent plastic deformation of the contact surfaces. An assessment of heat generated on bearing temperatures and the potential for thermal run away will require exercising the bearing thermal model for these conditions.

In summary, the current BMT design will produce several values of radial stiffness as the radial load is varied over a range of 4000 lbs. A radial load of 4000 lbs will probably plastically deform the contact surfaces of the unloaded bearing. If loads in this range are planned, a thermal analysis is recommended to evaluate the potential for thermal run away.

5.3.4 Radial Stiffness of the BMT 57 mm Bearings at 10,000 RPM

An analysis similar to the one reported in Section 5.3.3, was conducted to evaluate the radial stiffness of the 57mm bearing at two levels of axial preload. The previous analysis was done for a shaft speed of 30,000 RPM while the current analysis is for 10,000 RPM. Results of the 10,000 RPM data are shown in Figure 5.3.9. The 30,000 RPM case reported in Section 5.3.3 is reproduced for convenient comparison. As shown, the greatest effect of speed on bearing deflection occurs for the low radial loads and low axial loads. At the lower speeds, centrifugal force is not as great and the inner contact angle is not decreased as much (compared to the higher speed case) thus improving the radial stiffness. This effect is more pronounced at the lower axial loads due to the reduced preload effect on radial stiffness. As the radial load increases, this effect overrides the centrifugal effects and the stiffness values become almost independent of speed. Shown in Figure 5.3.10 are the contact stresses for the loading conditions indicated. These stresses are very close to the values reported in Section 5.3.3 for 30,000 RPM.

5.4 Evaluation of Bearing Carrier to Housing Clearance and the Effect of Misalignment on Bearing Operating Characteristics

Maintaining bearing carrier to housing clearances is important to assure freedom of axial movement during axial load application to the BMT. Binding of the carrier could distort the applied load that actually reaches the bearings, introducing unknown errors in test results. Furthermore, a locked carrier could preclude rapid unloading as a contingency measure.

Currently, the BMT design allows for a 1.3 mil diametrical clearance between carrier and housing. Results from a typical bearing thermal analysis was used to estimate the differential movement between the carrier and housing due to thermal growth. The following conditions were assumed in the thermal analysis:

Inlet fluid temperature	-305°F
Flow	6.3 lbs/sec per bearing set
Axial load	2500 lbs.

Results indicated an average temperature difference between carrier and housing of about 27°F with the carrier being the warmer of the two components. Based on this temperature difference, it is estimated that there will be an interference of about 0.1 mil (diametrical) between the carrier and the housing. These are steady operating conditions, therefore, there will be a clearance at the start and early part of the test run. In order to verify the thermal analysis and operating clearance, the previously requested carrier temperature measurements are essential.

ORIGINAL PAGE IS OF POOR QUALITY

FIGURE 5.3.9

BEARING RADIAL REACTION vs DEFLECTION

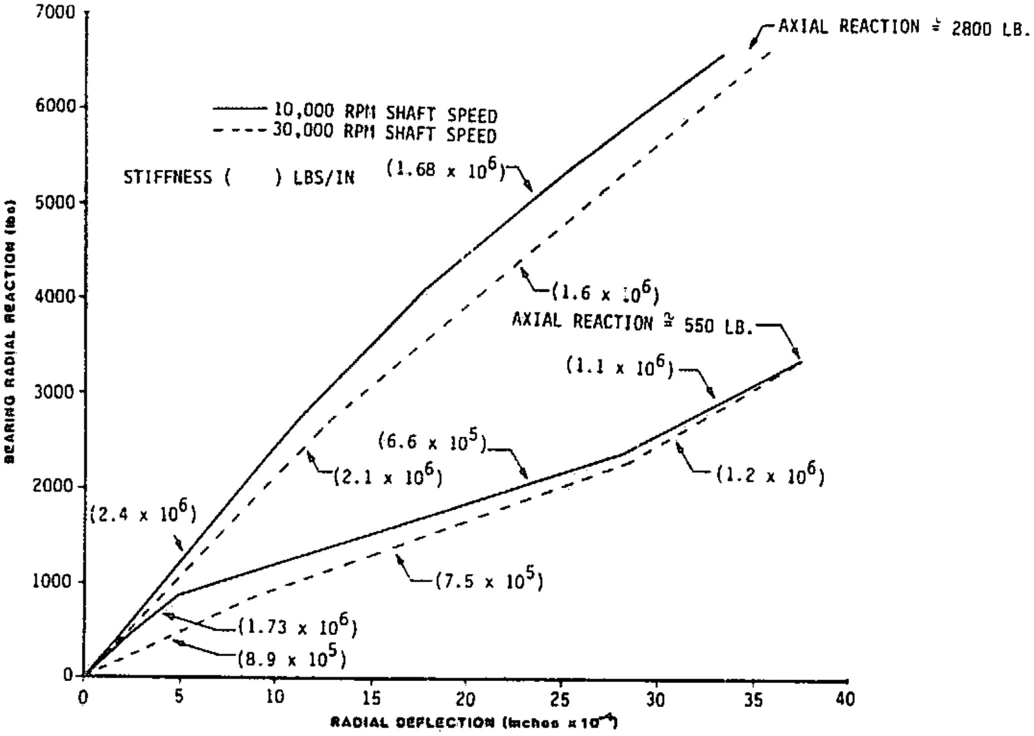

FIGURE 5.3.10

MAXIMUM CONTACT STRESS VS AXIAL AND RADIAL REACTIONS

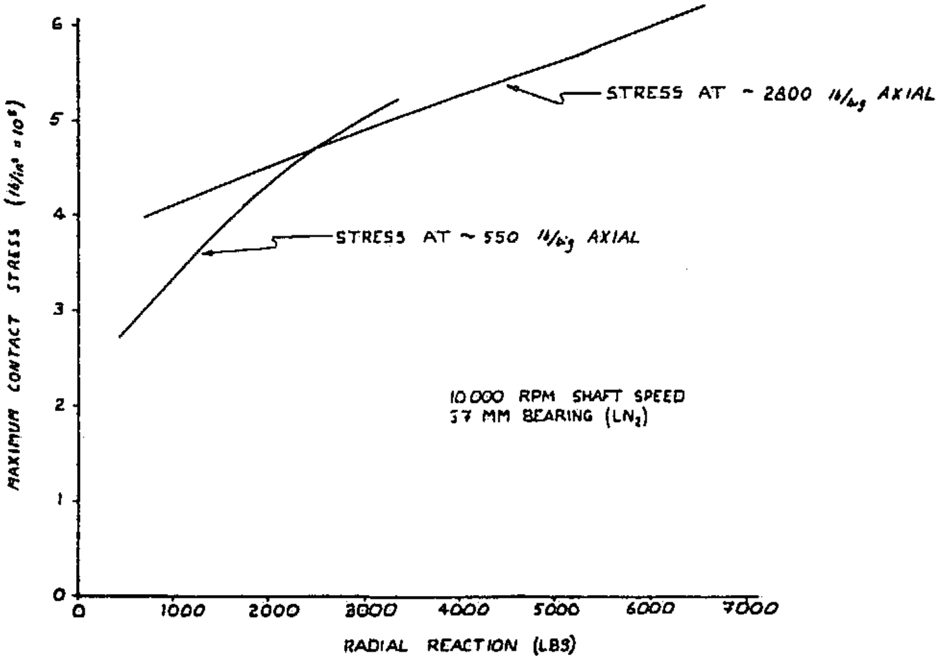

As clearances will exist during the early part of the test, analyses were done to investigate the effects of misalignment on bearing operation characteristics. Angular misalignments were determined as a function of carrier to housing clearances and the effect of these misalignments on bearing radial stiffness, ball speeds, contact angles, contact stress, and contact heat generation was determined. These effects were investigated for axial loads from 500 lbs/brg to 6000 lbs/brg, and radial loads of 100 to 500 lbs.

Figure 5.4.1 shows the potential for the carrier to tilt in the housing. The tilt angle θ is a function of the carrier diametrical clearance (C). From the geometry of the figure the following relations can be written:

$$1)\quad M = W \cos\theta - D \sin\theta$$

$$2)\quad M = \sqrt{D^2 + W^2 - (D + C)^2}$$

$$3)\quad D + C = D \cos\theta + W \sin\theta$$

Eliminating M and Cos θ from the above:

$$4)\quad \theta = \sin^{-1}\left[\frac{W(D + C) - D\sqrt{D^2 + W^2 - (D + C)^2}}{D^2 + W^2}\right]$$

Equation 4 provides the tilt or misalignment angle as a function of carrier diametrical clearance. Figure 5.4.2 provides misalignment angle as a function of diametrical clearance. As indicated the maximum expected clearance is 1.3 mils (carrier and housing at same temperature) giving a maximum misalignment angle of 2.25 minutes (.0375°).

5.4.1 Bearing Radial Stiffness Variations

The bearing radial stiffness as a function of azimuth angle is shown in Figure 5.4.3. In this figure, the zero azimuth angle corresponds to the "pinch" point caused by the misalignment of the outer race [the results from the "SHABERTH" bearing analysis program, Figure 5.4.4, are presented with the zero azimuth angle 180° out of phase from the "pinch" point]. The variation in stiffness shown is conservative because the reduction of the bearing misalignment angle as a function of axial load was not considered in the stiffness determination. These variations should not significantly affect synchronous radial motion of the shaft due to small rotor unbalance which was the main concern of possible large stiffness variations due to misalignment.

5.4.2 Bearing Operation Characteristics

The investigation of carrier misalignment on contact stresses, contact angles, ball speeds, and heat generated at the contacts required numerous "SHABERTH" computer runs with varying input parameters. The conditions shown in Figure 5.4.4 were investigated.

In reviewing the data, the most significant variations due to outer race misalignment is the ball orbital speed. This occurs for the 500 lb axial load condition. This is representative of tester bearings 1 and 4 with the normally accepted axial PA load of 2500 lbs. Comparisons of contact stresses, ball speed, and contact angles for the misaligned and normal conditions do not show significant variations in

FIGURE 5.4.1 CARRIER TILT IN HOUSING

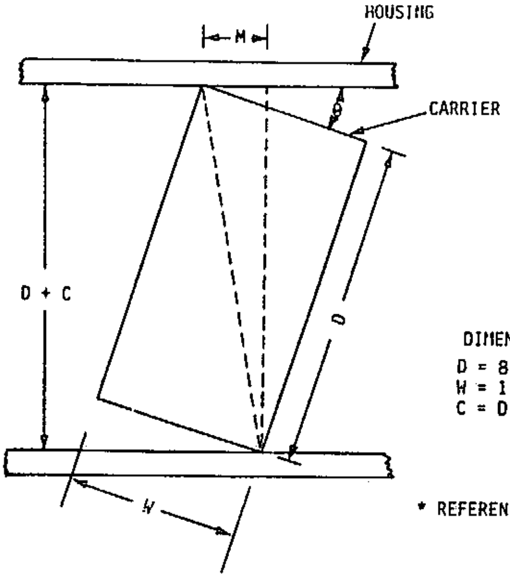

DIMENSIONS* (INCHES)
D = 8
W = 1.992
C = DIAMETRICAL CLEARANCE

* REFERENCE MSFC DRAWING 30A 84 009

FIGURE 5.4.2 OUTER RACE MISALIGNMENT AS A FUNCTION OF BEARING CARRIER DIAMETRICAL CLEARANCE

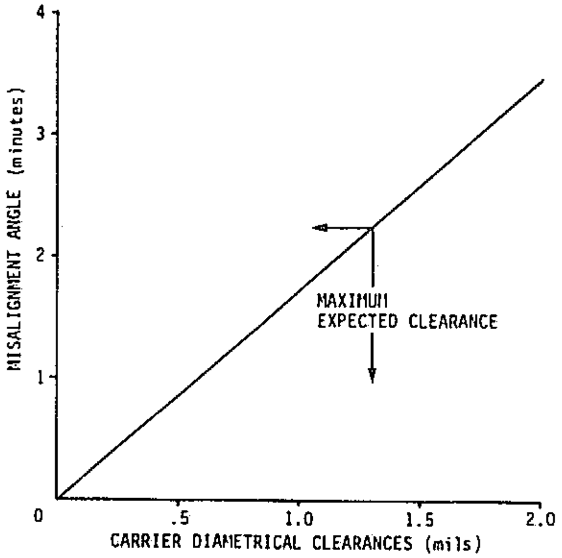

FIGURE 5.4.3 RADIAL STIFFNESS VERSUS AZIMUTH ANGLE

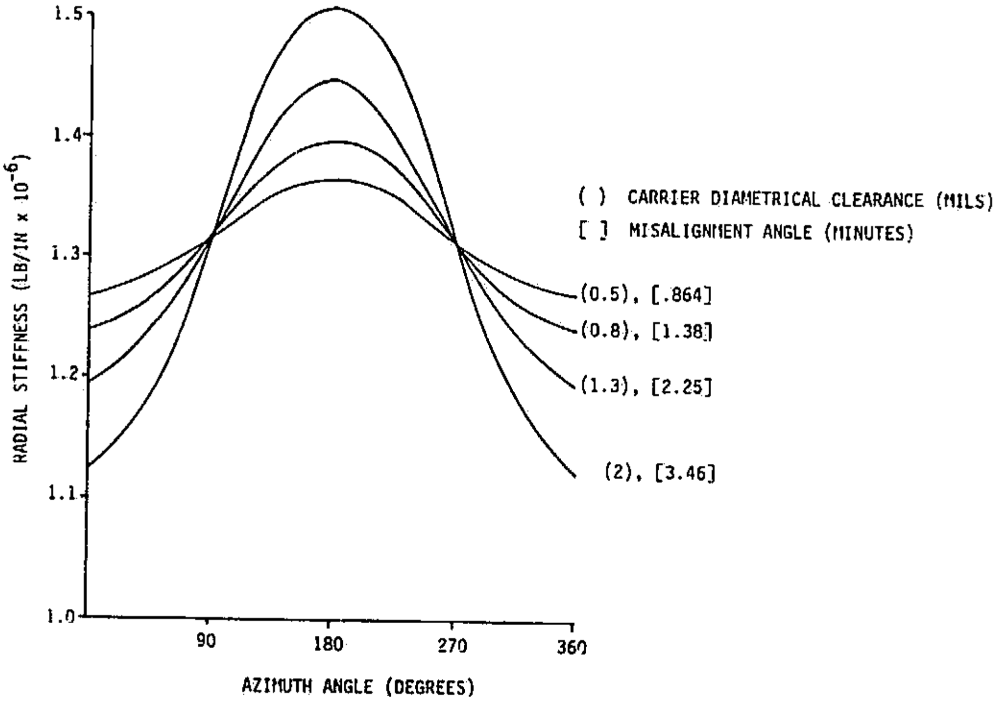

FIGURE 5.4.4. CONDITIONS INVESTIGATED FOR BEARING MISALIGNMENT EFFECTS

AXIAL LOAD (LBS.)	MISALIGNMENT ANGLES (DEG.)			
500	.0375	.0229	.01439	.01
2500	.0375	.0229	.01439	.01
6000	.0375	.0229	.01439	.01

AXIAL LOAD (LBS.)	RADIAL LOADS (LB.) (NO MISALIGNMENT)		
2500	100	300	500
6000	100	300	500

AXIAL LOAD (LBS.)	RADIAL LOADS (LB.)			MISALIGNMENT FOR EACH AXIAL/RADIAL LOAD COMBINATION (DEG)	
2500	100	300	500	.0375	.01
6000	100	300	500	.0375	.01

AXIAL LOAD (LBS.)	MISALIGNMENT ANGLES (DEG.) (BALL TO POCKET CLEARANCE OF 100 MILS.)			
500	.0375	.0229	.01439	.01

AXIAL LOAD (LBS.)	MISALIGNMENT ANGLES (DEG.) (RADIAL TEMP. DISTRIBUTION IN BEARING)			
2500	.0375	.0229	.01439	.01
6000	.0375	.0229	.01439	.01

FIGURE 5.4.5 OPERATING MISALIGNMENT VS INITIAL MISALIGNMENT AND AXIAL LOAD

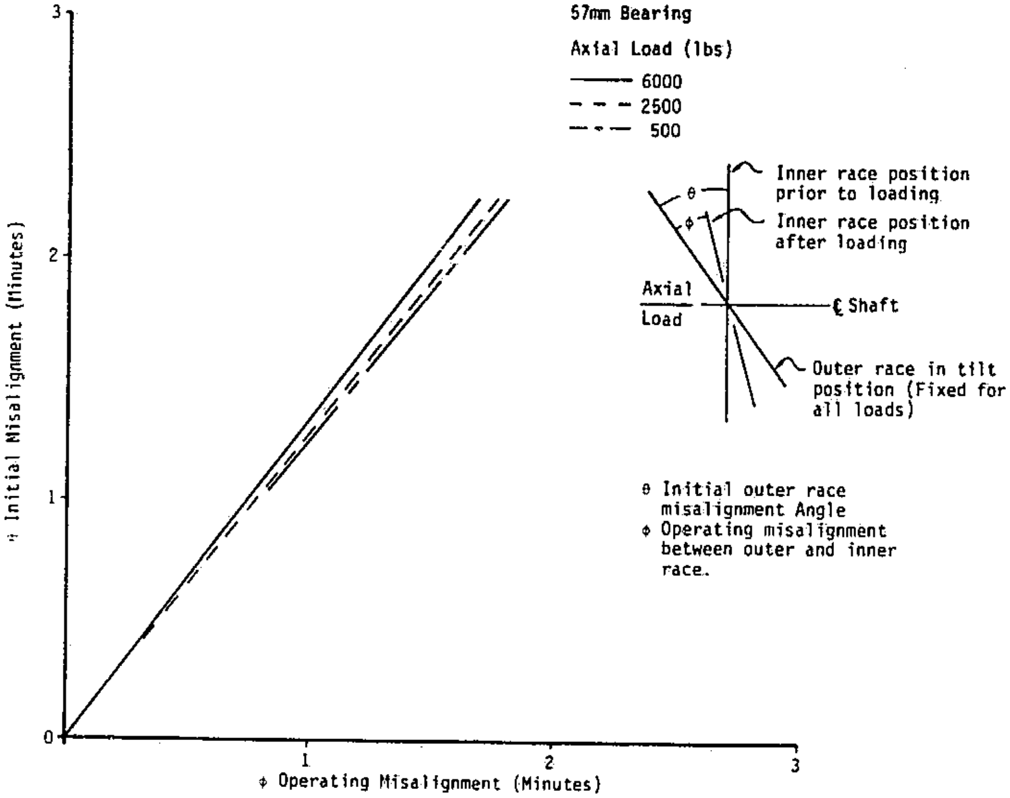

these parameters for the higher axial load cases. There is a maximum difference in ball orbiting speed of about 20 rad/sec for the 500 lb axial load condition. It is estimated that this causes ± 8.5 mil movement of the ball relative to the ball pocket center. This should not cause a problem since there is 25 mils diametrical clearance between ball and ball pocket.

5.4.3 Effect of Axial Load on Bearing Misalignment

The effect of axial load on operating misalignment is shown in Figure 5.4.5. As the axial load is increased, the inner race is forced to rotate thus decreasing the angle between the inner and outer race. The degree of rotation is obviously dependent not only on bearing characteristics but also the stiffness of the shaft since the shaft exerts a clockwise movement on the bearing inner race as the race is forced to rotate counter-clockwise due to the outer race misalignment. Shaft and bearing characteristics were included in the bearing/shaft model.

In summary, the analyses indicate no tester operational problems due to outer race misalignment with a carrier to housing clearance of 1.3 mils. Although the thermal analysis indicates a slight carrier to housing interference for steady state conditions, verification of this condition is necessary during early tester operation and should not be detrimental during the initial test phase in LN_2 when loads are relatively light. For higher loads and increased heat generation, further analysis is required to evaluate the adequacy of carrier to housing clearance. These analyses should use the thermal model "calibrated" by thermal data taken in the early BMT runs.

5.4.4 Potential Effects of Outer Race Misalignment on Shaft Assembly Balancing

An apparent shaft assembly unbalance was observed during balancing of the BMT rotating assembly. The cause was determined to be bearing carrier face run out. The carrier run out can in effect produce an angular misalignment in the bearing outer race. The purpose of this investigation is to develop an explanation as to how the outer race tilt could produce a synchronous load effect, which would appear to be a grossly out of balance shaft assembly.

As a start, the geometry change in the bearing was evaluated as the outer race was displaced. Figure 5.4.6 illustrates the geometric representation. As the outer race is rotated counter clockwise, the right ball moves upward and to the right and the left ball moves down and to the right. The center of the pitch circle is displaced in the positive y direction. The center of the circle formed by the outer race curvative center is displaced in the y direction (k) and in the x direction (h). Normally this is a static condition and the ball pitch circle would be displaced from the shaft center line by a constant value and there should be no shaft dynamic effects. However, the contact angle changes as a function of the azimuth angle. The contact angle is increased in the $\psi = 0^o$ position and decreases when $\psi = 180^o$. At $\psi = 90^o$, the contact angle is not changed. Assume an out of balance shaft assembly producing a synchronous load in the radial direction. Since the contact angle changes with azimuth location, the bearing radial stiffness also changes in the azimuth direction. Therefore, with a variable stiffness, the shaft can move radially in a dynamic manner synchronous with shaft speed. Consequently, a small unbalance can be magnified into an apparent large unbalance by outer race misalignment. The geometry shown in Figure 5.4.6 is obviously for an unloaded, static bearing. Loads and speed will change the configuration. However by superimposing the outer race misalignment effects on the configuration assumed by the bearing at speed and under load, the above explanation should still be valid.

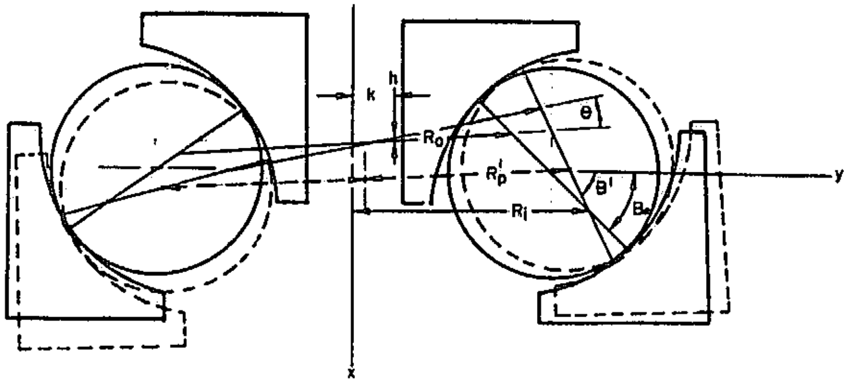

R_i = INNER RACE RADIUS
R_p = OUTER RACE RADIUS
B_o = INITIAL CONTACT ANGLE
Ψ = AZIMUTH ANGLE
R_p' = PITCH RADIUS AFTER MISALIGNING OUTER RACE
B' = CONTACT ANGLE AFTER MISALIGNMENT
h = DISPLACEMENT OF OUTER RACE RADIUS ALONG X-AXIS
k = DISPLACEMENT OF OUTER RACE RADIUS ALONG Y-AXIS
θ MISALIGNMENT ANGLE

FIGURE 5.4.6 DISPLACEMENT OF OUTER RACE WITH INNER RACE FIXED

FIGURE 5.4.7 CHANGE IN CONTACT ANGLE AS FUNCTION OF OUTER RACE MISALIGNMENT AND AZIMUTH LOCATION

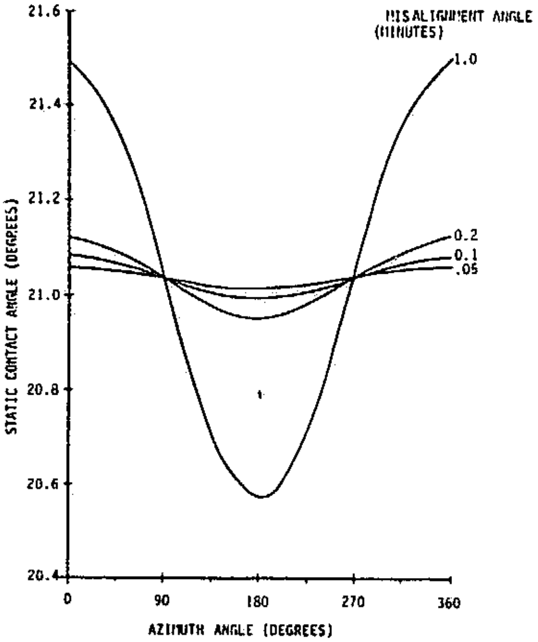

To investigate the sensitivity of the contact angle to outer race misalignment the following analysis was made. Assuming no deformation in the contact areas and very small axial displacement, $h \sim o$, the contact angle can be related to the misalignment angle as follows:

$$\mathrm{SIN}B' = \frac{R_o\theta}{A} \mathrm{COS}\psi + \mathrm{SIN}B_o$$

A is the distance between curvature centers.

The above equation is presented graphically in Figure 5.4.7. A one minute angle of misalignment introduces about 4.5% peak to peak variation in contact angle. The degree this affects radial stiffness and shaft assembly dynamics is yet to be determined.

An analysis to determine the stiffness variation is in work. "SHABERTH I" was coded to evaluate the stiffness variation with misalignment, but failed to run. "SHABERTH II" was subsequently coded to include outer race misalignment and it ran. These results will be bearing radial stiffness values that can be input to a bearing dynamic model for evaluating rotor/shaft dynamics.

5.5 Bearing Wear Track, Ball Pass Count, and Ball Spin Speed Analysis

A 57 mm bearing was modeled on the SHABERTH computer program with maximum clearances and an arbitrary temperature distribution radially across the bearing. The purpose was to determine if the observed bearing wear tracks could be matched within the known loads applied to the bearing tester. As shown in Figure 5.5.1, a fairly good match can be obtained with an axial load of 6500 pounds. For comparison, the calculated tracks for a uniform bearing temperature and nominal clearances are shown. The temperature gradient used was an assumed one which was selected to investigate the sensitivity of contact angle to increased diametrical clearances due to temperature differences. This information shows that the bearing tracks can be influenced by temperature and clearance as well as applied loads.

Cage speed data generated from SHABERTH was used to generate inner and outer race ball passes per minute. This data was compared with the data measured during tester operation. The comparisons, shown in Figure 5.5.2, indicate good agreement with the measured and calculated values. Also shown is the ball spin speed compared with the data derived from the tests. As illustrated, the above parameters are plotted as a function of the bearing axial reaction load.

5.6 Effects of Ball Drag on Operating Characteristics

The SHABERTH computer program has the capability of evaluating the effects of ball drag. Unfortunately, the treatment of the hydrodynamic effects have been programmed considering the properties of lubricants operating in a nominal temperature range of -60 to 600^{0}F. For example, the temperature correction for the lubricant density is given as:

$$\rho(T) = \rho(60^0F) - G(T - 60^0F)$$

where $\rho(60)$ and G can be input or a lubricant can be selected that has its properties already programmed. Obviously, O_2 does not exist as a liquid at 60^{0}F and the above equation does not account for a phase change from gas to liquid. Therefore, a ficti-

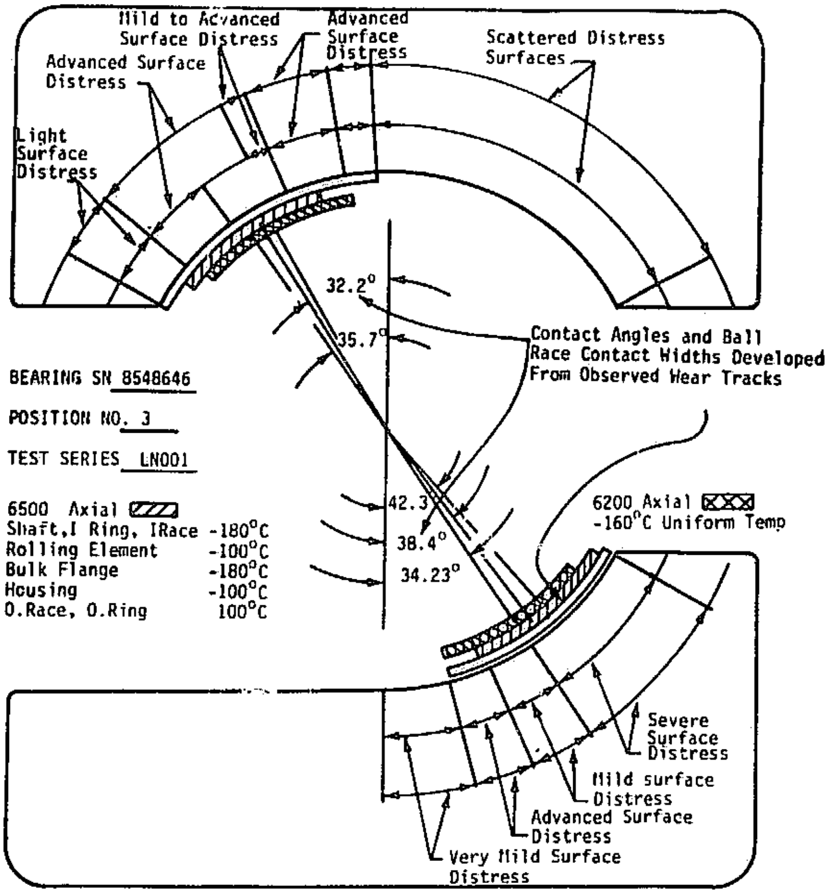

1 DEGREE = 0.04625 INCH AT 10X
MAGNIFICATION
BEARING 57-MM, P/N - RS007955 TURBOPUMP

FIGURE 5.5.1 COMPARISON OF CALCULATED AND OBSERVED WEAR TRACKS

FIGURE 5.5.2 COMPARISON OF ESTIMATED AND TEST RESULTS

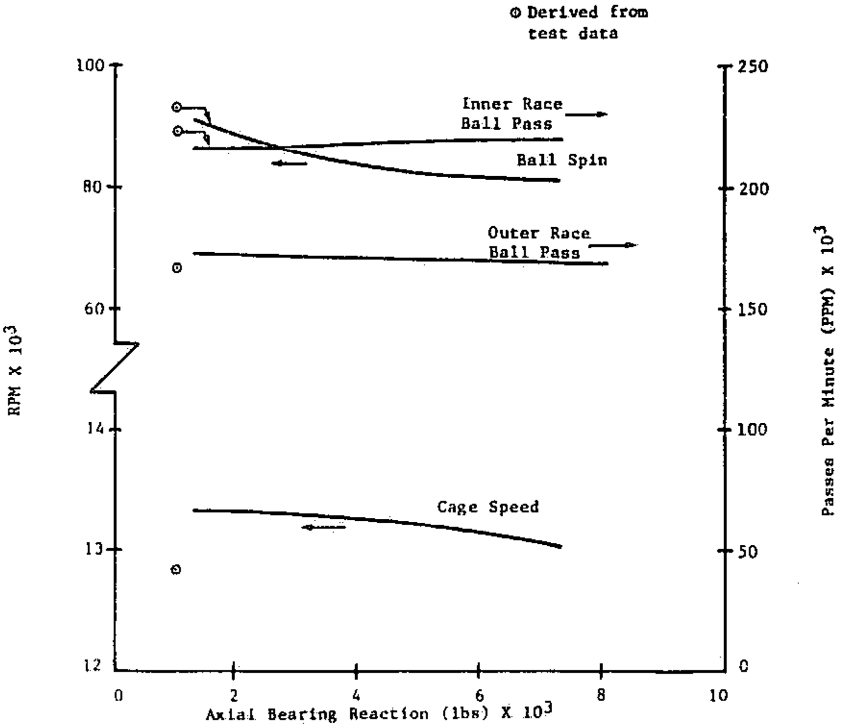

tious value for $\rho(60)$ can be used or a lubricant selected that has a density range covering LOX, when the appropriate temperature is used in the above equation.

Another problem associated with LOX as a fluid is caused by the way the program accounts for viscosity variations with temperature. Typical lubrication viscosity data have been correlated with the following expression:

$$\log_{10} \log_{10} (V + 0.6) = A - B \log_{10} (T + 460)$$

where A and B are constants determined by substituting the known values of viscosity (V) at T = 100°F and T = 210°F and solving the two resulting equations for A and B. For a low viscosity fluid such as LOX, the term (V+.6) is less than one thus requiring taking the log of a negative number.

To work around the above problems, SHABERTH was run at LOX temperature using a dry lubricant friction coefficient. The purpose was to determine the operating clearances at LOX temperature. These clearances will be used as input for a higher temperature run (temperature selected to obtain a match of lubricant and LOX density) with a fluid to determine the drag force on the balls.

The ball drag force is determined by:

$$Fw = \frac{\rho AvCv}{8g} (dmWo)^2$$

Av = ball frontal area
Cv = drag force; determined as a function of Reynolds Number
dm = bearing pitch diameter
Wo = ball orbital velocity (cage speed)
ρ = density of fluid in the bearing cavity

The density of the fluid in the bearing cavity is determined by:

$$\rho = XCAV\rho o$$

ρ_o is the density of the liquid and XCAV is an input variable defining the percent liquid in the bearing cavity. Obviously, the ball drag force can be varied by varying the value of XCAV. The technique for using SHABERTH for estimating ball drag effects is as follows:

1) Run SHABERTH at LOX temperatures to establish operating clearances.

2) Run SHABERTH at appropriate temperature to provide a lubricant density equivalent to LOX density.

3) Use the values of viscosity to calculate a Reynolds Number to determine the drag coefficient Cv, and calculate the drag force used by the program. Any value of drag force can be investigated by varying XCAV.

To date, successful runs have been made using this technique. The results are provided in Section 5.7.

5.7 Estimates of Ball Drag Forces, Torques, and Heat Generation

Proper manipulation of input data allows the SHABERTH bearing program to calculate the heat generated due to viscous work and drag on the orbiting balls in a low viscosity fluid such as LOX. This technique was explained in Section 3.4.6. Estimates of ball drag, torque, and heat generation can be made as a function of the percent liquid assumed to be in the bearing cavity. Shown in Figure 5.7.1 are the preliminary results of an analysis on the 57 mm bearing. As noted, the data are for a single bearing assumed to be operating in a stagnant fluid. The percent fluid in the cavity can be interpreted either as a low density fluid or the partial filling of the cavity with liquid.

Although bearing characteristics such as contact angle were not affected by ball drag, the fluid drag on the balls does cause ball slippage or skidding in a lightly loaded bearing. This effect is shown in Figure 5.7.2 which gives the ratio of cage-to- shaft speed as a function of bearing reaction, percent fluid in the cavity, and friction coefficient. Although this information should be considered preliminary due to convergence problems with the machine solution, the trends are believed to represent the physical characteristics. This problem should be overcome by going to a higher level of solution in the SHABERTH program.

As shown, the effect of increased flooding of the bearing cavity is to slightly reduce the cage rotational speed at bearing reaction loads above approximately 150 pounds. Below 150 pounds there is a significant reduction in cage speed indicating bearing slip on the inner race. A reduction in friction coefficient increases the ball slip which further reduces the cage speed as shown. This indicated that a combination of low axial load and high fluid drag can cause significant slip between the rolling elements and the inner race. The consequence of this is increased heat generated, wear, and shorter bearing life. The fluid density used in these analyses is representative of LOX.

The effects on bearing frictional and viscous heat generation are shown in Figures 5.7.3 and 5.7.4. Figure 5.7.3 provides data for a 50% flooded cavity and Figure 5.7.4 is data representing a 100% flooded cavity. As shown, the fractional heat generated increases, after passing through a minimum point, as the bearing reaction load is reduced. The effect is more severe for the 100% flooded cavity. These effects could be considerably more severe than indicated for some combinations of axial and radial loading. For instance, if a bearing is lightly loaded in the axial direction with significant slip between rolling elements and inner race, a sudden application of radial load will cause the friction forces between the ball and race to increase. Since the ball/cage mass cannot be instantaneously accelerated to the cage equilibrium speed, considerable damage can be done to the balls and races due to slippage under high loading. This input could explain the abnormal wear observed in the LN_2 tests for bearings 1 and 4 of the BMT. Efforts are under way to extend these analyses to include other friction factors and modify the fluid density to represent LN_2.

5.8 Effects of Bearing Preload on Cage Slip and Frictional Heat Generation

An analysis has been conducted to evaluate the effects of axial load on bearing cage speed and heat generation rates due to rolling element slip with respect to the inner race. The effects of viscous drag, due to the rolling elements rotating in the LN_2 coolant, was accounted for in modeling the 57 mm LOX turbopump bearing for analysis using the SHABERTH Bearing Analysis Computer Program.

FIGURE 5.7.1 HEATING AND BALL DRAG VS % FLUID IN CAVITY
(Single Bearing)

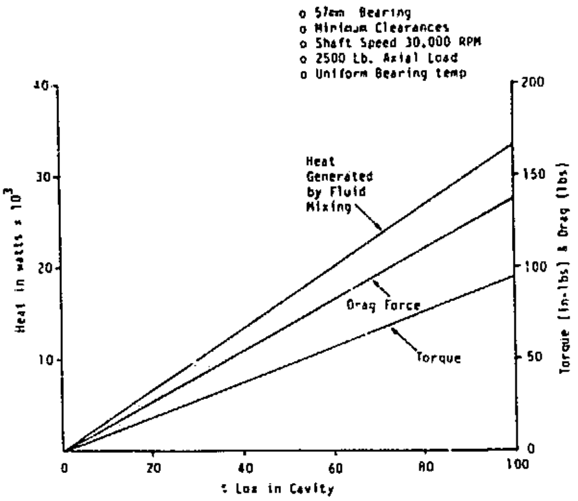

FIGURE 5.7.2

CAGE/SHAFT SPEED RATIO vs. AXIAL LOAD, % LOX IN BEARING CAVITY AND FRICTION COEFFICIENT

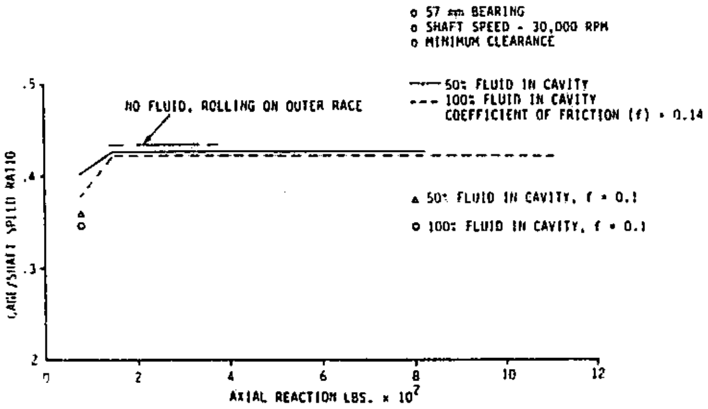

FIGURE 5.7.3

HEAT GENERATED vs. AXIAL LOAD (SINGLE BEARING) 50% FLUID IN CAVITY

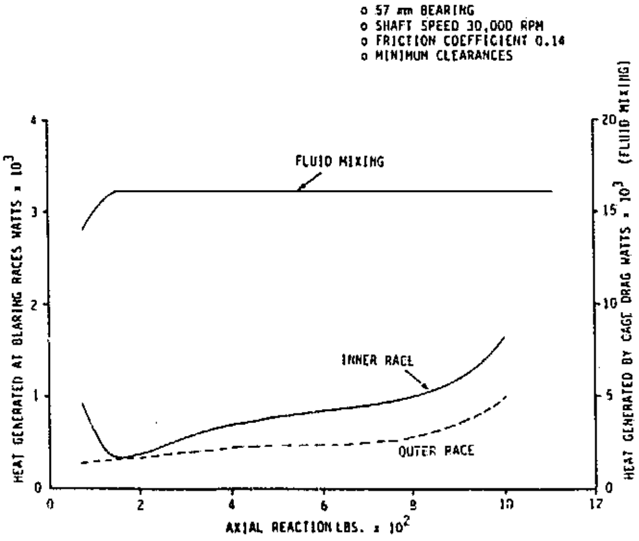

FIGURE 5.7.4

HEAT GENERATED vs. AXIAL LOAD 100% FLUID IN CAVITY

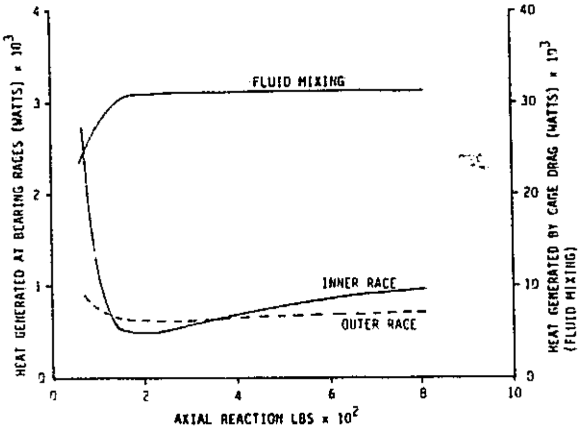

The objective was to determine the axial load that would allow the viscous drag force to overcome the contact friction forces to the extent that significant slippage could occur at the rolling element/face interfaces causing appreciable increases in inner race heat generation. Since the friction force is directly proportional to the coefficient of friction, which is not conclusively known, the friction coefficient was varied over a range from 0.08 to 0.22. The results of the investigation are shown in Figures 5.8.1 and 5.8.2. The data shown in Figure 5.8.1 for a friction coefficient of .08 indicate that, below a specific value of axial load, the heat generated at the inner race decreases to a minimum and then increases to a maximum. The same characteristic should occur for the other friction coefficients.

Inability of the computer program to converge to a solution at the lower levels prevented completing these curves in the low load region. It should also be observed for the friction coefficient of .08 that the heat generated by cage drag begins to decrease as the heat generated at the inner race begins to increase. Shown in Figure 5.8.2 is the cage/shaft speed ratio as a function of axial reaction, friction factor, and fluid drag. The upper horizontal line represents the case for no fluid drag. For these conditions, the cage to shaft speed ratio is about 43%. As shown, a decrease in friction force (friction coefficient) reduces the cage speed. Furthermore, a reduction in axial load reduces the cage speed dramatically at loads below about 300 lbs.

The results of this analysis provide a better understanding of why bearings 1 and 4 of the BMT were degraded even though they were lightly loaded in the axial direction. Based on these results, a design requirement should be to provide at least 400 lbs of preload in the bearings at all operating conditions.

5.9 Assessment of Bearing Wear by Measurement of Axial Deflection and Applied Load

It is desirable to have the capability to evaluate bearing wear subsequent to each test run. In principal this can be done by measuring the shaft deflection as a function of applied axial load, and correlating this information with the analytically developed curves shown in Figure 5.9.1. To assess the degree of wear, the information shown in Figure 5.9.1 was generated by developing the relationship between carrier axial load and bearing reaction and, by use of the Shaberth bearing code, developing the relationship between bearing reaction and shaft deflection. The data shown are for cryogenic temperatures since the deflection sensors are expected to be calibrated in this temperature range. Ambient temperature curves can be readily generated if required.

5.10 Bearing Operating Preloads

An analysis has been done to estimate the change in bearing preload, from the assembled room temperature value, as the bearing/shaft assembly is cooled from room temperature to LN$_2$ temperature and rotated to a speed of 30,000 RPM. At this point in the analysis, it is assumed that the shaft is not axially loaded; therefore, the bearing axial reactions are equal for all bearings and equal to the spring preload value at operating conditions.

Considering only the thermally induced axial loads and deflection, the following expressions can be written for the axial deflection of the shafts and components.

1) $$d\ell_s = \alpha_s \ell_s \Delta T - \frac{F_T \ell_s}{A_s E_s}$$

ORIGINAL PAGE IS OF POOR QUALITY

FIGURE 5.8.1
HEAT GENERATION VS AXIAL REACTION

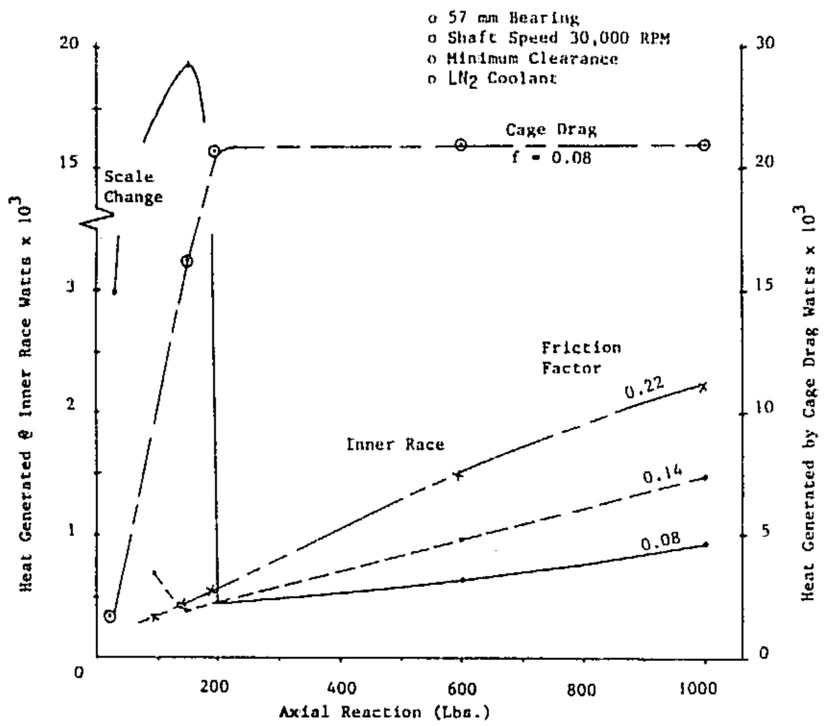

FIGURE 5.8.2
CAGE TO SHAFT SPEED RATIO

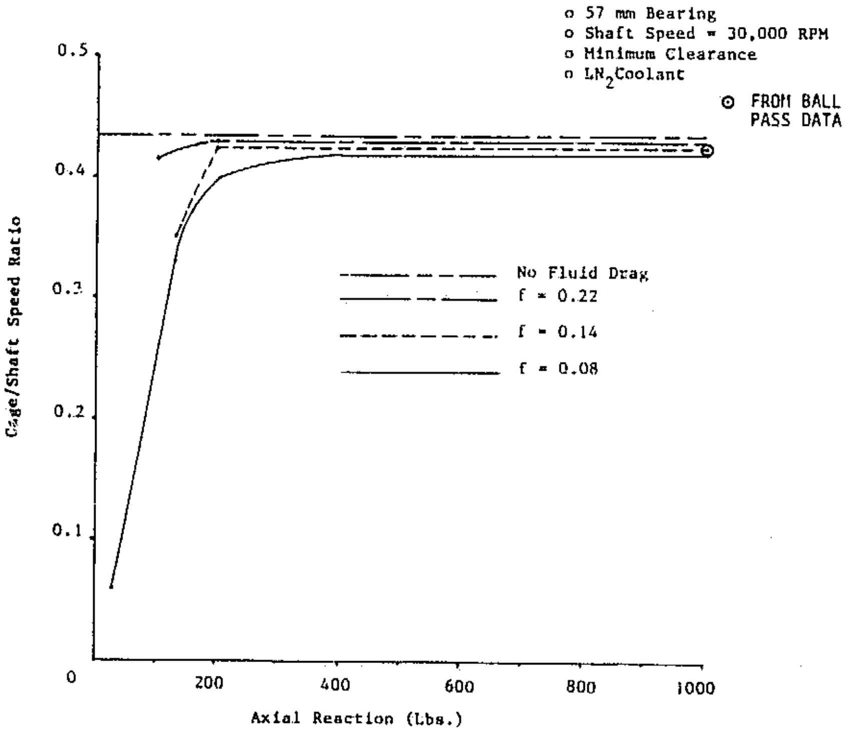

FIGURE 5.9.1
Static Deflection As a Function of Load and Ball Wear

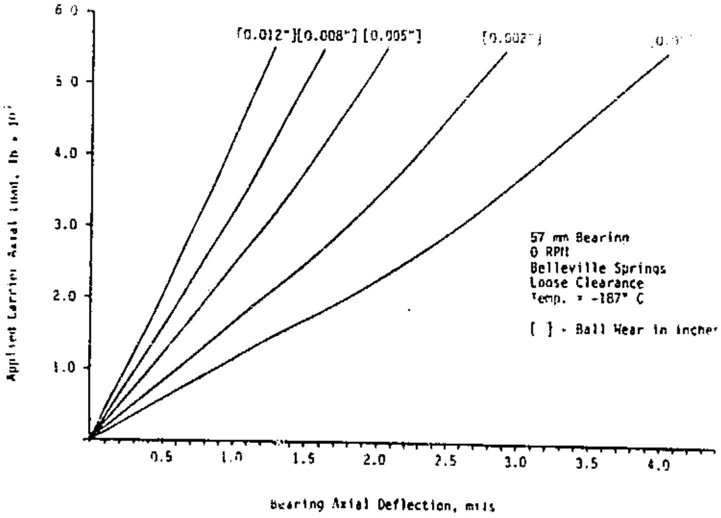

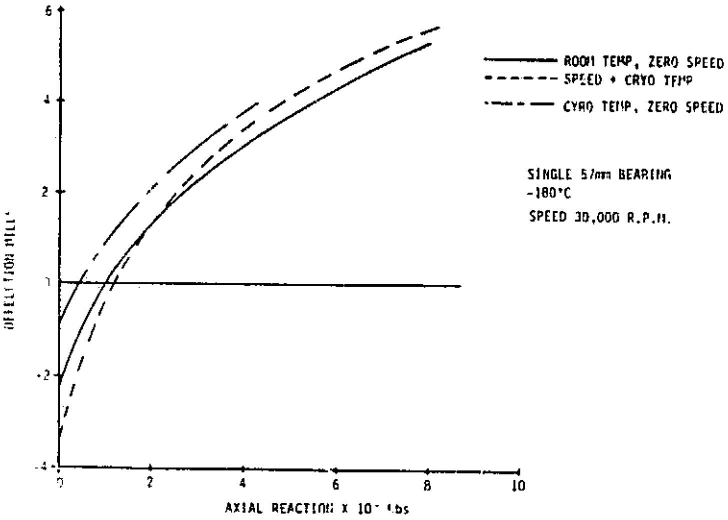

FIGURE 5.10.2 BEARING DEFLECTION Vs AXIAL REACTION

COMPONENT	MATRICE	LENGTHS (IN)	EFFECTIVE CROSS SECTIONALS AREA (102·)	$\frac{1}{F}$	ε (Psi) θ - 180°C	T·P
BEARING RACE	440C	.766	1.621	$4.86\times10^{-}$	$30.74\times10^{-}$	373
BEARING SEPERATOR	A286	.46	1.642	$6.49\times10^{-}$	$30.74\times10^{-}$	373
SPACER	A286	1.106	1.291	$6.49\times10^{-}$	$30.74\times10^{-}$	373
SEAL	K-MONEL	.86	1.853	$6.22\times10^{-}$	$26.4\times10^{-}$	373
SEAL SPACER	A286	.813	.91	$6.49\times10^{-}$	$30.74\times10^{-}$	373
NUT	K-MONEL	.4	1.362	$6.22\times10^{-}$	$26.4\times10^{-}$	373
SHAFT	WASPALLOY	5.171	2.216	$6.2\times10^{-}$	$33.89\times10^{-}$	373
SPRING	INCONNEL 718	.115	-	$6.22\times10^{-}$	$30.2\times10^{-}$	373
CARRIER TANG	INCONNEL 718	.103	-	$6.22\times10^{-}$	-	373

FIGURE 5.10.1 SHAFT/COMPONENT MATERIAL PROPERTIES AND GEOMETRY

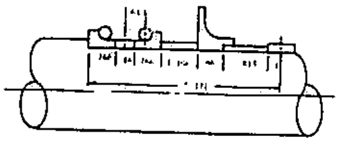

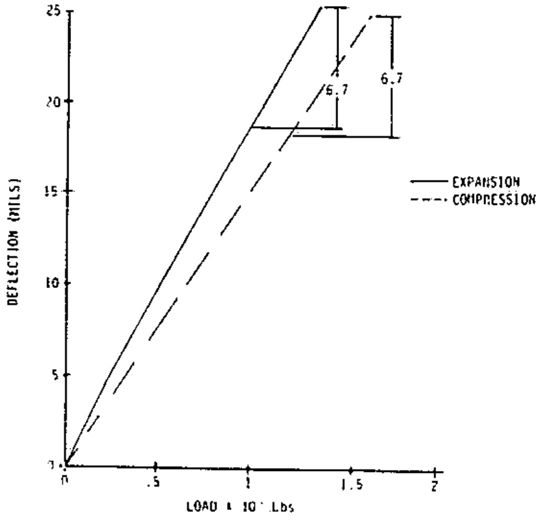

FIGURE 5.10.3 PRELOAD (BELLEVILLE) SPRING DEFLECTION Vs LOAD

2) $$d\ell_c = F_T \sum_{i=1}^{n} \frac{\ell_{ci}}{A_{ci}E_{ci}} + \sum_{i=1}^{n} \alpha_{ci}\ell_{ci}\Delta T$$

α - Thermal coefficient of expansion
A - Cross sectional area under load
E - Modulus of elasticity
F_T - Thermally induced load
ℓ - Length
s - Shaft
c - Components on the shaft

Since $d\ell_s = d\ell_c$ these equations can be solved for the thermally induced force and the axial deflections due to the temperature changes. The axial deflection of interest is the net deflection between one-half the bearing separator, one-half the bearing race, the bearing spring, and the carrier tang. Using the data provided in Figure 5.10.1, a net deflection of 0.1551 mils was estimated. This deflection is in the direction to compress the spring. Since the spring constant is between 55 and 65 lbs/mil (depending on direction of spring travel), this movement produces an insignificant change in preload.

An axial movement of the bearing can occur as a result of radial clearance changes caused by initial press fits, temperature changes, and shaft speeds. To assess these effects on bearing preload, bearing deflection curves at these different conditions were generated, as shown in Figure 5.10.2. Deflection curves are shown for three conditions; room temperature, cryogenic temperature, and cryogenic temperature and speed. As shown, fitting the bearing to the shaft causes an axial movement of the races which requires about a thousand pounds to return the races to their relative unmounted positions. Since the room temperature preload is approximately one thousand pounds, this is the initial condition from which the shaft/bearing system changes as the components are cooled down and brought up to speed. The effect of the cool down is shown, as well as the speed effect.

As indicated in Figure 5.10.2, the effect of cool down on bearing deflection is to release a small amount of preload, ~50 lbs. As shown in Figure 5.10.1, the thermal coefficient of expansion for the shaft is about 10% larger than the value for the inner race; therefore, the shaft shrinks from the inner race reducing the interference fit. This, in turn, increases the internal clearance of the bearing, allowing the outer race to move in a direction to reduce the spring preload. As the shaft reaches operational speed (30,000 RPM), the centrifugal force causes the inner race to grow, reducing the bearing internal clearance, causing the outer race to move in the direction to increase the preload. As shown in Figure 5.10.2, these are compensating effects and the operating preload is very near the room temperature value. It is important to realize that these conditions have been estimated for uniform temperature conditions (i.e., all bearing elements, shaft, and carrier are assumed to be at the same temperature). Temperature gradients across the bearing and in the bearing carrier could change these results. In addition, the spring constant is the room temperature value. Further analyses are needed to evaluate these effects.

Another factor affecting bearing preload is the preload spring hysteresis. This effect is shown in Figure 5.10.3. As shown, the spring has a different spring constant depending on the direction of travel. It is estimated that the preload value will vary about 20% depending on the direction of the spring action.

5.11 Interface Fit Between the Inner Race and Shaft

The bearing inner race is a force or interference fit on the tester shaft. This assembly is made at room temperature and the interference between the race and shaft changes as the tester is cooled to LN_2 temperature, rotated to test speed, and loaded. An analysis was done to estimate these changes at the various conditions from assembly to test.

Assuming that the assembly temperature is 20°C and the cold operating temperature is -180°C, the interference will change from 2.3 mils at room temperature to 1.2074 mils at -180°C. Rotation of the bearing shaft assembly to 30,000 per minute will reduce the interference to 0.6178 mils. A preload of 1000 lbs. will increase the interference to about 0.75 mils. Increased axial loading will "tighten" the interference of bearings 2 and 3 and loosen bearings 1 and 4. The interference for 1 and 4 will not be less than 0.6178 mils.

The above estimates are for uniform temperature of bearing race and shaft. This is not the case when bearing friction heat warms the inner race to a higher temperature than the shaft. The maximum temperature difference between the inner race and the shaft probably occurs during tester start when the heat generation, due to speed and load, is suddenly imposed on the chilled shaft and bearing. This transient condition has not been analyzed; however, a calculation was made to estimate the temperature difference between the inner race and shaft that would eliminate the interference fit. Assuming the shaft remained at -180°C, this analysis indicated about 38°C temperature difference between bearing inner race and shaft will cause the interference fit to be lost (i.e., if the inner race temperature attains an average temperature of -142°C, while the shaft average temperature remains at -180°C, the interference between inner race and shaft will be zero at 30,000 RPM and 1000 lbs axial reaction at the bearing).

Since the thermal model predicts an average temperature of only 28°C for an axial load of 2500 lbs and 30,000 RPM, there should be no problem in losing interference fit at steady operating conditions. However, as stated previously, the start transient could cause a temperature difference large enough to eliminate the interference fit for short periods of time. Although an increase in axial load tends to increase the interface pressure (between inner race and shaft), it also increases the heat generation rate. The steady conditions analyzed were for an axial load of 2500 pounds. It is expected, but not confirmed by analysis, that the increase in load will outweigh the thermal effects and the interference fit will be maintained at the higher load conditions. If the maintenance of an interference fit is critical to tester operation, a transient analysis should be done and additional higher loads investigated to verify that the interference is not lost for any possible operating condition.

The previous analyses show that the room temperature bearing preload is not significantly affected by cooling to LN_2 temperature and rotation of the shaft to 30,000 RPM. Temperature gradients across the bearing have been neglected and the temperature effect on bearing spring constant has not been included. Although the bearing internal clearances can be significantly affected, it is expected that temperature differences of less than about 150°F across the bearing will have little effect on the preload value. The temperature effect on spring constant will require further work. It should also be observed that the effect of speed is to increase the preload; therefore, at a shaft speed of 10,000 RPM, the preload will be slightly reduced (reduction will be less than ∿65 lbs.) compared to the value at 30,000 RPM.

The analyses relating the carrier load to bearing reactions shows that the unloaded bearings (1 and 4) will retain sufficient preload to prevent excess skidding and internal heat generation. It also shows that the uncertainty in bearing reaction due to preload spring hysteresis is approximately 20% maximum.

The interference fit between the inner race and shaft has been evaluated to determine the effects of temperature and speed. Although an interference is maintained at uniform operating temperatures and speed, temperature differences between the bearing inner race and shaft can be large enough to eliminate the interference. It has been estimated that interference fit will be lost at speed if the inner race temperature is greater than the shaft temperature by about 38°C. This assumes the shaft to be operating at -180°C which is a representative temperature when operating in LN_2. It presently appears that this can possibly occur only during start transients when the shaft and bearing are chilled and a sudden load and speed is imposed which heats the bearing before the shaft temperature has time to respond.

5.12 Fluid Film Thickness Analyses

5.12.1 Estimation of Film Thickness for 57 mm Bearing Operating in LN_2 and LOX

A cursory analysis was done to provide an "order of magnitude" estimate of the fluid film thickness for the 57mm bearing operating in LN_2. Although the viscosity of N_2 is over two orders of magnitude less than typical lubricating oil, the high speed of the bearing could partially compensate and provide some measure of separation of the contact surfaces. This could be an aid to the solid film lubricant in providing contact lubrication.

There are several major drawbacks in using current techniques to estimate fluid film thickness in N_2. These techniques have been developed for lubricating oils and such characteristics as compressibility, phase type, and extreme variations in temperature have not been considered. Furthermore, there is a lack of viscosity data for N_2 at the high pressures encountered in the contacts. Therefore, the error due to extrapolation to these pressures is not known. The assumption of incompressibility should provide optimistic values of film thickness. The assumed variation of viscosity with pressure (exponential law) could also be optimistic.

The results of the film thickness estimates are shown in Figure 5.12.1. As the temperature increases, the film thickness decreases rather suddenly and then levels off. The sudden decrease is characteristic of a liquid, and the leveling off is similar to the behavior of a gas whose viscosity increases with temperature. The estimate was not carried past 1000°R since viscosity for higher temperatures was not available. Figure 5.12.2 provides viscosity data at specified temperatures and pressures. Also shown are values for the pressure coefficient (λ) and μ_o'. The significance of these parameters will be discussed later. Comparing μ_o' with the viscosity values at 400 psia shows fairly good agreement at the lower and higher temperatures. Since the critical temperature of N_2 is 227°R, it is expected that the larger discrepancy at 300°R is due to rapidly changing properties near the critical point. N_2 properties were taken from Reference 35.

As shown, the film thickness varies from about 1.8μ to .03μ inches. Since the surface finish of the balls and races are 0.5μ and 6μ inches respectively, the ratio of film thickness to aspherity height varies from 0.3 to 0.05. Furthermore, thermal analyses of the bearings indicate that the race way temperatures are considerably greater than 170°R. Consequently, the film thickness to roughness ratio would be

**ORIGINAL PAGE IS
OF POOR QUALITY**

FIGURE 5.12.1 ESTIMATED FILM THICKNESS vs. TEMPERATURE FOR N_2

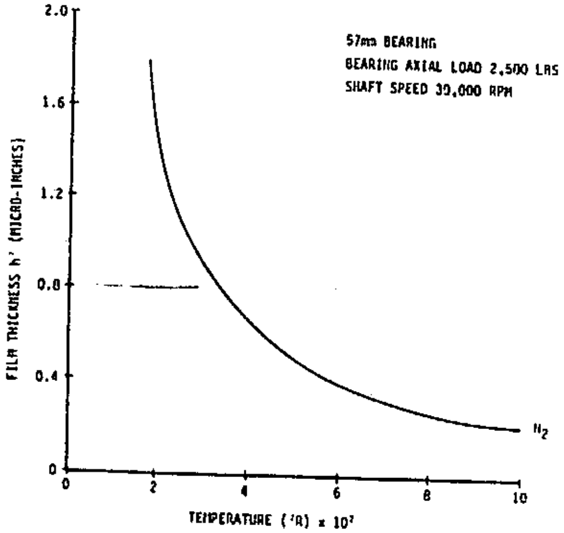

FIGURE 5.12.2 (N_2) VISCOSITY

TEMP °R \ PRESSURE PSIA	400	4000	5000	PRESSURE COEFFICIENT λ x 10-4	μ_0^* x 10-8
170	* 1.497	2.31	2.55	0.977	1.562
300	0.177	0.658	0.785	1.77	0.3242
500	0.254	0.354	0.393	1.04	0.233
1000	0.411	0.449	0.459	0.22	0.41

* VISCOSITY $\left(\mu \times 10^{-8} \quad \frac{LB - SEC}{IN^2}\right)$

FIGURE 5.12.3 O_2 VISCOSITY

Temp °R \ Pressure Psia	350	4000	5000	Pressure Coefficient λ x 10-8	μ_0^* x 10^{-8}
200	* 1.731	2.388	2.579	.769	1.756
300	.233	1.124	1.208	.721	.847
500	.305	.576	.651	1.224	12 .353
600	.345	.543	.597	.941	.373

*Viscosity $\mu \times 10^{-8} \frac{lb_f\text{-Sec}}{in^2}$

FIGURE 5.12.4 ESTIMATED FILM THICKNESS VS TEMPERATURE FOR O_2

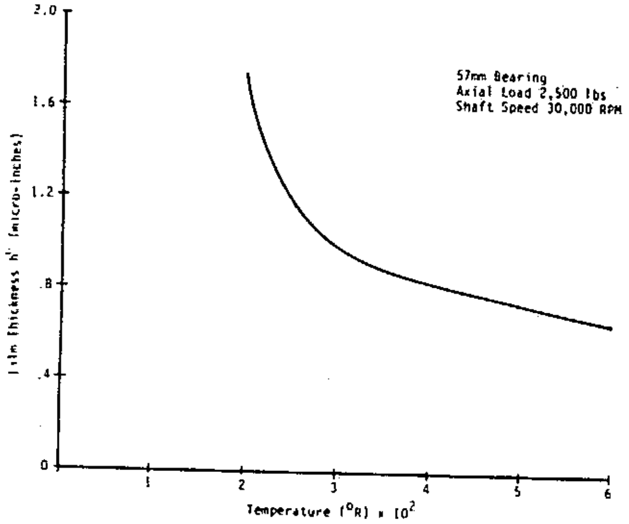

considerably less than 0.3. Bearing life adjustment factors, due to lubrication, does not adversely affect life predications for film thickness to roughness ratios less than about 4. SHABERTH I assumes dry friction for ratios less than 0.4.

Following is an outline of the method used to provide the estimated film thickness data shown in Figure 5.12.1.

Gurbin's formula for fluid film thickness is (see Reference 1):

$$h^\circ = 1.95\, R\, \frac{(G\overline{U})^{0.727}}{\overline{Q}_z^{\,0.091}}$$

$$G = \lambda E'$$

$$\overline{U} = \frac{\mu'_0 U}{E'R}$$

$$\overline{Q}_Z = \frac{Q_Z}{\ell E'R}$$

$$E' = \frac{E}{1-\nu^2}$$

(For Rolling Elements
of Same Material)

λ = Pressure Coefficient of Viscosity

μ'_0 = Fluid Viscosity as Reference Pressure

R = Equivalent Radius

U = Entrainment Velocity
$= (u_1 + u_2)/2$

E = Modulus of Elasticity

ν = Poisson's Ratio

This expression was developed from the incompressible Reynolds equation and elastohydrodynamic considerations including effects of contact surface deformation. The fluid viscosity is assumed to vary exponentially with pressure, and temperature is assumed to be constant. As given above, the expression is for line contact and must be slightly modified to represent ball bearings (point contact).

The terms in the above expressions are developed and grouped as follows:

<u>Entrainment Velocity</u>

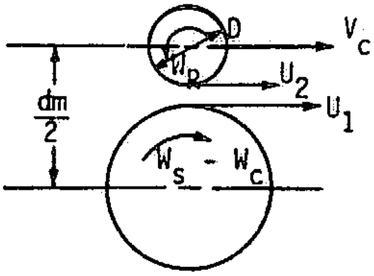

W_s = Shaft Speed

W_c = Cage Speed

α = Contact Angle

To determine the fluid entrainment velocity U refer to the above figure.

$$U_1 = 1/2\ (dm - D\mathrm{Cos}\alpha)\ (W_s - W_c)$$

$$U_2 = \frac{D}{2}\ W_R \mathrm{Cos}\alpha$$

For pure rolling, $U_1 - U_2$, and

$$U = 1/2\ (W_s - W_c) \left[\frac{1-\gamma}{\gamma}\right] D\mathrm{Cos}\alpha\ ;\quad \gamma = \frac{D}{dm}\mathrm{Cos}\alpha$$

to express W_c in terms of W_s note that the cage velocity V_c is 1/2 the absolute shaft velocity V_i, i.e.

$$V_c = 1/2\ dmW_c = 1/2\ V_i;$$

$$V_i = W_s\ (dm/2 - D/2\ \mathrm{Cos}\alpha) = 1/2\ W_s dm\ (1-\gamma)$$

$$1/2\ dmW_c = 1/2\ \ 1/2\ W_s dm\ (1-\gamma)$$

$$W_c = 1/2\ W_s\ (1-\gamma)$$

Substitution of W_c in the expression for U gives:

$$U = \frac{D}{4} W_s \left[\frac{1+\gamma}{\gamma}\right] \left[1-\gamma\right] \mathrm{Cos}\,\alpha$$

Therefore, the entrainment fluid velocity can be expressed in terms of bearing geometry, contact angle, and shaft speed.

Equivalent Radius (R):

$$R = \frac{1}{\frac{1}{R_1} \pm \frac{1}{R_2}} = \frac{R_1 R_2}{R_1 \pm R_2} = \frac{1/2D\ (1-\gamma)\ \mathrm{Cos}\,\alpha}{(1-\gamma)\ \mathrm{Cos}\,\alpha + \gamma}$$

For small values of α, Cos $\alpha \sim 1$, and

$$R = 1/2\ D\ (1 - \gamma)$$

Load Per Unit Length:

As stated earlier, the expression for Q_Z is for line contact and, for use with ball bearings, should be modified to represent point contact. The following represents the two contact configurations.

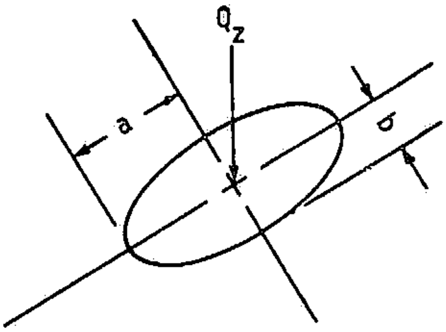

Point Contact

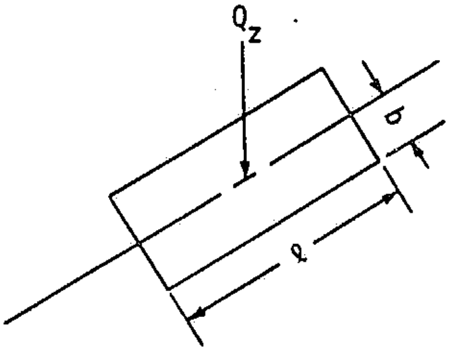

Line Contact

The maximum Hertz Pressure for point contact and line contact are as follows:

$$\sigma_{mp} = \frac{3\,Q_z}{2\pi ab} \quad \text{(Point Contact)}$$

$$\sigma_{m\ell} = \frac{2\,Q_z}{\pi \ell b} \quad \text{(Line Contact)}$$

Assuming equal Hertz pressures and loads for both contacts gives an equivalent length ℓ_E for the point contact.

$$\ell_E = \frac{4a}{3}$$

The dimensionless terms in Gurbin's equation can now be written as:

$$G = \gamma E'$$

$$\bar{U} = \frac{\mu_o'}{E'}\left[\frac{W_s}{2}\right]\left[\frac{1-\gamma}{\gamma}\right]\mathrm{Cos}\,\alpha$$

$$\bar{Q}_z = \frac{3}{2}\;\frac{Q_z}{aE'\;D(1-\gamma)}$$

$$E' = \frac{E}{1-\nu^2}$$

and Gurbin's equation can be expressed as:

$$h^\circ = 0.228\left[1/2\;D\;(1-\gamma)\right]^{1.091}\left[W_s\;\frac{1+\gamma}{\gamma}\;\mathrm{Cos}\,\alpha\right]^{.727}\left[\lambda\mu_o'\right]^{.727}\left[\frac{4aE'}{3\;Q_z}\right]^{.091}$$

where W_s = shaft speed in RPM

λ = pressure coefficient (in^2/lb)

μ_o' = viscosity ($lbs\text{-}sec/in^2$)

E' = 33×10^{-6} psi for steel bodies

This arrangement of variables illustrates the effects of speed, viscosity, and load on film thickness. The speed and viscosity parameters are raised to the same power and, therefore, are equally influential. The lower power value for the term containing the load renders the film thickness rather insensitive to load changes. Although high shaft speed can offset low fluid viscosity, the viscosity for N_2 is so low that the high speed of the tester is still insufficient to provide an adequate film thickness.

Estimation of Initial Viscosity and Pressure Coefficient (λ):

The exponential law relating viscosity to pressure used in Gurbin's equation is as follows:

$$\mu = \mu_0\,e^{\lambda P}$$

This implies that at P=0, $\mu = \mu_o$. Since the internal pressure of the bearing tester is approximately 400 psia, a correction was made to μ_o to account for this pressure level.

$$\mu = \mu_0 \, e^{\lambda(P-Po)} = (\mu o \, e^{-\lambda Po}) \, e^{\lambda P}$$

The parameter $\mu_o' \equiv (\mu_o e^{-\lambda Po})$ is used as the ambient viscosity in the film thickness expression. The pressure coefficient for each temperature level was determined as follows:

$$\lambda = \frac{1}{(P_1 - P_2)} \ln \frac{\mu_1}{\mu_2}$$

The values of μ_1, μ_2, P_1 and P_2 are shown in Figure 5.12.2. The estimated values of λ and μ_0 are also given in this figure.

A similar analysis was done to estimate the fluid film thickness for the 57mm bearing operating in oxygen. The details of the analysis are contained in the reference and will not be repeated here. The same assumptions and reservations discussed in the reference hold for this analysis. Figure 5.12.3 shows the fluid viscosity data, derived pressure coefficient, and estimated initial viscosity for O_2. Figure 5.12.4 shows the estimated fluid film thickness as a function of contact temperature. Lack of high temperature O_2 viscosity data limited the calculation to 600°R. As was shown with N_2, the film thickness for O_2 is too small to provide appreciable separation of the loaded contacts since typical surface finishes are on the order of 6μ inches.

5.12.2 Fluid Film Thickness Estimates for Material Fatigue Tester

The minimum lubricant film thickness was estimated for a material fatigue tester to investigate possible degradation of fatigue life due to loss of lubrication. The tester configuration and design characteristics are shown in Figure 5.12.5. The lubricant is MIL-L-7808G. The lubricant properties are also provided in Figure 5.12.5. The results indicate that the film thickness to roughness ratio (h/σ) is not large enough to provide full EHD boundary lubrication.

There are several correlations available in the literature for the estimation of lubricant film thickness. Dawson (1) developed the following formula to calculate minimum film thickness in a rolling contact.

$$1) \quad \frac{h}{R'_x} = 1.58(\lambda E')^{0.6} \left(\frac{\mu_o U}{E' R'_x}\right)^{0.7}$$

Grubin developed a similar formula:

$$2) \quad \frac{h}{R'_x} = 1.87 \left[\left(\frac{\lambda \mu_o U}{R'_x}\right)\right]^{.7} \Big/ \left[\left(\frac{w}{E' R'_x}\right)\right]^{.091}$$

FIGURE 5.12.5 TESTER CONFIGURATION AND LUBRICANT PROPERTIES

CALCULATED CONTACT GEOMETRY
a = .0162 IN
b = .0129 IN

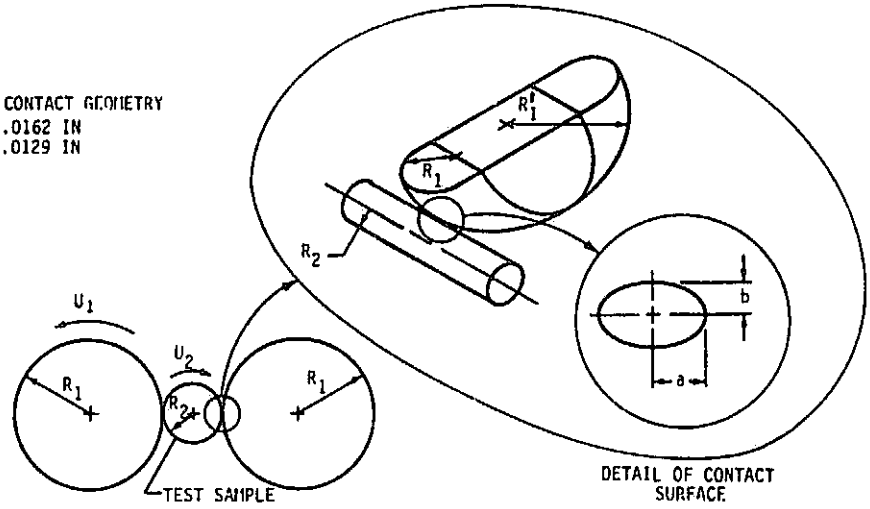

SPEED 10,000 RPM
LOAD 326 lbs
ESTIMATED CONTACT STRESS (MAX) = 737,000 psi

LUBRICANT TYPE	VISCOSITY $LBS\text{-}SEC/IN^2$	THERMAL CONDUCTIVITY $LBS/SEC^{\circ}R$	PRESSURE VISCOSITY EXPONENT* (IN^2/LB)
MIL-L-7808G	1.77×10^{-6}	.0189	1×10^{-4}

* DATA FOR MIL-L-7808G NOT AVAILABLE - ESTIMATED BY COMPARISON WITH LUBRICANTS OF SIMILAR VISCOSITY

FIGURE 5.12.6 LUBRICANT PROPERTIES*

MEAN PARAMETER	MIL-L-7808G	TYPE II ESTER	FLUOROCARBON	POLYPHENGLEITHER	SYNTHETIC PARAFFINIC
k_j^*	?	10.7	30.6	3950	43.8
$\hat{n}_j$	?	0.6	0.61	0.83	0.66
PROPERTIES					
VISCOSITY C.S.	12.8	29	298	358	443
DENSITY (gm/cm^3)	.9526	.85	1.59	1.05	.74
VISCOSITY $\left(\frac{lbs\text{-}sec}{in^2}\right)$	1.7686×10^{-6}	3.57x10-6	6.87×10^{-5}	5.45×10^{-5}	4.75×10^{-5}

* ALL PROPERTIES EXCEPT FOR MIL-L-7808G TAKEN FROM REF. 43

$R'_x = \frac{1}{R_1} + \frac{1}{R_2}$

λ = Viscosity pressure coefficient (in^2/lb)

μ = Ambient viscosity $\left(\frac{lbs - sec}{in^2}\right)$

U = Entrainment velocity = $\frac{U_1 + U_2}{2}$ (in/sec)

$W = \frac{W_T}{4/3a}$ = Load per unit length (lbs/in)

W_T = Contact surface load (lbs)

a = Semi major axis of contact ellipse (in)

$E' = \frac{2E}{\pi(1-\nu^2)}$ Assumes properties of wheel and roller to be equal

E = Modulus of elasticity (lbs/in^2)

ν = Poisson's ratio

The above relationships are for isothermal conditions. H. S. Cheng (42) developed a Grubin type inlet film thickness analysis including the thermal effects. The results of this work yield correction factors to the isothermal film thickness estimates as follows:

3) $$h_{min} = \emptyset_T \cdot \emptyset_s \cdot h_{min} \text{ (isothermal)}$$

$\emptyset_t$ is a reduction factor to account for the thermal effects on the lubricant and $\emptyset_s$ is a factor to account for side leakage in the contacts. Based on the lubricant properties, contact geometry, and entrainment velocity, these factors were estimated as follows:

$\emptyset_T = 0.87$

$\emptyset_s = 0.9$

Dawson's film thickness formula can be adjusted to account for thermal and side leakage as follows:

4) $$\frac{h_{min}}{R'_x} = 1.237\,(\lambda E')^{.6}\,\frac{\left[\frac{\mu_o U}{E'R'_x}\right]^{0.7}}{\left[\frac{W}{E'R'_x}\right]^{.13}}$$

A similar adjustment can be made to Gurbin's formula. The minimum film thickness estimated from equation 4 is 3.5μ inches. Gurbin's formula, including the reduction factors, provides a minimum film thickness of 6.2μ inches. The difference is due primarily to the differences in exponents assigned to the load terms in the two equations.

To further investigate the validity of these estimates, data from Reference (43) were compared with the above film thickness estimates. Figure 5.12.6 gives the lubricants tested and experimental correlation factors determined from the tests. As shown, the type II Ester has viscosity values closest to the MIL-L-7808G lubricant.

The film thickness data from reference 43 was correlated with the following formula.

$$5)\quad \frac{h_{min}}{R'_{x}} = \left[K^{*}_{J}\,\bar{U}\,\hat{n}_{J}\,\bar{P}_{HZ}^{(-.22)}\right]_{s}$$

ρ_s is a reduction factor for high stress conditions. These test data did not include stress conditions greater than 350ksi. Since the test fixture is stressed to 700ksi, a value of ρ_s could not be obtained directly from the test data. An optimistic value would be 0.5 which corresponds to a Hertz stress of 350ksi.

Using the correlation factors for type II Ester and the MIL-L-7808G fluid properties, the estimated film thickness from equation 5 is, 1.375μ inches.

The surface roughness for the sample and wheels were given as:

TEST SAMPLE	4μTO 8μ INCHES
WHEEL	6μ INCHES

The combined RMS surface roughness is therefore:

$$\sigma = \sqrt{(8\mu)^2 + (6\mu)^2} = 10\mu \text{ inch}$$

The results of the previous analysis are summarized below:

CORRELATION	MINIMUM FILM THICKNESS μ INCHES	FILM THICKNESS TO ROUGHNESS RATIO h/σ
Dawson	3.5	.35
Gurbin's	6.2	.62
Eq 5	1.4	.14

According to Reference (42), if h/σ >4, thick EHD film exists and the lubrication should be satisfactory. If 1> h/σ <4, partial EHD film exists and lubrication is most likely satisfactory but may deteriorate when h/σ approaches unity. If h/σ <1, lubrication is marginal and operation in this region is in general not recommended without boundary lubrication additives. Pitting, scoring and progressive wear are likely to occur.

5.13 Effect of Friction on Rolling Element Contact and Subsurface Stresses

The effects of friction on the magnitude and distribution of normal and shear stresses in rolling element contacts has been investigated. Reference 37 contains general expressions for the normal and sheer stresses for rolling elements producing line contact. Line contact allows the stress problem to be solved in closed form by the application of plane stress and plain strain assumptions. Although these assumptions do not hold for point contact, the trends identified in the line contact solutions should apply.

The effect of surface friction on the location of the maximum shear stress was determined by solving for shear stress and setting the derivative to zero. Figure 5.13.1 shows the results. As shown, the location of the maximum shear stress along the axis in the rolling direction (x axis) is a function of the coefficient of friction. Also shown is the expression of the maximum surface shear (T_{max}) as a function of friction. The maximum shear stress for zero friction occurs at a subsurface depth of ($z/a = 0.7861$), and the stress ratio is 0.3. This point is shown on the vertical axis of Figure 5.13.1. As shown in the figure, the maximum shear stress moves to the surface for friction factors greater than 0.19.

Shown in Figure 5.13.2 are the maximum surface principal stresses. As shown, these are all compressive stresses and occur in the surface as a function of the friction factor. The maximum tensile surface stress is shown in Figure 5.13.3, and occurs at ($-x/a=1$) in the contact surface.

This analysis shows that the magnitude and location of the maximum contact stresses can be significantly affected by the friction force in the contact surface. Since these stresses increase with increased friction, this effect can be especially important for rolling elements with marginal lubrication such as high speed bearings operating in cryogenics. These trends may help explain the surface failures observed in cryogenic bearing tests as opposed to the more common subsurface failures observed in well lubricated bearings.

This analysis has been restricted to line contact, a similar analysis for point contact requires evaluation of a three dimensional stress field and can best be handled by finite element computer codes.

5.14 Effects of Bearing Race Curvature and Diametral Clearances on Operating Characteristics

The LOX turbopump turbine end bearing has been evaluated to investigate the effects of increased inner race curvature and increased diametral clearance on various operating characteristics.

Figure 5.14.1 provides the friction heat generated per bearing pair as a function of radial reaction. The three curves shown represent different bearing parameters that were analyzed. The solid line curve represents a diametral clearance of .0036 inches, with a bearing contact angle of 19.95 degrees. The inner and outer race curvatures being 0.53. The alternating long and short dashed line is for a bearing with a diametral clearance of .0063 inches, a contact angle of 22.89 degrees and inner and outer race curvatures of 0.55 and 0.53 respectively. The dashed line represents a bearing having a diametral clearance of .0059, a contact angle of 22.14 degrees and inner and outer race curvatures of 0.55 and 0.53 respectively.

This analysis was performed using a shaft speed of 30,000 RPM and a friction coefficient of 0.20. The bearing component temperatures were assumed to be initially at -153°C, the temperature of liquid oxygen. A complete thermal analysis would be necessary to determine the appropriate bearing component temperatures. A 1000 pound preload was also placed on each bearing of the pair modeled.

Figure 5.14.2 illustrates the frictional heat generated at the inner and outer races per bearing pair. The frictional heat represented in Figures 5.14.1 and 5.14.2 would likely be more severe if the temperature distribution in the bearing were accounted for.

FIGURE 5.13.1 MAXIMUM SURFACE SHEAR STRESS AS FUNCTION OF FRICTION COEFFICIENT (LINE CONTACT)

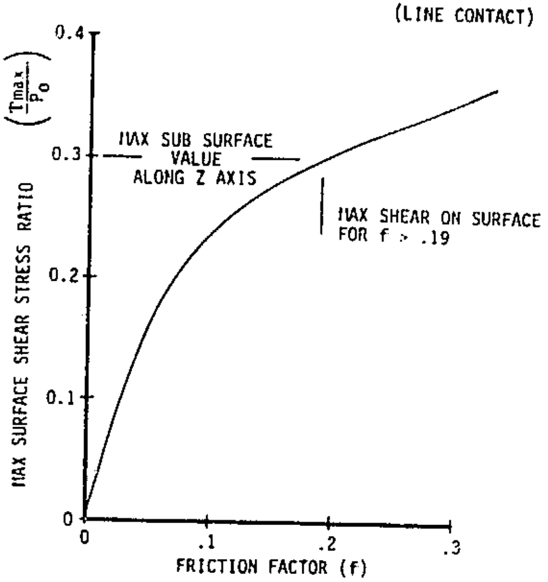

a = HALF WIDTH OF CONTACT AREA

P = NORMAL LOAD PER UNIT LENGTH

MAX SURFACE SHEAR OCCURS AT

$$\left(\frac{x}{a}\right) = f\sqrt{\frac{1}{1+f^2}}$$

$$\frac{T_{max}}{P_o} = (.2)\left[\sqrt{1+f^2} + 2.5f\right]$$

$$P_o = \frac{2P}{\pi a}$$

COORDINATE SYSTEM

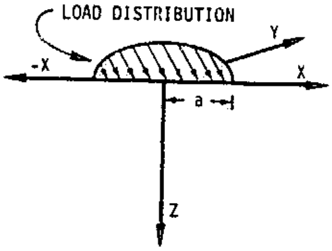

FIGURE 5.13.2 MAXIMUM PRINCIPAL STRESSES IN SURFACE vs FRICTION (LINE CONTACT)

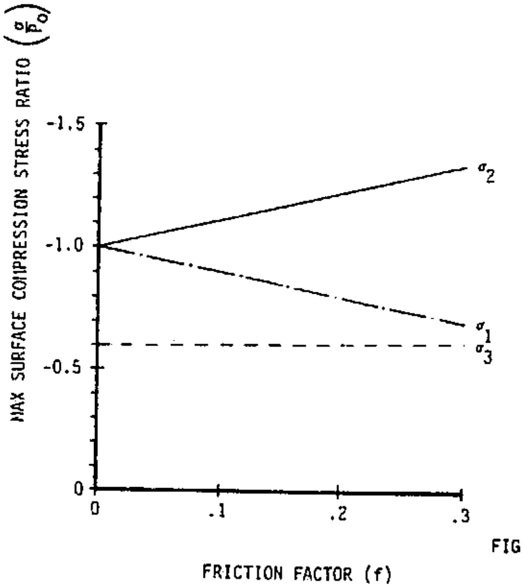

MAX STRESSES OCCUR AT:

$$\left(\frac{x}{a}\right) = f\sqrt{\frac{1}{1+f^2}}$$

$$P_o = \frac{2P}{\pi a}$$

FIGURE 5.13.3 MAXIMUM TENSILE SURFACE STRESS vs FRICTION (LINE CONTACT)

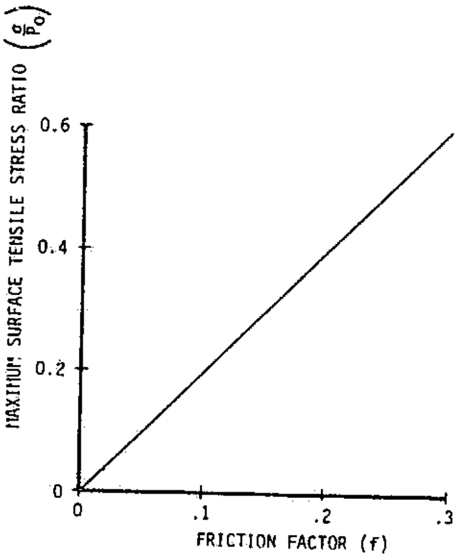

MAX STRESSES OCCUR AT:

$$\left(\frac{x}{a}\right) = -1$$

$$\sigma_1 = 2(P_o)f$$

$$P_o = \frac{2P}{\pi a}$$

FIGURE 5.14.1

TOTAL FRICTIONAL HEAT GENERATED - VS - RADIAL REACTION

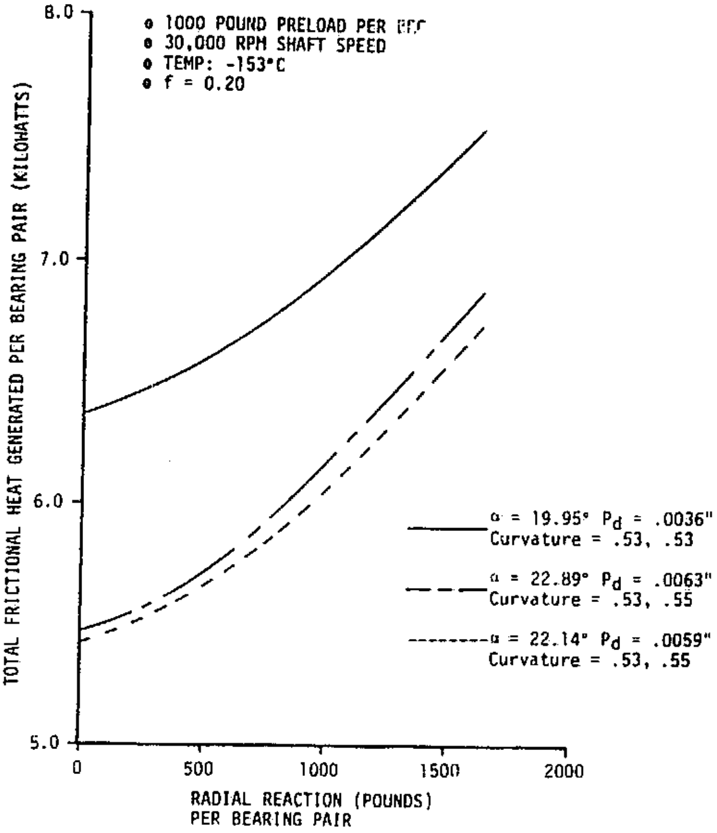

FIGURE 5.14.2

FRICTIONAL HEAT GENERATED AT INNER & OUTER RACE PER BEARING PAIR - VS - RADIAL REACTION

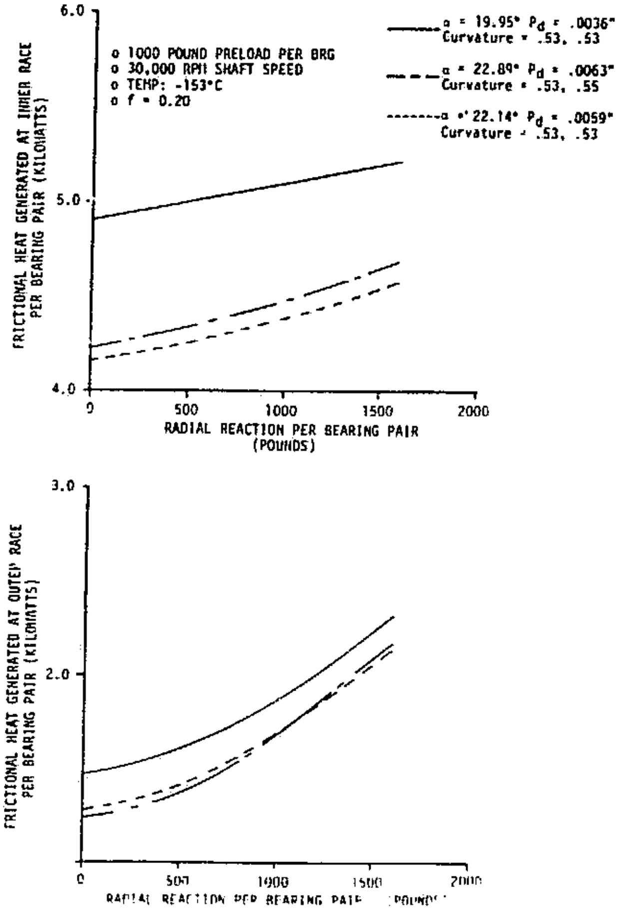

The maximum stress in the contact area as a function of radial reaction is shown in Figure 5.14.3. It can be seen that these stresses increase as the radial load increases, as would be expected. The two cases in which the inner and outer race curvature are 0.55 and 0.53 respectively appear to increase linearly and tend to coverage upon each other as the radial load increases. The control case (solid line) shows a non-linear increase as a function of radial reaction.

Figure 5.14.4 and 5.14.5 represent the minimum inner and outer contact angles as a function of radial loading. As shown in Figure 5.14.4, the inner contact angle decreases nonlinearly as the radial reaction increases. Figure 5.14.5 illustrates the linear decrease of the outer contact angle as the radial reaction increases. Also shown are the effects of the proposed design changes in curvature and clearances on operating contact angles.

The loss of internal or operating clearance as a function of radial reaction is represented in Figure 5.14.6. As shown, there is minimal reduction in clearance over the range of 0 to 2000 pounds radial reaction per bearing pair. Although the unmounted radial clearance change is 64% (current clearance = 3.6 mils; modified = 5.9 mils), the operating clearance change is ~112%.

Figure 5.14.7 illustrates the effects of race curvature and diametral clearance on bearing stiffness. The control case, with the smallest clearance, smallest contact angle and inner and outer race curvatures of 0.53 produces the least deflection and is therefore the stiffest case. The case with the next larger diametral clearance of .0059", and inner and outer curvatures of 0.55 and 0.53 respectively displays the next lowest deflection with the largest clearance case having the most bearing deflection. The stiffnesses are calculated to be 1.25 x 10^6 lbs/in for the control case (P_d - .0036"), 1.053 x 10^6 lbs/in for the case in which the diametral clearance is .0059" and 9.756 x 10^5 lbs/in for a clearance of .0063". The effects of including the bearing component temperature distribution due to thermal/mechanical interaction of the bearing would tend to reduce clearances and probably result in a stiffer bearing system than represented in Figure 5.14.7.

5.15 Estimate of Cage Forces Caused by Uneven Ball Wear for Turbopump 2309R1 Turbine End Bearing

An analysis was conducted to estimate the cage loads of the #3 bearing in HPOTP 2309R1 when the webbing between the #1 and #13 pockets failed. In this analysis, the cage loads were assumed to be caused by uneven ball wear. Potential inertia forces caused by rotating radial loads and ball/cage transient interactions were not considered. The objective was to determine if quasi-steady loads introduced by uneven ball wear could be severe enough to explain the cage failure. The ball wear measured after disassembly is shown in Figure 5.15.1.

The large variance in ball diameter measured (.499 in to .487 in) prevented a straight forward use of the Shaberth computer program because the equilibrium equations, as coded in Shaberth, use a constant diameter ball throughout the bearing. Therefore each ball had to be simulated separately taking into account the effect of the other, different size balls in the bearing. This was done by assuming that the largest ball in the bearing (D = .499 in) controlled the spacing between the inner and outer races, i.e., the bearing contains perfectly stiff races. This means that the free contact angle based on the largest diameter ball is used (D = .499 in, ALPHA = 23.168). This contact angle accounts for the increased diametral clearance caused by wear of the largest ball (twice the .001 in wear). When smaller balls are in the

FIGURE 5.14.3

MAXIMUM HERTZ STRESS - VS - RADIAL REACTION

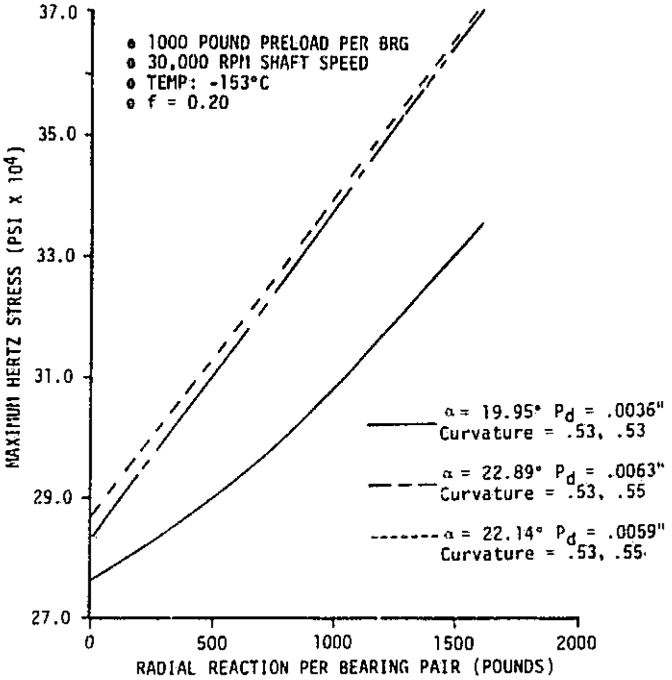

FIGURE 5.14.4

MINIMUM INNER CONTACT ANGLE - VS - RADIAL REACTION

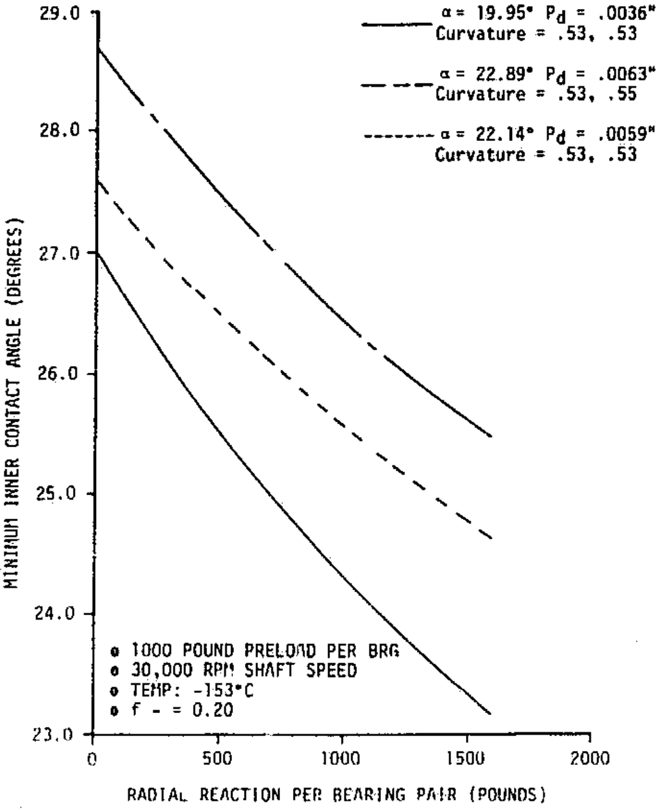

FIGURE 5.14.5

MINIMUM OUTER CONTACT ANGLE - VS - RADIAL REACTION

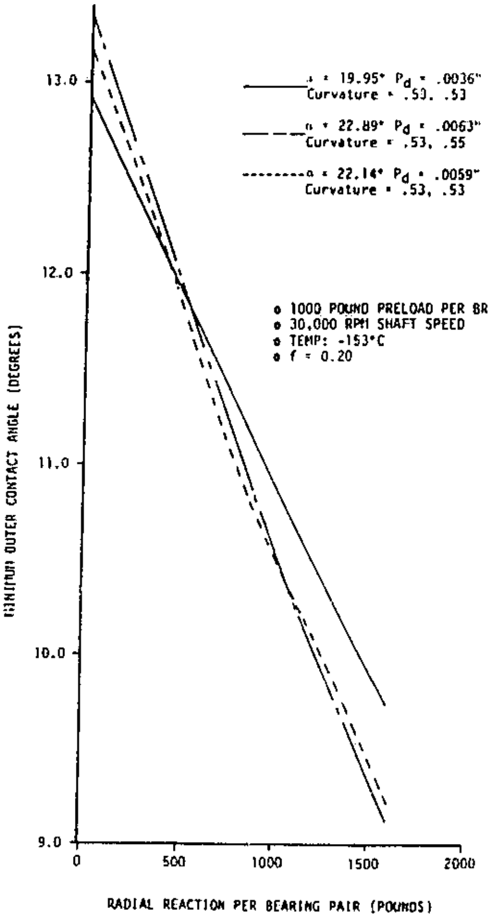

FIGURE 5.14.6

OPERATING CLEARANCE - VS - RADIAL REACTION

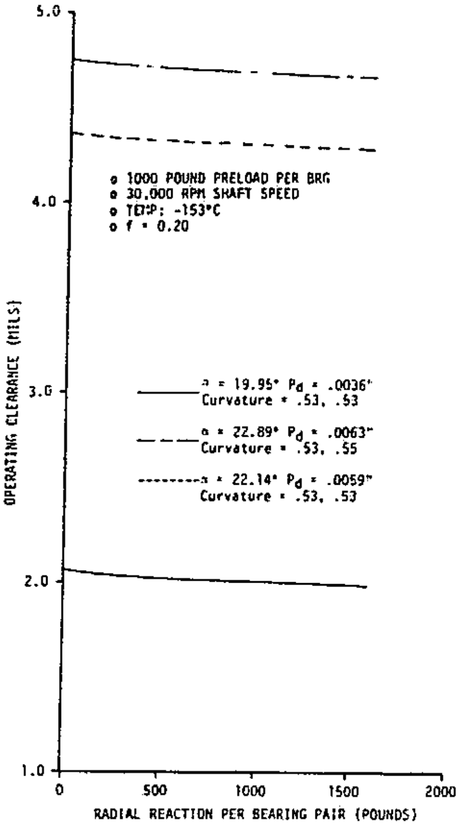

FIGURE 5.14.7 EFFECTS OF RACE CURVATURE & DIAMETRICAL CLEARANCES ON BEARING STIFFNESS

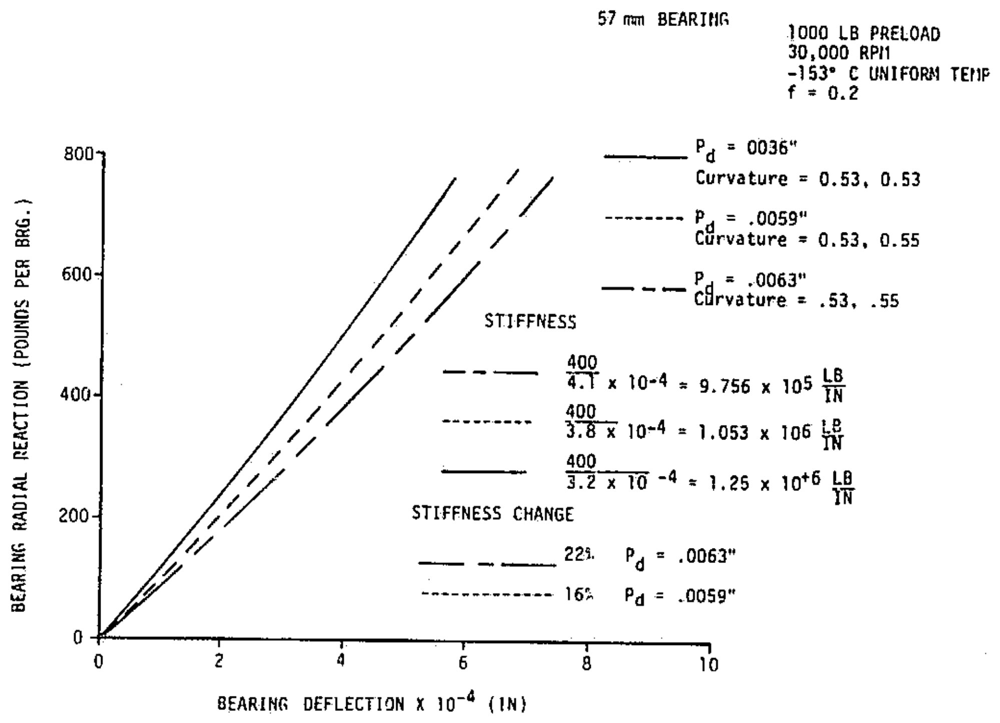

FIGURE 5.15.1 MEASURED BALL WEAR FROM FAILED BEARING
NUMBERS IN PARENTHESES ARE AVERAGES BETWEEN ADJACENT BALLS

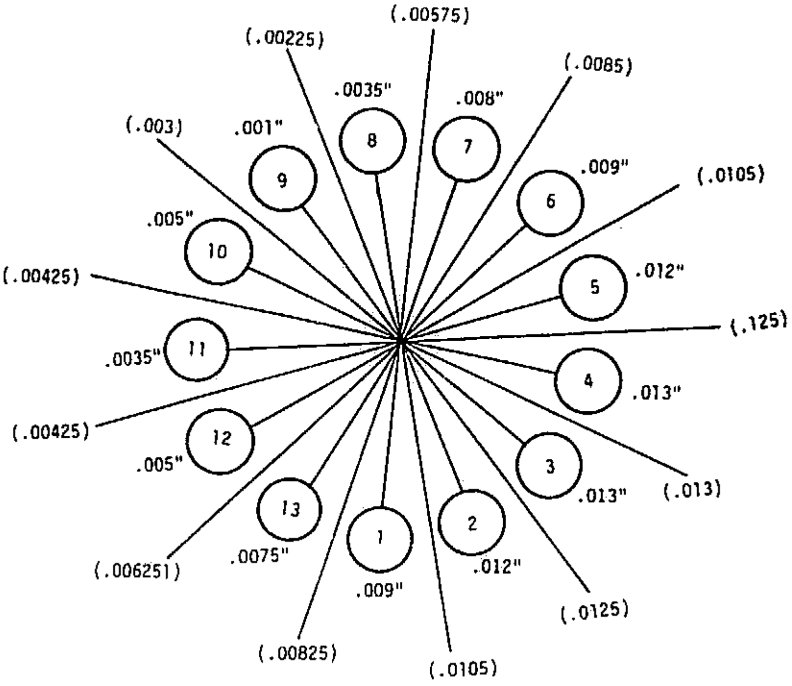

TO DETERMINE THE RELATIVE RADIAL CLEARANCE FOR BALL #3 ;

Diametral clearance for #3 (.013" + .003" = .016")	.016"
- Radial Play accounted for by largest ball (2 x .001 = .002")	-.002"
'Relative Radial Play' associated with ball #3	.014"

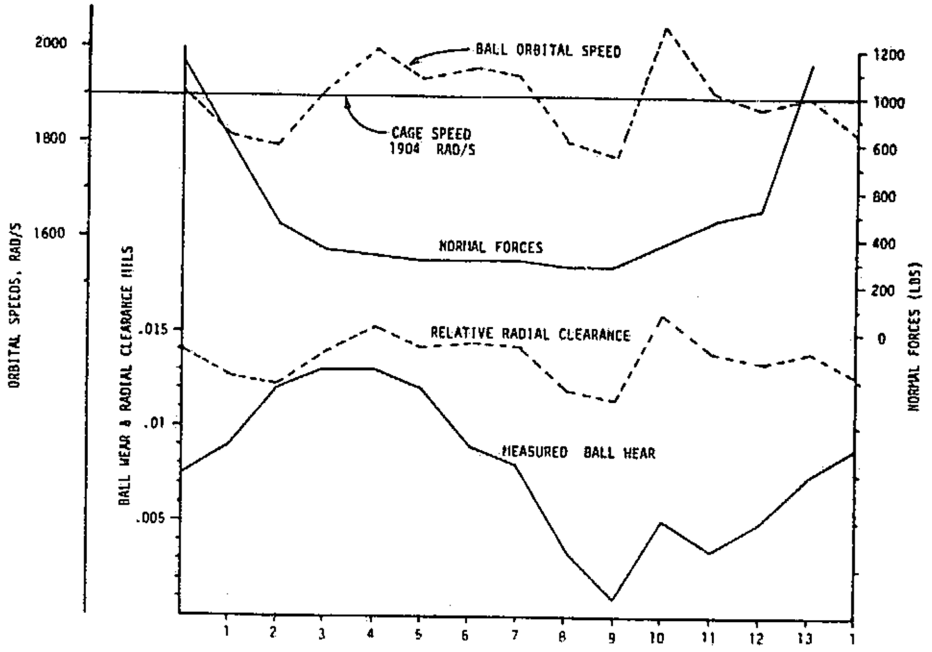

FIGURE 5.15.2 BEARING CHARACTERISTICS AS FUNCTION OF TEST BALL NUMBER

bearing with the largest, there is increased diametral clearance associated with each smaller ball. The difference between this clearance for each smaller ball and the clearance accounted for in the contact angle of the largest ball is considered to be radial play in the Shaberth input data. Figure 5.15.1 shows how this relative radial play is determined for ball #3. Figure 5.15.2 compares this clearance with the measured ball wear.

Figures 5.15.3 and 5.15.4 show the data generated when each ball (simulated by its radial play) was run with an 850 lb radial load and an 1000 lb axial preload. Normal forces and orbital speeds for each azimuth location are calculated and these are taken to be the values for a particular worn ball at different ball positions around the bearing. Therefore, from these tables, the complete bearing can be constructed at various orientations. Marked on the tables are the values for the normal forces and the orbital speeds when ball #13 is directly underneath the load. The normal forces and orbital speeds for this orientation are plotted in Figure 5.15.2.

Figure 5.15.5 shows the ultimate force required to break the cage at the minimum cross-section as a function of temperature. The tension force required to break the cage was taken, from this chart, to be approximately 2100 lbs. The use of this value assumes that, at the minimum cross-section, the cage webbing would be running at a relatively low temperature (-100°F) for the following reasons;

(1) The balls contact the cage only on the pocket sides in the direction of rotation, not on the webbing.

(2) The cage material is a fairly good insulator so that much of the heat generated at the contact would not be conducted around to the webbing, but would be carried away by the LOX flowing across the cage.

The cage speed shown in Figure 5.15.2 (1904 RADS/SEC) was estimated to be that speed which gave the lowest net force on the cage. Since all the balls are actually travelling at the cage speed, the plot of the orbital speeds for each ball provides an indicator of which balls are pushing the cage and which are being pulled by the cage. The force exerted on the cage pockets is then equal to the friction force between the balls and the races that must be overcome if slip is to occur. This same orientation is shown again in Figure 5.15.6. The arrows on Figure 5.15.6 show the direction of the friction forces on the cage pockets. This configuration was chosen first because it should give the largest tension force on the pocket that failed. However, as shown, even if all the dragging balls were segregated from those pushing the cage, the resultant force on the cage (491 lb) would not be enough to cause the failure.

Another orientation is shown in Figure 5.15.7, where the ball with the highest relative radial clearance (#10) is beneath the load. The worst cage force in this case is 623 lbs and this is also not enough to cause failure.

In summary, the model used here does not predict a cage failure due to quasi-steady loads induced by uneven ball wear. It appears that there is an unstable dynamic interaction between the balls and the cage that is not addressed by the quasi-steady state analysis described herein, which produces considerably higher loads resulting in the cage failure. An estimate of these forces would require a detailed dynamic analysis of the cage/ball system.

FIGURE 5.15.3

SUM OF NORMAL FORCES ON INNER AND OUTER RACE, LB

TEST BALL #	RELATIVE RADIAL CLEARANCE IN	Ball Position With Respect To Maximum Radial Load												
		1	2	3	4	5	6	7	8	9	10	11	12	13
1	.01275	1095	806	464	339	297	283	280	280	283	296	339	464	►806
	.01225	1077	799	461	334	291	276	273	273	276	291	334	►461	799
3	.014	1145	824	473	351	313	302	301	301	302	313	►351	473	824
4	.01525	1173	838	486	368	332	324	325	325	324	►332	368	486	838
5	.01425	1138	821	475	354	316	306	305	305	►306	316	354	475	821
6	.0145	1147	825	477	357	320	310	309	►309	310	320	357	477	825
7	.01425	1138	821	475	354	316	306	►305	305	306	316	354	475	821
8	.012	1060	788	456	331	288	►273	269	269	273	288	331	456	788
9	.0115	1068	795	456	327	►283	267	263	263	267	283	327	456	795
10	.016	1216	859	498	►380	347	341	343	343	341	347	380	498	859
11	.014	1145	824	►473	251	313	302	301	301	302	313	351	473	824
12	.0135	1128	►816	467	345	305	294	292	292	294	305	345	467	816
13	.014	►1145	824	473	351	313	302	301	301	302	313	351	473	824

AXIAL LOAD = 1000 LB $\alpha = 23.168^0$
RADIAL LOAD = 850 LB d = .499"

RESULTS FROM SHABERTH ANALYSIS OF FAILED BEARING

FIGURE 5.15.4

BALL ORBITAL SPEEDS, RAD / SEC

TEST BALL #	RELATIVE RADIAL CLEARANCE (LN)	Ball Position With Respect To Maximum Radial Load												
		1	2	3	4	5	6	7	8	9	10	11	12	13
1	.01275	1817	1817	1820	1825	1832	1839	1843	1843	1839	1832	1825	1820	1817◂
2	.01225	1790	1790	1793	1798	1805	1811	1815	1815	1811	1803	1798	1793◂	1790
3	.014	1904	1905	1908	1914	1921	1928	1932	1932	1928	1921	1914◂	1908	1905
4	.01525	1980	1980	1983	1989	1996	2004	2008	2008	2004	1996◂	1989	1983	1980
5	.01425	1913	1914	1917	1922	1930	1937	1941	1941	1937◂	1930	1922	1917	1914
6	.0145	1929	1930	1933	1939	1946	1953	1957	1957◂	1953	1946	1939	1933	1930
7	.01425	1913	1914	1917	1922	1930	1937	1941◂	1941	1937	1930	1922	1917	1914
8	.012	1783	1783	1786	1793	1798	1805◂	1809	1809	1805	1798	1792	1786	1783
9	.0115	1758	1759	1762	1767	1773◂	1780	1784	1784	1780	1773	1767	1762	1759
10	.016	2041	2042	2045	2051◂	2059	2066	2071	2071	2066	2059	2051	2045	2042
11	.014	1904	1905	1908◂	1914	1921	1928	1932	1932	1928	1921	1914	1908	1905
12	.0135	1874	1874◂	1877	1883	1890	1896	1901	1901	1896	1890	1883	1877	1874
13	.014	1904◂	1905	1908	1914	1921	1928	1932	1932	1928	1921	1914	1908	1905

AXIAL LOAD = 1000 LB $\alpha = 23.168°$
RADIAL LOAD = 850 LB d = .499"

RESULTS FROM SHABERTH ANALYSIS OF FAILED BEARING

ORIGINAL PAGE IS
OF POOR QUALITY

FIGURE 5.15.5 ULTIMATE FORCE VS TEMPERATURE
57 MM BEARING CAGE
GLASS FABRIC REINFORCED TEFLON - TFE WITH FABRIC

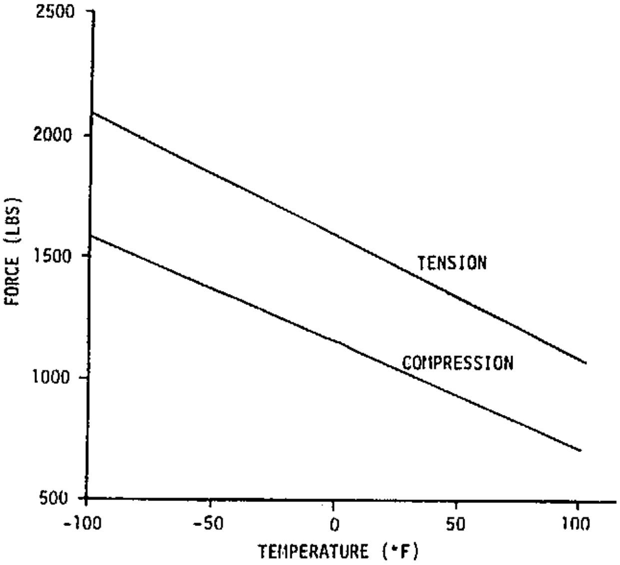

FIGURE 5.15.6 RADIAL LOAD DIRECTION PASSING THROUGH BALL # 13

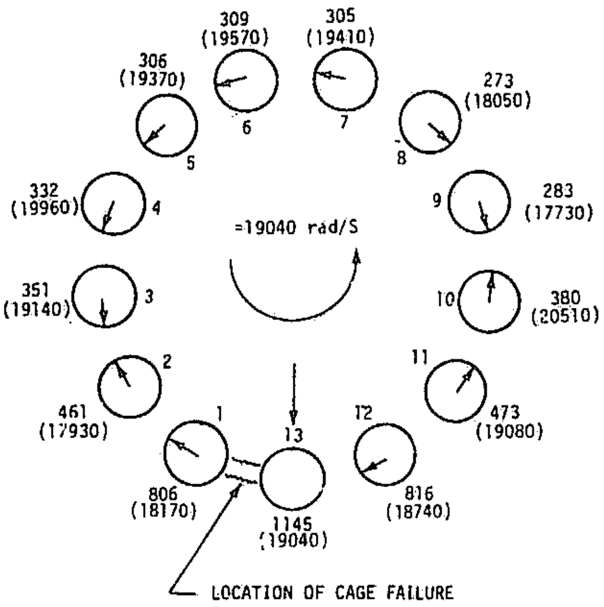

FORCE ON CAGE OF DRAGGING BALLS = (2639.).2 = 528 lb

FORCE ON CAGE OF PUSHING BALLS = (2456).2 = 491 LB

*ASSUMED FRICTION COEFFICIENT

FIGURE 5.15.7 RADIAL LOAD DIRECTION PASSING THROUGH BALL #10

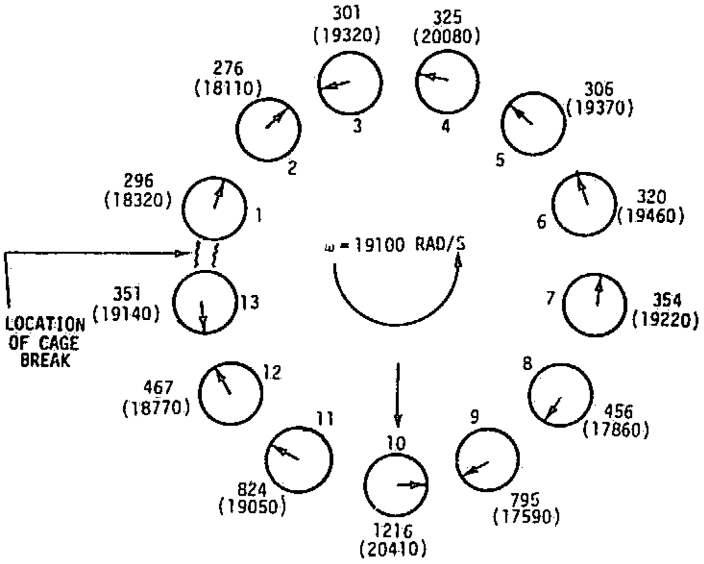

FORCE ON CAGE OF DRAGGING BALLS = (3114).2* = 623. LB

FORCE ON CAGE OF PUSHING BALLS = (3173).2 = 635. LB

*ASSUMED FRICTION COEFFICIENT

6.0 REFERENCES

1) "Rolling Bearing Analysis" by T. A. Harris, John Wiley & Sons, 1966.

2) NASA Report No. 793, "Experiments on Drag of Revolving Disks, Cylinders, and Streamline Rods at High Speeds", by T. Theodorsen and A. Regier.

3) Tallian, T. E., "On Competing Failure Modes in Rolling Contact", ASLE Transactions, 418-439, 1967.

4) Lundberg, G. and Palmgren, A., "Dynamic Capacity of Rolling Bearings" Acta Polytechnica, Mechanical Engineering Series 1, R.S.A.E.E., 403,7 (1947).

5) Tallian, T. E., "Weibull Distribution of Rolling Contact Fatigue Life and Deviations Therefrom". ASLE Transactions 5, 183-196, 1962.

6) Bambeger, E. N., Harris, T. A., "Life Adjustment Factors for Ball and Roller Bearings". ASME United Engineering Center, 345 East 47th Street, New York, NY 1971.

7) Weibull, W., "A Statistical Distribution Function of Wide Applicability", J. Applied Mechanics 18:293.

8) Chiu, Y. P., Tallian, T. E. and McCool, J. I., "An Engineering Model of Spalling Fatigue Failure in Folling Contact", the Subsurface Model, Wear, 17(1971) 433-446.

9) Tallian, T. E., "An Engineering Model of Spalling Fatigue Failure in Folling Contact", Engineering Discussion and Illustrative Examples, Wear 17(1971) 463-480.

10) Tallian, T. E., "The Theory of Partial Elastohydrodynamic Contacts", Wear 21(1972).

11) Tallian, T. E., and McCool, J. I., "An Engineering Model of Spalling Fatigue Failure in Rolling Contact" the Subsurface Model Wear 17(1971) 447-461.

12) Liu, J. Y., Tallian, T. E., and McCool, J. I., "Dependence of Bearing Fatigue Life on Film Thickness to Surface Roughness Ratio", ASLE Preprint 74 am - 7B-1, Presented May 1974.

13) Soda, N. and Yamomoto, T., "Effects of Tangential Traction and Surface Roughness on Mating Roller of CR-MO Steel on Rolling Fatigue Life of 0.45% Carbon Steel.

14) Lieblein, J. and Zelen, M., Statistical Investigation of the Fatigue Life of Deep-Groove Ball Bearings, Journal of Research of the National Bureau of Standards, Volume 57, No. 5, November 1956.

15) Hady, W. F., Allen, G. P., Johnson, R. L., "Boundary Lubrication Characteristics of a Typical Bearing Steel in Liquid Oxygen" NASA TN D-1580.

16) Barron, R. F.: Film Boiling of Liquid Nitrogen on a Sphere in an Enclosure. Adv. in Cryogenic Engng. 23, 305-213 (1978).

17) Berenson, P. J.: Film-Boiling Heat Transfer from a Horizontal Surface, ASME Trans., Journal of Heat Transfer, 83, Series C. No. 3, 351-358 (1961).

18) Bergles, A. E., et. al.: Two Phase Flow and Heat Transfer in the Power and Process Industries, Hemisphere Publ. Comp., (1981).

19) Burton, R. A., Staph, He. E.: Thermally Activated Seizure of Angular Contract Bearings, ASLE Trans. 10, 408-417 (1967).

20) Ellerbrock, H., Liningood, J. N. B., Straight, D. M.: Fluid Flow and Heat-Transfer Problems in Nuclear Rockets - NASA SP-20, pp 27-57.

21) Frost, Walter (ed.): Heat Transfer at Low Temperatures. Plenum Press, N.Y., N.Y., (1975).

22) Giarratano, P. J.; Smith, R. V.: Comparative Study of Forced Convection Boiling Heat Transfer Correlations for Cryogenic Fluids., Adv. in Cryogenic Engng. 11, 492-506 (1966).

23) Hendricks, R. C.; Graham, R. W.; Hsu, Y. Y.; Friedman, R.: Experimental Heat Transfer and Pressure Drop of Liquid Hydrogen Flowing Through a Heated Tube, NASA TN D-765.

24) Hendricks, R. C.; Graham, R. W.; Hsu, Y. Y.; Friedman, R.: Experimental Heat Transfer Results for Cryogenic Hydrogen Flowing in Tubes...; NASA TN D-3095.

25) Hendricks, R. C.; Papell, S. S.: Estimating Surface Temperature in Forced Convection Nucleate Boiling - A Simplified Method., Adv. in Cryogenic Engng 23, 301-304 (1978).

26) Hetsroni, Gad (ed): Handbook of Multiphase Systems, Hemisphere Publ. Corp., (1982).

27) Hsu, Y. Y.: A Review of Film Boiling at Cryogenic Temperatures, Adv. in Cryogenic Engng. 17, 361-381 (1972).

28) Hsu, Y. Y.; Cowgill, G. R.; Hendricks, R. C.: Mist-Flow Heat Transfer Using Single-Phase Variable-Property Approach, NASA TN D-4149.

29) Kosky, Philip G.: Studies in Boiling Heat Transfer to Cryogenic Liquids., University of California, Berkeley, Ph.D. (1966).

30) Kutateladze, S. S.: Fundamentals of Heat Transfer, Academic Press, Inc., N.Y., N.Y. (1963).

31) Osizik, M. N.: Basic heat Transfer, McGraw-Hill, (1977).

32) vonGlahn, U. H.: A Correlation of Film-Boiling Heat Transfer Coefficients Obtained with Hydrogen, Nitrogen, and Freon 113 on Forced Flow, NASA TN-2294.

33) VonBerg, R. L.; Williamson, K. D.; Edeskuty, F. J.: Forced-Convection Heat Transfer to Nitrogen in the Vicinity of the Critical Point. Advances in Cryogenic Engng., 15, 238-247 (1970).

34) Evaluation of Axial Lockup of Space Shuttle Main Engine Bearings from High Pressure Oxygen Turbopump (Contract No. NAS8-33576 - Task No. 105) Nov. 24, 1980. Final Report.

35) NBS Technical Note 648, "Thermophysical Properties of Nitrogen from the Fusion Line to 3500°R for Pressures to 150,000 psia", December 1973.

36) Hashin, Z. and Rotem, A. "A Cumulative Damage Theory of Fatigue Failure". Materials Science and Engineering, 34, 1978.

37) Stresses Due to Tangential & Normal Loads on an Elastic Solid with Applications to Some Contact Stress Problems, J. O. Smith and Chang Keng Liu.

38) Studies in Boiling Heat Transfer to Cryogenic Liquids, Kosky, Philip George, University of California, Berkley, Ph.D., 1966.

39) Handbook of Multi Phase Systems, Gad Hetsroni, McGraw-Hill Book Company.

40) Fundamentals of Heat Transfer, Samson Semenovich Kutateladze, Academic Press Inc., New York, NY

41) SHABERTH Computer Program Operation Manual Technical Report AFAPL-TR-76-90 October 1976.

42) Calculation of Elastohydrodynamic Film Thickness in High Speed Rolling and Sliding Contacts; H.S. Cheng, Mechanical Technology Inc. Report (MTI-67TR24)

43) Correlation of Elastohydrodynamic Film Thickness Measurements for Fluorocarbon, Type II Ester, and Ployphenyl Either Lubricants. NASA TN D-7825.

44) Weibull Distribution of Rolling Contact Fatigue Life and Deviations Therefrom, T. Tallian, ASLE Transactions S, 183-196, 1962.

45) Effect of Surface Hardness, Surface Finish, and Grain Size on Rolling Contact Fatigue Life of M-So Bearing Steel, R. A. Baughman, Journal of Basic Engineering, June 1960, p. 287-294.

46) Unlubricated High Temperature Bearing Studies, R. A. Baughman, E. N. Bamerger, Journal of Basic Engineering, June 1963, p. 263.